11-13-2017

A Multi-Scale Approach for Modeling Shock Ignition and Burn of Granular HMX

Pratap Thamanna Rao
Louisiana State University and Agricultural and Mechanical College

A MULTI-SCALE APPROACH FOR MODELING SHOCK IGNITION AND BURN OF GRANULAR HMX

A Dissertation

Submitted to the Graduate Faculty of the
Louisiana State University and
Agricultural and Mechanical College
in partial fulfillment of the
requirements for the degree of
Doctor of Philosophy

in

The Department of Mechanical and Industrial Engineering

by
Pratap Thamanna Rao
B.E., PES Institute of Technology, India, 2009
December 2017

This dissertation is dedicated to my parents Radha and Prahallada Rao, my sister Prarthana Rao, and my wife Kavya Dathathreya. Their love, encouragement, and support made this graduate experience possible and enjoyable.

Acknowledgments

I would first like to thank my advisor Dr. Keith A. Gonthier for his invaluable insight, guidance and support throughout the graduate school journey. He has helped me become a better student, researcher, and writer. I would also like to thank my advisory committee: Dr. Guoqiang Li, Dr. Mayank Tyagi, and Dr. John C. Flake, for agreeing to serve on my committee and for providing valuable critique and scientific advice. I thank the U.S. Defense Threat Reduction Agency (DTRA), and the U.S. Air Force Research Laboratory (AFRL/RWME) for sponsoring this research. I also thank the Department of Mechanical and Industrial Engineering for supporting me during my program and for giving me the opportunity to teach undergraduate Thermal Sciences Laboratory and Simulation Methods for Mechanical Engineers. I would also like to acknowledge the Center for Computation and Technology (CCT) at Louisiana State University for providing the high-performance computational resources without which this research would have been impossible.

I would like to thank my current and previous lab partners: Michael Crochet, Sunada Chakravrthy, John Gilbert, Mark Fry, and Joe Poynot for all the discussions we have had over the years on various technical topics and otherwise. Finally, I would like to thank my family and friends who have been a constant source of support throughout the graduate school journey.

Table of Contents

List of Tables

List of Figures

Abstract

Deflagration-to-detonation transition (DDT) in confined, low-density granular HMX (65%−85% Theoretical Maximum Density, TMD) occurs by a complex mechanism that involves compaction shock interactions within the material. Piston driven DDT experiments indicate that detonation is abruptly triggered by the interaction of a strong burn-supported secondary shock and a piston-supported primary (input) shock, where the nature of the interaction depends on initial packing density and primary shock strength. These interactions influence transition by affecting hot-spot formation within the micro-structure during pore collapse. In this study, meso-scale simulations of hot-spot formation in shock loaded granular HMX are used to guide the development of a new hot-spot based macro-scale ignition and burn (I & B) model. The model is conceptually similar to conventional I & B models but describes ignition in terms of pressure-dependent hot-spot formation rate and describes burn in terms of a dissipation-dependent regression rate that accounts for the onset of hot-spot facilitated burn for sufficiently strong shocks.

Inert macro- and averaged meso-scale predictions show good agreement, provided that the averaging area size is suitably selected. The I & B model reasonably predicts features representative of a Type−I DDT mechanism that is typical of particulate beds. The mechanism involves the formation of a solid-plug (i.e., a region having 100% TMD) within the bed that significantly affects reaction provided that the local dissipated work is insufficient to trigger hot-spot facilitated burn. Hence, the solid-plug affects the wave dynamics associated with transition. The model also predicts features characteristic of ignition and burn-controlled transition mechanisms and reasonably predicts time and distance to detonation over a wide range of piston impact speeds (150-600 m/s) and initial packing densities (68%−83% TMD). The shock strength required for transition from ignition to burn-controlled initiation increases with initial packing density, and is estimated to be approximately 0.2, 0.32, and 0.39 GPa for $\phi_0 = 0.68$, 0.77 and 0.83, respectively. Predictions also highlight conditions favorable for the formation of spontaneous combustion

waves whose propagation speed is influenced by shallow spatial gradients in solid volume fraction within the plug region.

Chapter 1
Introduction

Solid High Explosives are a class of combustible particulate solids that are widely used in military and commercial applications. Due to their high power producing capability ($\approx 1 \times 10^5$ GW/m^2) [1,2] they are often used in munitions, rocket propellants, mining, drilling, and explosive welding. Some of the commonly used explosive materials are Tetranitro tetrazocane (HMX: $C_4H_8N_8O_8$), Trinitro triazinane (RDX: $C_3H_6N_6O_6$), Pentaerythritol tetranitrate (PETN: $C_5H_8N_4O_{12}$), and Trinitrotoluene (TNT: $C_7H_5N_3O_6$). Typical grain sizes range from $1 - 500$ μm for these materials which are generally manufactured by pressing or casting explosive particles with a polymeric binder.

Safety of energetic materials during storage, handling, and transportation is important as accidental impact of these materials can lead to *combustion* and, if conditions are favorable, to *detonation* resulting in a catastrophic event. Davis [3] identified possible stimuli for accidental initiation of these materials and concluded that fire and impact are the most likely sources during the handling of explosives. Detonation of explosives is associated with shock-wave propagation velocities of $5-9$ km/s and pressures of $20-40$ GPa, conditions under which measurements are often difficult and uncertain. This difficulty in measurements necessitates the development of improved Modeling and Simulation (M&S) techniques that can predict the shock sensitivity and performance of explosives.

In this study, we consider initiation of granular explosives (GXs) by mechanical impact because of its relevance to sensitivity and the safe handling of these materials. Shock initiation of GXs is typically modeled as a planar piston impact problem, as shown in Fig. 1.1. Here, a rigid planar piston impacts the granular bed having ambient solid volume fraction ϕ_0 with a constant speed U_P. Solid volume fraction ϕ is defined as the ratio of volume occupied by explosive granules to the total volume and is generally expressed as percentage of theoretical maximum density (% TMD).

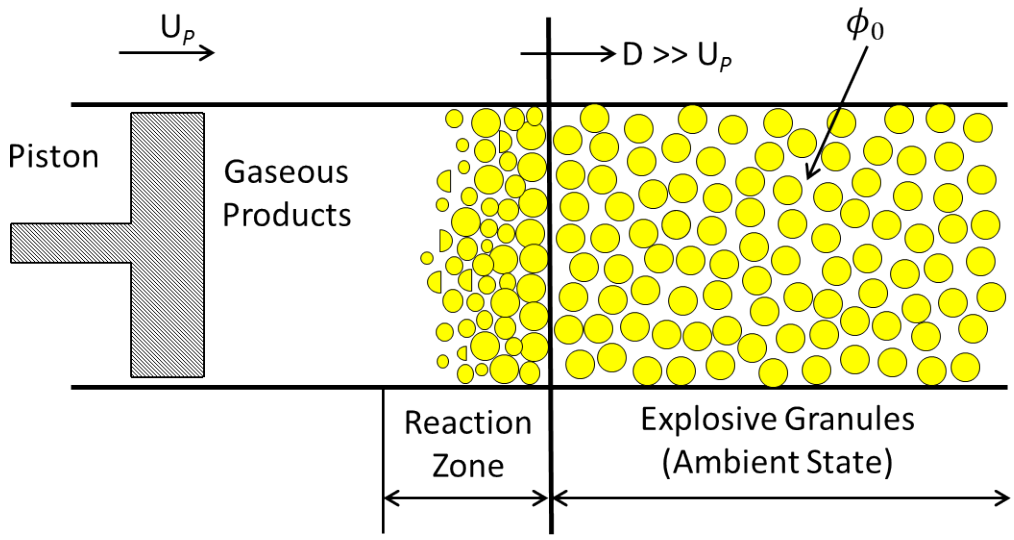

Figure 1.1: Schematic of the model problem. U_P is piston impact velocity and D is detonation wave speed. ϕ_0 is the initial solid volume fraction of the granular bed.

In this figure, transition to detonation has already occurred within the GX, and the resulting detonation wave travels to the right at a supersonic speed $D >> U_P$. Behind the detonation wave is a thin reaction zone, typically few millimeters depending on shock strength, where the reactant explosive material is converted to product gas due to adiabatic compression of the explosive by the lead shock that has sufficient strength to initiate chemical reaction. Due to reaction, mass, momentum and energy exchanges between solid and gas phases occur within this region.

Of particular importance to the energetics community is *Deflagration-to-Detonation Transition* (DDT) and *Shock-to-Detonation Transition* (SDT) of these materials. Deflagration refers to low speed and low pressure (0.3−0.5 km/s, 0.1−1.0 GPa) subsonic combustion, whereas detonation refers to high speed and high pressure (3−9 km/s, 1−10 GPa) supersonic combustion. DDT involves a weak input shock that leads to a burning process that terminates in detonation which can occur on millisecond time scales. SDT involves a strong input shock that starts the chemical reactions and develops into a steady detonation, usually on microsecond time scale. In both processes development of a shock wave is a key component and hence the two processes are not mutually exclusive. M&S techniques play a key role in understanding shock induced heating and subsequent transition to detonation

within energetic materials.

In practice, polymer-bonded explosive (PBX) is widely used that consists of explosive powder (RDX, HMX, TNT, etc.,) bound together in a polymer matrix (typically 5-10% polymer by weight). The focus of this study is on *granular HMX* which is categorized as high explosive due to its high power producing capability. HMX was discovered as a by-product in the production of RDX and is mostly used in its granular (binderless) form in initiators because of high shock sensitivity. Although it is as sensitive as RDX, it is seldom used alone in military applications but is normally mixed with another compound such as TNT and binder. Granular HMX is modeled because its compaction and detonation behavior are reasonably well-characterized and is commonly used as a surrogate for M&S of damaged explosives.

Shock sensitivity of explosives is influenced by the presence of heterogeneities (e.g., defects, voids, grain boundaries, porosity). It is widely accepted that if a strong shock propagates through an explosive, it gives rise to regions of localized high temperatures, known as *hot-spots*, which can trigger reaction and subsequent transition to detonation. First recognized in the seminal work of Bowden and Yoffe [4], hot-spot formation increases the sensitivity by localized ignition of the material. Of the many hot-spot formation mechanisms, a key formation mechanism is the result of shock wave interactions with heterogeneities present in the material. If conditions are appropriate, neighboring reactive hot-spots can thermally interact, and coalesce into bigger, more intense hot-spots resulting in significant volumetric energy release which can drive transition to detonation. Hot-spots can rapidly form over length scales that are much smaller than the average particle size, whereas the detonation of explosives resulting from low pressure impact often occurs slowly over comparatively large distance ($\approx$ 5 cm) [5, 6]. This disparity in scales has motivated continuum-based M&S at both the *meso-scale* and *macro-scale*. In particular, granular HMX is known to exhibit enhanced sensitivity due to the presence of intergranular pores which makes it a good choice for scientific and engineering study.

In this study, meso-scale M&S is used to track discrete interaction between particles ($\approx$ 4000-5000 particles) and to resolve thermo-mechanical fields within particles during shock induced pore collapse. While it is possible, given an appropriate constitutive theory, to pose a detailed model describing the complex contact mechanics, thermodynamics and chemistry occurring at the particle scale, it is infeasible to numerically resolve fine scale structures inherent in the model and to establish its engineering scale manifestation. Particular emphasis will be placed on characterizing how hot-spot formation depends on the effective (averaged) thermo-mechanical quantities such as pressure and dissipative work, and will be investigated as a basis for formulating improved hot-spot motivated macro-scale models.

Spatially averaged meso-scale fields will be used to guide development of a thermodynamically compatible macro-scale ignition and burn model that explicitly incorporates computationally derived relations between microstructure, shock strength and hot-spots. The theory is posed in terms of intrinsic functions that implicitly account for inter-phase interactions and dissipative phenomena occurring at meso-scale that are difficult to elucidate from macro-scale data. The constitutive model was used to computationally examine how shock induced transition to detonation in low density HMX is affected by input shock strength and initial packing density.

In this chapter, we first briefly discuss the background and motivation for study of shock induced heating and combustion of granular HMX. Next, a survey of the relevant experimental and modeling effort is discussed. Last, the specific objectives of this study, and an outline of the dissertation is given.

1.1 Literature Review

In this section, an overview of experimental and modeling work relevant to this study is provided.

1.1.1 Experimental

Experiments are reported in the literature that were conducted to identify the mechanism of transition to detonation in energetic materials. Some of the relevant experiments are those of Griffiths and Groocock [39], Campbell and co-workers [40–42], Korotkov and co-workers [44], Bernecker and Price [45–50], Samirant [52–54], McAfee and co-workers [5], Luebcke and co-workers [55,56], Sheffield and Engelke [38,67], Burnside and co-workers [58], Gifford and co-workers [59–61], and Parker and co-workers [62]. In 2015, Proud and co-workers [63] published a review that describes most experimental diagnostic techniques that have been used to study deflagration and detonation phenomena and serves as a good reference for further reading.

Detonation is mostly pictured as a violent, uncontrollable, catastrophic event. But this phenomena can be presented as a repeatable sequence of events that can be described in terms of conservation principles and material specific properties of the explosive. The following discussion is restricted to shock initiation and detonation phenomena of low density (65% - 85% TMD) GXs. Within the context of these materials, two possible transition mechanisms, DDT and SDT, based on increasing input shock strength, have been reported in the literature. A brief discussion of the two transition mechanisms along with the schematic of the overall process is first provided.

- **Deflagration-to-Detonation Transition**

Bernecker and Price [45] discussed a variety of DDT phenomenology in GX beds, and made qualitative and quantitative mechanistic arguments for the differences as a function of initial bed density. Gifford and co-workers [59] categorized DDT mechanisms as *Type I* (higher density packed and pressed beds) and *Type II* (poured and lower density beds).

Type I DDT was found to be typical of particulate granular beds with density greater than $50-70\%$ TMD ($30-50\%$ Porosity) and Type II DDT was found to be typical of poured lower density particulate beds with density less than 40% TMD (60% Porosity). McAfee [64] published a classic review where features observed in DDT of Type I and

Table 1.1: Phenomena observed/predicted for Type I and Type II types of DDT. Part of the table from Ref. [64] is reproduced here.

Type of DDT →	Type II		Type I	
Initial State →	Very low-density beds	Pour-density beds	Packed beds	Pressed beds
Phenomenon ↓				
Ignition	√	√	√	√
Conductive burning	√	√	√	√
Flame acceleration	√	√	√	√
Flame intrusion	√	√	√	
Channel Formation	√	√		
Convective burning	√	√	√-	
Thermal explosion		√	√	√-
Flame Jetting			√	
Compaction	√	√	√	√-
Compressive burning		√	√	√
Shock Formation	√	√	√	√
Detonation in compacted material	√	√	√	√
Detonation in pristine material	√-	√	√	√
Retonation	√	√	√-	

Type II particulate beds were clearly indicated. Because the focus of this work is on low-density granular beds, the features and differences observed in Type I and Type II DDT are reproduced in Table 1.1 for clarity. In particular, granular beds with 10-30% porosity are considered in this study. Therefore, Type I DDT phenomenology is most relevant and is discussed in greater detail in the following section.

Type I DDT Phenomenology

Much of today's understanding of the transition mechanism associated with Type I DDT of granular HMX can be attributed to McAfee and co-workers [5, 6]. They studied granular HMX confined in thickwalled steel tubes with x-radiography, light emission, stress gauges, and various ionization pin techniques. Complete details of the experimental characterization can be found in Ref. [5]; only details important to this study is highlighted here.

The HMX was initiated by driving a piston into the bed and a qualitative and quantitative analysis was discussed in terms of a mechanistic process. Key features observed in their analysis are summarized in Figure 1.2 which shows the state of the material and piston position at various snapshots in time of the DDT-Tube test experiment.

- At time t_0: This time represents the initial condition of the experiment. The piston, labeled **p**, is at rest and the unstressed granular HMX bed is at original density. In this experiment the initial density was 1.22 g cm^{-3} (65% TMD or 35% Porosity).
- At time t_1: Generally a burn chamber behind the piston propels it forward as it accelerates to an impact velocity of approximately 160 m/s. The motion of the piston generates and supports the propagation of a compaction wave, labeled **c**, that increases the density to 90% TMD. In this early induction period, as the material is compacted weak exothermic chemical reaction is initiated due to local heating mechanisms.
- At time t_2: The compaction wave **c** has propagated further into the tube. After an

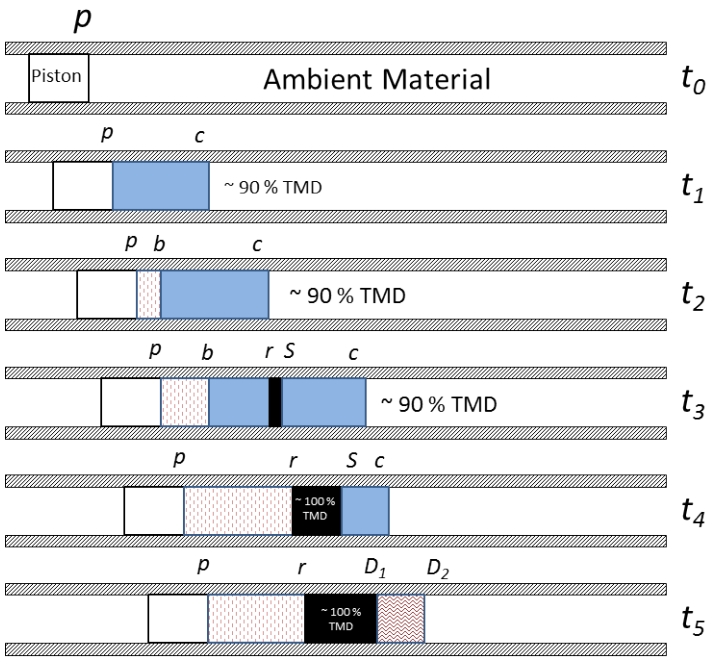

Figure 1.2: A schematic time sequence of DDT Tube Test. Different shading and textures note the boundaries of the various regions. Mechanism is detailed in the text.

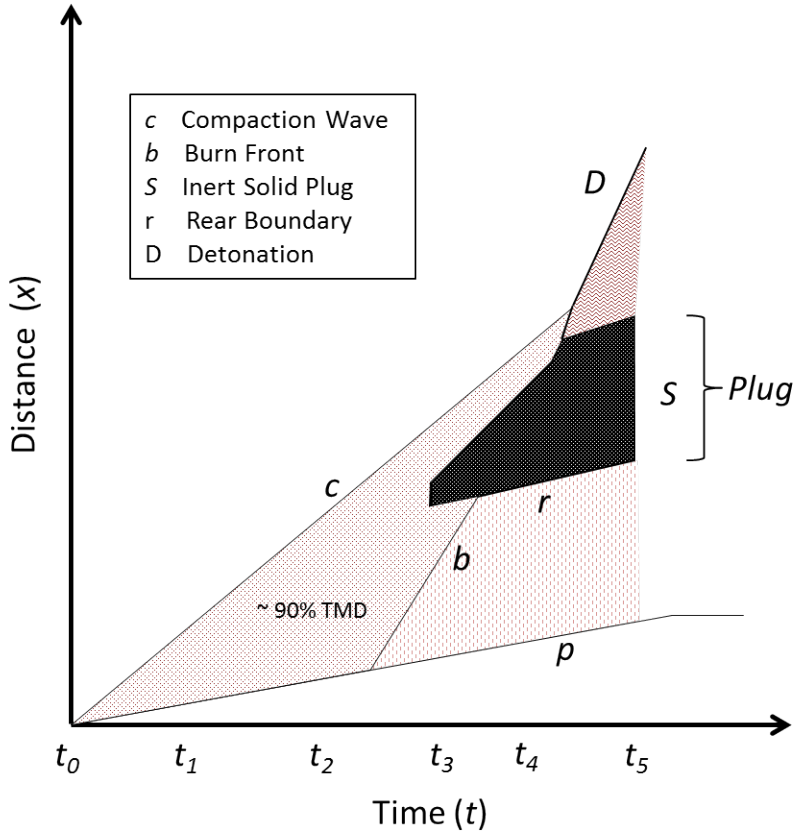

Figure 1.3: Generic $x-t$ diagram shows the same mechanism for DDT as that in previous figure. The time axis labels $(t_0 - t_5)$ correspond to the time snapshots. τ is induction-time.

induction delay (τ), the explosive-grains next to the piston start burning slowly to produce gaseous reaction products. The pressure of the gaseous reaction products starts building due to confinement provided by the steel tube, piston, and low permeability of the compacted material ahead of it. A burn-front, labeled **b** is seen to develop near the piston surface. This indicates the beginning of significant reaction (burning).

- At time t_3: As gaseous products accumulate, the rising gas pressure drives a secondary compaction wave into the already compacted material ahead of it. The secondary compaction wave further reduces porosity within the material and produces a near 100% TMD *solid-plug*. The bed permeability within the plug region is minimal and the burn rate drops by a factor of 20-30. The rear of the plug is labeled **r** and at the front of the plug a strong shock **S** develops (discussed next).
- At time t_4: At this time, the rear of the solid-plug is pushed strongly by the high-pressure gas accumulated behind it. The rear interface of the plug now acts as a virtual piston that drives the formation of a strong shock **S**. This shock propagates faster in the 90% TMD compact and the material behind the rear boundary **r** continues to burn. The ignition wave **b** essentially stops when it reaches the solid-plug as the burn rate drops due to low permeability of the compacted material [51].
- At time t_5: The shock **S** is now strong enough to initiate detonation by a normal shock-to-detonation transition in the 90% TMD bed at the head of the plug. The detonation velocity (D_1) is characteristic of the 90% TMD material and quickly becomes overdriven relative to the ambient material. The overdriven detonation subsequently overtakes the primary compaction wave **c** and propagates into the ambient material where the velocity is (D_2) characteristic of the original density material.

Figure 1.3 illustrates the transition mechanism in the characteristic $x-t$ plane which is useful for tracking wave and particle trajectories. After an induction time τ, an ignition front **b** develops next to the surface of the piston due to the increasing pressure generated by burning of explosive grains next to the piston. The ignition wave **b** grows in strength and further compacts the 90% TMD bed to a near 100% bed ahead of it. When the ignition wave **b** reaches the bottom of the plug **r**, it essentially stops because of the difference in burn rate between the 90% and 100% TMD compact. The material between the rear of the plug **r** and head of the plug continues to burn. The increasing pressure in the burning region adjacent to the plug accelerates the rear boundary **r**, which in turn rapidly accelerates the strong shock **S**. When the shock **S** is strong enough, a shock-to-detonation transition (SDT) takes place in the 90% compact whose velocity D_1 is characteristic of the 90% compact. The detonation slows to the velocity characteristic of the ambient bed to D_2 after it overtakes the compaction wave **c**.

In summary, the burn rate is slow at first, but increases after a induction time τ. The ignition wave is strengthened due to enhanced gas pressurization in the region between the piston surface and explosiive grains. When the shock **S** is strong enough, a shock-to-detonation transition takes place at the head of the plug. The induction period is determined by the extent of decomposition caused by the lead compaction wave **c**. This study by McAfee and co-workers [5, 6] concluded that even relatively moderate conditions (weak initiation) can lead to shock pressures high enough to shock-initiate HMX. McAfee and co-workers also presented results for HMX samples having an ambient density of 75% TMD. A similar sequence of events were observed but detonation did not occur at the head of the plug. The plug-shock was formed but was not strong enough to transition to detonation in this case.

Luebcke and co-workers [55, 56] have interpreted some of their optical measurements on Pentaamminecobalt Perchlorate (CP: $C_2H_{15}Cl_2CoN_{10}O_8$) and PETN. They observe a similar set of events with a rearward propagating wave originating in the plug region. They

characterize it as retonation wave having a lower velocity than the forward propagating detonation. Griffiths and Groocock [39] published streak photographs of piston driven Type I DDT in PETN having original bed density of 68% TMD. They pointed out similar events: fast reaction, onset of detonation at the head of the plug, detonation in the original bed, and a retonation.

Samirant [52–54] published a series of initiation data on RDX/wax and ball powder; most observations were consistent with a Type I DDT mechanism, but did not report plug formation. Baer and co-workers [57] presented both experimental and model analysis of DDT of CP using electronic streak data for 55% to 80% TMD. For 80% TMD samples, their streak photographs indicate a clear separation of the initial burn front and detonation. They have also discussed experiments where the transition mechanism changes from Type I to Type II for lower density samples. Similar transition mechanism and features have been predicted by simulations presented later in Chapter 5.

Similar sequence of events have been observed after a slow cook-off period by other DDT experiments [5,56], where combustion was directly initiated using gasless pyrotechnic igniters. A key purpose of these experiments was to identify the role of convective burning in DDT by eliminating pre-pressurization of the explosive bed. Results of these experiments supported the earlier observation made by Campbell [40–42] that convective burning is only important during early stages of burning. Complete details of other explosives that exhibit Type I DDT are available in the reference.

Type II DDT is characteristic of granular beds with approximately less than 40% TMD (60% Porosity). As the density decreases, the larger void fractions allow convective processes to play a more significant role. The bed also allows for gas intrusions, jetting, channeling and other non-planar processes making the interpretation of data from experiments complicated and difficult. Since the focus of this study is on granular beds with 10-30% porosity, a discussion of Type II DDT is not given here.

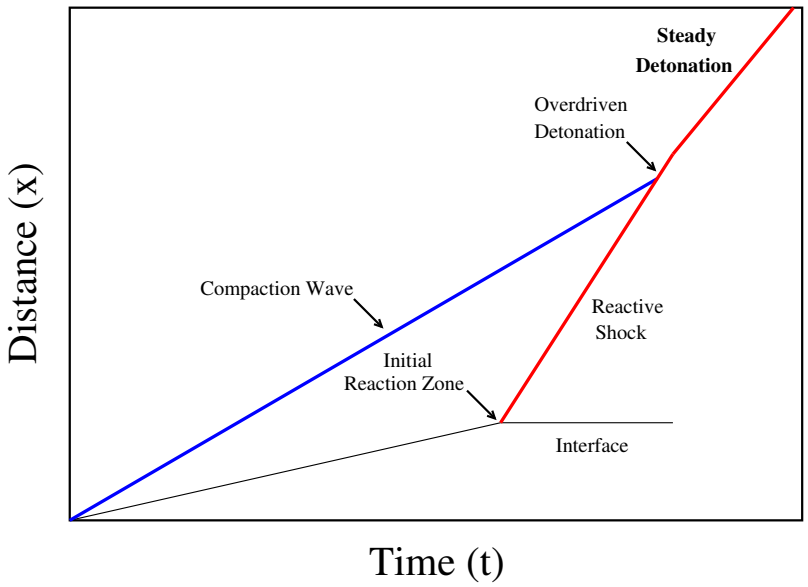

Figure 1.4: Time-distance diagram for a typical explosive SDT process.

- **Shock-to-Detonation Transition**

High speed piston-impact simulations directly transition to detonation by a shock-to-detonation transition mechanism. SDT in granular HE's was studied in detail by Campbell and co-workers [40], Sheffield and co-workers [67], and Chaiken [43] leading to much of the basic understanding that exists today. Figure 1.4 shows the time-distance diagram for a typical explosive SDT process. Following impact as the strong shock propagates through the material, all the porosity within the material is eliminated and the region around the impact zone is subjected to a temperature rise which quickly triggers reaction due to shock heating. This in-effect can be considered as a "hot-spot" facilitated burn (discussed in Section 5.1.2) that aids the formation of a large number of hot-spots which send out pressure waves that can coalesce to produce a strong shock. When the strong shock breaks out, it runs through pre-compacted and heated material by the input shock, causing a overdriven-detonation. With time this overdriven detonation settles to a detonation wave whose velocity is characteristic of the ambient bed.

- **Pop-Plot**

Detonation of energetic materials is often characterized by run distance-to-detonation and time-to-detonation for a sustained input shock. If run distance is measured for a

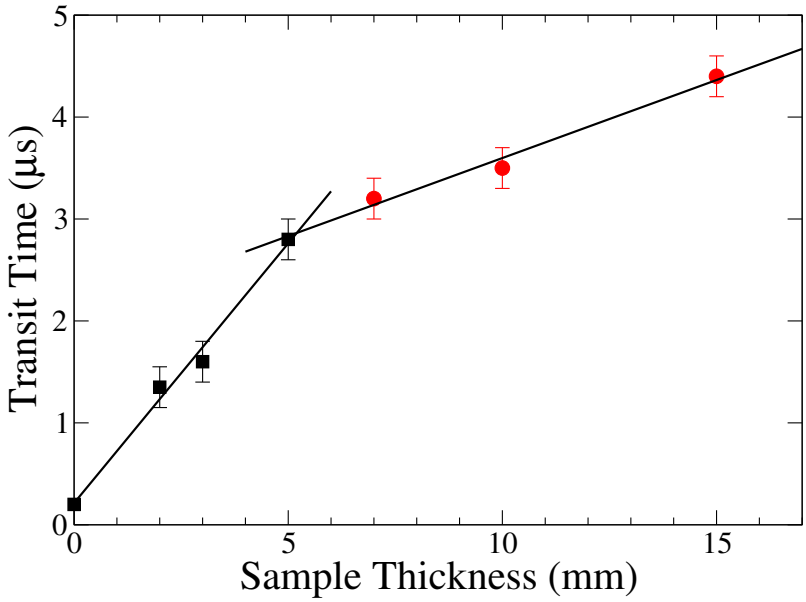

Figure 1.5: Typical transit time as a function of sample thickness plot for a particular input shock pressure. Lines are least square fits of the data [141].

number of different shock inputs, a log-log plot of the data can be made. This plot was first developed by Ramsay and Popolato [65], and is often called the *Pop-Plot*.

Run distances-to-detonation were estimated by Dick [141] for granular HMX using explosive plane-wave-lens driven cutback tests. As shown in Fig. 1.5, the average transit times through the HMX sample were measured and plots were made of transit time as a function of compact thickness and the run distance was estimated to be the point where the data changed slope. Dallman and Wackerle [66] measured run distances-to-detonation in explosively driven wedge experiments using optical techniques for PBX 9502. Pop plots for different explosives can be found in Ref. [67]. Several experiments were performed to measure average transit times through HMX samples at initial solid volume fraction of 65% for input pressures of 0.8 and 2.0 GPa and estimated the distances to detonation of about 5 and 3 mm, respectively. These measurements showed that increasing the porosity reduces the shock strength required for detonation within a given distance, i.e., the shock sensitivity increases as the porosity increases. A detailed examination of Pop-Plot data and predictions is given later in this thesis.

1.1.2 Modeling

Several modeling approaches have been formulated to describe reactive multi-phase flows containing solid particles and gas. In this study, a thermodynamically compatible macro-scale ignition and burn model is developed that explicitly incorporates meso-scale features of hot-spot formation within the context of a two-phase macro-scale constitutive theory that can be used for the analysis of engineering scale applications. A review of common approaches and burn models available in the literature is summarized below.

- **Meso-Scale Modeling**

Meso-scale modeling is suitable for analyzing phenomena occurring between and within grains such as the formation of hot-spots that can ultimately lead to ignition. As mentioned, initiation of GXs is intimately related to the formation of hot-spots. Various hot-spot formation mechanisms have been proposed which include inter-particle friction [69,74], plastic deformation of particles [24,70–72,74], particle fracture [73], adiabatic gas compression by interstitial void collapse [4,74], shock interaction between particles and voids causing jetting, plastic flow, particle fracture, and shock impedance mismatch between components of high explosives that leads to shock interactions.

Meso-scale M&S have been performed on both inert and reactive granular systems. Though meso-scale modeling is computationally expensive, advancements in computing have enabled the study of large scale systems involving thousands of particles. These simulations can extract important physical mechanisms that lead to *ignition* of energetic materials. In this study, ignition refers to the process where hot-spots undergo an induction (or incubation) period following shock passage during which they intensify and begin to interact at the pore scale leading to the onset of detectable burn at the macro-scale. The induction time following shock passage is referred to as the *ignition time*. Relevant meso-scale M&S studies include those of Menikoff [19,20], Mas and co-workers [25,26], Baer and co-workers [27], Benson and co-workers [70,78], Panchadhar and Gonthier [31], and Baura and co-workers [34].

Inert meso-scale simulations have been performed in both 2D and 3D. Two-dimensional simulations containing hundreds of particles have been performed by Kumar and co-workers [76] and Williamson [77]. Three-Dimensional simulations performed by Baer [24] consisted of thousands of multi-material particles. High pressure shock loading of particle ensembles have been carried out by Benson and co-workers [70,78], and Menikoff and co-workers [20], and low pressure simulations were carried out by Lowe and co-workers [79]. Panchadhar and Gonthier [31] developed a combined 2D Lagrangian finite-discrete element technique and numerically implemented it to efficiently simulate the impact response of large ensembles of particles ($\sim$ 2000-4000 particles). Their analysis indicated that viscoplastic dissipation during pore collapse affected the bulk temperature rise within the material, but frictional heating was resposible for high intensity hot-spots with temperatures in the range of 800-1500 K. Gilbert and co-workers [81] examined how the initial porosity of granular HMX affected statistical variations in hot-spot intensity, morphology, and spatial proximity behind sustained, piston supported waves.

Barua and co-workers [34] developed a cohesive finite element method (CFEM) framework that accounts for particle fracture and quantified the thermomechanical response of PBX and HMX. Rai and Udaykumar [37] have developed a numerical framework that uses an image to computation approach to analyze shock loading of real micro-structures of pressed HMX. Reactive meso-scale modeling and simulation have also been used to describe the DDT mechanism in granular explosives [24, 82, 83]. Baer [24] performed reactive meso-scale simulations using an ignition/growth two state history variable reactive burn (HVRB) model. The reaction was triggered at a pressure threshold and a pressure-dependent rate law described the extent of reaction.

Meso-scale M&S gives valuable information about hot-spots that can be used to formulate an ignition criterion to be used in macro-scale theories which establishes the induction period before the onset of vigorous burn. To the authors knowledge, none of the models discussed above have explicitly used meso-scale information to develop macro-scale theories.

Complete details about the ignition model developed in this study is given in Section 5.1.1. However, the length scales of typical explosive materials used in applications are on the order of centimeters or larger, which renders meso-scale M&S computationally expensive and impractical. This necessitates the use of macro-scale modeling techniques.

- **Macro-Scale Modeling**

The development of two-phase macro-scale DDT models dates back to the early 1960's. Relevant studies include those of Kuo and co-workers [84], Butler and Krier [8], Baer and Nunziato [7], Powers, Stewart and Krier [86–88], Saurel and co-workers [11], the Los Alamos National Laboratory DDT-Modeling group [12–15], Gonthier and Powers [10], Chinnayya and co-workers [16], Schwendeman and co-workers [135], and Crochet and Gonthier [89–91].

The two-phase model developed by Baer and Nunziato (BN) [7] has considerably influenced the energetics community and forms the basis for a large body of work. In their two-phase model both phases are fully compressible and an evolution equation for solid volume fraction is proposed based on the pore collapse model of Carroll and Holt [92]. The interphase exchange terms were selected such that entropy inequality is satisfied for the reacting mixture. In a series of publications, Bdzil and co-workers [12–15] critically reviewed the BN model and generalized the theory for a two-phase mixture. Gonthier [93] recently generalized the BN model to account for the existence of an arbitrary number of condensed phases and a gas product phase. Formulation of such a generic theory was motivated by desire to model both low and high pressure impact and initiation of heterogeneous energetic solids composed of several condensed phases (e.g., explosive, metal, oxidizer, binder, etc.) having distinct densities, velocities, temperatures and particle sizes. Crochet and Gonthier [89–91] further extended the model to include general chemical reactions between and within all phases and developed a computationally inexpensive method to solve the model equations.

Multi-phase continuum theories used to study shock initiation of GXs describe the effective (or bulk) response of the material and account for hot-spot processes using sub-

grid modeling. Various sub-grid models, known as *phenomenological burn models* that describe the formation, growth, and interaction of reactive hot-spots at the pore scale have been used. Developing a simple model that can incorporate meso-scale processes is a key objective of this work and the authors ongoing research. Most of these models have been traditionally applied to study SDT in PBX's having 0-5% porosity and more recently have been applied to study DDT in low-density GXs.

The widely used *Ignition and Growth Model* was developed by Lee and Tarver [94] to describe SDT in PBX's. This model assumes a single reaction progress variable λ, where the reaction rate is given by

$$\frac{d\lambda}{dt} = \underbrace{I \cdot (1-\lambda)^x \, \eta^r}_{\textbf{Ignition}} + \underbrace{G \cdot (1-\lambda)^x \, \lambda^y p^z}_{\textbf{Growth}} \tag{1.1}$$

and

$$\eta = \frac{V_0}{V_1} - 1 \tag{1.2}$$

Here λ is the fraction of explosive that has reacted; t is the time; V_0 is the initial specific volume of the explosive; V_1 is the specific volume of the shocked, unreacted explosive; p is pressure; and I, x, r, G, y and z are constants fit to pressure or velocity history data from one dimensional shock initiation experiments. The first term represents ignition of hot-spots and the second term represents subsequent growth of reaction. Here, a small fraction of the explosive is assumed to be ignited by the passage of the shock front, and the growth in reaction rate is controlled by the shock pressure. The presence of a large number of hot-spots can consume the explosive material within a few microseconds.

The term η^r was used to investigate various hot-spot formation mechanisms, where η is the relative compression of unreacted explosive that can be related through the unreacted equation of state to thermodynamic parameters involved in the initiation process. The second term in the equation describes the growth of the reaction. The constant G corresponds to a surface area to volume ratio and the p^z term represents a pressure dependent

regressive burn. Using this model, they were able to match experimentally determined run distance to detonation for various explosive mixtures undergoing sustained shock loading.

The DAGMAR Model applied to high-density PBX's was first developed by Wackerle and co-workers [95] and later improved by Anderson and co-workers [96]. In this model, the reaction rate is a function of lead shock pressure, equilibrium mixture temperature and first order reaction progress variable. The model parameters were calibrated to embedded manganin stress gauge data. The JTF Model developed by Johnson and co-workers [97] is a more elaborate version of an ignition and growth model. The reaction constitutes a multi-step mechanism having rates that are a function of the lead shock pressure, equilibrium mixture pressure and first order reaction progress variable. The model parameters were calibrated with embedded magnetic velocity gauge data [98]. The WSD Model developed by Wescott and co-workers [100] is a generalization of the ignition and growth model. The shock density is used to switch between rates calibrated to the ignition and propagation regimes. In each regime the rate depends on the local pressure and the reaction progress variable. In the CREST Model developed at Atomic Weapons Establishment (AWE) by Handley and co-workers [101], the reaction rate is independent of local flow variables behind the shock e.g. pressure and temperature but a function of reactant entropy. Two reaction progress variables are used to tune the reaction profile based on comparisons of embedded magnetic velocity gauge data [102].

Recently, Menikoff and Shaw [103] developed the SURF Model based on the ignition and growth concept, which incorporate three key physical effects: (1) the spatial number density of hot spots or burn centers, which depends on lead shock strength; (2) the growth of burn fronts triggered by burn centers, which depends on the local deflagration speed; and (3) a geometric factor that accounts for the overlap of deflagration wavelets from adjacent burn centers, which depend on material heterogeneities that determine the distribution of hot-spots.

Since most of these models are based on mixture theory formulations or volume average

methods, they inherently contain many disadvantages. The DAGMAR and JTF model uses artificial viscosity to control shock dissipation. The algorithm determines the lead shock by scanning viscous pressure profiles to determine the first local minimum. Numerical issues arise in this method when a compressive wave follows the lead shock. The WSD model detects the time of arrival of lead shock based on the maximum value of $\partial P/\partial t$ for each cell. The shock state is determined by a level set algorithm, which serves as a switch between the initiation and growth regimes. The CREST two-phase model uses solid entropy as a measure of the lead shock strength. However, Petitpas and co-workers [104] have identified issues with shock capturing in two-phase models in which the component energy equations are non-conservative. The success of these commonly used hot-spot motivated burn models also hinges on proper tuning of rather large parameter sets to initiation data. Though many parameters have a physical interpretation based on hot-spots, it is difficult to establish their values in the absence of hot-spot and initiation data for the particular meso-structure under consideration. A recent focus within the reactive solids community is to computationally examine the relationship between meso-structure and shock induced ignition and initiation due to current limitations in measuring hot-spot formation at the grain scale. Our current study focuses on low-density (high initial porosity) GX's, but adopts many of the key ideas from these existing models applied to PBX's.

1.2 Study Objectives

The two overall objectives of this work are: (1) to develop a thermodynamically compatible macro-scale ignition and burn model that explicitly incorporates computationally derived relations between microstructure, shock strength, and hot-spots; and (2) to predict and analyze detonation transition mechanisms by numerically simulating piston initiated DDT and SDT, and to compare with Pop-Plot data available from experiments. The model was used to computationally examine how shock induced transition to detonation in low density HMX is affected by input shock strength and initial packing density.

Specific objectives of this work include the following.

1. Inert single shock loading of granular HMX: Meso-scale simulations are performed to computationally examine how initial porosity influences dissipation rates within inert quasi-steady compaction wave profiles and to compare predictions to a macro-scale compaction theory. The meso-scale model tracks the evolution of thermomechanical fields within individual particles that result from pore collapse by compaction waves. Effective wave profiles are obtained by averaging meso-scale fields over space and time. The macro-scale theory predicts the variation in effective thermomechanical fields during compaction due to an imbalance between the effective solid pressure and a configurational stress. Particular emphasis is placed on comparing effective quasi-steady wave profiles obtained by meso-scale simulations to those given by a macro-scale compaction theory. Only the inert material response is considered so that the effects of dissipative heating mechanisms that give rise to ignition can be isolated and studied. It is desirable to determine the extent to which these independent descriptions give comparable results for wave profiles and end states.

   As a secondary objective, computational analysis is performed to characterize how rapid successive shock loading of low density HMX affects dissipation and ignition associated with the onset of vigorous burn. Meso-scale simulations are used to predict effective shock profiles and to examine hot-spot fields induced by pore collapse. Resolved shock profiles are compared to those given by the macro-scale compaction theory, and both are analyzed in a thermodynamic space that highlights *shock desensitization* effects.

2. Analysis of Detonation Transition Mechanisms: Piston driven DDT and SDT experiments indicate that detonation is abruptly triggered by the interaction of a strong combustion-supported secondary shock and a piston-supported primary (input) shock, where the nature of the interaction depends on initial packing density and primary shock strength. These interactions influence transition by

affecting dissipative heating within the microstructure during pore collapse.

A history-variable ignition model based on the variation in hot-spot formation frequency is used in a macro-scale model to numerically simulate piston-initiated DDT and SDT. The ignition model establishes the induction period before the onset of vigorous burn. The burn model is conceptually similar to traditional Ignition and Growth-type models but accounts for the onset of vigorous combustion in terms of parameters that are explicitly computed from hot-spot fields predicted by meso-scale M&S. The model provides a mostly phenomenological expression for the kinetics of the chemical reaction associated with burning of explosive grains. The gas pressure dependent model is widely accepted in the combustion literature and is regarded as empirical. A key objective of this study include predicting and analyzing two-phase detonation transition mechanisms from a wave interactions and phenomenological perspective.

This modeling and computational research advances fundamental knowledge of rate-dependent dissipative phenomena occurring within reactive solid explosives which is important for assessing their shock sensitivity. This thesis is organized as follows. The meso-scale M&S technique is discussed in Chapter 2. The mathematical and physical description of compaction induced dissipation is highlighted within the context of the meso-scale description. The two-phase macro-scale model is presented in Chapter 3. The governing equations are first presented followed by the formulation of additional evolution equations. The numerical method used to solve the system of equations is then presented. Chapter 4 gives the results for inert single shock loading of granular HMX. Chapter 5 gives the significant results for the analysis of detonation transition mechanisms. Finally, future work is given in Chapter 6.

Chapter 2

Meso-Scale Model

The meso-scale model tracks the temporal and spatial evolution of thermomechanical fields within large ensembles of deformable particles. A detailed exposition of the model equations, contact conditions, and constitutive theory is given in Refs. [30, 31]. Therefore, only a brief summary is given here that emphasizes features directly germane to this study. The deformation induced heating of the granular explosive is modeled as a multi-particle contact problem, and is formulated as an initial-boundary-value problem (IBVP) for the displacement field u and temperature field T, described by the mass, momentum and energy conservation equations.

2.1 Governing Equations and Dissipation

Evolution equations for mass, momentum and energy within particles are given by:

$$\dot{\rho} = -\rho \boldsymbol{\nabla} \cdot \dot{\mathbf{u}}, \tag{2.1}$$

$$\rho \ddot{\mathbf{u}} = \boldsymbol{\nabla} \cdot \boldsymbol{\sigma}, \tag{2.2}$$

$$\rho c_v \dot{T} = -\boldsymbol{\nabla} \cdot \mathbf{q} + \rho r, \tag{2.3}$$

where ρ is the local density, $\mathbf{u}$ is the displacement vector, $\boldsymbol{\sigma}$ is the Cauchy stress tensor, r is the deformation induced heating, $\mathbf{q}$ is the heat flux, c_v is the constant volume specific heat, and $\boldsymbol{\nabla} \equiv \partial(\bullet)/\partial \mathbf{x}$ is the spatial gradient operator. The time derivative of a variable is denoted by a "dot" above it. Particles are assumed to be initially stationary and stress free.

Mechanical and thermal contact conditions imposed along particle boundaries Γ are

Table 2.1: Thermomechanical properties of HMX used for the meso-scale simulations.

Property	HMX
Density (kg/m^3)	1903
Yield Stress (GPa)	0.37
Poisson's Ratio (-)	0.20
Young's Modulus (GPa)	24.0
Bulk Modulus (GPa)	13.33
Specific Heat (kJ/kg/K)	1.50
Thermal Conductivity (W/m/K)	0.5
Longitudinal Sound speed (km/s)	2.65
Shear Sound Speed (km/s)	2.29

given by

$$\boldsymbol{\sigma} \cdot \mathbf{n} = \mathbf{t}_c \qquad \text{on } \Gamma \ \forall \ \text{t}, \tag{2.4}$$

$$-k\boldsymbol{\nabla} T \cdot \mathbf{n} = q_f + q_c \qquad \text{on } \Gamma \ \forall \ \text{t}, \tag{2.5}$$

where $\mathbf{n}$ is the local unit normal vector to Γ, $\mathbf{t}_c$ is the local contact traction vector, q_f is local frictional heat flux, q_c is the local heat flux needed to impose ideal thermal contact, and k is the thermal conductivity. In addition to satisfying the conservation laws, the second law of thermodynamics is expressed by the Clausius-Duhem inequality as:

$$\rho \frac{d\eta}{dt} - \frac{1}{T}\left(\rho r - \nabla \cdot q\right) + \left(q \cdot \nabla\right)\frac{1}{T} \geq 0, \tag{2.6}$$

where η is the entropy density. The stress-strain behavior of the explosive grains is modeled by a hyperelastic, multiplicative, finite strain constitutive theory with a Von-Mises yield criterion and Perzyna viscoplastic flow rule. Friction is modeled using an Amontons-Coulomb stick-slip theory. Details of the constitutive theory are given in Refs. [30, 31]. Thermomechanical properties for HMX used in the simulations are listed in Table 2.1.

Because a key focus of this study is to examine dissipation within compaction waves, brief discussion about the energetics described by the meso-scale model is given here. The

total mass-specific deformation power is given by $\mathcal{P} = \boldsymbol{\sigma} : \mathbf{d}/\rho$, where:

$$\mathbf{d} \equiv \frac{\dot{\mathbf{F}}\mathbf{F}^{-1} + (\dot{\mathbf{F}}\mathbf{F}^{-1})^{\top}}{2} \tag{2.7}$$

is the strain rate tensor, and

$$\mathbf{F} = \mathbf{I} + \boldsymbol{\nabla}_0 \mathbf{u} \tag{2.8}$$

is the deformation gradient tensor, $\mathbf{I}$ is the second order identity tensor, and $\boldsymbol{\nabla}_0 \equiv \partial(\cdot)/\partial\mathbf{X}$ is the Lagrangian gradient operator. By partitioning $\mathbf{d}$ into elastic and plastic components (i.e., $\mathbf{d} = \mathbf{d}_e + \mathbf{d}_p$), and partitioning $\boldsymbol{\sigma}$ into volumetric and deviatoric components (i.e., $\boldsymbol{\sigma} = p\mathbf{I} + \overline{\boldsymbol{\sigma}}$), the deformation power may be expressed as

$$\mathcal{P} = \frac{1}{\rho}\left(\bar{\boldsymbol{\sigma}} : (\mathbf{d} - \mathbf{d}_p)\right) + \frac{p}{\rho}\mathrm{tr}(\mathbf{d} - \mathbf{d}_p) + \frac{1}{\rho}\left(\boldsymbol{\sigma} : \mathbf{d}_p\right). \tag{2.9}$$

where $\rho = \rho_0 \det(\mathbf{F})$ and ρ_0 is the initial density in the undeformed configuration. The terms on the right side of this equation represent shear, compression, and plastic work rates, respectively.

Within the context of this model, shear work results in a non-thermal change in stored shear strain energy, whereas compression and plastic work result in deformation induced heating [represented by r in Eq. (2.3)]. As shown in Refs. [31, 32], only plastic work is dissipative in that it causes an irreversible production of entropy. The local dissipation power is given by

$$T\dot{\eta} = \frac{1}{\rho}\left(\boldsymbol{\sigma} : \mathbf{d}_p\right) \geq 0, \tag{2.10}$$

where η is the mass-specific entropy. Friction work occurring at inter-particle boundaries is also dissipative when slip occurs; the frictional dissipation power is locally given by $T\dot{\eta}_f = \mathbf{t}_c \cdot \mathbf{v}_\mathbf{r}$, where $\mathbf{v}_\mathbf{r}$ is the relative slip velocity. Because frictional dissipation is localized at inter-particle contact surfaces, it does not appreciably contribute to the effective (or bulk) mass-specific dissipated energy. Therefore, dissipated energy by plastic work dominates

the effective response, though frictionally induced tangential surface tractions at inter-particle contacts can indirectly contribute to Eq. (2.10) by enhancing plastic deformation within particles. It is noted that frictional dissipation can, however, produce hot-spots that play a central role in determining the impact and shock sensitivity of reactive solids; comprehensive discussions and analysis of hot-spot formation is given in Refs. [31,34,80,81].

Particle fracture is not modeled in this study despite evidence indicating that it can cause changes in microstructure during quasi-static compaction of granular HMX [58,125]. Because HMX has a low fracture surface energy (approximately $\gamma_f \approx 0.05$ J/m^2) [33], it is energetically inconsequential compared to the effective dissipated work induced by shocks. For example, if the average particle size of HMX decreases from approximately $d_1 = 60$ μm to $d_2 = 10$ μm due to fracture of spherical particles, then the change in particle surface area is approximately given by $\Delta A \approx 6(1/d_2 - 1/d_1)/\rho_0 = 263$ m^2/kg. The mass-specific fracture energy is approximately $e_f \approx \gamma_f \Delta A = 13$ J/kg which is much less than the plastic work associated with shock induced pore collapse (30-100 kJ/kg). Therefore, fracture will minimally influence shock profiles analyzed in this study, though it may substantially alter hot-spot formation at the particle-scale.

The meso-scale model equations are computationally integrated subject to the boundary conditions using a combined finite and discrete element technique. The finite-element method (FEM) is used to numerically integrate the unsteady 2-D conservation equations and the viscoplastic flow rule governing inelastic deformation, whereas the discrete element method (DEM) is used to account for interactions between particles. The DEM utilizes a conservative potential based penalty method in which the normal contact traction between particles is estimated by penalizing their penetration, and frictional tractions are estimated using a penalty regularized Amontons-Coulomb law. The initial particle configuration is generated using a pseudo-gravity drop method that consists of two steps. First, an initial packing arrangement is generated by randomly placing particles within the domain so that their centers lie outside the volume encompassed by other particles. Then, forces

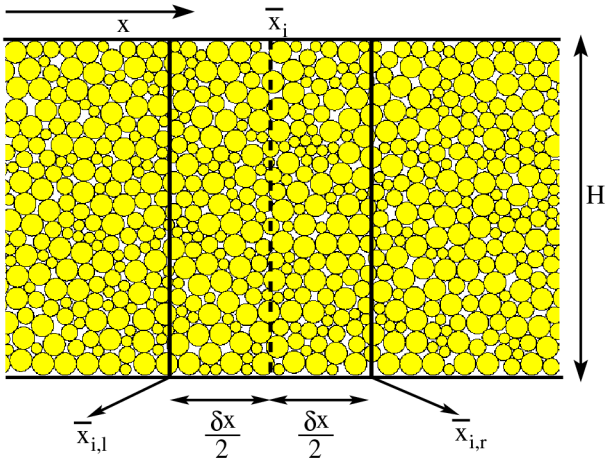

Figure 2.1: Schematic of the transverse averaging window used to obtain effective 1-D profiles from mesoscale fields.

arising due to particle overlap drives rearrangement of particle positions in such a way as to eliminate overlap while continuously settling under the influence of a gravitational force. Particles are discretized using constant strain triangular elements, where each particle contains approximately 400-800 finite elements for all simulations performed in this study, depending on its size. The combined FEM/DEM algorithm has been verified, and is nominally second-order accurate in both space and time. A detailed discussion of the computational technique, model validation, and verification is given by Panchadhara and Gonthier [30]. The model was further verified in the works of Gilbert and co-workers [81], and Chakravarthy and co-workers [80].

2.2 Averaging of Meso-Scale Fields

It is necessary to average (filter) meso-scale field predictions to obtain effective shock profiles that can be examined and directly compared to those predicted by the macro-scale theory. Time averaging is particularly important for low density materials having locally large spatial fluctuations in porosity that can result in large temporal fluctuations in spatial shock structure.

The averaging procedure used in this study is as follows. First, one-dimensional (1D) effective shock profiles are obtained at fixed time by spatially averaging mesoscale fields

over suitably chosen windows; a typical window is illustrated in Fig. 2.1. To estimate the average of a generic variable Φ at an axial location $x = \bar{x}$, a window having area A_{total} is locally positioned at $\bar{x}$ which represents a rectangle of length δx and width H, and an appropriate average is computed based on all finite elements contained within the window. Mass weighted averages are computed for variables that represent mass specific quantities, such as velocity (mass-specific momentum) and mass-specific power and dissipation rate [given by Eqs. (2.9) and (2.10)]. Variables that represent volume specific quantities, such as mass density (volume specific mass) and stress (volume specific energy), are computed using area weighted averages. For a variable Φ, at an axial position $x = \bar{x}_i$, mass and area weighted averages are respectively defined by

$$\overline{\Phi}_m(\overline{x}_i) = \frac{\int_{A_s} \rho\Phi \; dA}{\int_{A_s} \rho \; dA}, \qquad \overline{\Phi}_a(\overline{x}_i) = \frac{\int_{A_s} \Phi \; dA}{A_s}, \tag{2.11}$$

where A_s is the total area of explosive mass contained within the averaging window. Discrete representations of these averages are given by

$$\overline{\Phi}_m(\overline{x}_i) = \frac{\sum_{j=1}^{\mathcal{N}_a(i)} \rho^{(j)}\Phi^{(j)}A^{(j)}}{\sum_{j=1}^{\mathcal{N}_a(i)} \rho^{(j)}A^{(j)}}, \tag{2.12}$$

$$\overline{\Phi}_a(\overline{x}_i) = \frac{\sum_{j=1}^{\mathcal{N}_a(i)} \Phi^{(j)}A^{(j)}}{\sum_{j=1}^{\mathcal{N}_a(i)} A^{(j)}}, \tag{2.13}$$

where $\Phi^{(j)}$ is the value of the variable at the centroid of a finite element, $A^{(j)}$ is its current area, $\rho^{(j)}$ is its current density, and $\mathcal{N}_a(i)$ is the number of finite elements within the window. The smoothness of average profiles depends on both the number of axial positions n for which the running average is computed and the window width δx, and is most sensitive to the choice of δx. High-frequency fluctuations in variables result if δx is too small, whereas excessively smeared profiles result if it is too large. Therefore, it is necessary to establish a rationale for determining an appropriate window size that will provide meaningful comparisons with the macro-scale theory, as discussed below.

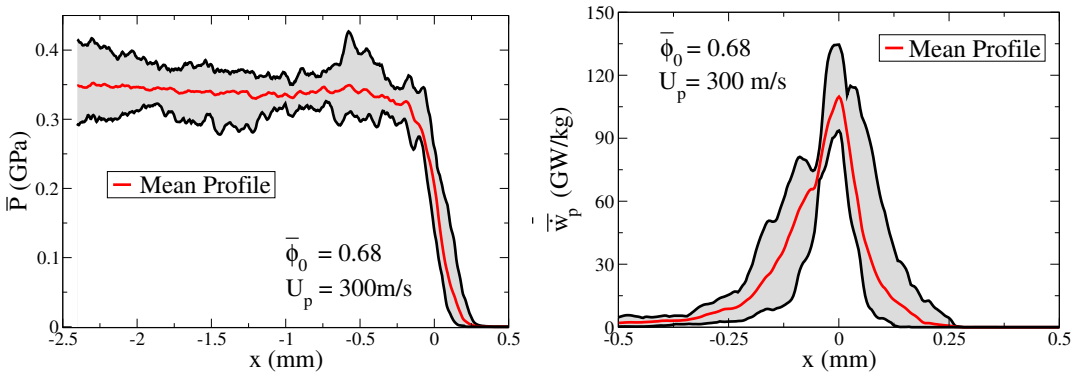

(a)

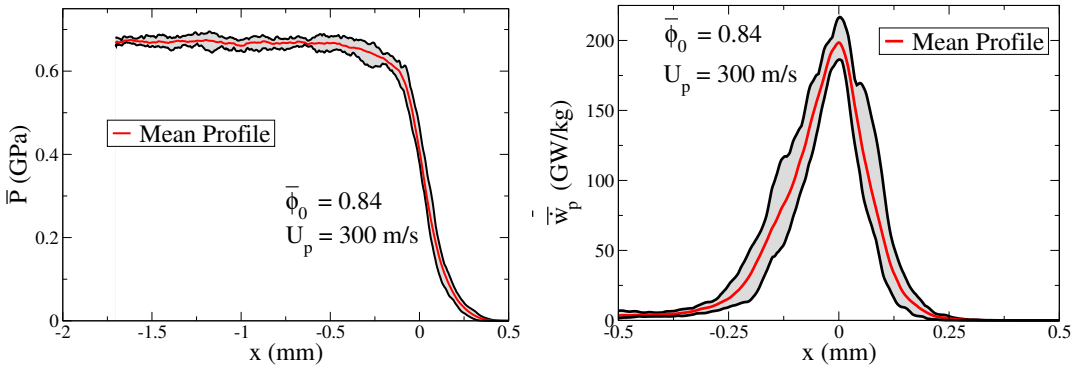

(b)

Figure 2.2: Ensemble averages used to obtain quasi-steady shock pressure and dissipation rate profiles predicted by mesoscale simulations for $U_p = 300$ m/s: (a) $\overline{\phi}_0 = 0.68$ and (b) $\overline{\phi}_0 = 0.84$.

Second, the ensemble average of effective quasi-steady profiles at different times is computed for a given simulation to account for temporal variations. Figure 2.2 illustrates bounds on the computed variation in quasi-steady profiles for solid pressure and mass-specific dissipation rate [given by Eq. (2.10)] for $\overline{\phi}_0 = 0.68$ and $\overline{\phi}_0 = 0.84$ at $U_p = 300$ m/s. The bounds are identified by spatial superposition of computed quasi-steady effective profiles. Corresponding ensemble average profiles are indicated in red in the figure. Larger spatial fluctuations are predicted for materials having lower packing density. The peak dissipation rate within a quasi-steady shock can vary by nearly 100% which may significantly affect the material's local heating response resulting in stochastic ignition behavior. [81] Because this study is concerned with effective dissipation within compaction shocks, profiles presented in this paper represent averages in space and time.

Figure 2.3 illustrates how the effective pressure and dissipation rate profiles vary with δx for $\overline{\phi}_0 = 0.68$ and $U_p = 300$ m/s, where $10 \leq \delta x \leq 200$ μm. The dissipation rate is expressed by $\overline{\dot{w}_p} = \overline{T\dot{\eta}}$ using Eq. (2.10). High frequency fluctuations result for approximately $\delta x < 30$ μm, whereas smeared profiles result for $\delta x > 140$ μm. Pressure profiles are less sensitive to δx than dissipation rate profiles. Only minor variations in shock width result for $\delta x < 50$ μm, which is easily seen in the dissipation rate profiles which vanish in the equilibrium states surrounding the shock. In this case, $\delta x = 50$ μm is chosen for purposes of comparison to the macro-scale theory because it results in a nearly converged shock width (≈ 0.4 mm) and minimal fluctuations. A similar rationale is used to identify appropriate window sizes for other values of $\overline{\phi}_0$ and U_p.

Last, the axial length of the computational domain associated with quasi-steady shock propagation was identified using shock position-time and shock speed-time data obtained by post-processing meso-scale velocity fields. For each simulation, the meso-scale velocity field was spatially filtered to obtain effective profiles with increasing time, with shock position defined by the axial location where the effective velocity within the shock is 50% of the prescribed piston speed value U_p. The shock position-time data were then differentiated to

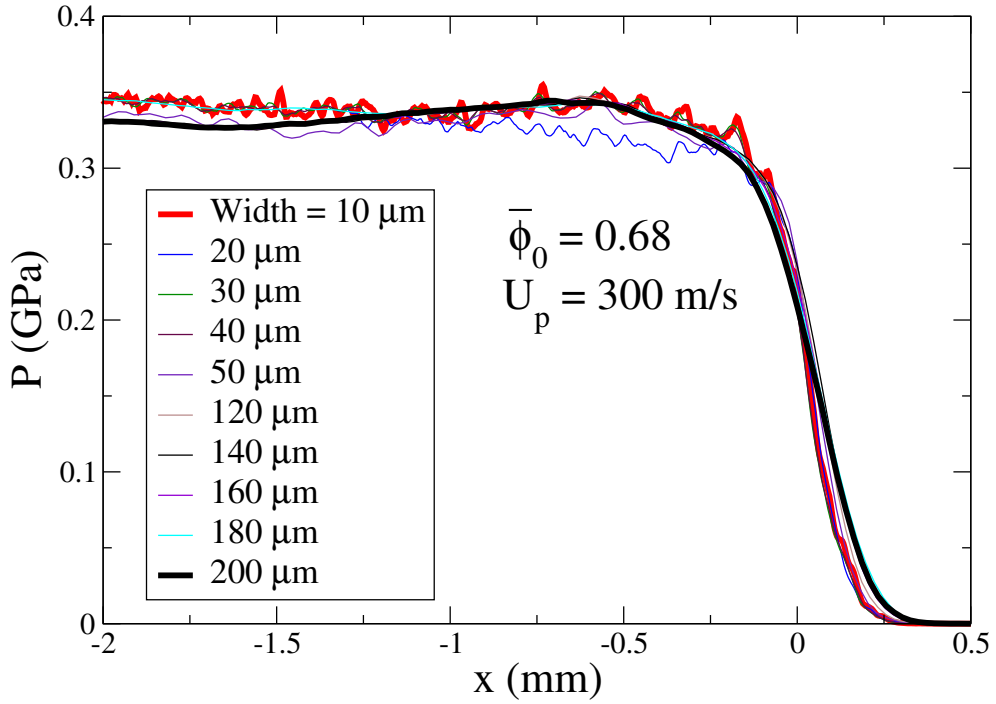

(a)

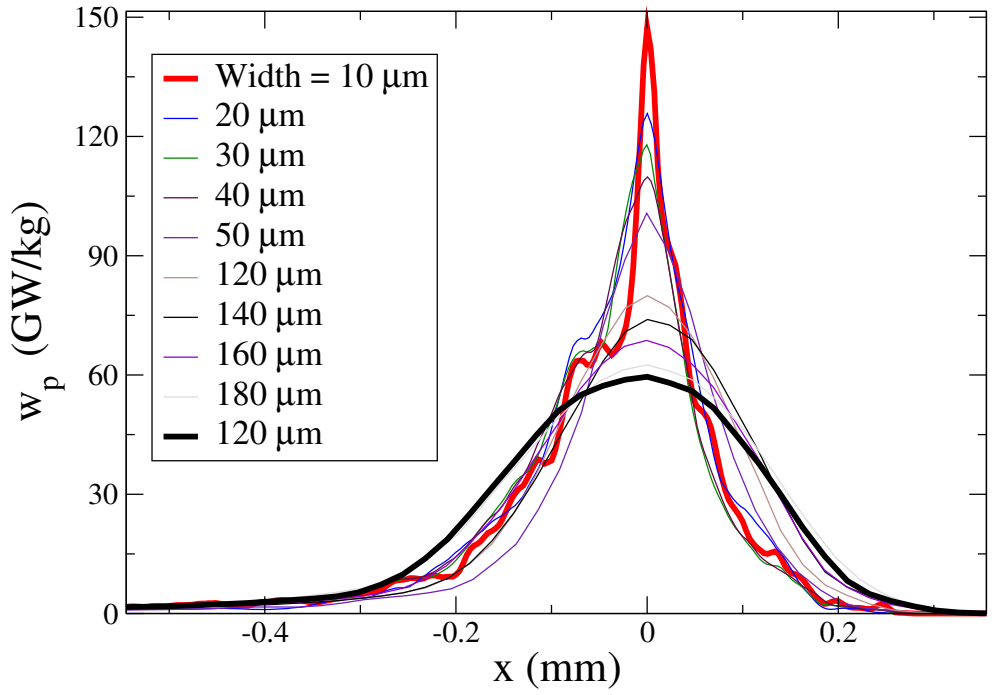

(b)

Figure 2.3: Meso-scale predictions for the variation in shock profiles with averaging window width for $\overline{\phi} = 0.68$ and $U_p = 300$ m/s: (a) effective pressure and (b) effective dissipation rate.

obtain shock speed data, and the position-speed data were combined to identify the axial location at which the shock speed was approximately constant. Predictions indicate that quasi-steady shocks develop rather quickly following impact.

Chapter 3
Macro-Scale Model

3.1 Introduction

The macro-scale model tracks the evolution of effective thermomechanical fields within granular solid explosive based on a hydrodynamic compaction theory that accounts for elastic deformation. In this study we consider the behavior of a reacting, two-phase mixture of solid and gas. The motion of the individual particles of the gas and solid can be conceptually averaged and replaced by the motion of a continuum, which leads to the mathematical description of inter-penetrating continua, a gas-phase continuum inter-penetrating a solid phase continua. To arrive at the multi-phase flow equations two approaches are available:

- Mixture Theory Approach
- Averaging Approach

In this study, we adopt a mixture theory approach, where the multi-phase flow equations are postulated, and restrictions on the constitutive relations are derived from general principles of continuum mechanics. The derived equations are incomplete, in the sense that they must be closed by specifying constitutive relations such as equations of state for the solid and gas phase.

Modeling an object as continuum assumes that the substance of the object fills the space it occupies. Modeling objects in this way ignores the fact that matter is made of atoms, and so is not continuous; however, on length scales much greater than that of interatomic distances, such models are highly accurate. Fundamental physical laws such as the conservation of mass, momentum and energy may be applied to such models to derive differential equations describing the behavior of such objects, and some information about the particular material studied is added thorough constitutive relations.

Materials, such as solids, liquids and gases, are made up of molecules separated by "empty" space. On a microscopic scale, materials have cracks, grain boundaries and dis-

continuities. However, certain physical phenomena can be modeled assuming the materials exist in continuum, meaning the matter in the body is continuously distributed and fills the entire region of space it occupies. A continuum is a body that can be continually sub-divided into infinitesimal elements with properties being those of the bulk material. The validity of the continuum assumption may be verified by a theoretical analysis, in which either some clear periodicity is identified or statistical homogeneity and ergodicity of the micro-structure exists. More specifically the continuum hypothesis hinges on the concepts of a representative volume element (RVE) and separation of scales based on the Hill−Mandel condition.

The two-phase continuum model, used in this study was formulated by Crochet and Gonthier [89–91] and later improved by Rao and Gonthier [110–112], is described in this chapter. First the dimensional model equations along with the constitutive relations used to complete the system of equations is given in Section 3.2.1. Second, the theory behind macro-scale dissipation which is key to ignition and initiation is given in Section 3.2.2.

3.2 Mathematical Modeling

The mathematical description of the two-phase model consists of a system of hyperbolic partial differential equations representing the balance of mass, momentum and energy for each phase, coupled with a compaction law and saturation constraint. The mass, momentum and energy are conserved for the mixture, but not conserved separately for each phase. Some of the source terms in the momentum and energy conservation equations are proportional to the gradient of the volume fraction of the solid phase. These terms are known as nozzling terms and prevent the governing hyperbolic system of equations to be expressed in conservative form and cause significant numerical difficulties in solving the system of equations.

3.2.1 Governing Model Equations

The one-dimensional model equations in the Eulerian coordinate system are given by the following:

$$\frac{\partial}{\partial t}\left[\phi_s \rho_s\right] + \frac{\partial}{\partial x}\left[\phi_s \rho_s u_s\right] = \mathcal{C} \tag{3.1}$$

$$\frac{\partial}{\partial t}\left[\phi_s \rho_s u_s\right] + \frac{\partial}{\partial x}\left[\phi_s \rho_s u_s^2 + P_s \phi_s\right] = P_g \frac{\partial \phi_s}{\partial x} + \mathcal{M} \tag{3.2}$$

$$\frac{\partial}{\partial t}\left[\phi_s \rho_s E_s\right] + \frac{\partial}{\partial x}\left[\phi_s \rho_s u_s \left(E_s + \frac{P_s}{\rho_s}\right)\right] = P_g u_s \frac{\partial \phi_s}{\partial x} + \mathcal{E} \tag{3.3}$$

$$\frac{\partial}{\partial t}\left[\phi_g \rho_g\right] + \frac{\partial}{\partial x}\left[\phi_g \rho_g u_g\right] = -\mathcal{C} \tag{3.4}$$

$$\frac{\partial}{\partial t}\left[\phi_g \rho_g u_g\right] + \frac{\partial}{\partial x}\left[\phi_g \rho_g u_g^2 + P_g \phi_g\right] = -P_g \frac{\partial \phi_s}{\partial x} - \mathcal{M} \tag{3.5}$$

$$\frac{\partial}{\partial t}\left[\phi_g \rho_g E_g\right] + \frac{\partial}{\partial x}\left[\phi_g \rho_g u_g \left(E_g + \frac{P_g}{\rho_g}\right)\right] = -P_g u_s \frac{\partial \phi_s}{\partial x} - \mathcal{E} \tag{3.6}$$

$$\frac{\partial \phi_s}{\partial t} + u_s \frac{\partial \phi_s}{\partial x} = \mathcal{F}_s + \frac{\mathcal{C}}{\rho_s} \tag{3.7}$$

$$\frac{\partial}{\partial t}\left[\phi_s \rho_s B_s\right] + \frac{\partial}{\partial x}\left[\phi_s \rho_s B_s u_s\right] = \beta_s \left(\mathcal{F}_s + \frac{\mathcal{C}}{\rho_s}\right) + B_s \mathcal{C} \tag{3.8}$$

$$\phi_s + \phi_g = 1 \tag{3.9}$$

$$P_s = P_s(\rho_s, T_s) \tag{3.10}$$

$$e_s = e_s(\rho_s, P_s, \phi_s) \tag{3.11}$$

$$P_g = P_g(\rho_g, T_g) \tag{3.12}$$

$$e_g = e_g(\rho_g, P_g) \tag{3.13}$$

In these equations, the subscripts s and g denote the quantities associated with the solid/explosive and gas phase respectively. Independent variables are time t and position x. Dependent variables are as follows: the phase volume fraction ϕ_s and ϕ_g; the phase density ρ_s and ρ_g; the phase particle velocity u_s and u_g, measured with respect to a stationary reference frame; the phase pressure P_s and P_g; the phase specific total energy E_s and E_g; the phase specific internal energy e_s and e_g; the solid phase intergranular stress β_s; the solid phase compaction dissipation w_d; and an ignition variable λ_I which is discussed

in the following paragraphs.

Equations (3.1), (3.2) and (3.3) are evolution equations for mass, momentum and total energy of the solid/explosive phase. Equations (3.4), (3.5) and (3.6) are evolution equations for the mass, momentum and total energy of the gas phase. Equation (3.7) and (3.8) is the evolution equations for the solid volume fraction, and the compaction potential energy, respectively.

The source terms on the right hand side of the governing equations [Eqs. (3.1-3.7)] involve undifferentiated exchange terms and differentiated non-conservative source terms. The non-conservative/nozzling terms are proportional to the gradient of the solid volume fraction, $\partial\phi_s/\partial x$. These terms model interphase momentum and energy transfer that occurs as a result of an effective change in cross-sectional area of a virtual stream tube of the gas phase. The exchange source terms include compaction ($\mathcal{F}_s$), the conversion of energetic solid to gas due to chemical reactions ($\mathcal{C}$), and the exchange of momentum ($\mathcal{M}$), and the energy ($\mathcal{E}$) due to the relaxation process of drag and heat transfer.

The source term $\mathcal{C}$ in Eqs. (3.1) and (3.4) account for the exchange of mass from solid to gas due to combustion. Of particular importance to this study is the volumetric mass exchange term $\mathcal{C}$ that governs the explosive combustion rate. It is common to take $\mathcal{C} = \mathcal{C}(\rho_s, \phi_s, P_g)$, where the functional dependency on gas pressure reflects strand burn data. Because ignition results from dissipative heating at the pore scale during shock compaction, it is plausible to use an expanded expression that accounts for the role of hot-spots in triggering ignition. To this end, a dimensionless ignition variable λ_I is defined such that

$$\mathcal{C} = \begin{cases} 0 & \text{for } \ 0 \leq \lambda_I < 1 \\ f & \text{for } \ \lambda_I = 1. \end{cases} \tag{3.14}$$

Here, it is assumed that the induction period corresponding to $0 \leq \lambda_I < 1$ involves negligible gas production and is energetically inconsequential at the macro-scale. The subsequent burn phase is described by the function f. Because a key focus of this study is development

of ignition and burn model, a detailed discussion along with the evolution equations is given in Section 5.1.2.

The momentum exchange source term $\mathcal{M}$ in Eqs. (3.2) and (3.5) is given by [135]:

$$\mathcal{M} = \mathcal{C}u_s + \left(\delta + \frac{\mathcal{C}}{2}\right)(u_g - u_s) \tag{3.15}$$

It accounts for two forms of momentum exchange between solid and gas. First, the gas is gaining that momentum associated with the solid that is being converted into gas due to combustion. Second, there is exchange of momentum due to solid particle-gas drag interaction. The drag term provides a relaxation mechanism which drives the phases towards velocity equilibrium, $u_s = u_g$. The drag coefficient characterizes the rate at which the velocity equilibration occurs.

The energy exchange source term $\mathcal{E}$ in Eqs. (3.3) and (3.6) is given by [135]:

$$\mathcal{E} = \left(E_s + \frac{\beta_s}{\rho_s}\right)\mathcal{C} + (\mathcal{M} - \mathcal{C}u_s)\,u_s + \mathcal{H}\,(T_g - T_s) \tag{3.16}$$

It accounts for three forms of energy exchange between the solid and gas. Energy exchange due to combustion, and particle-gas drag work, and thermal energy exchange between solid and gas is accounted for. E_s and $\mathcal{H}$ refer to the total energy of the solid phase and interphase heat transfer coefficient respectively.

Equation (3.7) is a dynamic compaction equation governing changes in solid volume fraction due to compaction and combustion of the material. This equation was first proposed by Baer and Nunziatio [7] and it allows for modeling of rate-dependent material compaction that is important in evolution of detonation of granulated material. The source term $\mathcal{F}_s$ in the compaction law [Eq. (3.7)] is given by:

$$\mathcal{F}_s = \frac{1}{\mu_c}\phi_s\phi_g\,(P_s - P_g - \beta_s) \tag{3.17}$$

where μ_c is the compaction viscosity and β_s is the intergranular stress (configuration pressure). In the absence of chemical reaction ($\mathcal{C} = 0$), the compaction rate provides a relaxation mechanism which drives the mixture towards pressure equilibrium, ($P_s = P_g + \beta_s$), where the compaction viscosity μ_c characterizes the rate at which pressure equilibrium occurs. Equation (3.8) also proposed by Baer and Nunziato [7] defines the compaction potential energy function $B_s(\phi_s)$, which arises due to changes in the solid volume fraction due to intergranular stresses β_s within the material. This quantity represents grain-scale mechanics in the bulk-scale. Intergranular stresses have been measured by quasi-static experiments [125], and curve fits to available data can be used to specify the functional form of β_s [79]. In this study, the expression used for the intergranular stress has been adopted with slight modification from Ref [90]:

$$\frac{\beta_s}{\phi_s \rho_s} = \begin{cases} 0 & , \ 0 < \phi_s < \phi_0 \\ -\Lambda_s \left(\phi_s - \phi_0\right)^{n_s} \dfrac{\ln\left[k_s - (\phi_s - \phi_0)\right]}{\left[k_s - (\phi_s - \phi_0)\right]} & , \ \phi_0 \leq \phi_s < 1 \end{cases} \tag{3.18}$$

where Λ_s, n_s and k_s are empirically determined, and ϕ_0 is the initial solid volume fraction corresponding to initially stress-free and motionless bed. Equation (3.18) requires that $\beta_s = 0$ for $\phi_s = \phi_0$ and as $\phi_s \to 1$, the intergranular stress equilibrates to the crush-up pressure of HMX (700 MPa). Equation (3.9) gives the relation relation between ϕ_s and ϕ_g.

The total energies of the solid and gas phase appearing in Eqs.(3.3) and (3.6) are given by:

$$E_s = \widehat{e_s} + \frac{u_s^2}{2} \quad ; \quad E_g = e_g + \frac{u_g^2}{2} \tag{3.19}$$

where $\widehat{e_s} = e_s + B_s(\phi_s)$ and e_g is the specific internal energy of the solid and gas phase, respectively. The internal energy of the solid is the sum of internal energy of the pure solid e_s and the compaction potential energy $B_s(\phi_s)$ of the solid. Equations (3.10-3.11) and (3.12-3.13) are functional dependencies for the thermal and caloric equations of state (EOS) for solid and gas, respectively. In this study, we employ a Mie-Gruneisen EOS for

Table 3.1: Parameters used in Mie-Gruneisen (solid) and JWL (gas) EOS.

Mie-Gruneisen			JWL		
Parameter	Value	Units	Parameter	Value	Units
Γ_s	1.10	-	ω	0.30	-
ω_s	2740	m/s	A	778.3	GPa
s	2.0	-	B	7.071	GPa
ρ_s^0	1900	kg/m^3	R_1	4.20	-
c_{ve}	1500	J/kg/K	R_2	1.0	-

the solid phase and a Jones-Wilkins-Lee EOS for the gas phase.

The Mie-Gruneisen EOS used to describe the solid phase is of the form:

$$P_s - P_{sH} = \frac{\Gamma_s}{\nu_s^0}\left(\widehat{e_s} - e_{sH}\right), \tag{3.20}$$

where

$$P_{sH} = \left[\frac{\omega_s}{\nu_s^0 - s\left(\nu_s^0 - \nu_s\right)}\right]^2 \left(\nu_s^0 - \nu_s\right) \quad ; \quad e_{sH} = \frac{1}{2}\left[\frac{\omega_s\left(\nu_s^0 - \nu_s\right)}{\nu_s^0 - s\left(\nu_s^0 - \nu_s\right)}\right]^2 \tag{3.21}$$

Here, $\nu_s = 1/\rho_s$ are the specific volumes, and Γ_s are constant Gruneisen coefficients. These incomplete equations of state are compatible with the Hugoniots $D_s = \omega_s + su_s$, where D_s are shock speeds, and ω_s and s are empirically determined constants [133]. Values of the equation of state parameters used in this study are summarized in Table 3.1. The JWL EOS used for the gas phase is of the form:

$$e_g\left(P_g, \rho_g\right) = \frac{1}{\omega\rho_g}\left[P_g - A\left(1 - \frac{\omega v_{st}}{R_1 v_g}\right)e^{Z_1} - B\left(1 - \frac{\omega v_{st}}{R_2 v_g}\right)e^{Z_2}\right] \tag{3.22}$$

where ω, A, B, R_1, R_2 are empirical constants, and Z_1, Z_2 are given by: $Z_1 = -R_1 v_g/v_{st}$ and $Z_2 = -R_2 v_g/v_{st}$. The values of the constant used in the EOS together with the ambient properties in given in Table 3.1.

The source terms in Eqs. (3.1 - 3.6) have to be formulated accurately to satisfy mixture mass, momentum and energy conservation. To this end, summing Eqs.(3.1) and (3.4), Eqs.

(3.2) and (3.5), and Eqs. (3.3) and (3.6), homogeneous differential equations for mixture mass, momentum and energy are obtained.

$$\frac{\partial}{\partial t}\left[\phi_s\rho_s + \phi_g\rho_g\right] + \frac{\partial}{\partial x}\left[\phi_s\rho_s u_s + \phi_g\rho_g u_g\right] = 0, \tag{3.23}$$

$$\frac{\partial}{\partial t}\left[\phi_s\rho_s u_s + \phi_g\rho_g u_g\right] + \frac{\partial}{\partial x}\left[\phi_s\rho_s u_s^2 + \phi_g\rho_g u_g^2 + P_s\phi_s + P_g\phi_g\right] = 0, \tag{3.24}$$

$$\frac{\partial}{\partial t}\left[\phi_s\rho_s E_s + \phi_g\rho_g E_g\right] + \frac{\partial}{\partial x}\left[\phi_s\rho_s u_s\left(E_s + \frac{P_s}{\rho_s}\right) + \phi_g\rho_g u_g\left(E_g + \frac{P_g}{\rho_g}\right)\right] = 0. \tag{3.25}$$

Consequently the solid-gas mixture mass, momentum and energy are conserved. In addition to the conservation constraints, the source terms are constructed such that, the change in total entropy of the mixture due to any thermodynamic activity is non-negative. It is formulated such that the mixture entropy satisfy the following evolution equation [126]

$$\frac{\partial}{\partial t}\left[\phi_s\rho_s\eta_s + \phi_g\rho_g\eta_g\right] + \frac{\partial}{\partial x}\left[\phi_s\rho_s u_s\eta_s + \phi_g\rho_g u_g\eta_g\right] \geq 0, \tag{3.26}$$

where η_s and η_g are the mass-specific entropy of the solid and gas, respectively.

3.2.2 Macro-Scale Dissipation

Of particular importance are the effective heating rates and bulk temperature rise induced by compaction shocks when the material is dynamically loaded. Dissipative heating by compaction shocks in granular explosives can locally trigger the onset of chemical reactions that can spread and subsequently lead to detonation under suitable confinement. The mass-specific deformation power is give by:

$$\frac{de_s}{dt} = \underbrace{\frac{d\mathcal{B}}{dt}}_{\text{Shear}} + \underbrace{\frac{de_{\rho_s}}{dt}}_{\text{Compression}} + \underbrace{\frac{dw_d}{dt}}_{\text{Compaction}} \tag{3.27}$$

where, $d\left(\bullet\right)/dt \equiv \partial\left(\bullet\right)/\partial t + \mathbf{v}\cdot\nabla\left(\bullet\right)$ is the Lagrangian derivative. In Eq. (3.27), $d\mathcal{B}/dt$ implicitly accounts for the rate of stored compaction energy at the particle scale due to shear, de_{ρ_s}/dt accounts for compression work rate, and dw_d/dt accounts for the dissipative

compaction work rate, which vanishes in the slow compaction limit (i.e., $P_s \to P_g + \beta_s$). The rate-dependent stored compaction energy, compression heating rate and dissipatve compaction work rate are given by:

$$\frac{d\mathcal{B}}{dt} = \frac{\beta_s}{\rho_s \phi_s} \frac{d\phi}{dt}, \tag{3.28}$$

$$\frac{de_{\rho_s}}{dt} = \frac{P_s}{\rho_s^2} \frac{d\rho_s}{dt}, \tag{3.29}$$

$$\frac{dw_d}{dt} = \Lambda \frac{d\phi_s}{dt} \tag{3.30}$$

respectively, such that

$$\frac{de_s}{dt} = \frac{\beta_s}{\rho_s \phi_s} \frac{d\phi}{dt} + \frac{P_s}{\rho_s^2} \frac{d\rho_s}{dt} + \Lambda \frac{d\phi_s}{dt} \tag{3.31}$$

In particular, dissipative heating (dw_d/dt) due to compaction shocks is important to this study as it can locally trigger the onset of chemical reactions that can spread and subsequently lead to detonation under suitable confinement. Therefore, the burn model developed in Section 5.1.2 is also dependent on dissipative heating by compaction shocks. To facilitate integration of Eq. (3.30), it is convenient to express it in Eulerian coordinates and is given by

$$\frac{\partial}{\partial t} \left[\phi_s \rho_s w_d \right] + \frac{\partial}{\partial x} \left[\phi_s \rho_s u_s w_d \right] = \phi_s \rho_s \Lambda \frac{d\phi_s}{dt} + w_d \mathcal{C} \tag{3.32}$$

where the source term Λ in Eq. (3.32) is given by:

$$\Lambda \frac{d\phi_s}{dt} = \begin{cases} 0 & \text{if } \frac{d\phi_s}{dt} < 0 \text{ or } \phi_s \leq \phi_0 \\ \frac{(1-\phi_s)}{\mu_c \rho_s} \left(P_s - P_g - \beta_s \right)^2 & \text{otherwise.} \end{cases} \tag{3.33}$$

Using Eq. (3.7), the condition ($d\phi_s/dt < 0$) can be re-expressed as:

$$\frac{d\phi_s}{dt} < 0 \quad \Rightarrow \quad P_s < (P_g + \beta_s) - \left(\frac{\mathcal{C} \mu_c}{\rho_s \phi_s \phi_g} \right) \tag{3.34}$$

In this work, dissipative compaction work (w_d) is a shock history-dependent variable and is defined as the work corresponding to each solid/explosive grain frozen at the value it had as the compaction waves propagates through the ambient bed. For inert simulations prescribing the compaction dissipation source term Λ is straight forward in that ($d\phi_s/dt$) is always positive implying irreversible loading of the material that leads to material compaction. However, for reactive simulations prescribing the source term is complicated due to simultaneous occurrence of compaction (loading) and combustion (unloading) of the material.

To address these effects, the source term for loading of the material ($d\phi_s/dt > 0$ and $\mathcal{C} = 0$), is given the first term on the right of Eq. (3.32) that dominates where Λ is given by Eq. (3.33). For burn dominated regimes where the material unloads in the sense particles lose physical contact and intergranular stress vanishes ($d\phi_s/dt < 0$, and $\mathcal{C} \neq 0$), $\Lambda = 0$ and the dissipation is essentially zero. For conditions where the material is loading ($d\phi_s/dt > 0$) and unloading ($\mathcal{C} \neq 0$) simultaneously provided $\phi_s > \phi_0$, contributions from both terms on the right of Eq. Eq. (3.32) determine the dissipative work. w_d is also assumed inconsequential for $\phi_s \leq \phi_0$, since the grains are no longer in mechanical contact due larger void fractions of the bed.

Combining Eqs. (3.1−3.7) with the second law of thermodynamics gives the strong form of the compaction dissipation inequality:

$$T_s \frac{d\eta_s}{dt} = \frac{(1-\phi_s)}{\mu_s \rho_s} \left(P_s - P_g - \beta_s\right)^2 \geq 0 \tag{3.35}$$

where η_s is the mass-specific granular solid entropy. Within the context of this model, the right had side of Eq. (3.35 is non-negative. Gonthier and co-workers [93] have shown that this thermodynamic description is compatible with the partitioning of Helmholtz free energy of the form:

$$\psi\left(\rho_s, T_s, \phi_s\right) = \psi_s\left(\rho_s, T_s\right) + B_s\left(\phi_s\right) \tag{3.36}$$

where ψ_s is the mass-specific solid phase free energy. Here, ψ_s is the thermal component of free energy and B_s is the compaction potential energy.

3.3 Numerical Method

The numerical method developed initially by Kurganov and Tadmore (KT) [114–116] and later adopted by Crochet [90] to solve the two-phase model equation is discussed in this section. The vector form of the model Eqs. (3.1)-(3.7) in Cartesian coordinates is given by:

$$\frac{\partial \mathbf{q}}{\partial t} + \frac{\partial \mathbf{f(q)}}{\partial x} = \mathbf{g(q)}\frac{\partial \phi_s}{\partial x} + \mathbf{s(q)}, \qquad t > 0, \qquad x \in [L_1, L_2], \tag{3.37}$$

where t is time, x is the spatial variable, $\mathbf{q}$ is the vector of conserved variables, $\mathbf{f(q)}$ is the flux vector, $\mathbf{g(q)}$ is the vector associated with nonconservative nozzling sources, $\mathbf{s(q)}$ is the phase interaction source vector, and L_1 and L_2 are the spatial domain boundaries. This system of $N_{eq} = 10$ equations is degenerate hyperbolic with eigenvalues ζ_k given by:

$$\zeta_k = u_s, u_s \pm c_s, u_g, u_g \pm c_g \tag{3.38}$$

for $k = 1, 2, ..., N_{eq}$, where u_s and u_g are the particle velocities of the explosive/solid phase and gas phase, respectively, and c_s and c_g are the corresponding sound speeds. The eigenvalues $\zeta_k = u_s$ appears 5 times for the explosive/solid phase and $\zeta_k = u_g$ appears 3 times for the gas phase, while remaining eigenvalues are distinct.

The system of model equations are numerically integrated using a total variation diminishing (TVD) high-resolution finite volume shock-capturing scheme. The advantage of this scheme over conventional upwind schemes is that no Riemann solvers are needed which require specific eigenstructure for the problem to be known. Due to typically small length and time scales associated with velocity and pressure relaxation zones, the system of equations (3.37) is numerically stiff. To address this problem, the model equations are numerically solved on the computational grid using a fractional time-step method proposed

initially by Strang [117]. The splitting method is given by:

$$\mathbf{q}^{n+1} = \mathcal{K}_{\Delta t/2}\{\mathcal{S}_{\Delta t/2}\left[\mathcal{K}_{\Delta t/2}(\mathbf{q}^n)\right]\} \tag{3.39}$$

Here, $\mathbf{q}^n$ and $\mathbf{q}^{n+1}$ are the numerical approximations at time t^n and t^{n+1}, respectively; where $t^{n+1} = t^n + \Delta t$. $\mathcal{K}$ and $\mathcal{S}$ are numerical integration operators associated with solid/gas convection and source term effects, respectively. During the convective step, the source terms in Eq. (3.37) are set to zero and the convective terms are set to zero for the source step:

$$\mathcal{K}_{\Delta t/2} \quad : \qquad \frac{\partial \mathbf{q}}{\partial t} + \frac{\partial \mathbf{f}(\mathbf{q})}{\partial x} = \mathbf{g}(\mathbf{q})\frac{\partial \phi_s}{\partial x}, \quad \mathbf{q}(x,0) = \mathbf{q}^n, \quad \mathbf{q}\left(x, \frac{\Delta t}{2}\right) = \mathbf{q}^{(1)}, \tag{3.40}$$

$$\mathcal{S}_{\Delta t} \quad : \qquad \frac{\partial \mathbf{q}}{\partial t} = \mathbf{s}(\mathbf{q}), \qquad\qquad \mathbf{q}(x,0) = \mathbf{q}^{(1)}, \quad \mathbf{q}(x,\Delta t) = \mathbf{q}^{(2)}, \tag{3.41}$$

$$\mathcal{K}_{\Delta t/2} \quad : \qquad \frac{\partial \mathbf{q}}{\partial t} + \frac{\partial \mathbf{f}(\mathbf{q})}{\partial x} = \mathbf{g}(\mathbf{q})\frac{\partial \phi_s}{\partial x}, \quad \mathbf{q}(x,0) = \mathbf{q}^{(2)}, \quad \mathbf{q}\left(x, \frac{\Delta t}{2}\right) = \mathbf{q}^{n+1}. \tag{3.42}$$

Here $\mathbf{q}^{(1)}$ and $\mathbf{q}^{(2)}$ are intermediate states. Given the solution $\mathbf{q}^n$ at time t^n, the technique solves the convective problem over a time increment $\Delta t/2$, then the source problem is solved over a time increment Δt, and finally the convective problem is solved again over a time increment $\Delta t/2$ in order to advance the solution to time t^{n+1}. The process is repeated until the desired final time is reached. The initial conditions for each successive differential equation to be integrated is a solution obtained from the previous step. Since the total number of steps involved in advancing the solution is two, the accumulated numerical error results in a scheme that is globally second-order accurate in time. Therefore the numerical method can be described in two sections. In Section 3.3.1, the inclusion of local source terms is first discussed. In Section 3.3.2, the convective step is discussed which is significantly complex due to presence of nonconservative nozzling terms.

3.3.1 Source Step

The source step, is given by:

$$\frac{\partial \mathbf{q}}{\partial t} = \mathbf{s}(\mathbf{q}) \tag{3.43}$$

An implicit stiff ordinary differential equation (ODE) solver contained in the software package LSODE (Livermore Solver for Ordinary Differential Equations) [118–120] is used to numerically integrate these equations. The solution obtained at the grid points from the convective step is used as an initial condition to solve the system of ODE's. The system of ODE's are numerically integrated over the CFL-restricted time step Δt, which is twice the size of time step used in the convective step. The source terms are functions of the local, cell-center variables $\mathbf{q}$, therefore the system of equations 3.37 are decoupled and solved independently at each spatial grid point. LSODE was chosen largely because it is convenient and a well-tested package for solving stiff systems of ODE's.

3.3.2 Convective Step

The convective step poses significant numerical difficulties since the convective operator $\mathcal{K}$ includes sources that are proportional to the volume fraction gradient. The solid volume fraction gradients locally accelerate the gas flow in a manner similar to the effects of cross-sectional area variation in single-phase, quasi one-dimensional flows, with the porosity $1-\phi_s$ corresponding to the duct area.

Crochet proposed an extension of the Kurganov-Noelle-Petrov (KNP) [121] method that is less diffusive version of the original KT scheme. The one-dimensional version of the governing equations (3.37) is given by:

$$\frac{\partial \mathbf{q}}{\partial t} + \frac{\partial \mathbf{f}(\mathbf{q})}{\partial x} = \mathbf{A}(\mathbf{q})\frac{\partial \mathbf{q}}{\partial x} \tag{3.44}$$

where the dyadic tensor $\mathbf{A}(\mathbf{q}) = \mathbf{g}(\mathbf{q})(\partial \phi_s / \partial x)$. The computational domain is discretized into N computational cells of uniform width Δx. Figure 3.1 is a schematic of the computational domain along with the numerical scheme, which is also shown in Reference [90].

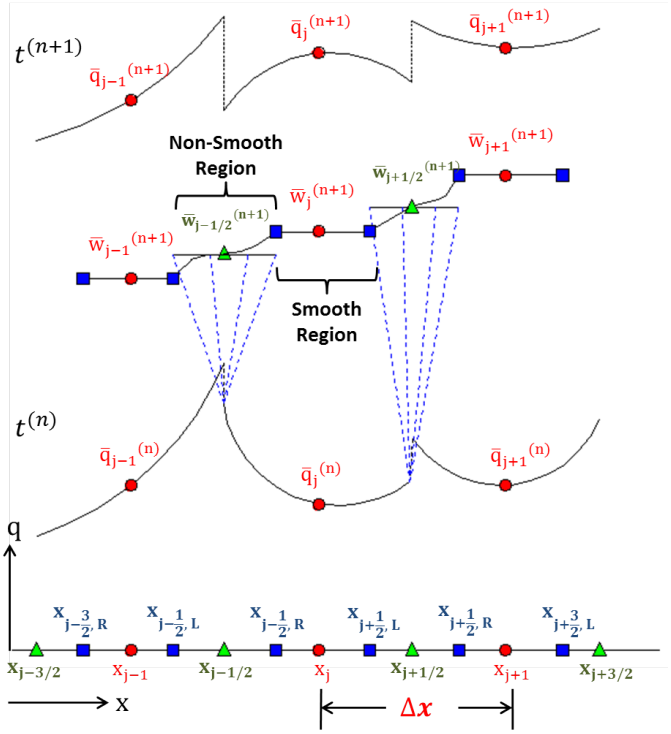

Figure 3.1: Schematic of the Kurganov-Noelle-Petrov Numerical Scheme.

The cell-centers are located at $x_j = j\Delta x$ for $j = 1, 2, ..., N$. For fixed time t, the running spatial average of the solution is defined as:

$$\overline{\mathbf{q}}(x) = \int_{x-\Delta x/2}^{x+\Delta x/2} \mathbf{q}\ (x,t)\ dx \tag{3.45}$$

Within each computational cell $C_j = \left[x_{j-1/2}, x_{j+1/2}\right]$, the cell averages $\overline{\mathbf{q}}_j$ are computed from initial conditions. These averages are evolved explicitly in time. At time $t^{(n)}$, the solution within each computational cell is reconstructed using a sequence of piecewise-continuous polynomials $\mathbf{p}_j(x)$ and the cell averages $\overline{\mathbf{q}}_j^{(n)}$.

The approximate solution is generally discontinuous at the cell boundaries $\left[x_{j-1/2}, x_{j+1/2}\right]$, resulting in a series of Riemann problems with centered simple waves propagating from the cell interfaces. The KT, KNP and the scheme developed by Crochet obtain the approximate solution at time $t^{(n+1)} = t^n + \Delta t^{(n)}$ by integrating Eqs. (3.37) over two portions of the spatial domain: the non-smooth region where wave propagation near the cell boundaries,

and the smooth region unaffected by these disturbances. The sub-domains are denoted by:

$$\Omega_I = \left[x_{j+1/2,l}, x_{j+1/2,r}\right] \times \left[t^{(n)}, t^{(n+1)}\right]$$
$$\Omega_{II} = \left[x_{j-1/2,r}, x_{j+1/2,l}\right] \times \left[t^{(n)}, t^{(n+1)}\right]$$

respectively. Integration of Eqs. (3.37) over the two sub-domains results in the construction of a intermediate solution $\mathbf{w}^{(n+1)}$ over a staggered grid, which is then projected back to to the original grid using an averaging procedure to obtain $\overline{\mathbf{q}}^{(n+1)}$.

The reconstructed values of the solution $\overline{\mathbf{q}}^{(n)}$ at the cell boundaries $x_{j+1/2}$ are given by:

$$\mathbf{q}^{-}_{j+1/2} = \mathbf{p}_j(x_{j+1/2}) \tag{3.46}$$
$$\mathbf{q}^{+}_{j+1/2} = \mathbf{p}_{j+1}(x_{j+1/2}) \tag{3.47}$$

where the polynomials $\mathbf{p}_j$ is given by:

$$\mathbf{p}_j = \sum_{i=0}^{N} \mathbf{K}_j^{(i)} \left(x - x_j\right)^i \tag{3.48}$$

Here, N is the order of the polynomial, and the constant coefficient $\mathbf{K}_j^{(i)}$ is determined from the reconstruction technique. During the time step $\Delta t^{(n)}$ the most rapid disturbances at the cell boundaries propagate to the locations $x_{j+1/2,l} = a^{-}_{j+1/2}\Delta t^{(n)}$ and $x_{j+1/2,r} = a^{+}_{j+1/2}\Delta t^{(n)}$, where:

$$a^{+}_{j+1/2} = \max\left\{\lambda_{max}\left[\frac{\partial \mathbf{f}}{\partial \mathbf{q}}\left(\mathbf{q}^{-}_{j+1/2}\right)\right], \lambda_{max}\left[\frac{\partial \mathbf{f}}{\partial \mathbf{q}}\left(\mathbf{q}^{+}_{j+1/2}\right)\right], 0\right\}, \tag{3.49}$$

$$a^{-}_{j+1/2} = \min\left\{\lambda_{min}\left[\frac{\partial \mathbf{f}}{\partial \mathbf{q}}\left(\mathbf{q}^{-}_{j+1/2}\right)\right], \lambda_{min}\left[\frac{\partial \mathbf{f}}{\partial \mathbf{q}}\left(\mathbf{q}^{+}_{j+1/2}\right)\right], 0\right\}, \tag{3.50}$$

where λ_{max} and λ_{min} are the maximum and minimum eigenvalues of the flux Jacobian matrix.

In the fully discrete form, the averages of the solution at the cell centers are given by the following equation, with the details for derivation and evaluations found in Reference [90]:

$$\begin{aligned}\overline{\mathbf{q}}_j^{(n+1)} =& \frac{1}{\Delta x}\{\mathbf{K}_{j-1/2}^{(0)} a_{j-1/2}^{+}\Delta t^{(n)} + \left[\Delta x + \left(a_{j+1/2}^{-} - a_{j-1/2}^{+}\right)\Delta t^{n}\right]\overline{\mathbf{w}}_j^{(n+1)} \\ & - \mathbf{K}_{j+1/2}^{(0)} a_{j+1/2}^{-}\Delta t^{(n)}\} + \mathcal{O}\left[\left(\Delta t^{(n)}\right)^2/\Delta x\right]\end{aligned} \tag{3.51}$$

where the updated, staggered solution $\overline{\mathbf{w}}_j^{(n+1)}$ is given by:

$$\begin{aligned}\overline{\mathbf{w}}_j^{(n+1)} =& \sum_{i=0}^{N}\frac{\mathbf{K}_j^{(i)}}{i+1}[\left(\frac{\Delta x}{2}\right)^{i}\sum_{k=0}^{i}(-1)^k + \left(\frac{\Delta x}{2}\right)^{i-1}\left(a_{j-1/2}^{+}\Delta t^{(n)}\right)\sum_{k=0}^{i}(-1)^k k \\ & + \left(\frac{\Delta x}{2}\right)^{i-1}\left(a_{j+1/2}^{-}\Delta t^{(n)}\right)\sum_{k=0}^{i}(-1)^k(i-k)] \\ & - \frac{1}{\Delta x + (a_{j+1/2}^{-} - a_{j-1/2}^{+})\Delta t^{(n)}}\int_{t^{(n)}}^{t^{(n+1)}}\left(\mathbf{f}_{j+1/2,l} - \mathbf{f}_{j-1/2,r}\right)\, dt \\ & + \frac{1}{\Delta x + (a_{j+1/2}^{-} - a_{j-1/2}^{+})\Delta t^{(n)}}\int_{t^{(n)}}^{t^{(n+1)}}\int_{x_{j-1/2,r}}^{x_{j+1/2,l}}\mathbf{A}(\mathbf{q})\frac{\partial \mathbf{q}}{\partial x}\, dxdt + \mathcal{O}\left[(\Delta t)^2\right]\end{aligned} \tag{3.52}$$

where $\mathbf{f}_{j+1/2,r} = \mathbf{f}\left[\mathbf{q}(x_{j+1/2,r}, t^{(n)}\right]$ and $\mathbf{f}_{j+1/2,l} = \mathbf{f}\left[\mathbf{q}(x_{j+1/2,l}, t^{(n)}\right]$. The flux and nozzling source integrals can be evaluated using a quadrature that provides the desired order of accuracy. Crochet also formulated a semidiscrete form of the nonconservative system of equations in which the flux and nozzling integrals need not be evaluated using a quadrature. The final form of the semidiscrete scheme is obtained by manipulating Eq .(3.51) and is given by the following equation:

$$\frac{d\mathbf{q}_j}{dt} = \frac{1}{\Delta x}\left[\mathbf{F}_{j-1/2} - \mathbf{F}_{j+1/2} + \frac{a_{j-1/2}^{+}}{a_{j-1/2}^{+} - a_{j-1/2}^{-}}\mathbf{I}_{j-1/2} + \mathbf{I}_j - \frac{a_{j+1/2}^{-}}{a_{j+1/2}^{+} - a_{j+1/2}^{-}}\mathbf{I}_{j+1/2}\right] \tag{3.53}$$

where

$$\mathbf{F}_{j+1/2} = \frac{a_{j+1/2}^{+}\mathbf{f}_{j+1/2}^{-} - a_{j+1/2}^{-}\mathbf{f}_{j+1/2}^{+}}{a_{j+1/2}^{+} - a_{j+1/2}^{-}} + \frac{a_{j+1/2}^{+}a_{j+1/2}^{-}}{a_{j+1/2}^{+} - a_{j+1/2}^{-}}\left(\mathbf{q}_{j+1/1}^{+} - \mathbf{q}_{q+1/2}^{-}\right) \tag{3.54}$$

and

$$\begin{aligned}
\mathbf{I}_{j-1/2} &= \int_{x^-_{j-1/2}}^{x^+_{j+1/2}} \mathbf{A}(\mathbf{q})\, \frac{\partial \mathbf{q}}{\partial x}\, dx \\
\mathbf{I}_{j} &= \int_{x^+_{j-1/2}}^{x^-_{j+1/2}} \mathbf{A}(\mathbf{q})\, \frac{\partial \mathbf{q}}{\partial x}\, dx \qquad (3.55) \\
\mathbf{I}_{j+1/2} &= \int_{x^-_{j+1/2}}^{x^+_{j+1/2}} \mathbf{A}(\mathbf{q})\, \frac{\partial \mathbf{q}}{\partial x}\, dx. \qquad (3.56)
\end{aligned}$$

The details of the derivations and evaluations can be found in the Reference [90]. Crochet also developed a technique used to minimize numerical diffusion and evaluated the nozzling source and discussion on those is outside the preview of this study and complete details can be found in the reference. Therefore, the one-dimensional semidiscrete central scheme formulation in Eqs. (3.37) forms a system of nonliner ODE's. The resulting system of ODE's can be solved at each cell center using a standard ODE solver. To integrate in time, a third-order Runge-Kutta (RK) scheme is used to retain high temporal accuracy. The computation proceeds in three steps:

$$\begin{aligned}
\mathbf{q}_j^{(1)} &= \mathbf{q}_j^{(n)} + \Delta t^{(n)} \mathcal{K}\left(\mathbf{q}_j^{(n)}\right), \\
\mathbf{q}_j^{(2)} &= \frac{3}{4}\mathbf{q}_j^{(n)} + \frac{1}{4}\mathbf{q}_j^{(1)} + \frac{1}{4}\Delta t^{(n)} \mathcal{K}\left(\mathbf{q}_j^{(1)}\right), \qquad (3.57) \\
\mathbf{q}_j^{(n+1)} &= \frac{1}{3}\mathbf{q}_j^{(n)} + \frac{2}{3}\mathbf{q}_j^{(2)} + \frac{2}{3}\Delta t^{(n+1)} \mathcal{K}\left(\mathbf{q}_j^{(2)}\right).
\end{aligned}$$

Chapter 4
Inert Shock Loading of Granular HMX

In this chapter, the evolution of an inert compaction wave due to compression of granular HMX by action of a moving piston is considered. A compaction wave refers to the propagation of a finite disturbance in solid volume fraction due to local mechanical stress imbalance. It has been shown by experiments that material compaction plays a significant role in DDT and SDT of GXs [45–47]. In the following section, simulations of inert uniaxial shock loading of granular HMX at both the meso- and macro-scale is discussed. In particular, emphasis is placed on comparing effective quasi-steady wave profiles obtained by averaging meso-scale fields to those given by a independent macro-scale theory. Key objective of this section is to determine the extent to which these individual descriptions applied to the same problem compare.

4.1 Single Shock Loading

The paradigm for this study is illustrated in Figs. 4.1 and 4.2. The meso-scale analysis describes two-dimensional (2D), plane strain loading of a large ensemble of deformable HMX particles. The representative ensemble shown in Fig. 4.1 consists of approximately 4000 randomly packed, initially circular particles having an average size of $\overline{d} = 60$ μm with a narrow distribution. The average initial solid volume fraction of the ensemble is $\overline{\phi}_0 = 0.835$ and all inter-particle pores are massless. Though the assumptions of 2D plane strain and circular particle geometry are restrictive, they enable leading-order effects of packing density on compaction shock dissipation to be examined based on well-resolved computations; they also form a basis for systematically examining the effects of other micro-structural features and three-dimensionality in the future. Periodic conditions are imposed along transverse boundaries of the computational domain, and a free condition is imposed at the far-field axial boundary. A rigid piston impacts the material with constant

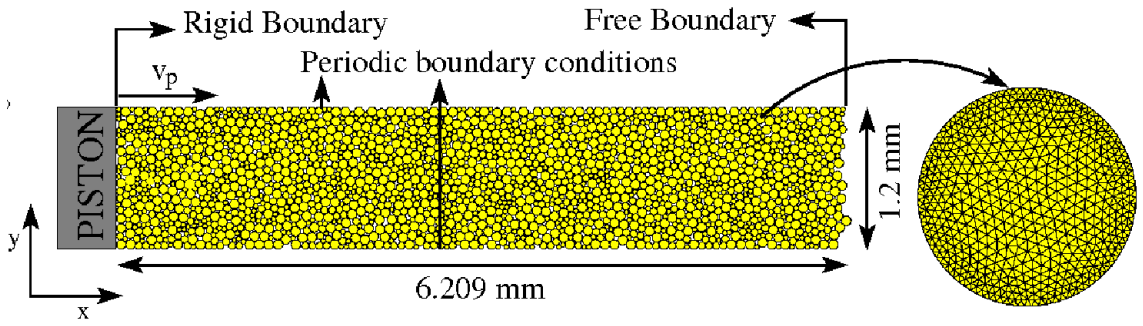

Figure 4.1: Representative computational domain and boundary conditions used for the meso-scale simulations.

speed U_p causing the rapid development and subsequent propagation of a quasi-steady compaction shock having speed D. Shock strength is characterized in terms of effective pressure $\overline{P}$ which depends on both $\overline{\phi}_0$ and U_p. Figure 4.2(a) illustrates a computed piston supported shock having speed $D = 2136$ m/s for $\overline{\phi}_0 = 0.84$ and $U_p = 500$ m/s. The shock quickly develops into a quasi-steady wave following impact, as indicated by its position-time curve in Fig. 4.2(b), and its pressure $\overline{P} = 1.6$ GPa is sufficiently high to eliminate porosity. The shock speed is lower than the ambient sound speed of solid HMX (≈ 2740 m/s) due to energy dissipation and dispersion associated with pore collapse.

As already discussed in chapter 2, quasi-steady compaction shock profiles are obtained by first filtering thermomechanical fields at fixed times and then performing ensemble averaging of the resulting spatially filtered profiles, as illustrated in Fig. 4.3 for the case shown in Fig. 4.2. This procedure is necessary to obtain the relation between effective packing density, shock pressure, and dissipated work, and to obtain effective profiles that can be directly compared to those given by the macro-scale theory. Fluctuations in spatially filtered profiles are relatively small for $\overline{\phi}_0 = 0.84$, but become more pronounced as $\overline{\phi}_0$ decreases.

4.1.1 Results

Results are given in this section that illustrate the variation in compaction shock end states and profiles with shock strength and initial packing density. Emphasis is placed

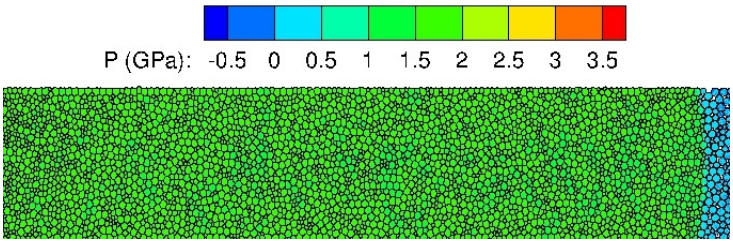

(a)

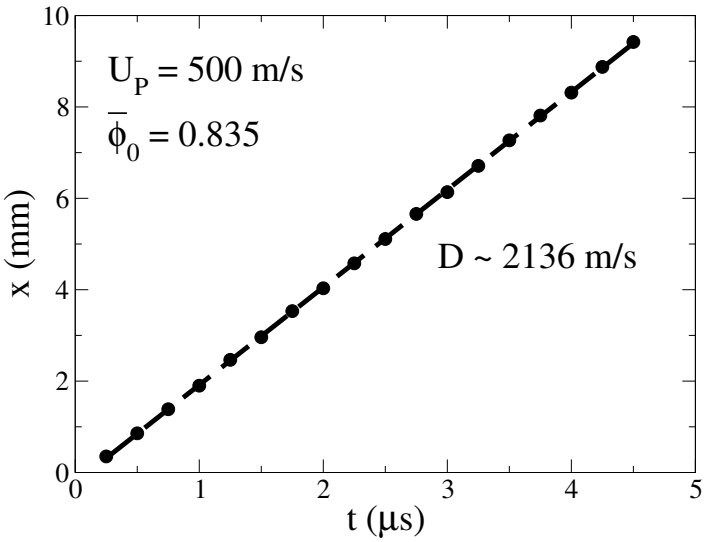

(b)

Figure 4.2: Development of a quasi-steady compaction shock corresponding to $U_p = 500$ m/s and $\phi_0 = 0.84$: (a) pressure contours at $t = 4.5$ μs; (b) shock position as a function of time indicating a quasi-steady shock speed of $D \approx 2136$ m/s.

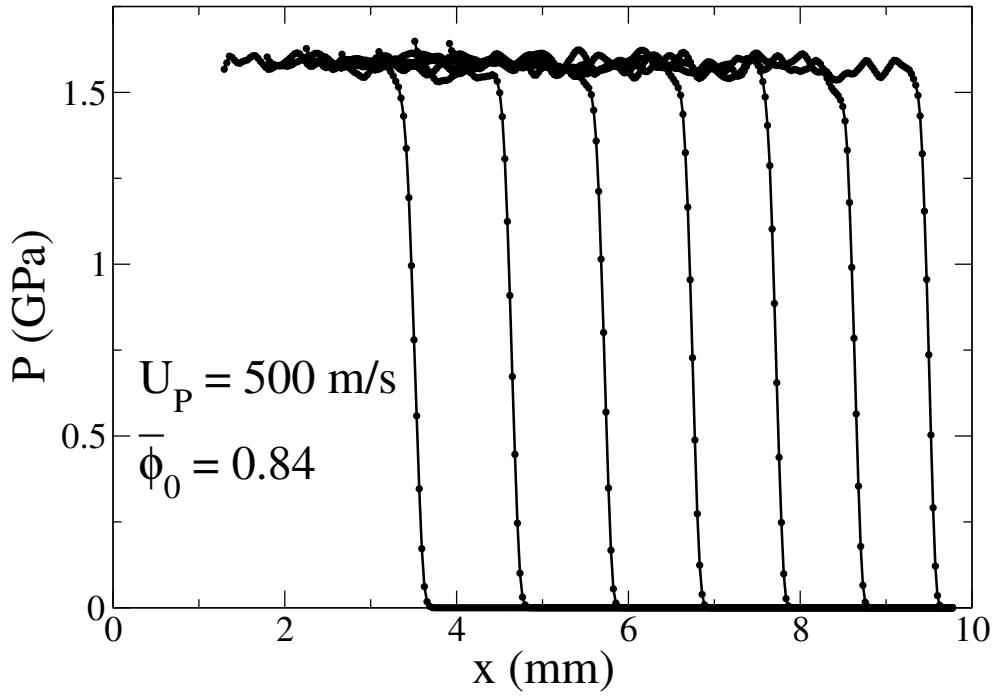

(a)

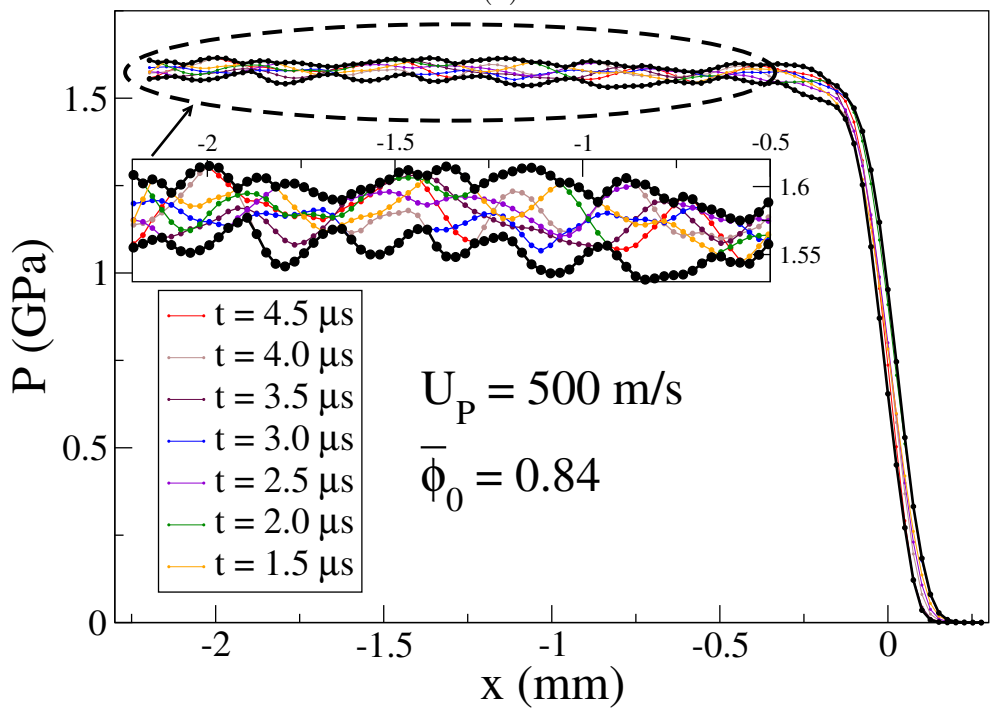

(b)

Figure 4.3: Development of a quasi-steady compaction shock corresponding to $U_p = 500$ m/s and $\phi_0 = 0.84$: (a) effective quasi-steady pressure profiles at advancing times; and (b) superposed quasi-steady profiles highlighting local fluctuations.

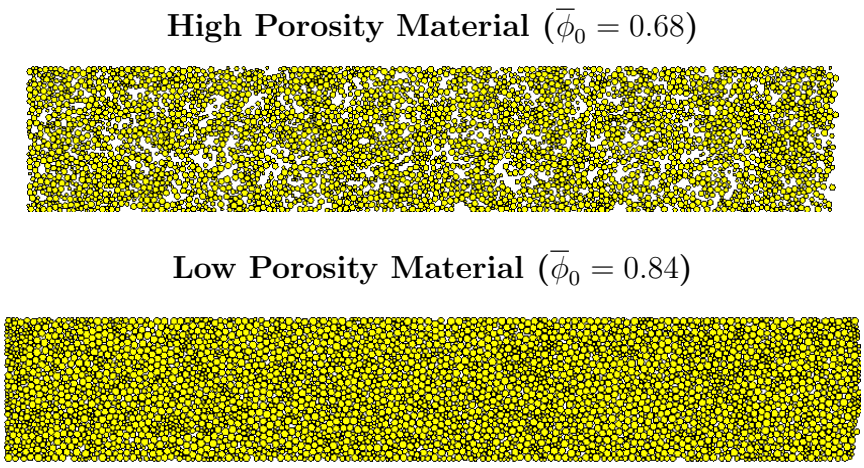

Figure 4.4: Representative initial particle ensembles generated by the pseudo-gravity settling algorithm.

on examining effective dissipation power and dissipated work within shocks because they represent a primary heating mechanism that can trigger combustion [17]. Effective dissipation power for the meso-scale theory is given by $\overline{\dot{w}_d} = \overline{T\dot{\eta}}$ and is computed by averaging Eq. (2.10) using Eq. (2.12); dissipated work $\overline{w}_d$ is computed by integrating Eq. (2.10) in time and averaging the result. Dissipation power for the macro-scale theory is directly computed using Eq. (3.35), and dissipated work is computed by integrating this result in time. Dissipation power also provides a good indication of shock width because it vanishes in both the ambient and shock end state.

Materials examined in study have an initial solid volume fraction within the range $0.68 \leq \overline{\phi}_s \leq 0.84$ and a mean particle size of $\overline{d} = 60$ μm with a narrow distribution. Figure 4.4 shows particle ensembles having $\overline{\phi}_s = 0.68$ and 0.84. Significant local fluctuations in packing density exist within low density material that can influence shock propagation and dissipation, as discussed below. Simulations are performed for piston speeds within the range $100 \leq U_p \leq 500$ m/s because of their relevance to deflagration- and shock-to-detonation transition. The meso-scale algorithm used in this study, implemented using FORTRAN 90, was executed on 64, 2.66 GHz Dual Core Xeon 64-bit processors workstations having 4 GB RAM each. One-dimensional parallelization was accomplished by

dividing the spatial domain into transverse sectors containing 50-60 particles each, and by assigning each sector to a specific processor. MPI libraries were used to exchange information between processors at sector boundaries. A typical run time for a single meso-scale simulation was approximately 3 days.

4.1.2 Shock End State

Figure 4.5 compares shock end states in the U_p-D and U_p-$\overline{P}$ Hugoniot planes, where D is the steady shock speed and $\overline{P} = \overline{P\ \phi} = P_s\phi$ is the effective pressure behind the shock predicted by both mesoscale simulations and macroscale compaction theory. Effective pressure is a commonly used measure of shock strength. Also shown in the figure are data for granular HMX having $\overline{\phi}_0 = 0.66$ [67] and $\overline{\phi}_0 = 0.99$ [136]. For fixed U_p, both D and $\overline{P}$ increase with increasing $\overline{\phi}_0$ due to higher acoustic impedance of the material and enhanced stress bridging between particles within shocks.

Overall, agreement between predictions and data is consistent and reasonable. At higher packing densities, the compaction theory predicts lower shock speeds for approximately $U_p \leq 250$ m/s, and predicts higher shock pressures for $U_p \geq 250$ m/s, compared to the mesoscale simulations. This critical value of piston speed separates two compaction shock regimes: a low pressure regime referred to as strength dominated because material strength is important in preventing complete pore collapse and a high pressure regime referred to as pressure dominated because the pressure is sufficient to eliminate porosity [139]. Material strength plays a less significant role than pressure for pressure dominated shocks. Discrepancies in shock speed for strength dominated waves are due to inter-particle friction in the meso-scale simulations which effectively enhances material rigidity under plane-strain confinement and results in enhanced stress transmission and lower dissipation. Because friction is less consequential for pressure dominated shocks, better agreement between U_p-D Hugoniots is predicted. Discrepancies in shock pressure, which are most pronounced for pressure dominated shocks, are due to differences in the equation of state used by the two descriptions. Structures analyzed in this study largely represent pressure dominated

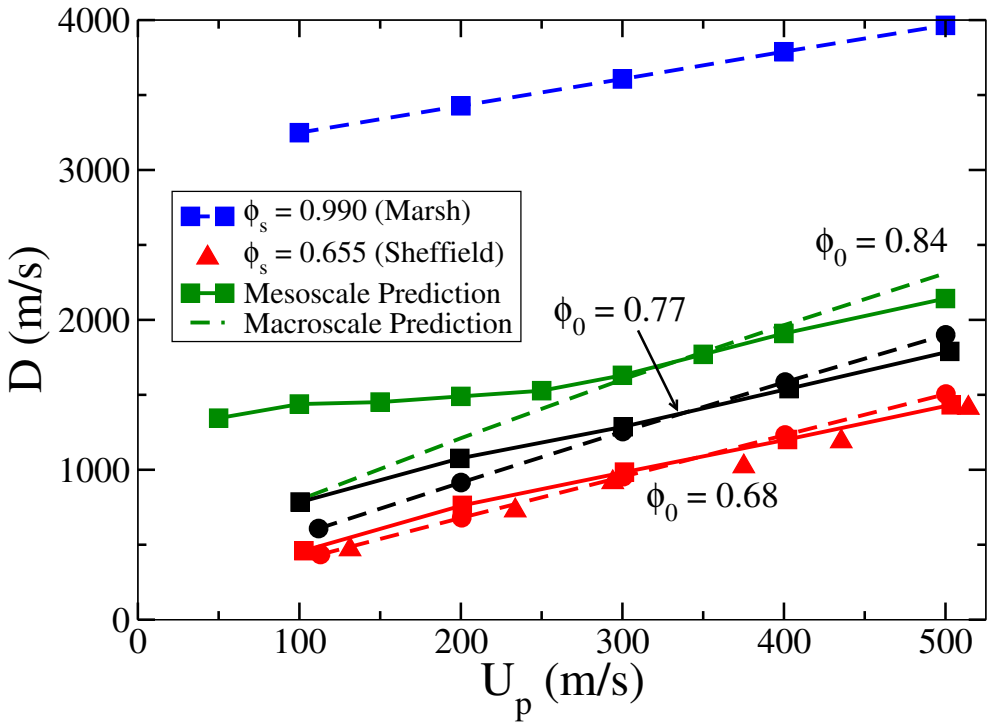

(a)

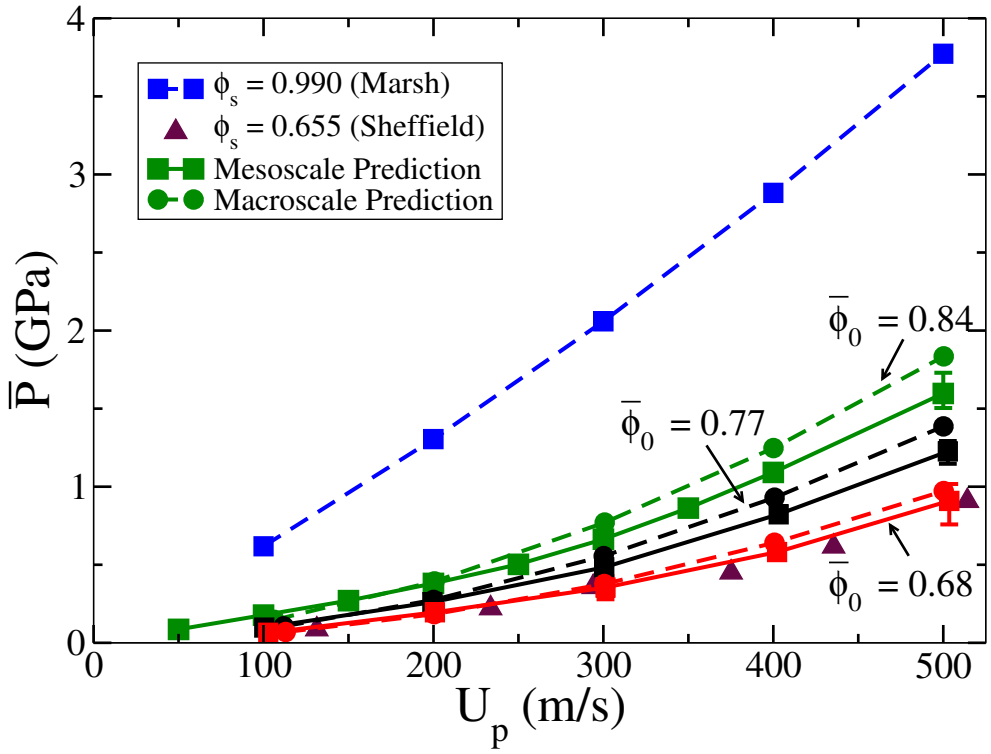

(b)

Figure 4.5: Effective shock end states (Hugoniots) predicted by the meso-scale simulations and compaction theory for different initial particle packing densities ($0.68 \leq \overline{\phi}_s \leq 0.84$): (a) U_p-D plane and (b) U_p-P plane.

shocks.

4.1.3 Spatial Shock Profile

Figures 4.6−4.8 illustrate the computed variation in spatial shock profile with $\overline{\phi}_0$ for $U_p = 300$ m/s and 500 m/s. These profiles connect the ambient material state to the quasi-equilibrium state behind the shock. Shown in the figures are profiles for effective pressure, dissipation power, and dissipated work, respectively, expressed in a shock-attached reference frame. Meso-scale simulations fundamentally resolve shock width based on interactions between particles whereas it is modeled by the value of viscosity μ in the compaction theory.

Several observations are noteworthy regarding shock width and dissipation. First, shock widths predicted by meso-scale simulations and compaction theory are comparable suggesting that the value of viscosity $\mu = 40$ kg/(m s) used with the compaction theory is compatible with a micro-structure having a nearly uniform particle size of $\overline{d} = 60$ μm. Dissipation rate profiles indicate that shock width is weakly dependent on initial packing density for ranges considered in this study, and that it appreciably decreases with increasing shock strength.

Second, computed dissipation power profiles shown in Fig. 4.7(a-b) qualitatively agree, but quantitative discrepancies exist. Bars are shown on mesoscale profiles indicating the range of fluctuations in effective peak dissipation power within compaction shocks due to local spatial variations in density. The fluctuations are substantial, and are approximately 50% of their ensemble average values. This sensitivity is more pronounced for dissipation power than other integrated quantities because it represents a time rate of change in dissipated work. Peak dissipation power increases with shock strength, and discrepancies between the compaction theory and mesoscale simulations become more pronounced due to differences in their equations of state. Both descriptions indicate that the effective peak dissipation power increases with ϕ_o for fixed U_p. This result is important because experiments on the shock loading of low density explosives indicate a reduction in shock sensitivity

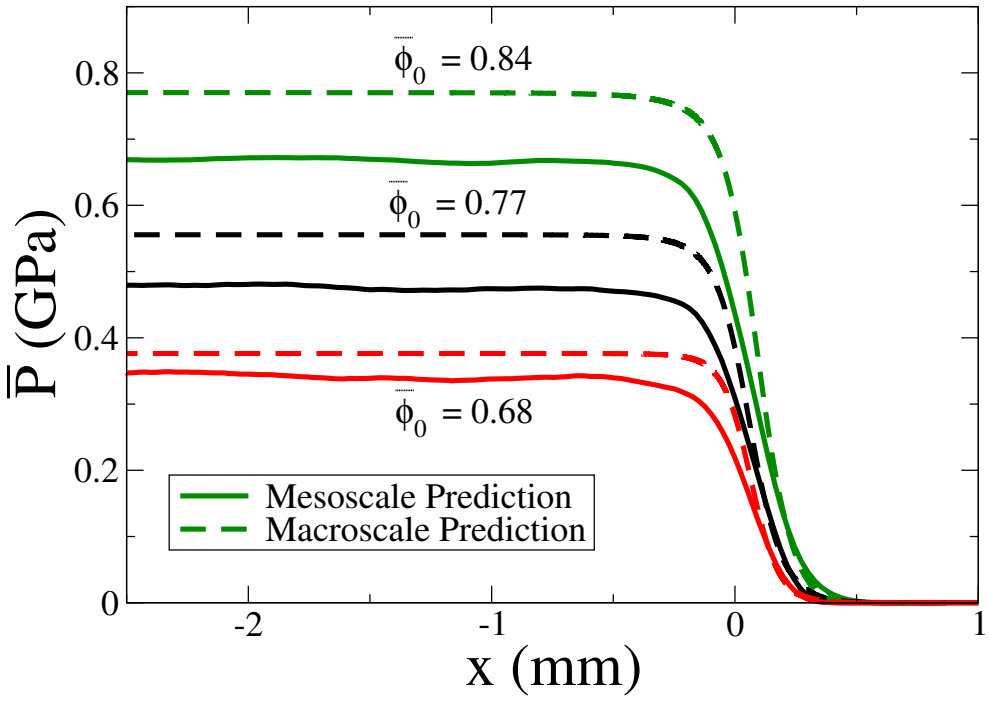

(a)

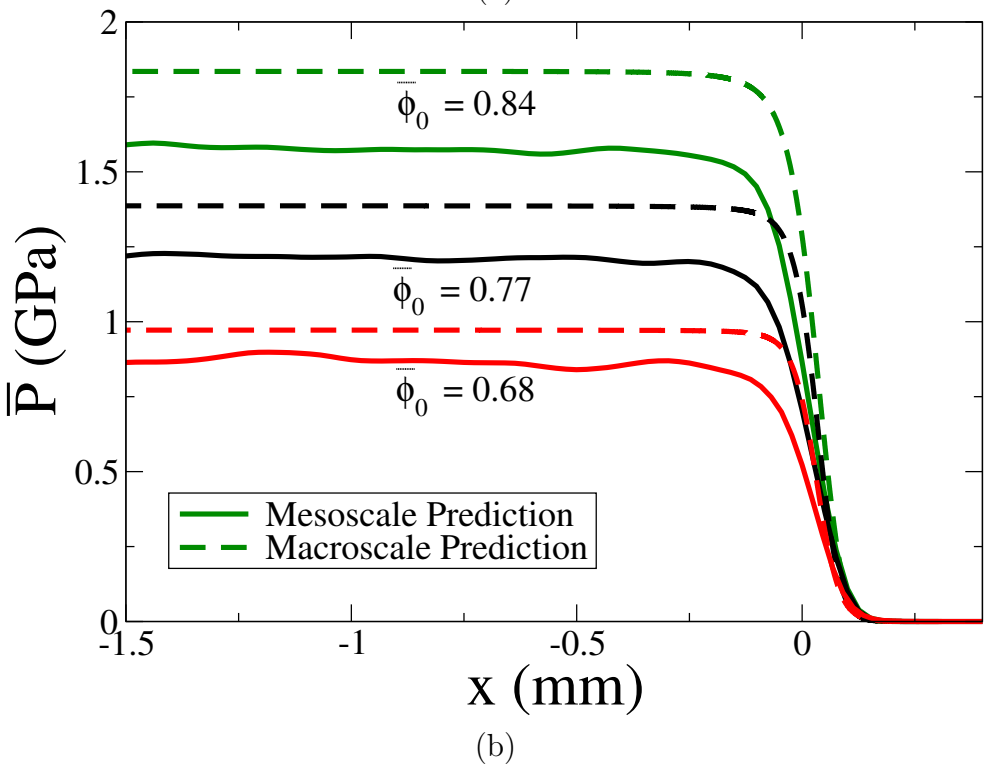

(b)

Figure 4.6: Comparison of meso- and macro-scale predictions for the variation in effective pressure $\overline{P}$ with ϕ_0: (a) $U_p = 300$ m/s and (b) $U_p = 500$ m/s.

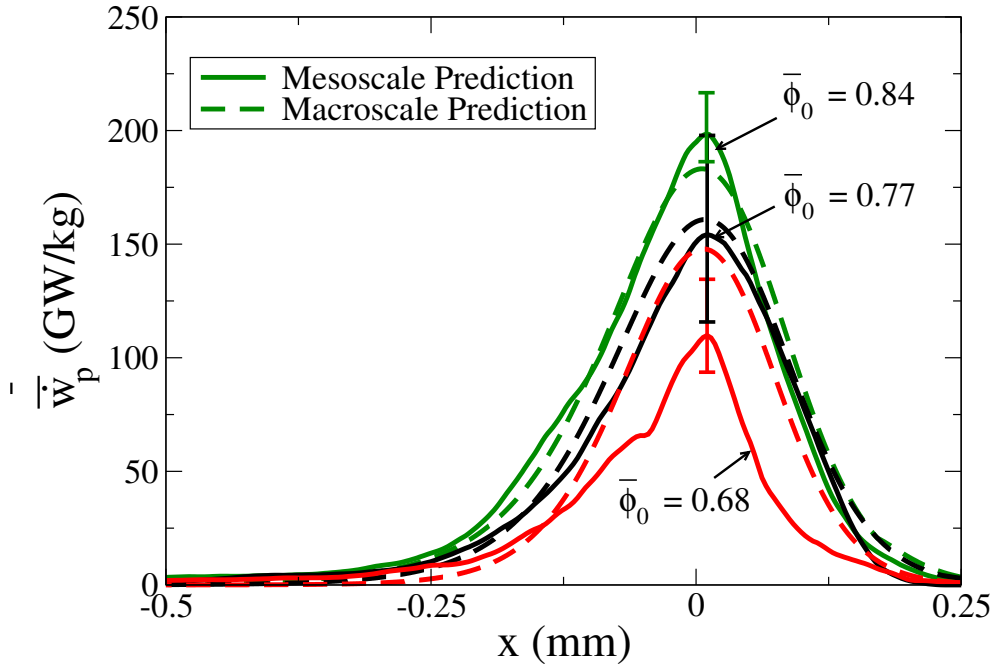

(a)

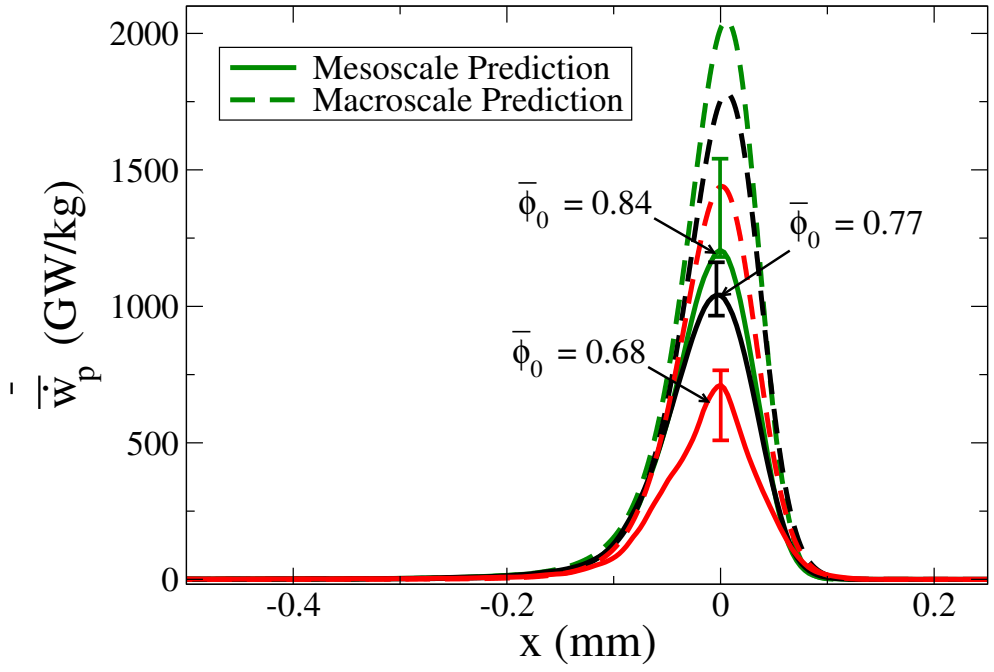

(b)

Figure 4.7: Comparison of meso- and macro-scale predictions for the variation dissipative work rate $\overline{w_p}$ with ϕ_0: (a) $U_p = 300$ m/s and (b) $U_p = 500$ m/s.

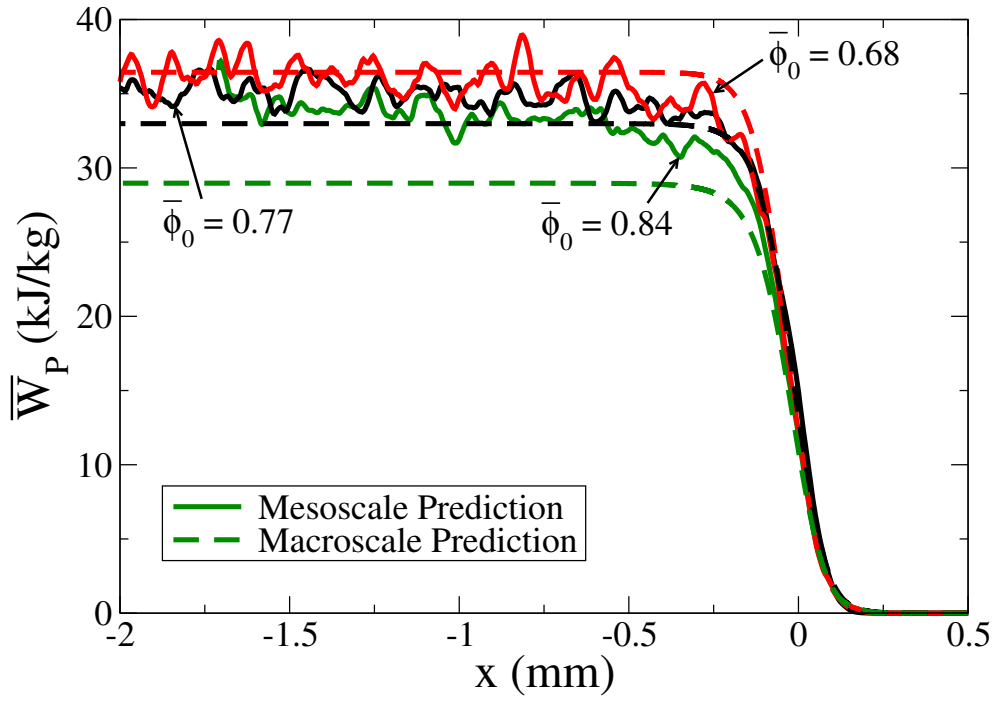

(a)

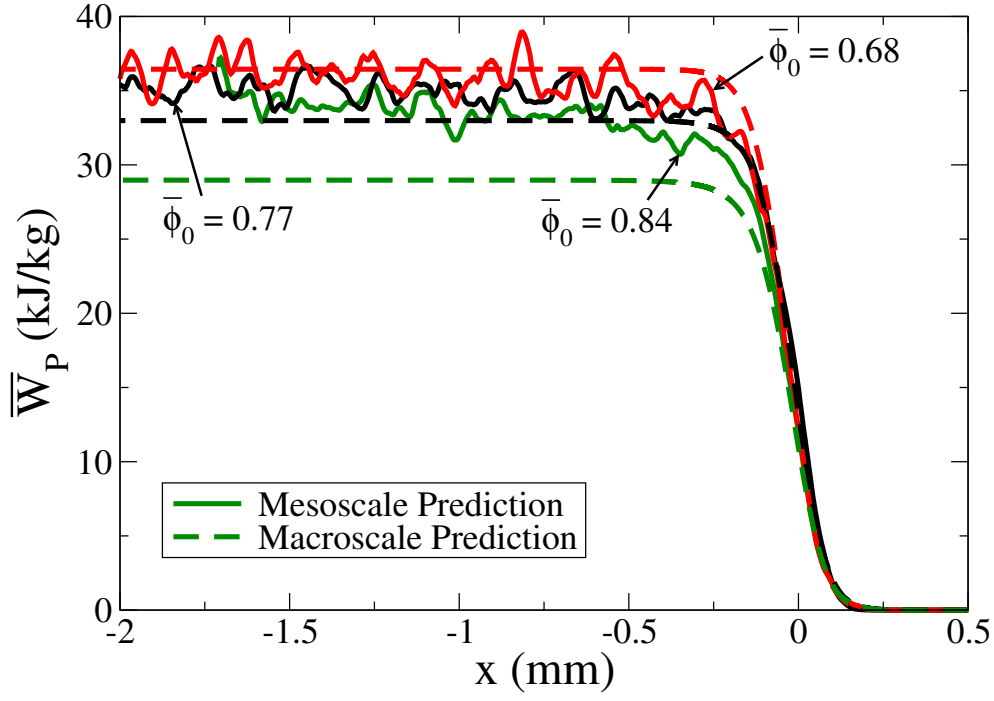

(b)

Figure 4.8: Comparison of meso- and macro-scale predictions for the variation in dissipative work ($\overline{W_P}$) within compaction shocks with ϕ_0: (a) $U_p = 300$ m/s and (b) $U_p = 500$ m/s.

with increased packing density; therefore, dissipation power by itself is not an accurate measure of shock sensitivity. Dissipated work profiles, obtained by integrating dissipation power across shocks, are shown in Fig. 4.8(a-b). Though peak dissipation power increases with ϕ_0 for fixed U_p, dissipated work decreases. An increase in dissipated work increases the effective temperature rise which is compatible with enhanced sensitivity; consequently, it represents a plausible means to characterize shock induced ignition and burn in that it implicitly accounts for hot-spot formation. Moreover, dissipated work can principally account for shock desensitization because it is influenced by shock loading history [110].

Shock impedance increases with packing density resulting in faster and stronger shocks for fixed U_p. It is also insightful to examine how dissipated work is affected by packing density for equal strength shocks. To this end, U_p-$\overline{P}$ Hugoniot relations are used to express U_p in terms of $\overline{P}$. Figure 4.9 shows the variation in effective dissipated work with shock pressure and packing density predicted by both the compaction theory and mesoscale simulations. Predictions indicate that the relation between dissipated work and pressure is well-described by the power-law $\overline{w}_d = a\overline{P}_s^n$, where both the prefactor a and the exponent $n = \partial \log \overline{w}_d / \partial \log \overline{P}_s$ depend on $\overline{\phi}_0$. The value of n is predicted to monotonically increase from $n = 1.13$ for $\overline{\phi}_0 = 0.68$ to $n = 1.20$ for $\overline{\phi}_0 = 0.84$ which is indicative of enhanced pressure sensitivity. A consequence of this prediction is that differences in shock dissipation with packing density decrease, albeit slowly, as shock pressure increases. It is interesting that the measured variation in run distance to detonation with input shock pressure (referred to as a Pop-plot curve) for low density HMX having comparable packing densities to those studied here indicates a similar trend. Measurements show that the run distance $l \sim \overline{P}_s^{-m}$, where the constant exponent $m = -\partial \log l / \partial \log \overline{P}_s$ slightly increases with packing density [140]. If it is assumed that $l \sim \overline{w}_d^{-1}$ to leading-order, then $n \sim m$. Though speculative due to complex hot-spot formation, chemistry, and multi-phase transport associated with shock initiation, the similar dependency of shock dissipation and Pop-plot curves on packing density warrants additional study.

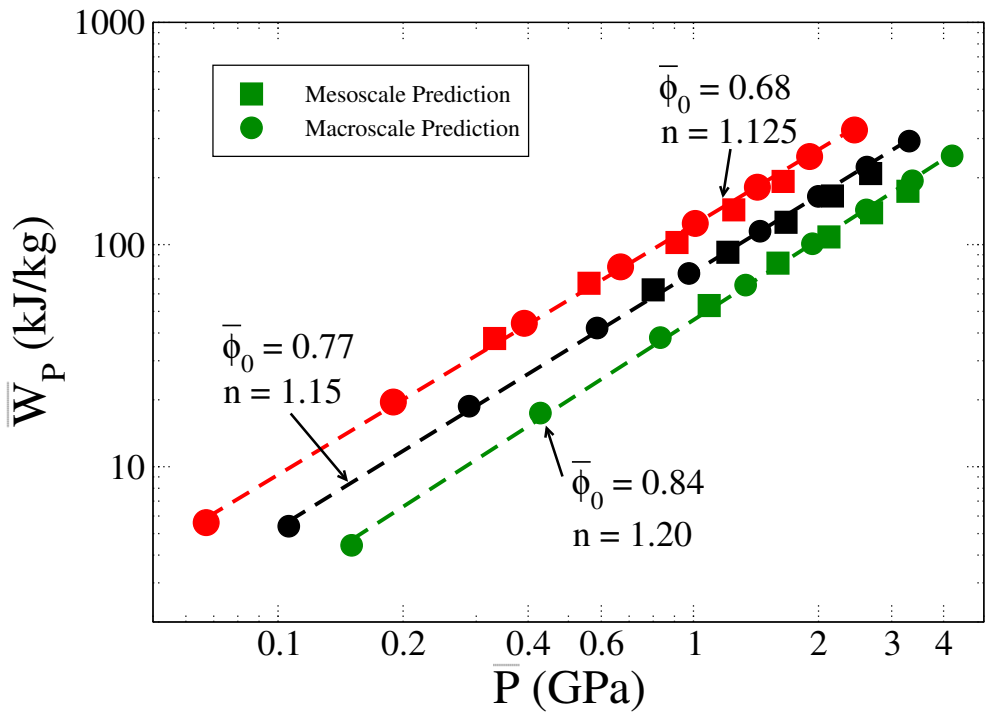

Figure 4.9: Variation in dissipated work with shock pressure predicted by the mesoscale simulations and compaction theory.

4.1.4 Shock Rise Time

Gas gun experiments often measure stress and velocity histories following particles (i.e., Lagrangian coordinates) from which shock rise times can be determined [67]. Rise time is important because it establishes the time scale of dissipative heating induced by pore collapse within shocks. Data indicate that rise time not only depends on shock strength but also on material micro-structure, particularly particle size.

Figure 4.10 shows particle velocity histories computed by the compaction theory and mesoscale simulations for U_p = 300 m/s and 500 m/s, respectively; time shifts between histories corresponding to different values of $\overline{\phi}_0$ are not significant and are included for ease of presentation. For consistency with experiments, rise time is estimated as the time between the 5% and 95% of maximum particle velocity levels [67].

The variation in computed shock rise time with U_p is shown in Fig. 4.11(a) for different values of $\overline{\phi}_0$. Also shown in the figure are data reported by Sheffield and co-workers [67]

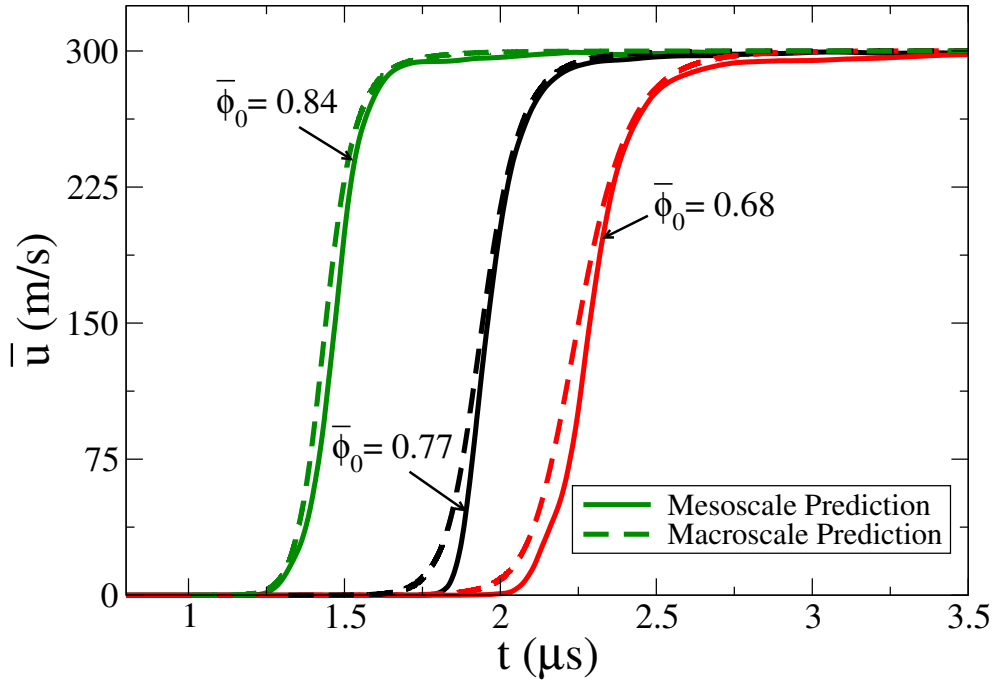

(a)

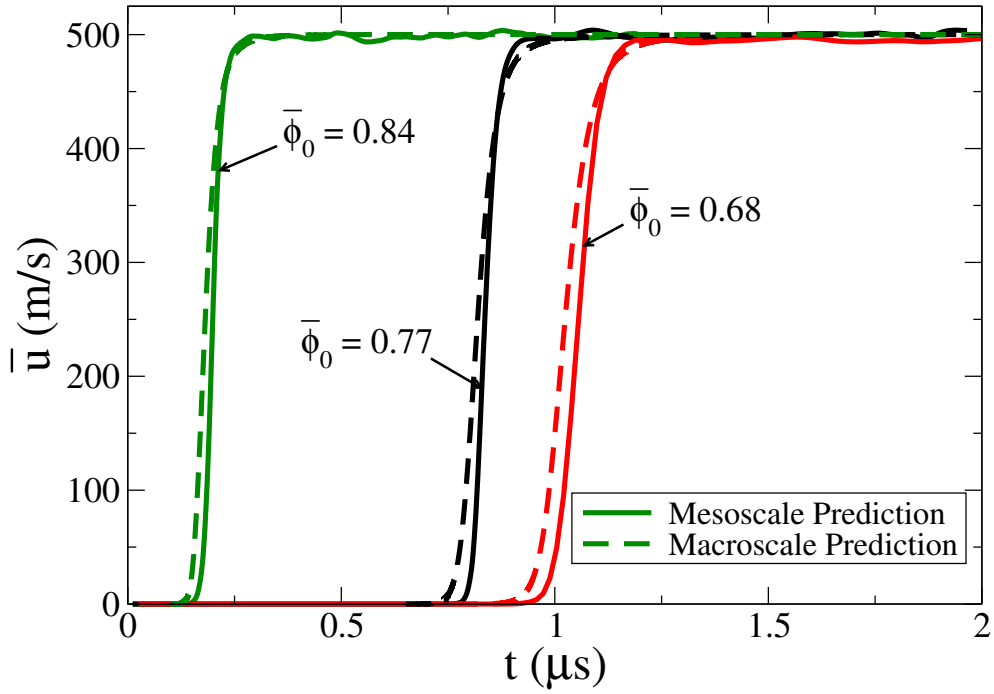

(b)

Figure 4.10: Particle velocity histories predicted by the mesoscale simulations and compaction theory: (a) $U_p = 300$ m/s and (b) $U_p = 500$ m/s.

for low density HMX. Data are shown that highlight variations due to packing density and particle size: here, "coarse" HMX refers to material having a mean particle size of ≈ 120 μm; and "fine" HMX refers to material having a mean size of $\approx$ 10-15 μm but also having some larger particles of ≈ 50 μm. No information about the particle size distribution is provided in Ref. [67]. The data indicate that rise time decreases with increasing U_p and is more sensitive to particle size than packing density. Measured rise times for fine HMX are 0.1 μs or less for the entire range of U_p, whereas rise time increases with decreasing piston speed for coarse HMX reaching a value of ≈ 0.5 μs for $U_p \approx 300$ m/s. Because the meso-scale simulations performed in this study are for ensembles having a mean particle size of 60 μm with a narrow distribution, they are more representative of coarse HMX than fine HMX. Both the compaction theory and meso-scale simulations give rise time estimates that qualitatively agree with data for coarse HMX, though greater sensitivity to $\overline{\phi}_0$ is predicted than indicated by the data. Because particle size influences rise time, quantitative discrepancies between computed estimates and the data may be partly due to variations in particle size distribution.

It is insightful to examine how rise time is affected by packing density for equal strength shocks. Shown in Fig. 4.11(b) are the computed estimates and data given in Fig. 4.11(a) expressed as a function of effective shock pressure. To this end, U_p-$\overline{P}$ Hugoniot data given in Fig. 4.5(b) for $\overline{\phi}_0 = 0.65$ were used to express U_p in Fig. 4.11(b) in terms of $\overline{P}$. The compaction theory and meso-scale simulations give similar results that exhibit a power-law relation $\tau_r = b\overline{P}^{-z}$, where the exponent $z \approx 1$ and the prefactor b has a weak dependence on $\overline{\phi}_0$. Agreement in computed rise times suggests that a constant value of viscosity may be reasonably assumed if the material has a narrow particle size distribution.

A simple estimate for rise time can be obtained from Eq. (3.7). Because most shocks considered in this study are pressure dominated resulting in the elimination of porosity, it is reasonable to assume that $P_s \gg \beta$. If it is further assumed that $P_s \approx$ constant, which is

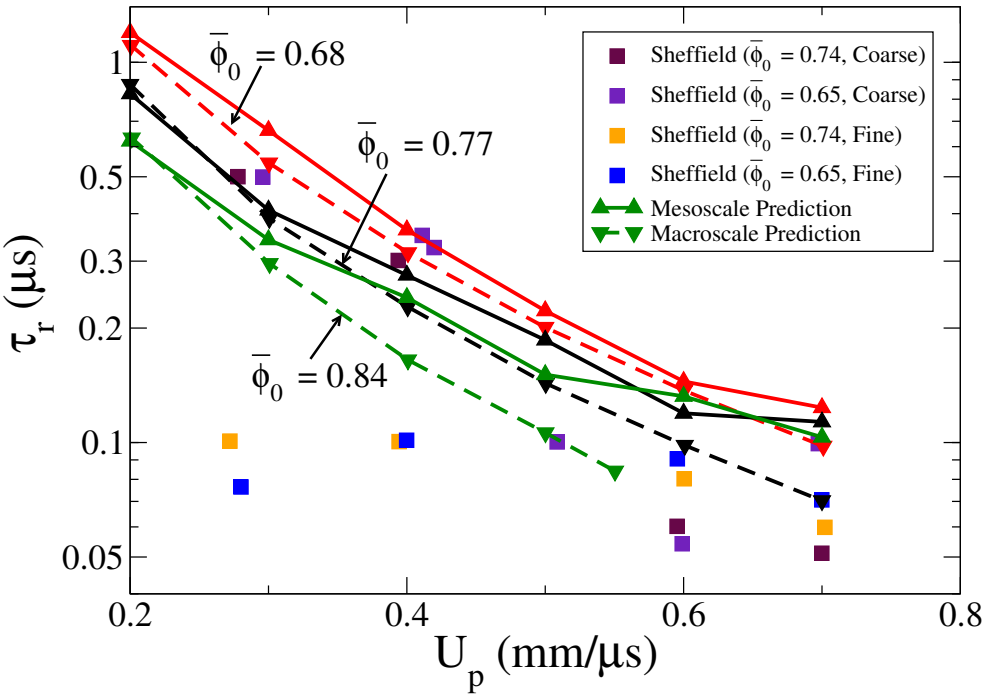

(a)

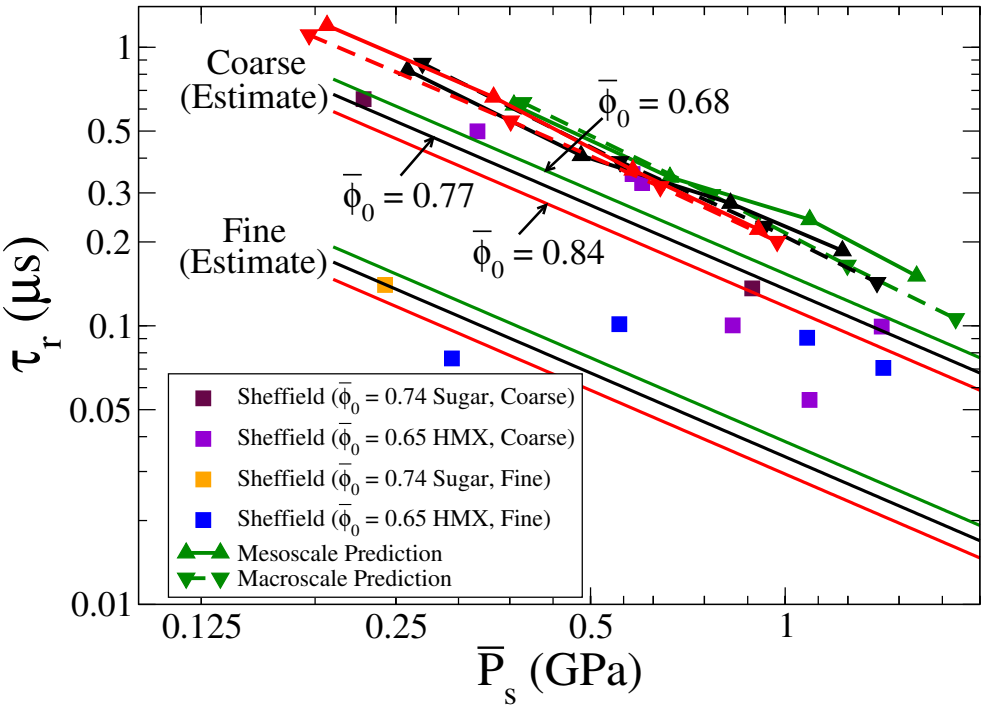

(b)

Figure 4.11: (a) Variation in shock rise time with U_p predicted by the mesoscale simulations and compaction theory. Also shown in the figure are data reported by Sheffield [67]; (b) Variation in shock rise time with shock pressure predicted by the meso-scale simulations and compaction theory. Estimates given by Eq. (4.1) were obtained using $\mu = 40$ kg/(m s) for coarse particles and $\mu = 10$ kg/(m s) for fine particles

compatible with a strong shock approximation, then Eq. (3.7) gives

$$\tau = \left(\frac{\mu}{P_s}\right) \int_{\overline{\phi}_0}^{\phi} \frac{d\phi'}{\phi'\,(1-\phi')} = \left(\frac{\mu}{P_s}\right) \ln\left(\frac{1-1/\overline{\phi}_0}{1-1/\phi}\right) \tag{4.1}$$

where τ is time. This expression implies that $\phi \to 1$ asymptotically as $\tau \to \infty$. An estimate for rise time τ_r can be obtained by evaluating $\tau(\phi = 0.99)$. This estimate indicates that $\tau \sim \mu P_s^{-1}$ and that it weakly depends on $\overline{\phi}_0$ in agreement with data. The viscosity μ may be assumed to monotonically decrease with particle size in that smaller particles will cause faster stress equilibration rates due to higher frequency pressure reverberations within and between particles.

Also shown in Fig. 4.11(b) are estimates based on Eq. (4.1) for $\overline{\phi}_0 = 0.68$, 0.77, and 0.84. Two values of viscosity are used: $\mu = 40$ kg/(m s), the value used throughout this study, which is representative of coarse HMX, and $\mu = 10$ kg/(m s) which is representative of fine HMX. Equation (4.1) properly characterizes the shock pressure dependence $z \approx 1$ obtained by meso-scale simulations, but is conservative because it ignores the configurational stress that implicitly accounts for material strength resulting in faster rise times. Scatter in the rise time data for fine HMX may again be attributable to the presence of large (~ 50 μm) particles embedded within the material. In a mixture of fine and large particles, it is possible that fine particles control rise time for weak and spatially dispersed shocks, and that large particles (even in relatively low concentrations) affect rise time for strong and thin shocks causing it to approach that of coarse HMX. This possibility may be computationally examined by meso-scale simulations of materials having prescribed particle size distributions, and the appropriate dependence of μ on micro-structure can be established. Departures from power-law behavior may also result as shock strength increases due to the onset of flow instabilities along pore surfaces that result in significant hydrodynamic jetting and vorticity.

4.2 Conclusions

Meso-scale simulations were performed on large ensembles of deformable particles to computationally characterize how dissipation within quasi-steady compaction shocks is affected by shock strength and packing density. The particles, which are representative of the explosive HMX, had an average size of 60 μm with a narrow distribution to isolate effects of packing density from those due to more complex distributions. Effective shock profiles, obtained by averaging meso-scale fields over space and time, explicitly account for resolved particle scale interactions within shocks. These profiles were compared to predictions given by an established macro-scale theory that describes shock compaction in terms of state variables that are conventionally interpreted as the average manifestation of particle scale fields. Emphasis was placed on examining dissipation power, dissipated work, and shock rise time because of their relevance to the ignition and burn of granular reactive solids.

Effective shock end states and spatial profiles computed by meso-scale simulations compare favorably to those given by the compaction theory. Shock speed and pressure increase with density for fixed piston speed due to higher acoustic impedance of the material and enhanced stress bridging between particles within shocks. Shock width is relatively insensitive to initial density, but significantly decreases with increasing shock strength. Increasing density is shown to increase the dissipation rate within shocks but decrease the integrated dissipated work over shock profiles which is indicative of reduced sensitivity. Consequently, dissipation rate by itself cannot properly account for observed phenomena such as shock induced ignition, burn, and desensitization, whereas dissipated work represents a plausible history-dependent thermodynamic quantity that can principally account for these effects. The development of dissipation-dependent macroscale Ignition and Burn (I&B) models for low density granular explosives is an ongoing topic of authors research [110]. Such models are analogous to entropy-based I&B models used to describe shock initiation of plastic-bonded explosives [101].

Quantitative discrepancies between the meso-scale simulations and compaction theory are largely due to differences in their equations of state and are more appreciable for pressure dominated shocks that are sufficiently strong to eliminate porosity. Despite such discrepancies, both descriptions indicate that the relation between dissipated work and pressure is well-described by a power-law having a density-dependent pressure prefactor and exponent. The value of the exponent is predicted to monotonically increase with density which is indicative of enhanced pressure sensitivity. A similar pressure sensitivity has been observed for the shock induced run distance to detonation for low density HMX. Though possibly fortuitous, these analogous sensitivities suggests that run distance to detonation may also be controlled by shock dissipation to leading-order; this issue warrants additional study.

Mesoscale simulations and the compaction theory indicate that the relation between shock rise time and pressure is well-described by a power law having an inverse pressure dependence with a prefactor that is weakly dependent on initial density and an exponent that has an approximate value of unity. This relation is confirmed by a simple analytical estimate for rise time based on the compaction theory. Comparisons indicate that the assumption of constant viscosity in the compaction theory is reasonable for a material having a nearly uniform particle size distribution. Computed rise times compare favorably to data for coarse HMX (mean particle size ~ 120 μm), whereas data for fine HMX (mean particle size ~ 10 μm, with some embedded particles of ~ 50 μm) indicate faster rise times, particularly for low pressure shocks [67]. The fine HMX data also indicate a lower sensitivity of rise time to pressure which may be due, in part, to the bimodal size distribution.

This study demonstrates how meso-scale simulations may be used to examine the effect of micro-structure on the thermomechanics of compaction shocks in granular reactive solids. These simulations may also be used to assess the validity of assumptions imposed by macro-scale theories and to provide rigorous interpretations of their predictions. In addition to the development of I&B models, another focus of the authors' ongoing research

is on characterizing how variations in particle size distribution influence compaction shock dissipation and rise time.

4.3 Successive Shock Loading

As a secondary objective modeling study is performed to characterize how rapid successive shock loading of low-density HMX affects dissipation and ignition. It is well established that a primary (or lead) shock can desensitize the material to subsequent shocks by reducing porosity. This phenomenon, referred to as shock desensitization, has been observed to occur during DDT of low density granular explosives in which complex interactions between impact and combustion-supported shocks influence the initiation process. In this study, a computational analysis is performed to characterize how rapid successive shock loading of low density HMX affects dissipation and ignition associated with the onset of vigorous burn. Meso-scale simulations are used to predict effective shock profiles and to examine hot-spot fields induced by pore collapse. Though this study has not been used directly, several key ideas from the outcome of this study have contributed to better understand this thesis. Interested readers are referred to Appendix B and Ref. [111] for detailed discussion on successive shock loading.

Few noteworthy points from the study useful for this thesis are listed here. As discussed in Section 5.1 history variable based on shock-induced dissipative work is shown to result in ignition fields that qualitatively differ from those based on shock pressure. In most simulations presented later in this thesis, The lead shock strength is sufficient to eliminate most porosity resulting in relatively small additional increases in dissipation by the secondary shock. Consequently, in all cases the value of dissipation induced by the secondary shock is substantially lower than that induced by a single shock of equivalent pressure which is indicative of significant shock desensitization. Based on an analysis of hot-spots, appreciable hot-spot agglomeration only results as the secondary shock overtakes the lead shock for the values of imposed piston impact velocities. This prediction demonstrates how the strength of the secondary shock needed to induce hot-spot agglomeration is dependent

on the strength of the lead shock and the value of ϕ_0. Increasing ϕ_0 tends to suppress dissipation and enhance desensitization.

Chapter 5
Analysis of Detonation Transition Mechanisms

Piston driven DDT experiments indicate that detonation is often abruptly triggered by the interaction of a strong combustion-supported secondary shock and a piston-supported primary (input) shock, where the nature of the interaction depends on initial packing density (ϕ_0) and primary shock strength (P_s). These interactions influence transition by affecting dissipative heating within the micro-structure during pore collapse. In this study, a loading history dependent ignition model based on variation in hot-spot formation frequency and a gas pressure dependent burn model is used in a macro-scale theory to numerically simulate piston-initiated DDT and SDT. The ignition model establishes the induction period before the onset of vigorous burn. The key objective of this study is the prediction and analysis of detonation transition mechanisms for shock initiation of low density granular HMX.

In this chapter, Section 5.1 focuses on utilizing correlations of predicted hot-spot fields with micro-structure and shock strength to formulate an ignition and burn model for shock induced initiation of low density HMX. The burn model is conceptually similar to traditional Ignition and Growth-type models but accounts for the onset of vigorous combustion (referred to as ignition) in terms of parameters that are explicitly computed from hot-spot fields predicted by meso-scale M&S. The induction time behind a compaction shock required for ignition is assumed to be inversely proportional to the formation rate of hot-spots by the shock. The burn model is implemented in the two-phase macro-scale model discussed in Chapter 3.1 to examine its effect on shock induced ignition and subsequent growth to detonation.

Next, numerical predictions of piston-initiated DDT and SDT are given in Sec 5.2. Various features observed in the transition mechanisms are highlighted and discussed, and

the results of the DDT simulations are presented for a parameter set that fits the LANL DDT experiment. Most reactive ignition and burn models use this experiment as a baseline to calibrate model parameters. In Section 5.3, the fitted model is used to obtain the run distance-to-detonation and time-to-detonation as a function of the input shock pressure (Pop-Plot). Lastly, in Section 5.4, a detailed parametric analysis for the burn model is discussed.

5.1 Ignition and Burn Model

The volumetric mass exchange term $\mathcal{C}$ in Eq. (3.1) describes the explosive combustion rate. It is common to take $\mathcal{C} = \mathcal{C}(\rho_s, \phi_s, P_g)$, where the dependency on gas pressure reflects strand burn data. It is plausible to use a modified expression that accounts for the induction period prior to macro-scale ignition. To this end, a dimensionless ignition variable λ_I is defined such that:

$$\mathcal{C} = \begin{cases} 0 & \text{for } \ 0 \leq \lambda_I < 1 \\ f & \text{for } \ \lambda_I = 1. \end{cases} \tag{5.1}$$

Here, it is assumed that negligible gas is produced during the induction period corresponding to $0 \leq \lambda_I < 1$ as hot-spots cook-off within the micro-structure. It is further assumed that the induction period is energetically inconsequential at the macro-scale. The subsequent burn phase associated with gas production and energy release is described by the function f.

5.1.1 Ignition Model

The ignition model is constructed to account for the shock loading history of the material. Similar history variable approaches, such as the History Variable Reactive Burn (HVRB) model, have been used to account for detonation initiation and propagation in PBXs based on the material's pressure loading history [127]. In this study, rate equations for λ_I are posed in terms of solid pressure and dissipative compaction work so that differences in the models can be examined for successive shock loading of granular HMX. Pressure is chosen because it represents a conventional measure of shock strength, whereas

dissipative compaction work is chosen because of its relevance to hot-spot formation.

- **Pressure-Dependent Ignition**

  A rate equation for the ignition variable λ_I in terms of pressure is given by

$$\frac{d\lambda_I}{dt_s} = \frac{1}{t_r}\left(\frac{P_s - P_0}{P_r}\right)^m, \tag{5.2}$$

where t_r and P_r are a reference time and pressure, m is a history variable exponent, and P_0 is the ambient material pressure ($P_0 = 0$ in this study because the material is initially stress free). The Lagrangian derivative of the explosive solid is given by $d/dt_s \equiv \partial/\partial t + u_s \partial/\partial x$. Integrating Eq. (5.2) gives

$$\lambda_I(t_s) = \frac{1}{t_r}\int_0^{t_s}\left(\frac{P_s - P_0}{P_r}\right)^m dt' \tag{5.3}$$

which is valid following explosive material points. Assuming a sustained discontinuous shock having constant pressure P_s, with $P_0 = 0$ and $t_s = 0$ immediately ahead of the shock, then Eq. (5.3) gives:

$$\lambda_I = \left(\frac{t_s}{t_r}\right)\left(\frac{P_s}{P_r}\right)^m \tag{5.4}$$

where t_s is time since shock passage. For ignition, $\lambda_I = 1$ and $t_s = \tau$; thus, $1 = (\tau/t_r)(P_s/P_r)^m$. The time scale t_r can be established once an expression for $\tau(P_s)$ is empirically and/or computationally prescribed.

Meso-scale M&S can be used to obtain an expression for $\tau(P_s)$ based on statistical aspects of hot-spot formation. Hot-spots are regions of elevated temperature that have the potential to thermally explode because they possess sufficient thermal inertia to overcome conductive losses. To this end, hot-spot material was identified by performing a level-cut through meso-scale predicted temperature fields $T(\mathbf{x}, t)$ at a predefined threshold temperature T_{th} within material located behind a sustained compaction shock. In this study, the term hot-spot refers to material having $T \geq T_{th}$. For example, the resulting

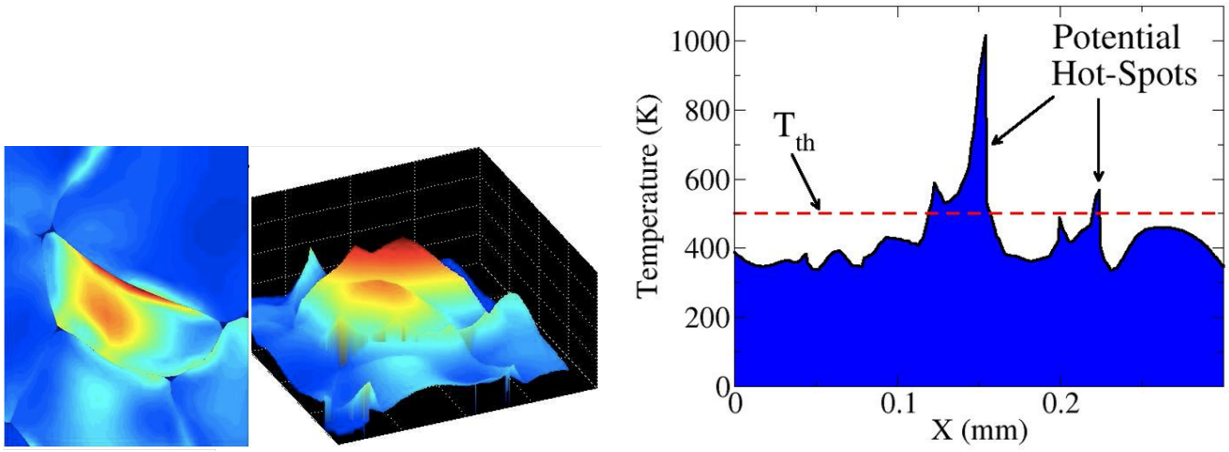

Figure 5.1: Illustration of the temperature thresholding technique to identify hot-spots. Here, $T_{th} = 500$K denotes the temperature threshold.

level-cut, illustrated in Fig. 5.1, produces a hot-spot temperature field that contains N hot-spots, $\hat{A}^1(\mathbf{x},t), \hat{A}^2(\mathbf{x},t), ..., \hat{A}^N(\mathbf{x},t)$, enclosed by contours $\hat{\Gamma}^1(\mathbf{x},t), \hat{\Gamma}^2(\mathbf{x},t), ..., \hat{\Gamma}^N(\mathbf{x},t)$. This thresholding technique partitions the domain $\hat{A}\,(\mathbf{x},t)$, into two disjoint sets, $A_{HS}\,(\mathbf{x},t)$ and $\overline{A}_{HS}\,(\mathbf{x},t)$, such that:

$$\begin{aligned} A_{HS}\,(\mathbf{x},t) \cup \overline{A}_{HS}\,(\mathbf{x},t) &= A\,(\mathbf{x},t) \\ A_{HS}\,(\mathbf{x},t) \cap \overline{A}_{HS}\,(\mathbf{x},t) &= \emptyset \end{aligned}$$

where $A_{HS}\,(\mathbf{x},t) = \hat{A}^1\,(\mathbf{x},t) \cup \hat{A}^2\,(\mathbf{x},t) \cup ... \cup \hat{A}^N\,(\mathbf{x},t)$. The domain $A_{HS}\,(\mathbf{x},t)$ contains all hot-spot material in $A(\mathbf{x},t)$ for a given material realization and piston speed, while the region $\overline{A}_{HS}(\mathbf{x},t)$ contains lower temperature material. This technique filters out cooler material enabling a quantitative description of hot-spot features. It is noted that hot-spot morphology (i.e., shape, size, etc.) is sensitive to simulation resolution and the choice of T_{th}. In this study, $T_{th} = 500$ K was chosen which is slightly above the $\beta - \delta$ phase transition temperature of HMX; as such, this value reasonably indicates the onset of chemical activity, though exothermic combustion requires $T > T_{th}$ and is dependent on hot-spot size. Complete details on hot-spot characterization is available in Refs. [80,81]; only details pertinent to this study are highlighted here.

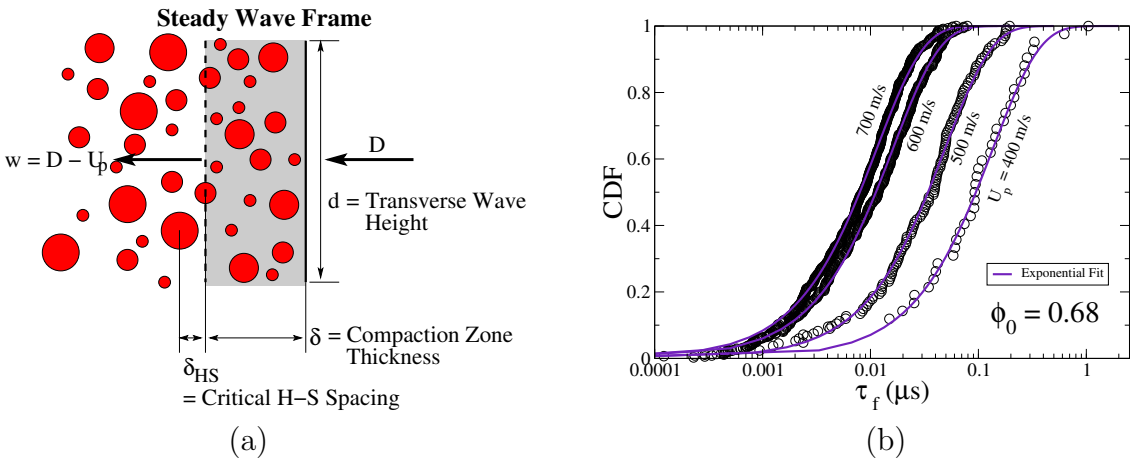

Figure 5.2: (a) An illustration of the reactive hot-spot axial spacing used to compute the formation time between successive hot-spots based on their centroid locations. (b) Predicted cumulative distribution of reactive hot-spot formation times for $\overline{\phi}_0 = 0.68$.

Because the analysis is performed for steady shocks, it is convenient to analyze hot-spots in a shock-attached frame, as conceptually shown in Fig. 5.2(a). In this frame, unstressed porous material enters the shock at speed D and stressed compacted material leaves the shock at speed $w = D - U_p$. The spatial shock structure has a finite thickness δ due to energy dissipation and dispersion. Though the compacted state possesses fluctuations in thermomechanical fields, its effective (or average) pressure may be used to characterize shock strength. Hot-spots are formed within the shock due to inelastic pore collapse, emerging from the shock at a frequency that depends on both meso-structure and wave strength.

Each hot-spot is identified by the location of its area centroid enabling the formation rate to be established. For a given simulation, the formation time, defined as the time between successive formation of hot-spots within the wave, is estimated by:

$$\tau_f = \frac{\delta_{HS}}{D - U_p} \tag{5.5}$$

where δ_{HS} is the axial distance between nearest upstream neighbor centroids in the compacted state. This definition of τ_f, which establishes the effective formation rate, is in-

fluenced by both hot-spot spacing and shock speed. It is plausible that meso-structures having comparable hot-spot spacing but different shock speeds will have different ignition times because their formation rates will differ. Figure 5.2(b) gives predicted distributions in hot-spot formation time for $\overline{\phi}_0 = 0.68$. Formation time distributions are approximately exponential indicating that hot-spot formation represents a time-invariant Poisson process for steady shocks. The cumulative exponential distribution function is given by

$$F(\tau_f) = 1 - \exp\left(-\overline{\lambda}\tau_f\right), \tag{5.6}$$

where $\overline{\lambda}$ is the effective formation rate/frequency. Predicted variations in $\overline{\lambda}$ with shock strength and meso-structure characterized by ϕ_0 are summarized in Fig. 5.3(a) in terms of U_p for $\overline{\phi}_0 = 0.68$, 0.77, and 0.84. The effective hot-spot formation rate represents a balance between nucleation, growth, and agglomeration of hot-spots as wave strength increases. *Nucleation* refers to the formation or seeding of new hot-spots in the vicinity of inter-particle contact surfaces, whereas growth and agglomeration refer to an increase in hot-spot size and the coalescence of neighboring hot-spots due to plastic flow, respectively. Because reactive hot-spots are identified by their area centroids which is independent of their size, agglomeration causes a reduction in $\overline{\lambda}$ when it dominates nucleation as hot-spots become ubiquitous. The predicted variation in $\overline{\lambda}$ with effective shock pressure $\overline{P}$ for the nucleation region can be characterized by a power-law

$$\overline{\lambda} = a\overline{P}^n. \tag{5.7}$$

The computed data and best-fit curves for each $\overline{\phi}_0$ are shown in Fig. 5.3(b); values for the power-law parameters are listed in Table 5.1. Both the prefactor a and exponent n vary with initial packing density. As $\overline{\phi}_0$ increases for fixed $\overline{P}$, the effective bulk modulus of the material increases resulting in volumetric stiffening and faster waves, and hot-spot spacing increases due to enhanced stress transmission between particles; consequently, $\overline{\lambda}$ decreases.

Table 5.1: Computed power-law parameters for hot-spot nucleation based on meso-scale M&S.

ϕ_0	a/I^* (μs^{-1}GPa^{-n})	n
0.68	1.609	2.12
0.77	0.451	2.49
0.84	0.112	2.68

However, because $n = \partial \log \overline{\lambda} / \partial \log \overline{P}$, the reactive hot-spot formation rate increases more rapidly with pressure for dense material.

The ignition time behind steady shocks τ^* is expressed in terms of a cumulative ignition function that depends on meso-structure and shock strength through $\overline{\lambda}$ and $\overline{P}$. The cumulative hazard (ignition) function corresponding to an exponential distribution of hot-spot formation times is given by

$$\mathcal{I}(\tau) = \int_0^\tau \overline{\lambda} \, d\tau' = \overline{\lambda}\tau, \tag{5.8}$$

where $\mathcal{I}(\tau)$ represents the specific accumulation of hot-spots behind the shock over time. It is assumed that ignition occurs when $\mathcal{I} = \mathcal{I}^*$, where the value of $\mathcal{I}^*$ is a material-specific parameter. From Eq. (5.8), the ignition time is given by $\tau^* = \mathcal{I}^* \overline{\lambda}^{-1}$ which can be expressed in terms of $\overline{P}$ and $\overline{\phi}_0$ using Eq. (5.7). The relation for ignition time is then given by

$$\overline{P}^n \tau^* = \frac{\mathcal{I}^*}{a}. \tag{5.9}$$

This relation is qualitatively similar to that used to empirically describe the onset of vigorous burn in Piston Driven Compaction (PDC) experiments for the DDT of granular explosives [131,132]. These experiments show that $n \approx 2$ which is close to the values listed in Table 5.1. To complete the description, it is necessary to estimate the ratio $a/\mathcal{I}^*$ for a given microstructure. Currently, the estimate is obtained by using a single datum for the time to vigorous burn at a fixed shock strength, as discussed in Ref. [110,111], though additional means of establishing an estimate are being explored. Best fit values for $a/\mathcal{I}^*$

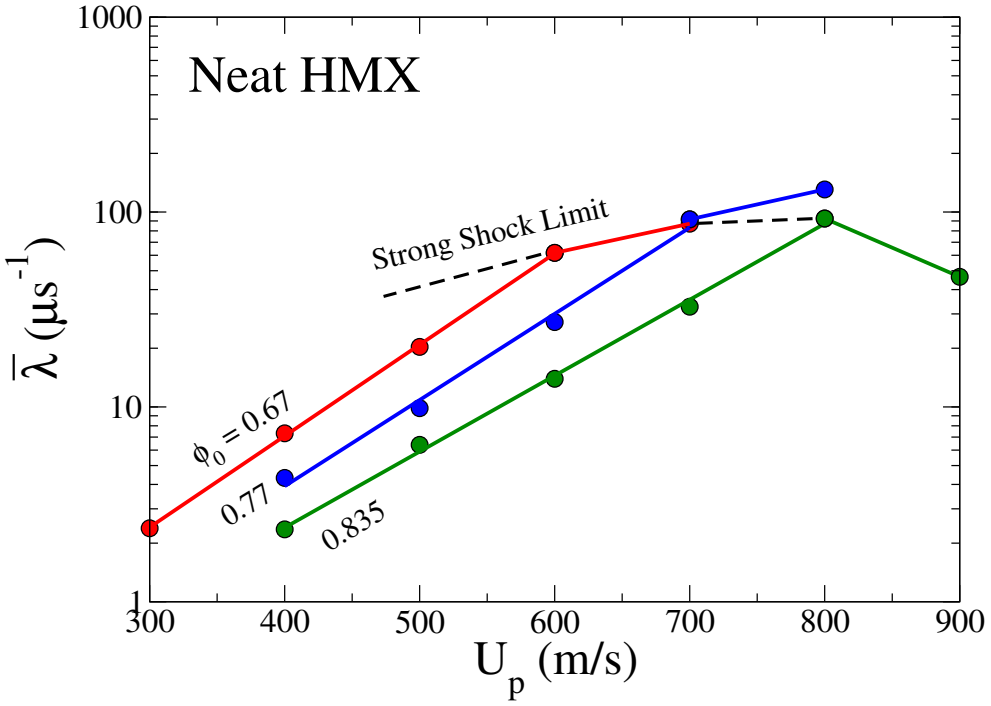

(a)

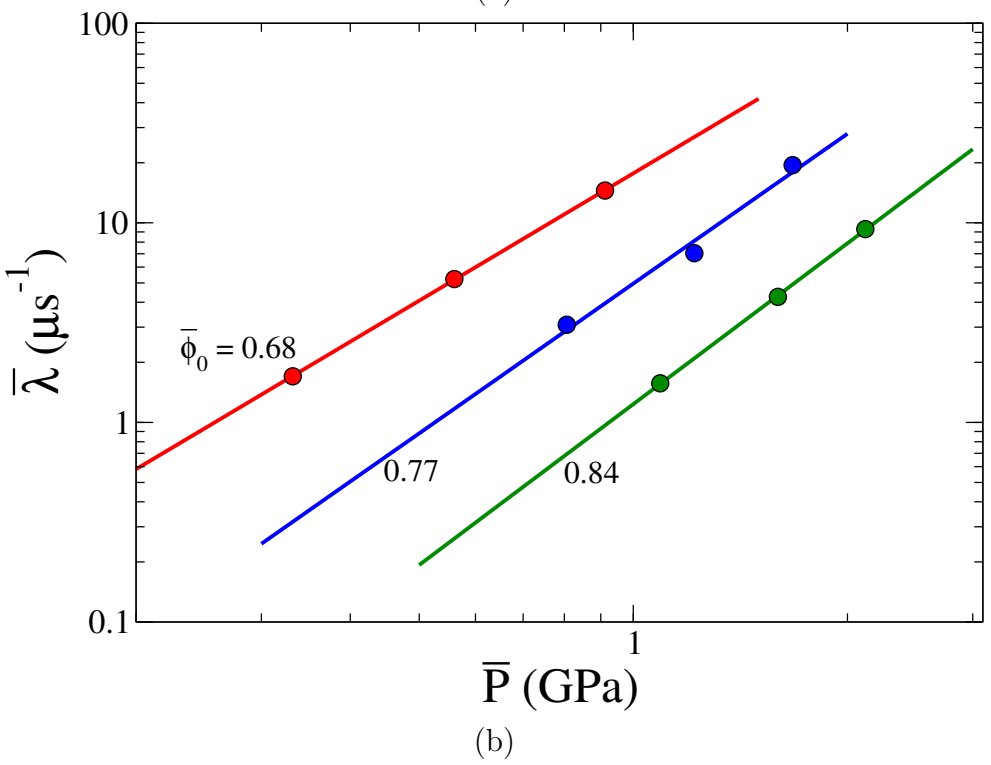

(b)

Figure 5.3: The predicted effective hot-spot formation rate $\overline{\lambda}$ as a function of (a) supporting piston speed U_p and (b) effective wave pressure $\overline{P}$.

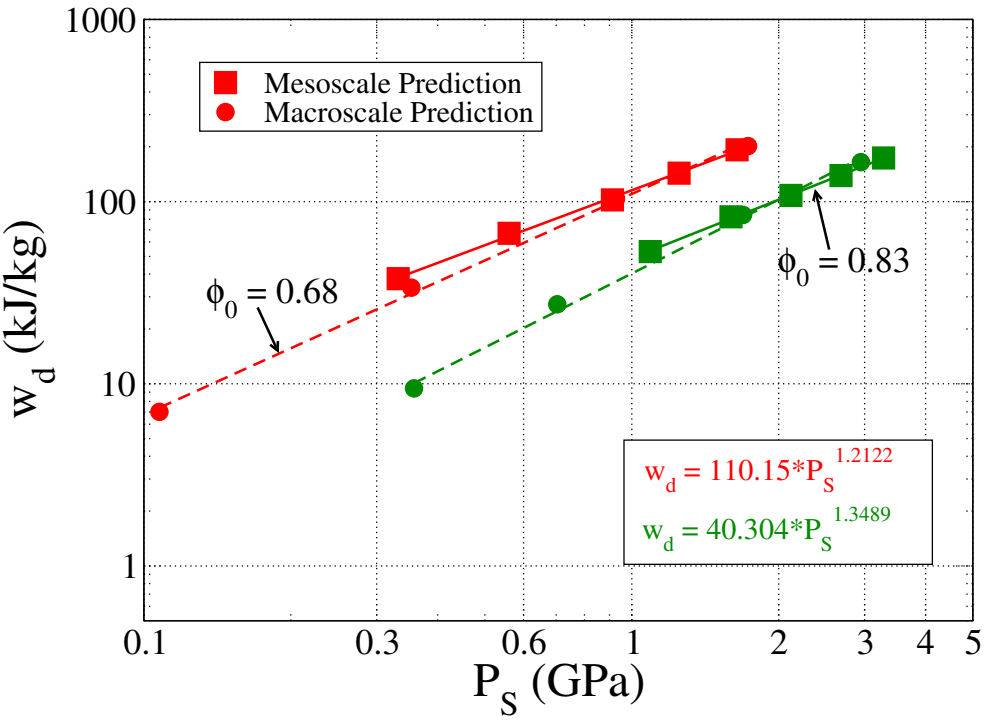

Figure 5.4: Predicted variation in mass-specific dissipative compaction work w_d (kJ/kg) with shock pressure P_s (GPa) for granular HMX.

and n are listed in Table 5.1 for $\phi_0 = 0.68$, 0.77 and 0.84.

Taking $\tau(P_s) = (a/I^*)P_s^n$ and $m = n$, then the characteristic time t_r in Eq. (5.2) is given by $t_r = (a/I^*)^{-1}P_r^{-n}$. Though the values of $a/\mathcal{I}^*$ and n are determined in this study based on sustained single shock loading, it is assumed that the resulting rate expression [Eq. (5.2)] is valid for more complex loading scenarios such as successive shocks. The validity of this assumption requires additional scrutiny.

- **Dissipation-Dependent Ignition**

For sustained shocks, the shock pressure P_s can be related to the mass-specific dissipative compaction work w_d allowing an alternative form of Eq. (5.2) to be obtained. As shown in Fig. 5.4, simulations suggest a power-law relation $w_d = bP_s^k$ for fixed ϕ_0. Using this relation, Eq. (5.2) can be re-expressed as

$$\frac{d\lambda_I}{dt_s} = \frac{1}{t_r}\left(\frac{w_d}{w_r}\right)^{\gamma}, \tag{5.10}$$

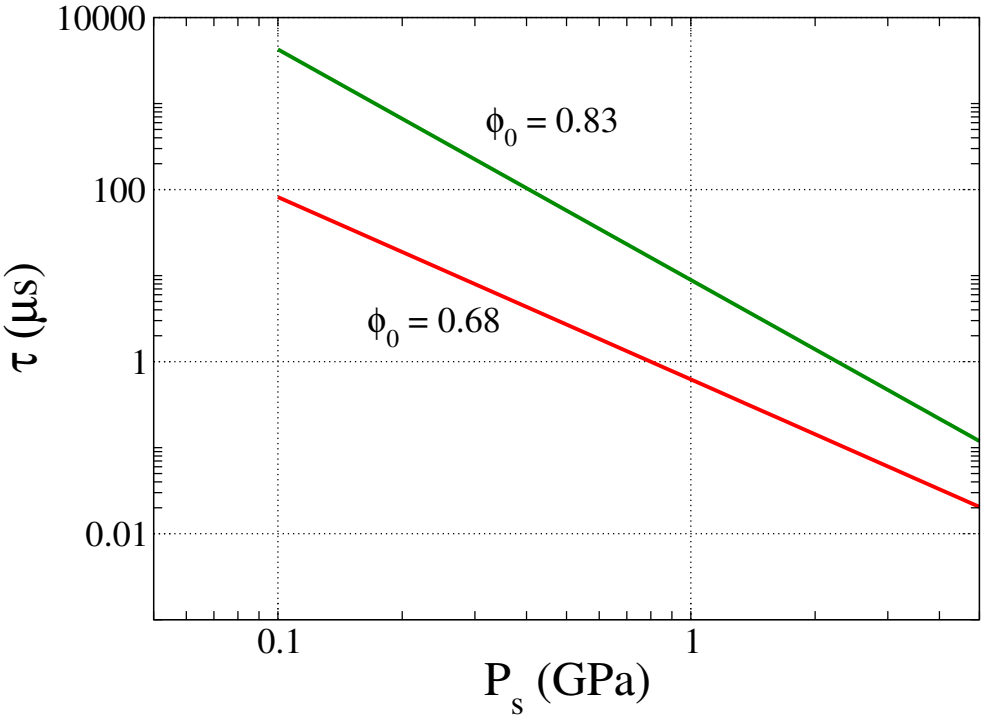

(a)

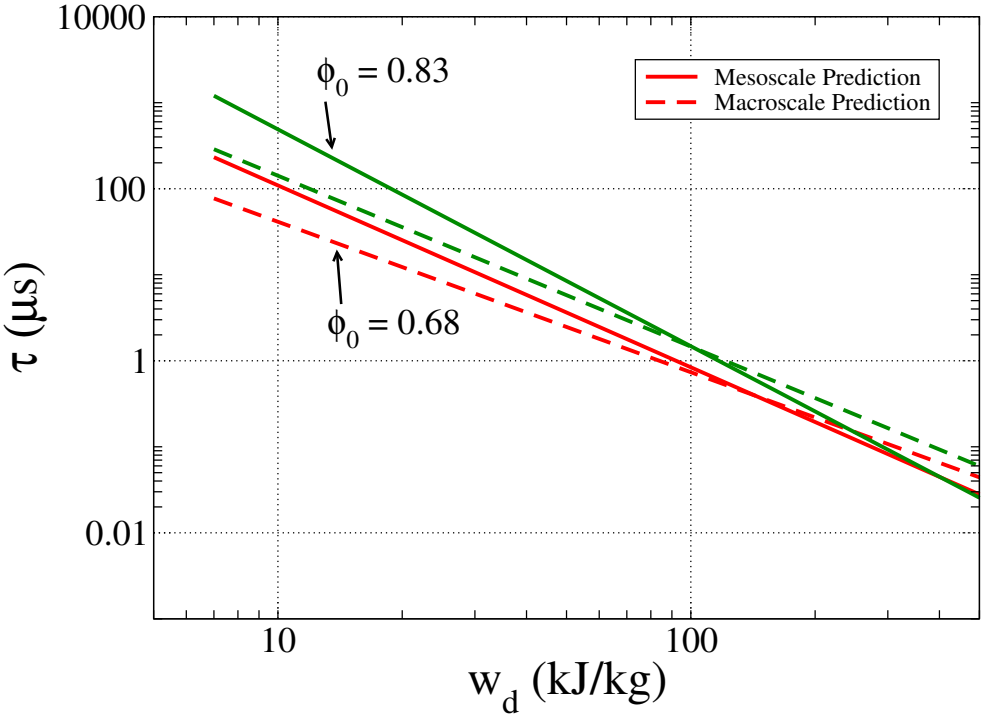

(b)

Figure 5.5: Predicted variation in ignition time with (a) shock pressure and (b) dissipative compaction work for granular HMX.

where $w_r = bP_r^k$, $t_r = (a/I^*)^{-1}(w_r/b)^{-\gamma}$, and $\gamma = n/k$. Integrating Eq. (5.10) gives

$$\lambda_I(t_s) = \frac{1}{t_r}\int_0^{t_s}\left(\frac{w_d}{w_r}\right)^{\gamma}\, dt'. \tag{5.11}$$

For sustained shocks, Eqs. (5.3) and (5.11) give identical results, but they can give substantially different results for more complex loading scenarios. Unlike the pressure-dependent model which is based on the state variable P_s, the dissipation-dependent model has the potential advantage of describing shock desensitization because of its explicit dependence on the monotonically increasing path function w_d. This assertion warrants additional study and is not used in this study. This modeling effort is part of the author's future work.

Figure 5.5 shows the variation in ignition time τ with P_s and w_d for sustained single shock loading of granular HMX having $\phi_0 = 0.68$ and 0.84. Also shown in Fig. 5.5(b) are corresponding ignition time curves based on meso-scale simulation data. Discrepancies between the meso- and macro-scale curves are due to differences in their constitutive relations for HMX that result in the variations in power-law expressions $w_d = bP_s^k$ seen in Fig. 5.4. Increasing ϕ_0 results in an increase in τ for fixed P_s and w_d. The slopes $\partial \log \tau/\partial \log P_s$ and $\partial \log \tau/\partial \log w_d$ increase with ϕ_0 indicating enhanced sensitivity to variations in shock strength. This prediction is consistent with initiation time and Pop-plot data for both granular HMX and HMX-based plastic bonded explosives (PBXs) [67, 140, 141]. As discussed later, a consequence of this feature is that ignition times and transition lengths corresponding to different initial densities tend to converge as shock strength increases.

5.1.2 Burn Model

A discussion on the formulation of burn following ignition (defined by $\lambda_I = 1$) is given in this section. The volumetric mass exchange term $\mathcal{C}$ describes the explosive combustion rate. The burn-rate expression associated with gas production and energy release is generally of the form:

$$\mathcal{C} = \epsilon\left(\theta + P_g\right), \quad \text{for} \;\; \lambda_I = 1. \tag{5.12}$$

where ϵ is a dimensional shape factor, θ (≈ 0 for DDT simulations, since $P_g \gg \theta$) is a function of the thermodynamic state of both solid and gas, and P_g is the pressure of the gas phase. This burn rate provides a mostly phenomenological expression for the kinetics of the chemical reaction associated with burning of explosive grains. This gas pressure dependent burn rate is widely accepted in combustion literature and regarded as empirical [128].

Combustion of HMX occurs in three steps: solid decomposition, pyrolysis, and gas-phase combustion. However, in the limit of fast chemistry it can simply be assumed to occur in a single step. Hence, the reactant solid explosive is directly converted to the reaction product gas. The shape factor ϵ accounts for three effects: the available burn surface-to-volume ratio of the grains, the depletion of the particle size due to reaction, and a characteristic recession velocity for the individual particles; it is given by:

$$\epsilon = \alpha \left(\frac{\phi_s}{d_0} \right) \frac{\rho_s u_{ref}}{P_{ref}} \tag{5.13}$$

where α represents a dimensionless volumetric burn surface area prefactor that is used to describe the kinetics of different processes during transiton to detonation, d_0 is the initial particle size, and u_{ref} is the characteristic recession velocity corresponding to pressure P_{ref}. The ratio $\frac{\phi_s}{d_0}$ is the burn surface area-to-volume ratio of the grains, which depend on the material heterogeneities. The interpretation of the LANL DDT experiment [5] is used here as a guide to model α. Though the transition process is continuous, prominent phases are depicted in Fig. 5.6. Interpretation of the phases is as follows:

1. **Early Induction Phase:** The early induction phase is shown in Fig. 5.6(1). In this phase, as the right propagating piston comes in contact with the ambient material it transmits energy into the material through forward propagating gas and solid acoustic waves. These forward propagating acoustic waves generate and support the propagation of a compaction wave that decreases the porosity and increases the density of the ambient material. This phase terminates when macro-scale ignition occurs and hot-spots produced in this

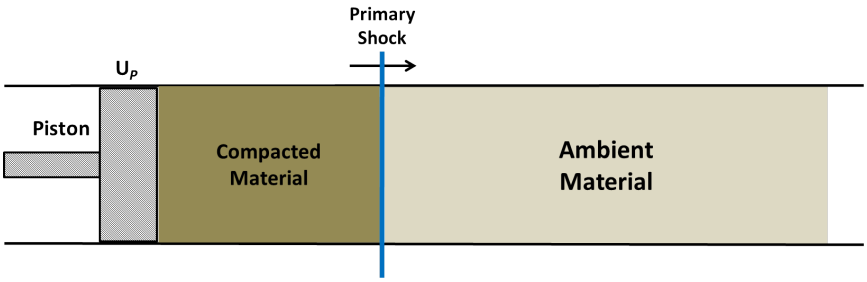

(1): Early Induction Phase ($0 \leq \lambda_I < 1$)

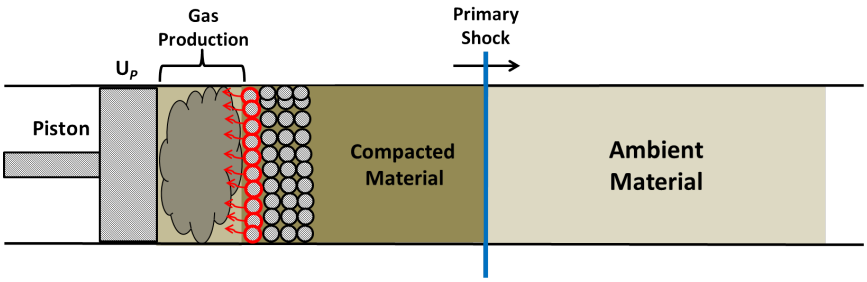

(2): Low-Speed Regressive Burn Phase ($\lambda_I = 1$)

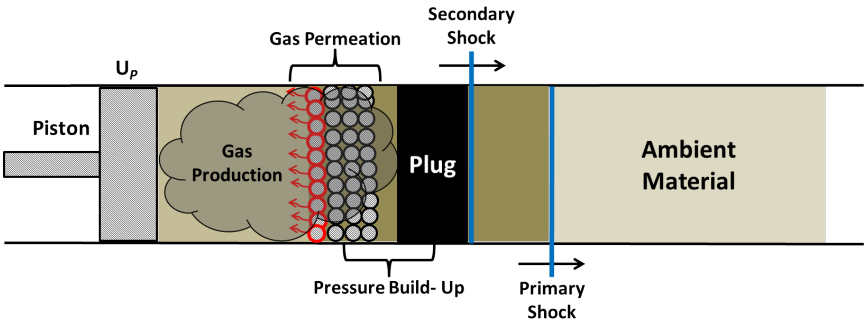

(3): Secondary-Shock/Solid-Plug Formation Phase

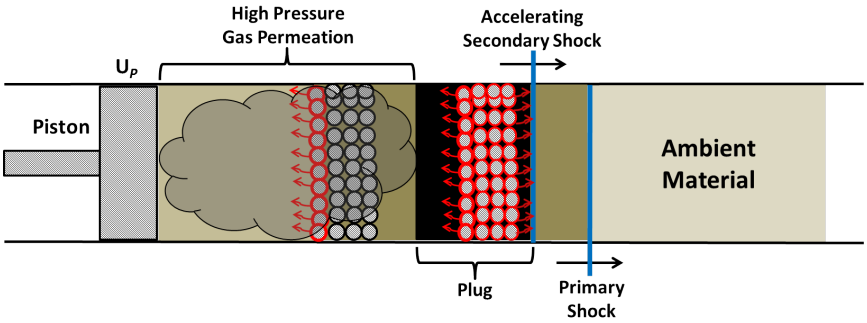

(4): Solid-Plug Acceleration Phase

Figure 5.6: Following ignition, illustration of (1) early induction phase; (2) low-speed regressive burn phase; (3) secondary-shock/solid-plug formation phase; and (4) solid-plug acceleration phase of the LANL DDT experiment. This illustration is used as a guide to establish the expression for volumetric burn surface area prefactor α. The schematic is shown in the piston-attached frame and U_P is piston impact velocity. Explosives grains are shown as shaded circles and the gas phase is shown as an expanding cloud.

phase are primarily due to pore collapse. It is assumed that this phase is energetically inconsequential at the macro-scale.

2. **Low-Speed Regressive Burn Phase:** As seen in Fig. 5.6(2) following ignition ($\lambda_I = 1$), the explosive-grains next to the piston surface start burning slowly to produce gaseous reaction products that start accumulating in the region between the piston surface and slow burning explosive grains. Subsequently, the reaction rate, albeit slowly, increases and a burn front is seen to form near the piston surface. The pressure of the gaseous reaction products starts building due to confinement provided by the piston, the tube walls and low permeability of the already compacted material ahead of it. Since the reaction rate and pressurization of gaseous reaction products is minimal, the kinetics of this phase can be assumed to be uniform and a constant value $\alpha = \alpha_0$ is used for the volumetric burn surface area prefactor.

3. **Secondary-Shock/Solid-Plug Formation Phase:** As the accumulation of gaseous product increases, the rising gas pressure drives burn supported compression waves (secondary compaction wave) in the already compacted material ahead of it. Figure. 5.6(3) shows this phase. This secondary compaction wave further reduces the porosity within the material to produce a nearly full density "solid-plug" (i.e., $\phi_s \approx 1$), slightly ahead of the burn front. The bed permeability ($\kappa \to 0$) within the plug region is minimal and the burn rate drops by a factor of 20-30. This reduction in material permeability restricts the flow of hot-gas through the bed, which results in the formation and propagation of a strong shock within the plug (discussed in next phase). Therefore, to describe the kinetics of this phase, a critical value of solid volume fraction ϕ_c is defined beyond which the burn rate is minimal and the corresponding burn surface area prefactor $\alpha_1 < \alpha_0$ for $\phi_s > \phi_c$ is defined.

4. **Solid-Plug Acceleration Phase:** In this phase, shown in Fig. 5.6(4), the rear interface of the "solid-plug" is pushed strongly by the high-pressure gas accumulating behind it. The rear interface of the plug now acts as a virtual piston that drives the formation

of a strong shock within the plug that can enhance dissipation and promote "hot-spot-facilitated" burn. When the shock dissipation within the plug reaches a threshold value $w_d > w_c$, high surface-area is available for burn due to the growth and agglomeration of intense hot-spots. The reaction rate significantly increases causing the onset of detonation. Therefore, to describe the kinetics of this phase, a critical value of dissipation w_c is defined beyond which the burn rate is maximum and the corresponding burn surface area prefactor $\alpha_2 > \alpha_0, \alpha_1$ for $w_d > w_c$.

Hence, $\alpha = \alpha(\phi_s, w_d)$, where w_d is mass specific dissipative compaction work that accounts for shock dissipation, and ϕ_s accounts for effects of bed permeability on the burn. Using the above discussion, the volumetric burn surface area prefactor is given by the following expression:

$$\alpha = \alpha_0 \left[1 + \frac{1}{\left(1 + \exp\left(\frac{-(w_d - w_c)}{\Delta w}\right)\right)\left(1 + \exp\left(\frac{-(\phi_s - \phi_c)}{\Delta \phi}\right)\right)} \right] - \frac{\alpha_1}{\left(1 + \exp\left(\frac{-(\phi_s - \phi_c)}{\Delta \phi}\right)\right)} + \frac{\alpha_2}{\left(1 + \exp\left(\frac{-(w_d - w_c)}{\Delta w}\right)\right)} \quad (5.14)$$

where α_0, α_1, α_2, ϕ_c, w_c, Δw and $\Delta \phi$ are constants. Δw and $\Delta \phi$ allows for smooth transitions between the phases and also control the width of burn transition zones.

Though not shown here, several numerical experiments were performed to calibrate this expression [Eq. (5.14)] by replicating features of the LANL DDT experiment. For simulations presented in this work, values of the chosen constants are given in TABLE 5.2. Figure 5.7 gives the variation of α with ϕ_s and w_d. As seen in the figure, this expression reflects a transition from normal low-speed regressive burn (characterized by α_0) for weak shocks to hot-spot facilitated burn (characterized by α_2) for strong shocks that have high values of ϕ_s and w_d. Hot-spot facilitated burn is associated with a significant increase in burn area due to the ubiquitous formation of closely spaced hot-spots.

The parameter ϕ_c is chosen based on DDT tube test data that indicate a reduction

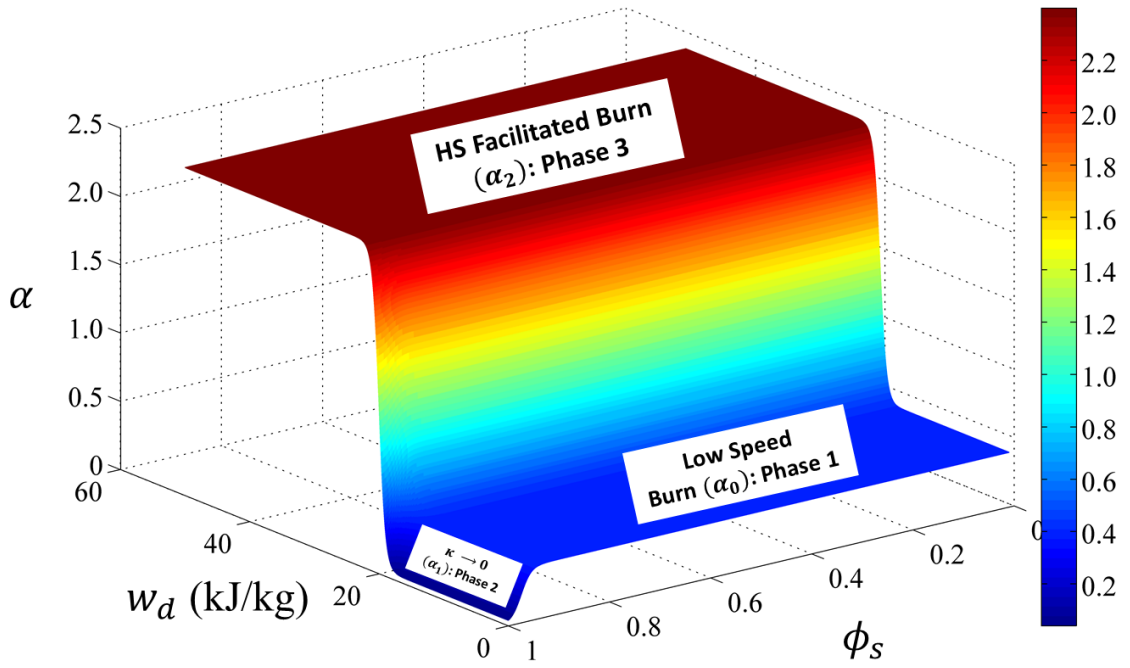

Figure 5.7: Variation of the volumetric burn surface are prefactor α with w_d and ϕ_s. The figure clearly shows the regions where the burn rate is dominated by α_0, α_1 and α_2. The region where the permeability $\kappa \to 0$ is also highlighted.

in burn rate by a factor of 20−30 for approximately $\phi_s > 0.95$. w_c is chosen based on inert meso-scale simulations that indicate that $w_d > 20$ kJ/kg causes widespread agglomeration of hot-spots suggesting the likelihood of fast reactive hot-spot interaction times. Recently, Gambino and co-workers [130] proposed an Arrhenius rate law to describe the chemical kinetics of the reaction process that uses a ignition temperature threshold of 315 K corresponding to a bulk temperature rise of $\Delta T = 15$ K. In this study, $w_d = 20$ kJ/kg corresponds to a comparable bulk temperature rise of $\Delta T = w_d/c_v$ of 13 K. The final expression for the burn rate f is given by:

$$f = \alpha \left(\frac{\phi_s}{d_0}\right) u_{ref} \rho_s \left(\frac{P_g}{P_{ref}}\right) \tag{5.15}$$

where α is given by Eq. (5.14). For initally spherical particles, $\alpha = 6$ gives a physical prespective indicative of complete/saturated burning of the spheres surface. Different detonation transition mechanisms (discussed later) can be described by Eq. (5.15) due its

Table 5.2: Parameter values used to compute α.

Parameter	Value	Units
α_0, α_1	0.4	-
α_2	2.0	-
d_0	100	μm
u_{ref}	0.1	m/s
P_{ref}	0.1	GPa
w_c	20	kJ/kg
ϕ_c	0.975	-
Δw	0.5	kJ/kg
$\Delta\phi$	10^{-6}	-

dependence on ϕ_s, P_g, and w_d. Though conceptually similar to other models [142,143], this model incorporates microstructure-dependent hot-spot predictions obtained by meso-scale M&S and accounts for hot-spot facilitated burn in terms of compaction shock dissipation to better characterize shock interaction effects.

5.2 Results

Having discussed the ignition and burn model, simulation results are presented in this section. The numerical shock capturing algorithm discussed in Chapter 3 involves the production of numerical anomalies at startup due to the imposition of a velocity discontinuity at the piston surface. In Section 5.2.1, a discussion is given on the cause, effect and treatment of these anomalies. In Sections 5.2.2−5.2.4, predictions are given that illustrate how ignition and burn affect the shock loading of low density HMX having $0.68 \leq \phi_0 \leq 0.83$. Simulations are performed for piston speeds within the range $150 \leq U_P \leq 600$ m/s because of their relevance to DDT/SDT; these cases span the range of weak to strong shock initiation and key features of the simulations are highlighted and discussed.

In this study, weak-shock initiation refers to simulations where the dissipative compaction work behind the fully developed primary compaction wave is $w_d \leq w_c$, resulting in initially low-speed regressive burn. Strong-shock initiation refers to simulations where the dissipative compaction work behind the lead compaction wave is $w_d > w_c$, resulting in prompt hot-spot facilitated burn.

5.2.1 Solution Strategy

Figure 5.8 shows the spatial variation in density (ρ_s), temperature (T_s), and dissipative compaction work (w_d), prior to ignition in the solid phase for a piston initiated DDT simulation; as such, the simulation up until the time shown is inert. An undershoot in density, and an overshoot in temperature and dissipative compaction work, is predicted in the vicinity of the piston interface due to a start up error produced by the velocity discontinuity imposed at $\xi = 0$ at $t = 0$. Such over- and under- shoots are referred to as an artificial entropy layer [144, 145] in the literature. This is a well-documented artifact of numerical shock capturing methods and has the potential to prematurely trigger chemical reactions.

Both meso-scale and macro-scale M&S predict an artificial entropy layer at the piston-explosive interface. However, the entropy layer predicted in meso-scale M&S is partly

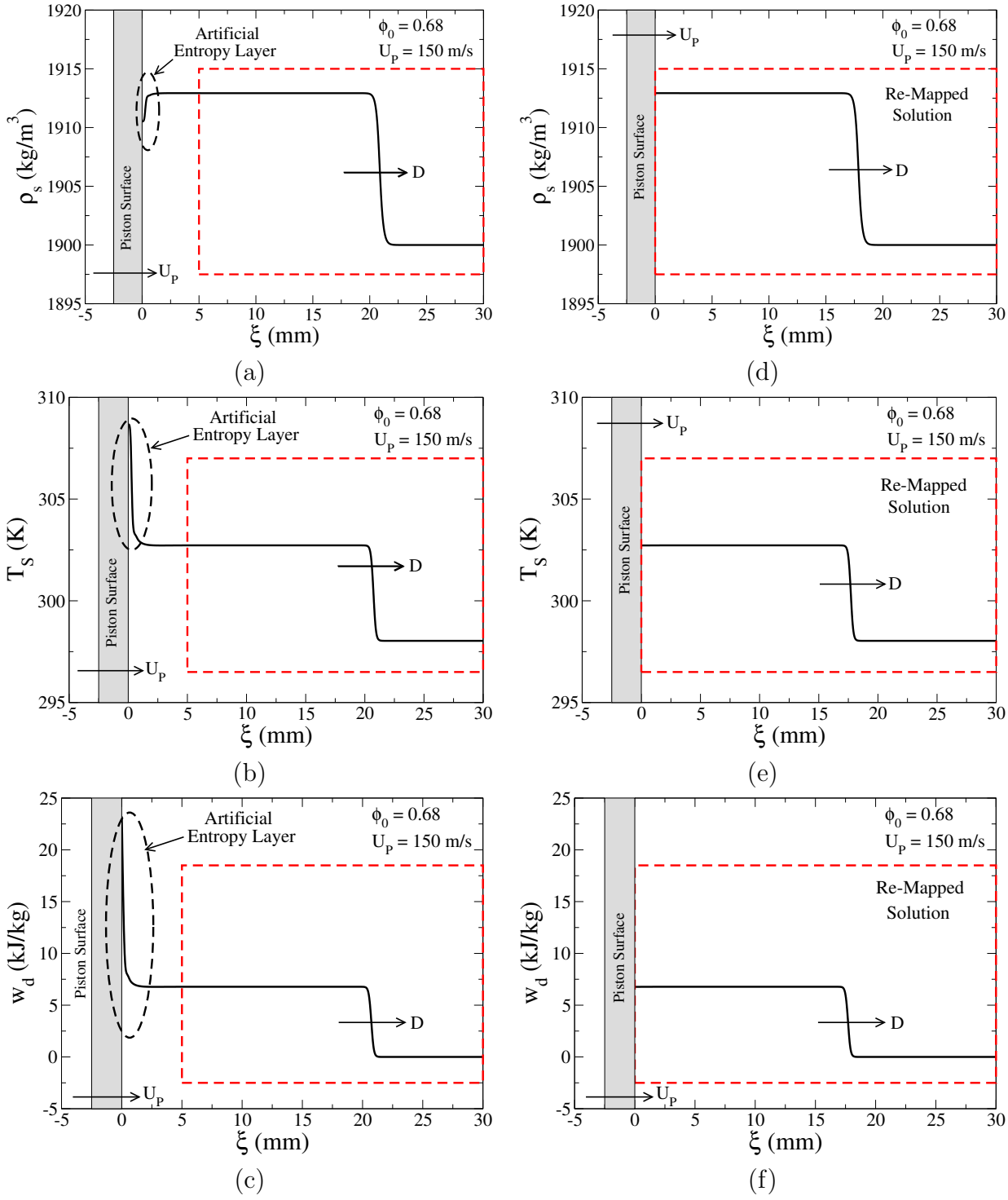

Figure 5.8: Predicted: (a) Solid phase density ρ_s; (b) solid phase temperature T_s; and (c) dissipative compaction work w_d; affected by artificial entropy production at the piston interface. Re-Mapped solution of (d) ρ_s; (e) T_s; and (f) w_d for $\phi_0 = 0.68$ and $U_P = 150$ m/s at $t = 52$ μs following impact.

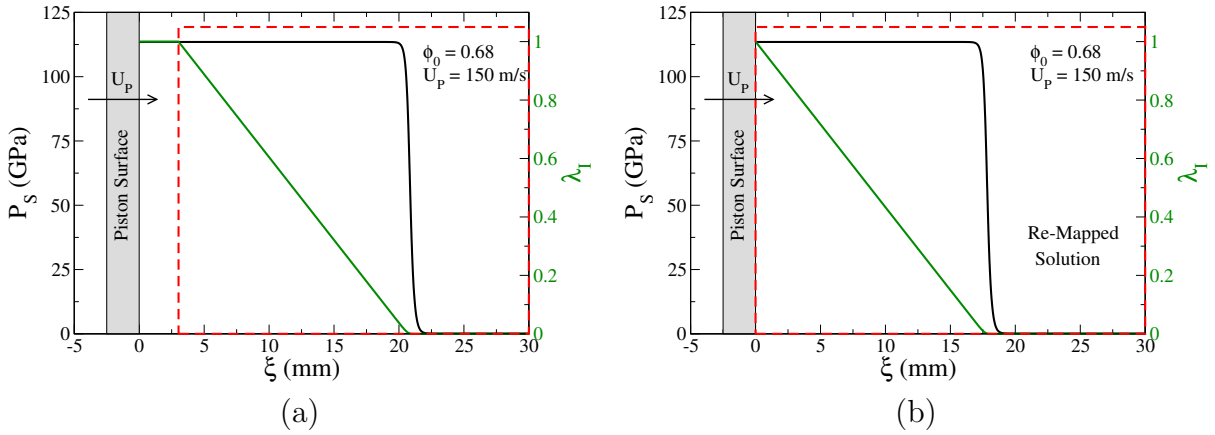

Figure 5.9: Predicted: Solid phase pressure P_s and ignition variable λ_I not affected by artificial entropy production for $\phi_0 = 0.68$ and $U_P = 150$ m/s at $t = 52$ μs following impact.

physical and partly artificial. The physical entropy layer results due interactions between the planar piston interface and explosive particles that give rise to frictional dissipation. This dissipation causes an increase in material temperature and is responsible for high intensity hot-spots with temperatures in the range of 800-1500 K. Additionally, wave reflections from the interface can amplify pressure and shear within the material resulting in enhanced plastic deformation. In both the meso- and macro-scale models, the piston moving to the right transmits energy to the ambient granular bed through forward propagating gas and solid acoustic waves. This energy transmission involves shock interactions at the piston wall, as demonstrated by the various simulations presented later in the chapter. When these shocks interact with the rigid piston interface, numerical anomalies are observed because of the large (infinite) impedance mismatch between the two materials.

Menikoff and Lackner [146] presented a simple analysis to explain this phenomenon. They considered a case of symmetric shock collision which is equivalent to shock reflection from a rigid wall. It was shown that the conservation laws reduce to two equations for the unknown shock position, and the difference in the relative energies of the incoming and outgoing shock is not zero. This causes a mathematical inequality and affects the degeneracy of the equations, and the states behind the outgoing shock are not uniform. When a shock wave impacts a material interface, there is a separate conservation law

for the mass of each material. This leads to four equations for three unknowns. The entropy anomaly can be large when the equation of state of two materials is very different. Therefore, it is difficult to determine to what extent this entropy layer is physical and to the authors knowledge no perfect numerical fixes exist.

In this study, a simple numerical manipulation technique that theoretically does not affect the solution is adopted to circumvent this problem. As seen in Figs. 5.8(d-f), prior to ignition ($0 \leq \lambda_I < 1$) the predicted solution is modified by eliminating the small region of the computational domain in the vicinity of the piston affected by the entropy layer. New initial conditions are extracted from the steady solution and re-mapped onto the original domain. This re-mapped solution is used to initialize a new simulation for which the ignition variable $\lambda_I \approx 1$ (Ignition) at the piston surface ($\xi = 0$). Figures 5.9(a-b) shows the spatial variation of solid phase pressure (P_s) and ignition variable (λ_I) for a simulation. Here no anomalies exist in the vicinity of the piston-explosive interface in solid pressure because across an entropy wave pressure and solid volume fraction remain unaffected. Therefore, the ignition variable that is pressure dependent also remains unaffected. This technique allows for triggering the combustion as prescribed by the ignition and burn model without altering the accuracy of the simulation.

In the remainder of the thesis, all indicated times are relative to the ignition time for a given simulation unless otherwise stated. Time since impact and ignition are related by $t = t_{ign} + \tau$, where t_{ign} is the ignition time, and τ is the later time corresponding to the steady detonation.

5.2.2 Weak−Shock Initiation

The first case considered is the baseline for the simulations presented in this work. For meaningful comparison, the initial stress-free and motionless bed corresponding to an initial solid volume fraction $\phi_0 = 0.68$ and a piston impact of $U_P = 150$ m/s used here is similar to the LANL DDT experiment.

Plot Characteristics

Figure 5.10(a) gives solid volume fraction (ϕ_s) contours in the $\tau - \xi$ characteristic plane. Solid volume fraction contours are used to quantitatively and qualitatively assess the condition of the material during transition. The contours show material compaction by the primary compaction wave (**c**), secondary compaction wave (**b**), and the conversion of solid to gas by combustion. Figure 5.10(b) gives bulk pressure ($\overline{P} = P_s\phi_s + P_s\phi_s$) contours in the $\tau - \xi$ plane. The pressure contours are used to qualitatively assess wave interactions during transition. The contour shows the predicted primary wave (**c**), secondary wave (**b**) and steady detonation wave (**D**) trajectories. The contour also gives the location of onset of "low-speed" burn (X_1), the onset of rapid-burn (X_2) and the location where the secondary wave overtakes the primary wave. A key objective of this study is to analyze the detonation transition mechanism from a wave interactions perspective, and this plot facilitates tracing of the different wave trajectories and their interaction. Because predictions upto ignition are effectively inert, all contour plots and spatial profiles in the remainder of this thesis are plotted from time since ignition. The time axis on contour plots do not essentially start from $\tau = 0$; as such, the time since visible macro-scale activity is plotted for clarity and usefulness.

Figures 5.11 and 5.12 give the piston-attached spatial profiles for ϕ_s, P_s, w_d, and u_s as the solution evolves into a steady detonation, using $N = 2000$ computational cells and a resolution $\Delta\xi = 25$ μm. These profiles connect the state of the material behind and ahead of the corresponding shocks. These plots are helpful in tracking the variation of flow variables and dependent quantities that are observed during transition.

Transition Mechanism

As seen in Figs. 5.10(a) and 5.11(a), the fully developed primary (input) compaction wave, labeled **c**, reduces the porosity within the material and propagates at about 396 m/s, corresponding to a input shock pressure of 0.115 GPa. The predicted solid volume fraction in the compacted region is $\phi_s = 0.93$ and the dissipative compaction work is approximately $w_d = 7$ kJ/kg. This lead compaction wave propagates a relatively long distance into the

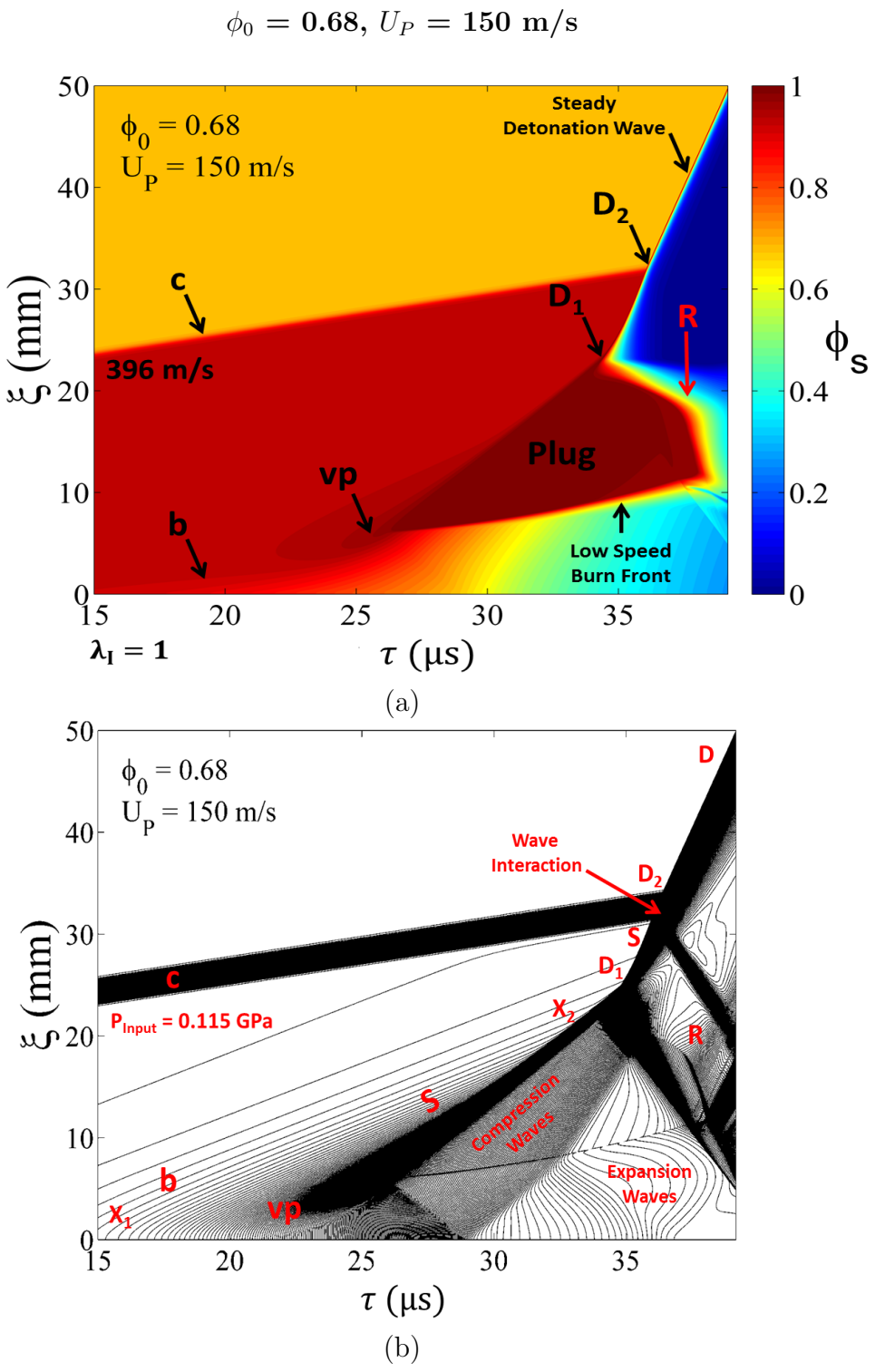

Figure 5.10: Predicted: (a) solid/explosive volume fraction contours; and (b) bulk pressure contours; in the generic $\tau - \xi$ diagram showing the predicted trajectories of primary compaction wave **c**, burn supported secondary compaction wave **b**, the rearward plug boundary **vp**, strong shock **S**, and forward propagating steady detonation wave **D** for $\phi_0 = 0.68$ and $U_P = 150$ m/s. X_1 is the location of onset of low-speed regressive burn, X_2 is the location of onset of "hot-spot" facilitated burn, and R is the location of onset of spontaneous reaction waves.

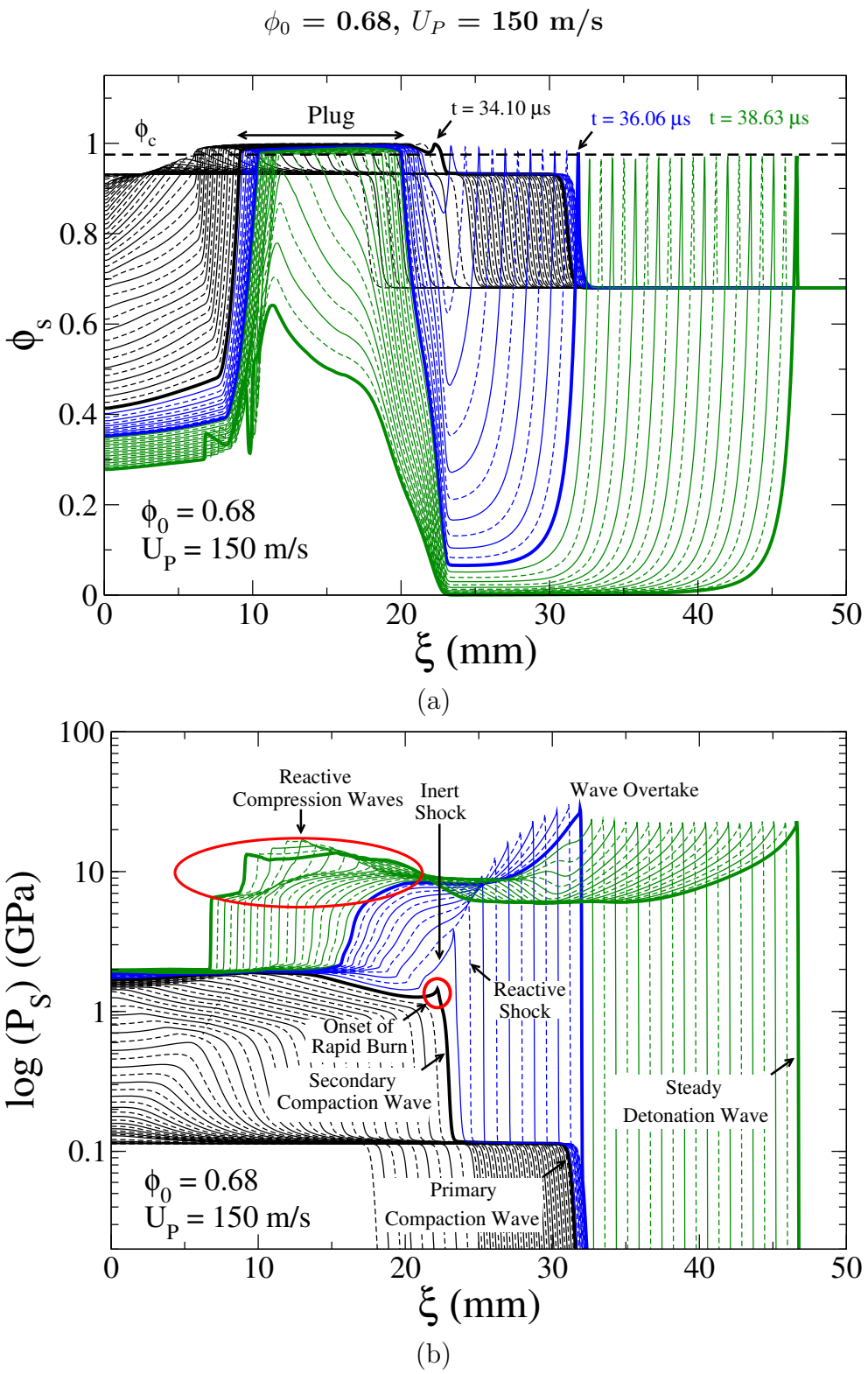

Figure 5.11: Predicted spatial variation in (a) solid/explosive volume fraction ϕ_s; and (b) solid phase pressure P_s; for $\phi_0 = 0.68$ and $U_P = 150$ m/s.

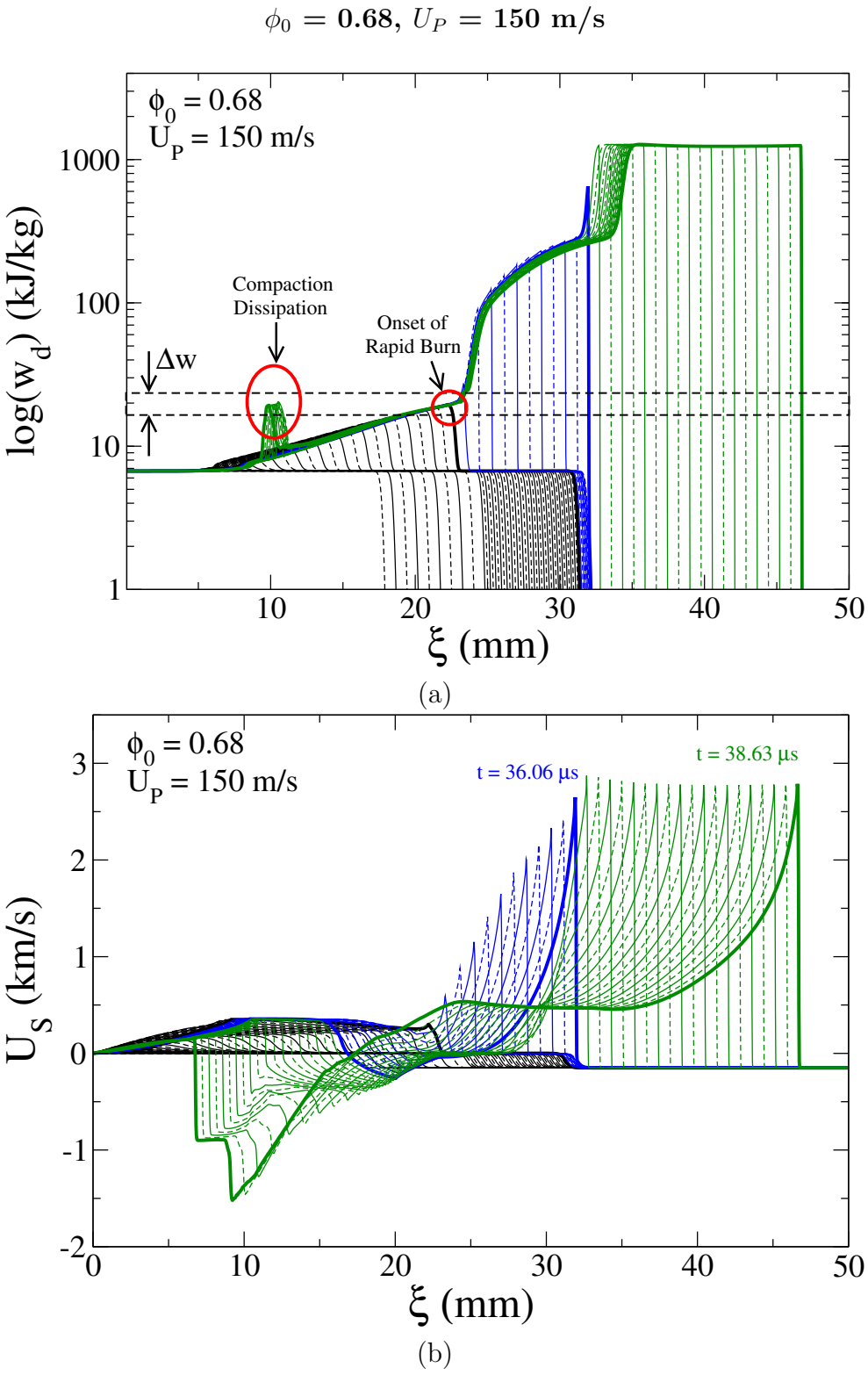

Figure 5.12: Predicted spatial variation in (a) dissipative compaction work w_d; and (b) solid phase particle velocity U_s; for $\phi_0 = 0.68$ and $U_P = 150$ m/s.

ambient material prior to the onset of ignition (vigorous burn) near the piston surface at approximately $t_{ign} = 43$ μs. The predicted dissipative compaction work w_d behind the primary wave for this case is lower than the threshold w_c, resulting in an initially "low-speed" regressive burn.

Subsequently, regressive burn near the piston surface drives the formation of a secondary compaction wave, labeled **b**, due to the low permeation of combustion gases into denser material precompacted by the primary shock. This secondary compaction shock eliminates the residual porosity resulting in the formation of a inert-solid-plug that increases in width as the shock propagates forward [5, 123]; the existence of the high density plug is highlighted in Figs. 5.10(a) and 5.11(a) which show contours and spatial wave profiles of solid volume fraction in the $\tau - \xi$ characteristic plane and $\xi - \phi_s$ plane, respectively.

The strength of the burn supported secondary wave increases in time to form a strong shock, labeled **S**, as indicated by the converging contours in Fig. 5.10(b), and the increase in pressure in Fig. 5.11(b) and dissipative compaction work in Fig. 5.12(a). As $w_d \to w_c$, then α quickly increases resulting in hot-spot facilitated burn which significantly intensifies secondary wave dissipation to $w_d > 200$ kJ/kg. Inert meso-scale simulations show that such a large value of w_d is sufficient to cause widespread agglomeration of hot-spots indicating the likelihood of fast reactive hot-spot interaction times [81]. At location, labeled D_1, the rapid onset of vigorous burn results in a thermal-explosion-like (or SDT-like) event which produces a forward propagating reactive shock and a backward propagating weak shock.

The forward propagating reactive shock quickly transitions to detonation becoming overdriven relative to the ambient material. At location, labeled D_2, the overdriven detonation subsequently overtakes the primary compaction wave and propagates into the ambient material as it relaxes to a CJ detonation ($D_{CJ} \approx 5.8$ km/s). This case demonstrates a complex transition mechanism that is typically referred to as Type$-$I DDT where the transition mechanism is ignition controlled in that the ignition induction time is long compared to that required for transition following ignition.

As the detonation wave propagates forward, the backward propagating weak shock enters the plug and slowly increases in strength and is predicted to abruptly transition into a strong reactive compression wave through the formation of a knee−like structure at location R as indicated in Fig. 5.10(a). It is insightful to examine this phenomena and a simple analysis is given here to better understand the predicted features. It is important to note here that, the solid plug determines the dynamics of the backward propagating weak shock because of its low bed permeability ($\kappa \to 0$) and experimental evidence of drop in burn rate.

Figure 5.13(a-c) gives the magnified view of the evolution of solid phase pressure P_s, solid volume fraction contours, and solid volume fraction ϕ_s with position, respectively, within the solid-plug. To perform the analysis, the spatial variation in solid/explosive volume fraction at a particular instant in time highlighted in the figure is chosen. Assuming negligible convective effects, the evolution of the explosive/solid volume fraction is given by:

$$\frac{d\phi_s}{dt} = -\frac{\mathcal{C}}{\rho_s} \tag{5.16}$$

where the source term $\mathcal{C}$ that accounts for the exchange of mass from solid to gas due to combustion is given by:

$$\mathcal{C} = \alpha \left(\frac{\phi_s}{d_0}\right) u_{ref} \rho_s \left(\frac{P_g}{P_{ref}}\right) \tag{5.17}$$

The variation in solid volume fraction $\phi_s(\xi) = \overline{\phi_0}(\xi)$, where $\overline{\phi_0}(\xi)$ is the variation in solid volume fraction corresponding to the chosen spatial profile. Gas pressure P_g and solid density ρ_s are assumed to be constant, and the evolution of solid volume fraction is now given by:

$$\frac{d\phi_s}{dt} = -\alpha \left(\frac{\overline{\phi_0}(\xi)}{d_0}\right) u_{ref} \left(\frac{P_g}{P_{ref}}\right) \tag{5.18}$$

Integrating Eq. (5.18) gives:

$$\phi_s\left(t;\xi\right) = \overline{\phi_0}\left(0;\xi\right) \exp\left[-\frac{\alpha}{d_0} u_{ref} \frac{P_g}{P_{ref}} t\right] \tag{5.19}$$

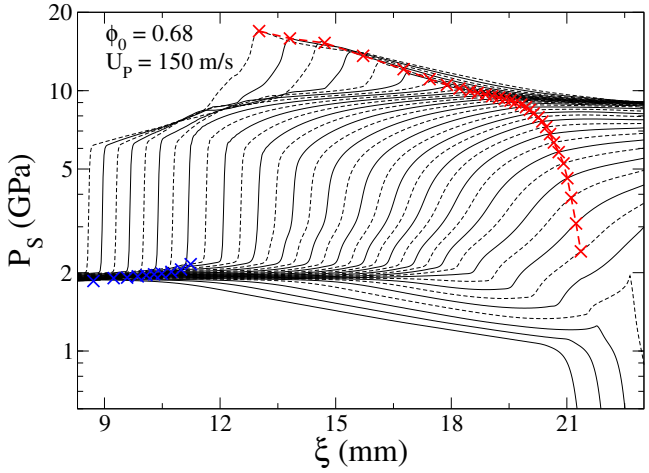

(a)

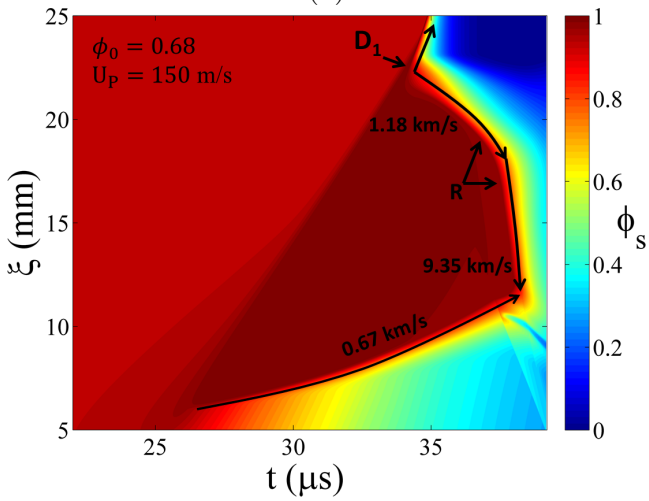

(b)

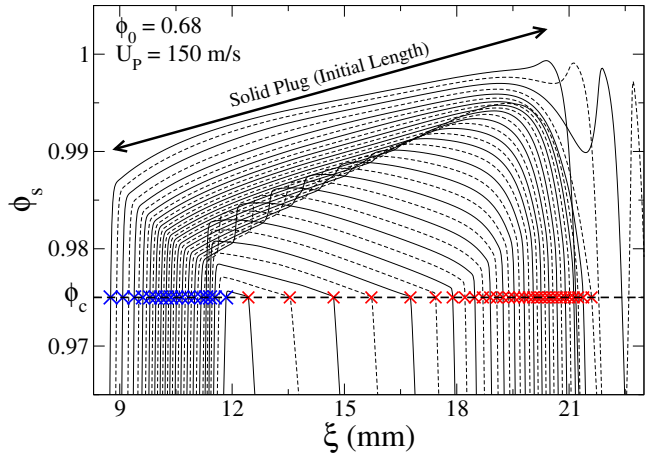

(c)

Figure 5.13: Magnified view of (a) solid pressure P_s with position; (b) solid/explosive volume fraction contours; and (c) solid/explosive volume fraction ϕ_s; within the solid-plug for $\phi_0 = 0.68$ and $U_P = 150$ m/s. Blue and Red X point markers in (a) and (c) indicate the forward and backward propagating burn-front locations at the back and front of the plug, respectively.

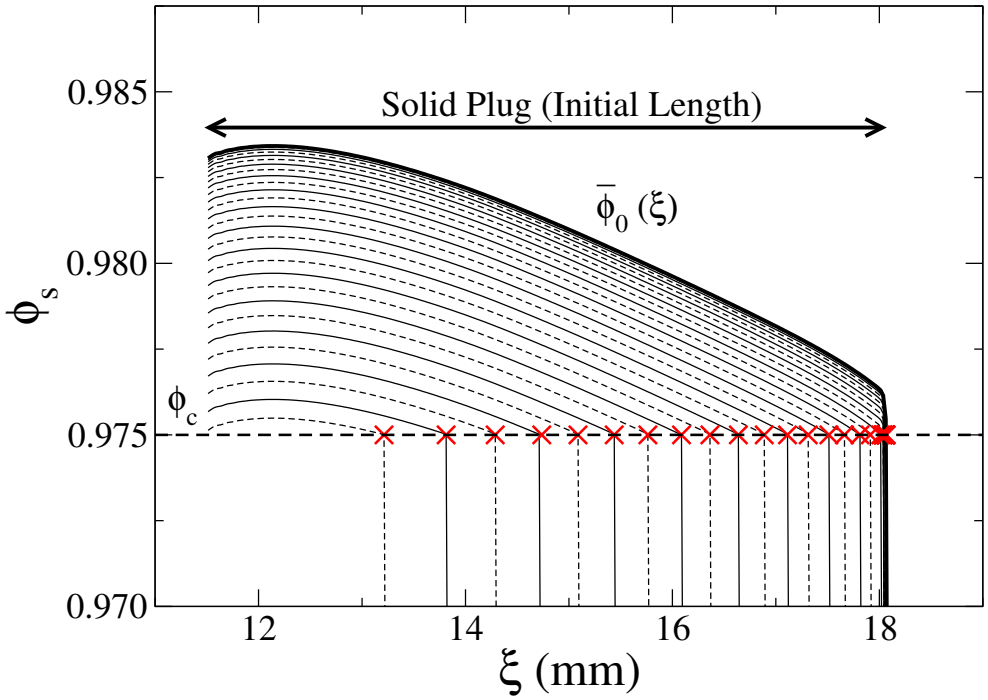

(a)

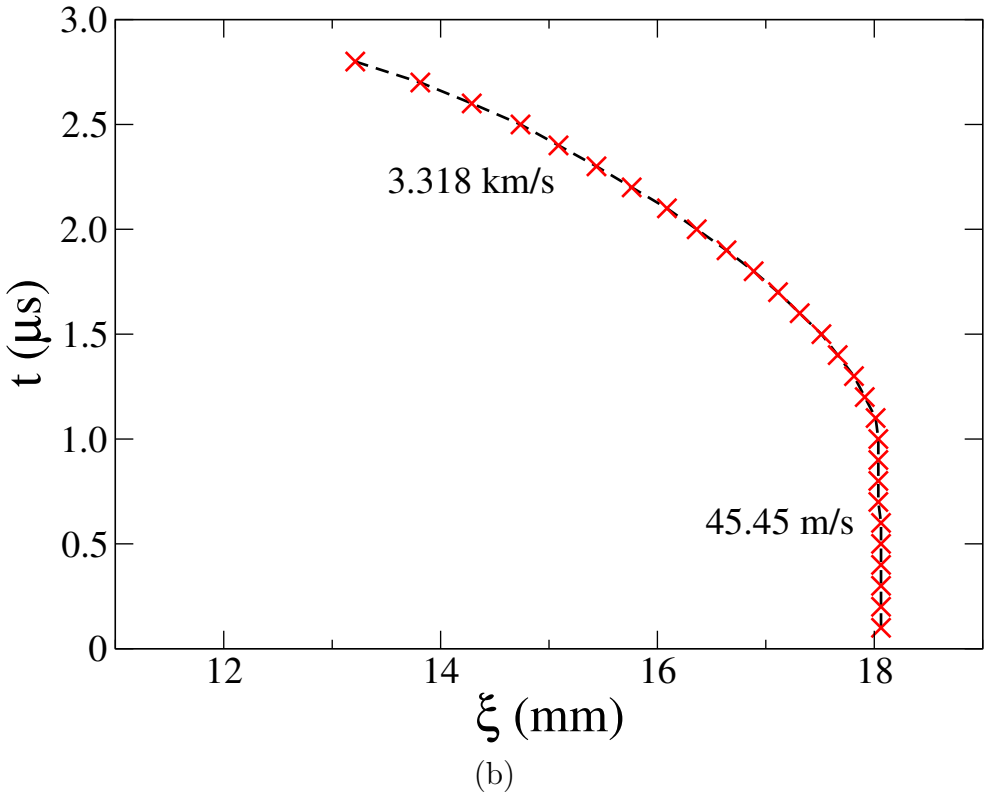

(b)

Figure 5.14: (a): Predicted spatial variation in solid/explosive volume fraction ϕ_s within the plug region; and (b) Burn-front location at the head of the plug as a function of time; using the simple analysis for $\phi_0 = 0.68$ and $U_P = 150$ m/s. Red X point markers indicate location of burn-front at the front of the plug.

which is valid following explosive material points. ϕ_c is chosen to track the location of burn-front since it corresponds to the critical value of solid volume fraction where the burn regime switches from low-speed regressive burn to burn controlled by bed permeability. The blue and red X point-markers highlighted in Figs. 5.13(a) and 5.13(c) indicate the forward and backward propagating burn front locations at the back and front the solid-plug, respectively. To this end, for $\phi_s = \phi_c$, Eq. (5.19) gives the location and for time Eq. (5.19) can be re-expressed as:

$$t = -\frac{d_0 P_{ref}}{\alpha u_{ref} P_g} \ln \left[\frac{\phi_c}{\overline{\phi_0}(\xi)} \right] \tag{5.20}$$

Differentiating Eq. (5.19) with respect to time gives the expression for velocity of propagation of burn-front:

$$\frac{d\xi}{dt} = \alpha \left(\frac{\overline{\phi_0}(\xi)}{d_0} \right) u_{ref} \left(\frac{P_g}{P_{ref}} \right) \frac{1}{d\phi_0/d\xi} \tag{5.21}$$

Using Eqs. (5.16−5.21), the predicted spatial variation in solid volume fraction and burn-front location as a function of time can be reconstructed using this simple analysis and is shown in Fig. 5.14(a) and Fig. 5.14(b), respectively. As the shock strengthens the velocity of propagation of burn-front is approximately 45.45 m/s but exponentially increases (by construction) to about 3.318 km/s through the formation of a knee-like structure. Gasdynamic experiments on homogeneous and exothermically reacting gases suggest that DDT may occur through Zel'dovich or shock wave amplification by a coherent energy release (SWACER) [105] gradient mechanism when spatial gradients in temperature and concentration occur due to turbulent mixing of reaction products with unburned gas. The unburned gas having the mimimal indution time is first ignited and a shock wave is generated by this primary explosion that propagates to the next layer. The next layer has a slightly longer ignition delay and the shock wave initaites explosion of this layer, and the released energy strengthens this wave and advances to the adjacent layer, and so on. Thus, the concentration gradient provides a method of coherent energy release with respect

to propagating spontaneous reaction shock that can result in detonation in the mixture. For brevity, complete details on spontaneous reaction waves are not given here and can be found in Refs. [106–108].

Using the gas-dynamics analogy, as seen in Figs. 5.13(c) and 5.14(a), a shallow gradient in composition (solid volume fraction) results in a weak reactive shock propagating into the plug. Within the solid-plug the material permeability is low and the prescribed volumetric burn surface area prefactor is $\alpha_1 < \alpha_0$. As the material is consumed slowly, the rising gas pressure drives burn supported compression waves in the already compacted material ahead of it. As the strength increases due to restricted flow of hot-gas through the bed, abrupt transition to a strong reactive compression wave analogous to spontaneous reaction shock is predicted at location R. The backward propagating shock is is often mentioned in literature but the phenomenology associated with it is not completely characterized as it is difficult to capture the complete set of events due to loss of confinement (tube splitting) during DDT tube test. However, few expeiments [147,148] and private communication with the LANL DDT-Modeling group [149] report their evolution during the DDT of low-density solid high-explosives. As seen in Fig. 5.13(c), the spontaneous reaction wave propagates at about $D = 9.35$ km/s and subsequently overtakes the "low-speed" burn-front at the back of the plug further enhancing the burn leading to complete consumption of the plug.

Figure 5.15 shows the steady forward-propagating detonation structure that consists of a shock wave in both the solid explosive and the gas phase. During transition to detonation, the solid shock is accelerated ahead of the gas shock as seen in Fig. 5.15(b) (inset) before waves approach steady speed. Since the solid shock accelerates ahead of the gas shock, the CJ detonation predicted has a compaction-led spatial structure. The thin reaction zone is followed by a Taylor expansion wave (not shown in the figure) which relaxes the pressure to the ambient at the piston surface. This structure is consistent with the theory available in literature [137]. Complete details on detonation wave structure and analysis can be found in Refs. [90, 135]. The analytical steady end-state solution discussed in

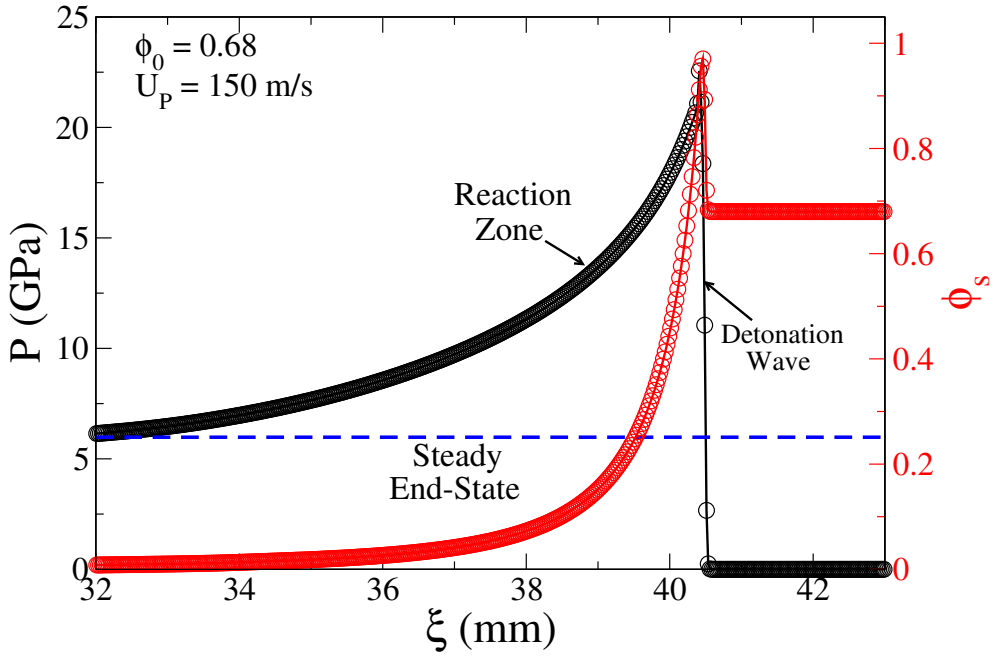

(a)

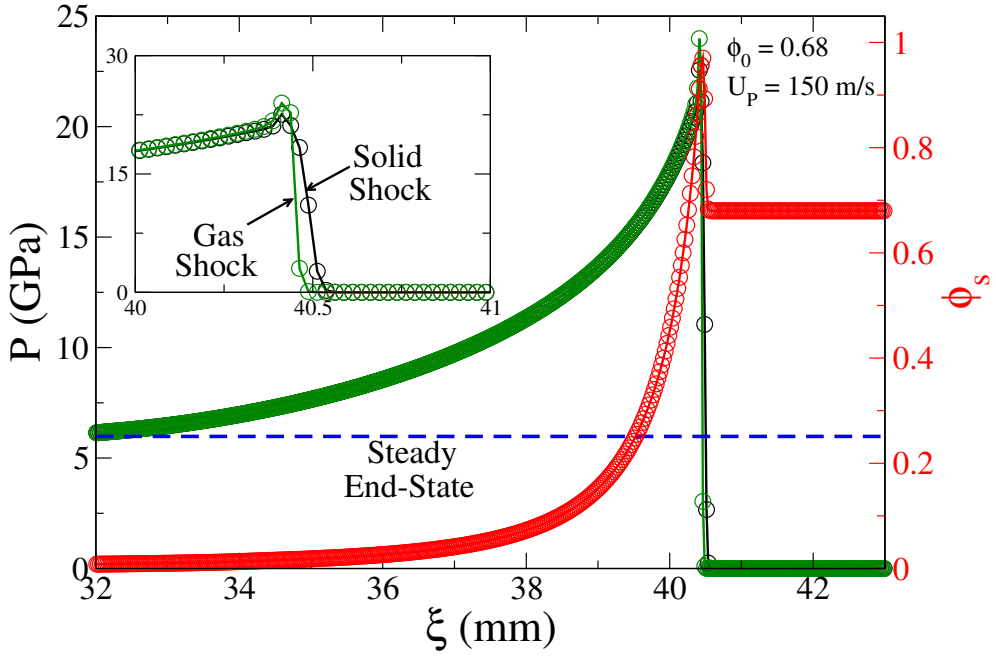

(b)

Figure 5.15: Predicted: (a) steady detonation spatial profile of and solid phase pressure and solid volume fraction and; (b) steady detonation spatial profile of solid phase pressure, gas pressure and solid volume fraction for $\phi_0 = 0.68$ and $U_P = 150$ m/s.

Appendix A is used here to verify the results obtained from the macro-scale model. The steady solution obtained from simulations show good agreement with the end-state analysis. Several features observed in this simulation are also predicted to occur in simulations discussed later. For brevity, the discussion for those simulations are referred back to the baseline case and features specific to those simulations are highlighted.

In summary, the following points are noteworthy. First, unlike shock pressure which decreases as the overdriven detonation shock overtakes the primary compaction shock, shock dissipation significantly increases. Thus, burn models based on shock pressure may improperly predict combustion induced by compaction shock interactions within the material which are important for describing hot-spot effects including desensitization. Second, compaction-led detonations (using the terminology of Schwendeman, et al., [135]) are predicted due to the low permeability of the material to combustion gases. Such structures are plausible in that they involve a thin lead shock in the solid component that compacts (at least partially) explosive particles resulting in high dissipation that promptly triggers vigorous burn behind the shock. The thickness of the compaction shock is approximately two mean particle diameters.

- **Parametric Analysis**

For direct comparison, simulation predictions for material having $\phi_0 = 0.77$ and $\phi_0 = 0.83$ for a piston speed of $U_P = 150$ m/s are given here. For a fixed U_P, increase in packing density (ϕ_0) results in higher wave speeds (D) and stronger shocks (P_s) due to increased acoustic/shock impedance of the material and enhanced stress bridging between particles within shocks. However, for fixed U_P, an increase in packing density (ϕ_0) results in lower dissipative compaction work (w_d) due to fewer sites available for pore-collapse in high density materials. A detailed discussion on the variation of shock strength (P_s) and dissipative compaction work (w_d) with increasing packing density (ϕ_0) is given in Sec. 4.1.3.

Figures 5.16 and 5.17 give comparative predictions of solid volume fraction (ϕ_s) contours and bulk pressure ($\overline{P} = P_s\phi_s + P_g\phi_g$) contours in the $\tau - \xi$ characteristic plane,

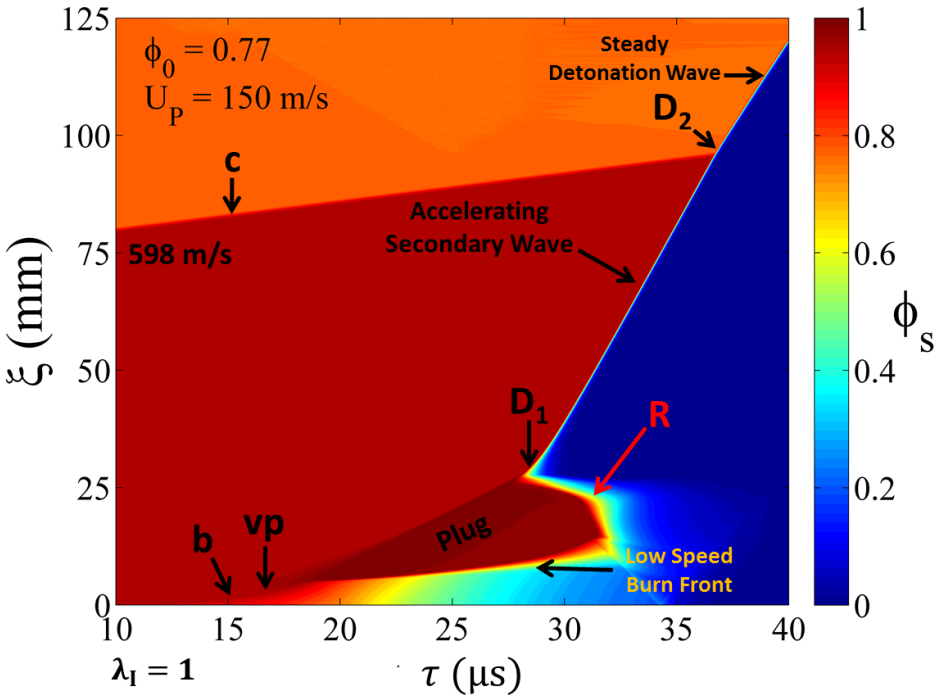

(a)

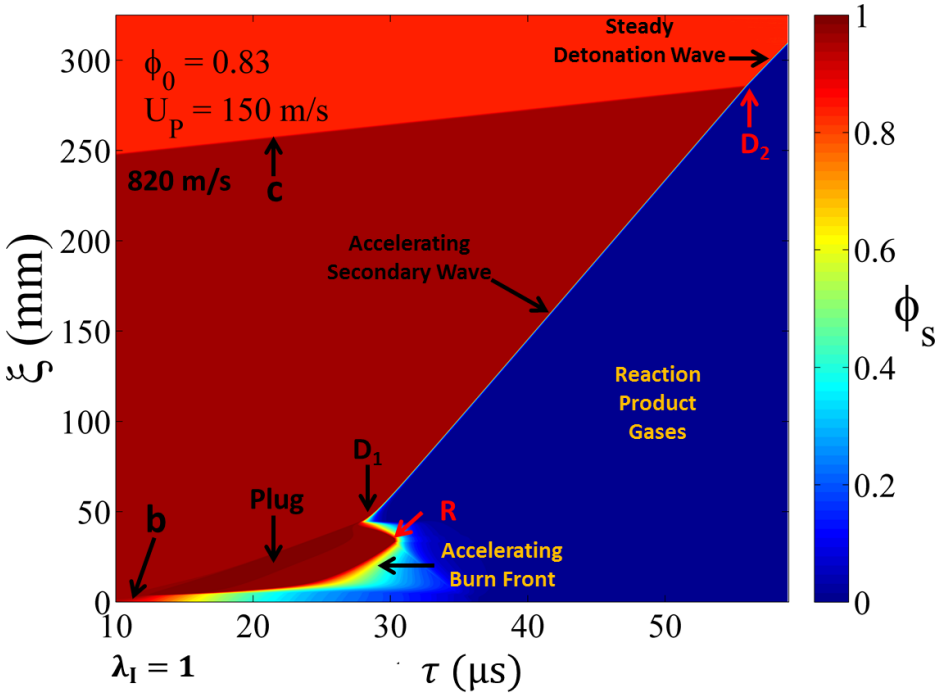

(b)

Figure 5.16: Predicted solid/explosive volume fraction contours in the generic $t - \xi$ diagram showing the predicted trajectories of primary compaction wave **c**, burn supported secondary compaction wave **b**, the rearward plug boundary **vp**, strong shock **S**, and forward propagating steady detonation wave **D**; for (a) $\phi_0 = 0.77$ and $U_P = 150$ m/s; (b) $\phi_0 = 0.83$ and $U_P = 150$ m/s. X_1 is the location of onset of low-speed burn, X_2 is the location of onset of rapid burn, and R is the location of onset of spontaneous reaction waves.

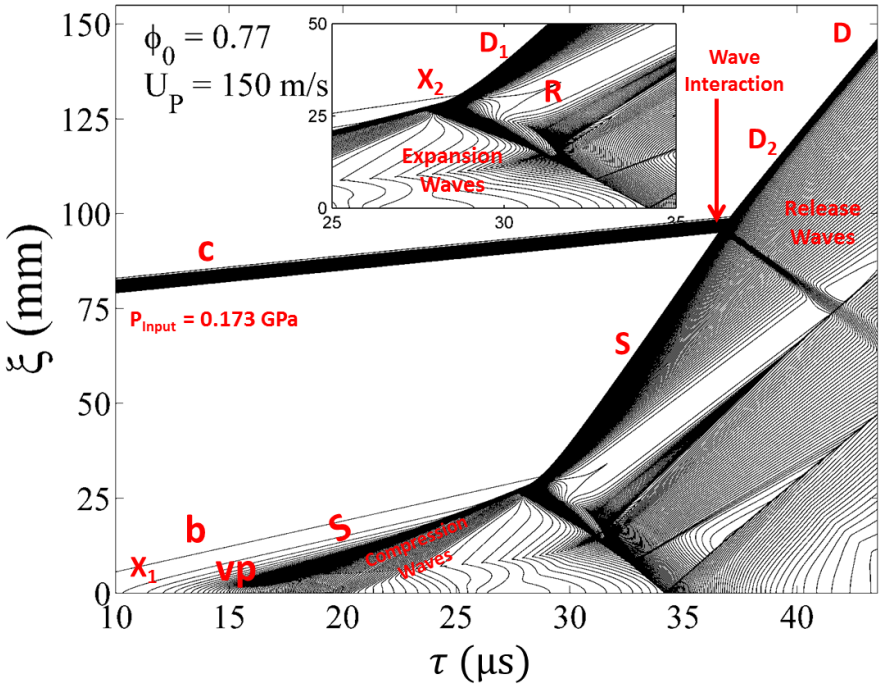

(a)

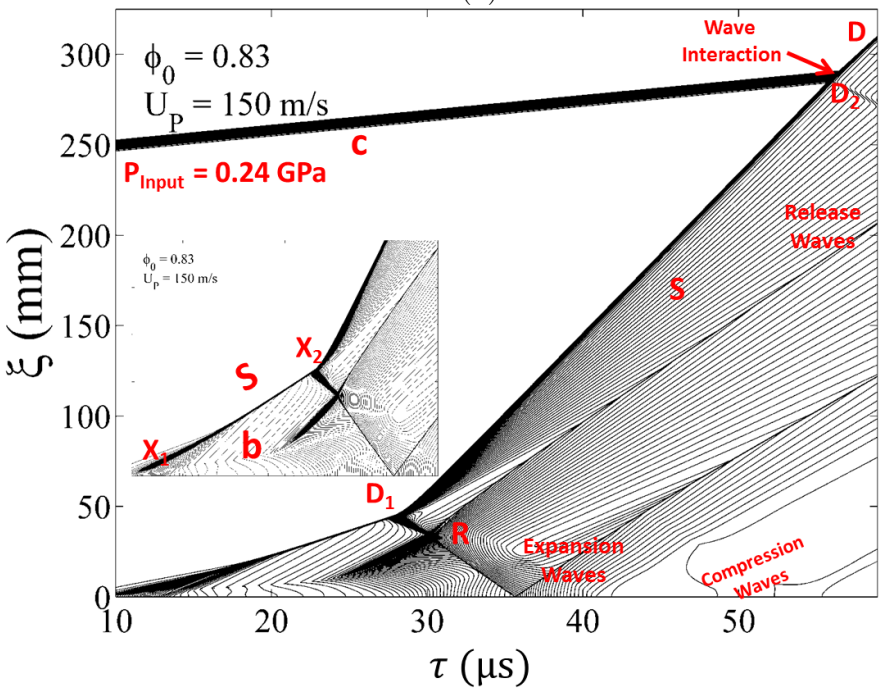

(b)

Figure 5.17: Predicted bulk pressure contours in the generic $t - \xi$ diagram showing the predicted trajectories of primary compaction wave **c**, burn supported secondary compaction wave **b**, the rearward plug boundary **vp**, strong shock **S**, and forward propagating steady detonation wave **D** for (a) $\phi_0 = 0.77$ and $U_P = 150$ m/s; (b) $\phi_0 = 0.83$ and $U_P = 150$ m/s. X_1 is the location of onset of low-speed burn, X_2 is the location of onset of rapid burn, and R is the location of onset of spontaneous reaction waves.

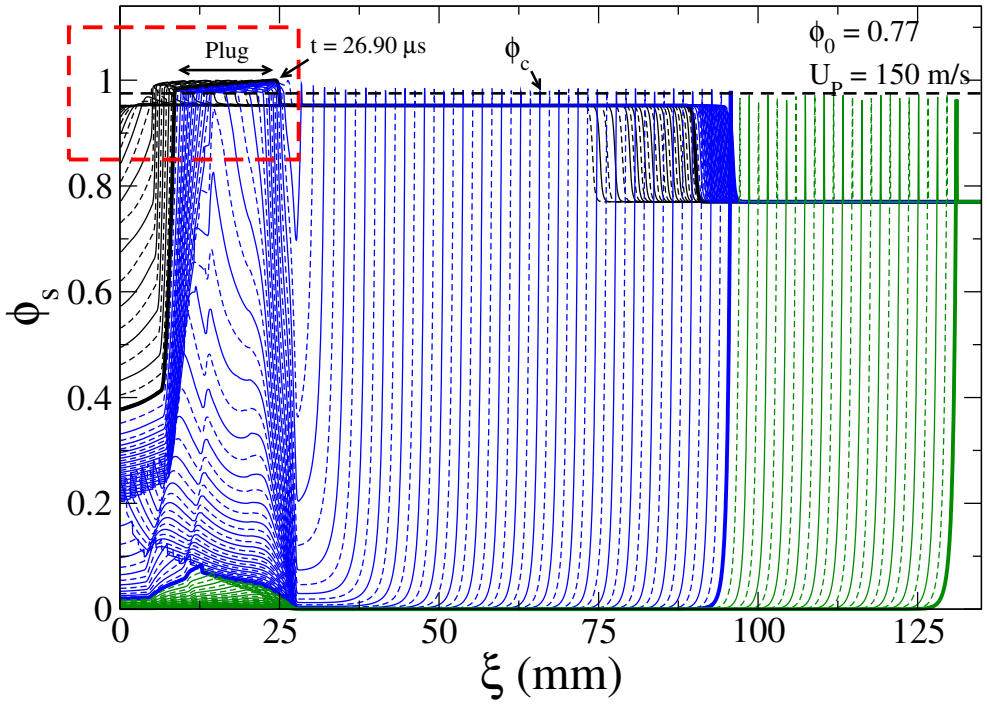

(a)

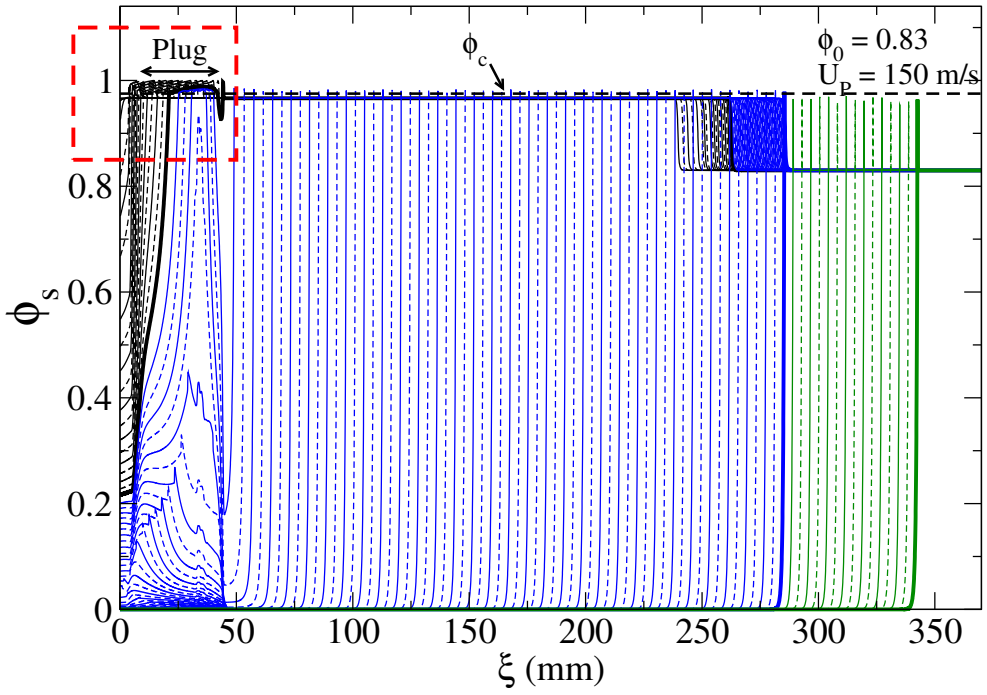

(b)

Figure 5.18: Predicted spatial variation in solid/explosive volume fraction for (a) $\phi_0 = 0.77$ and $U_P = 150$ m/s; (b) $\phi_0 = 0.83$ and $U_P = 150$ m/s.

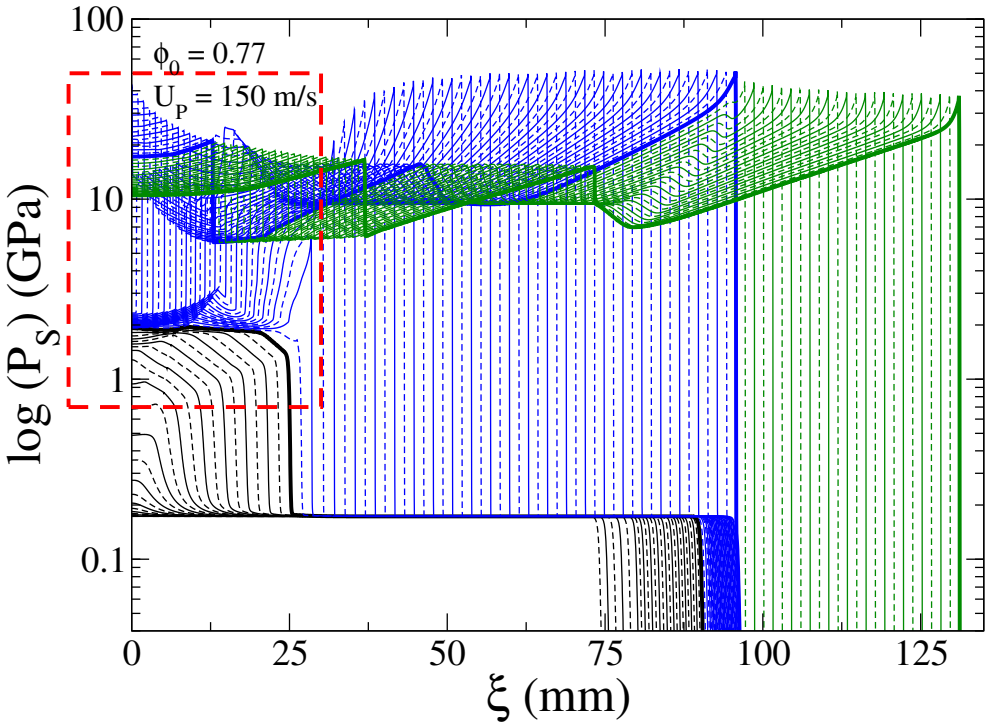

(a)

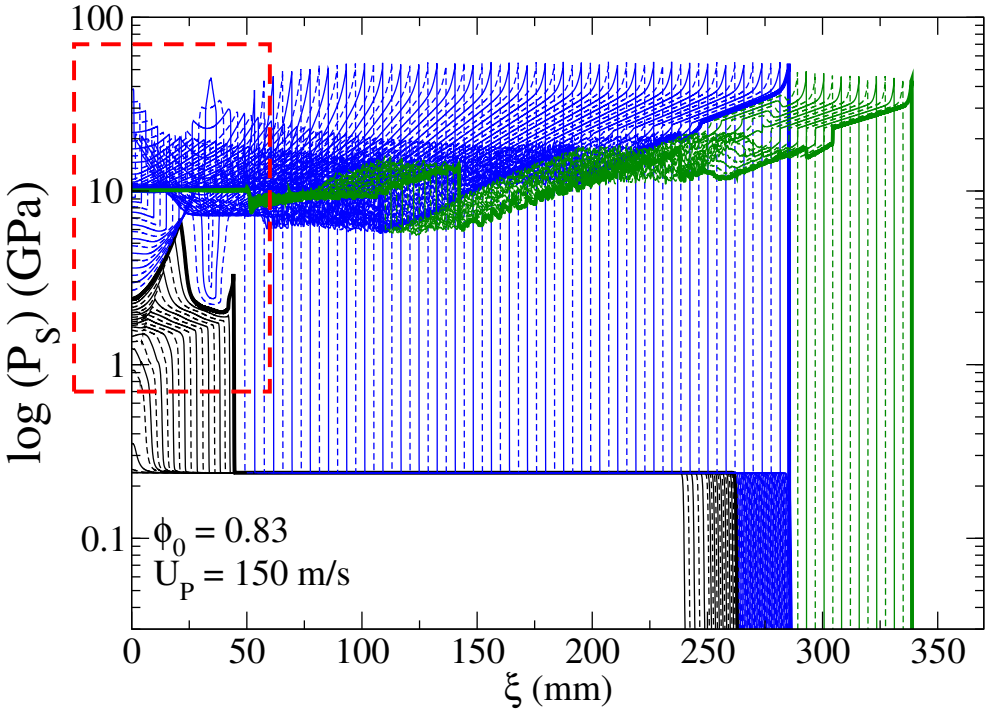

(b)

Figure 5.19: Predicted spatial variation in bulk pressure for (a) $\phi_0 = 0.77$ and $U_P = 150$ m/s; (b) $\phi_0 = 0.83$ and $U_P = 150$ m/s.

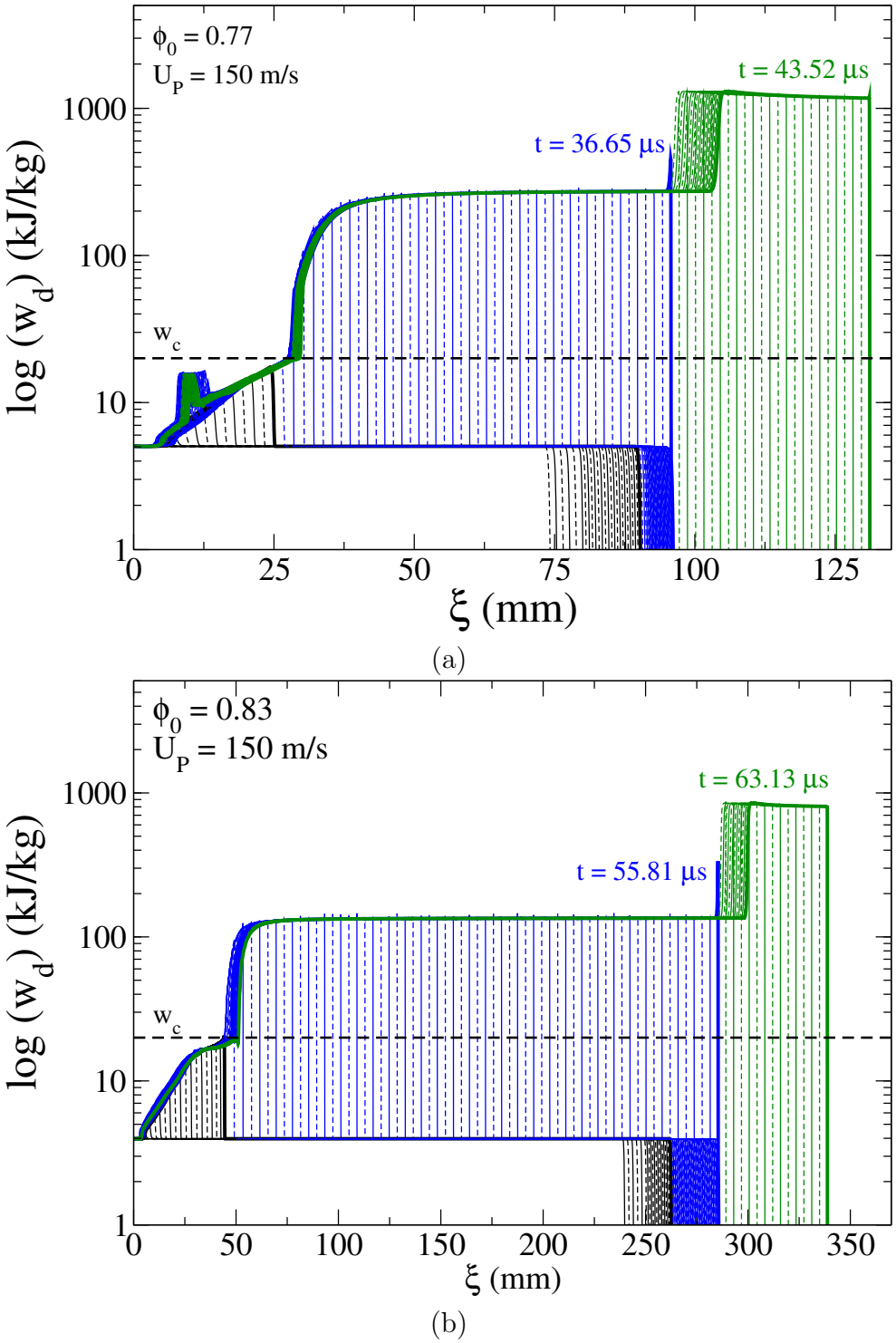

Figure 5.20: Predicted spatial variation in dissipative compaction work with position for (a) $\phi_0 = 0.77$ and $U_P = 150$ m/s; (b) $\phi_0 = 0.83$ and $U_P = 150$ m/s.

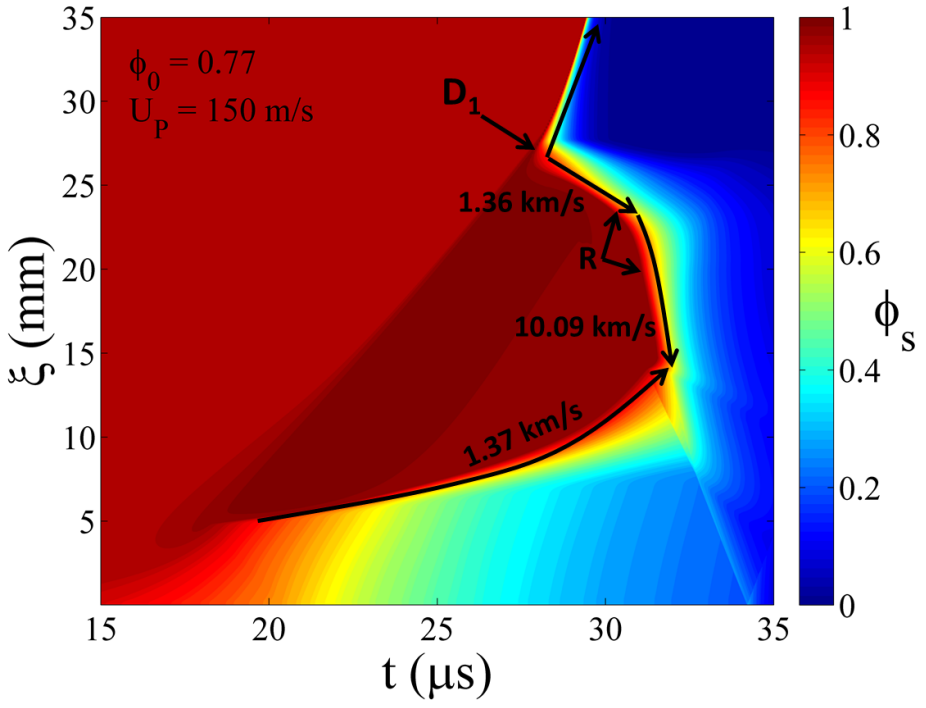

(a)

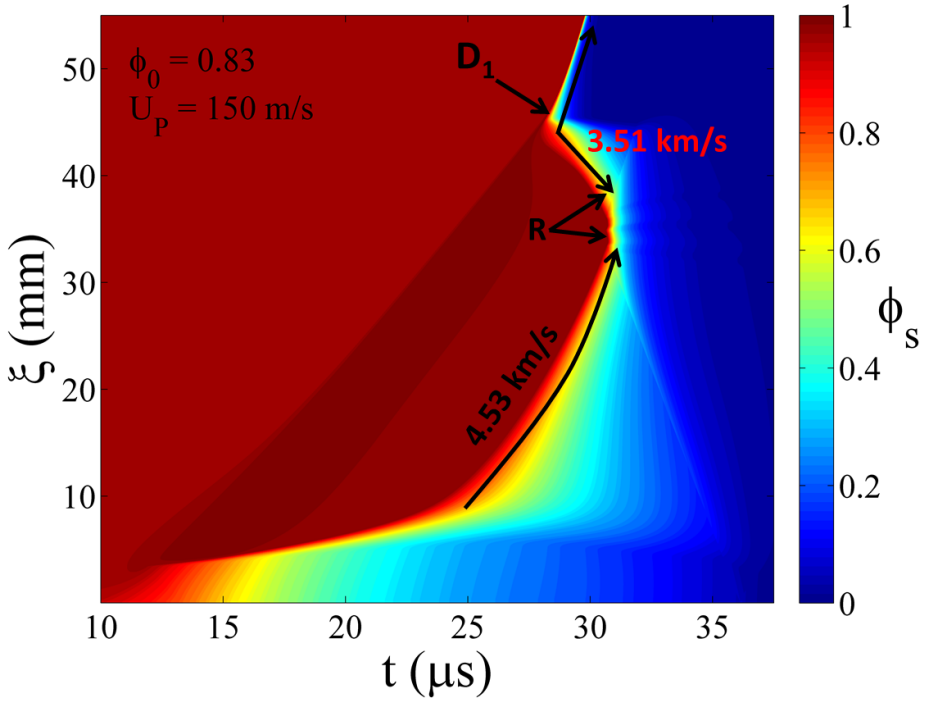

(b)

Figure 5.21: Magnified view of explosive/solid volume fraction contours within the plug region for (a) $\phi_0 = 0.77$ and $U_P = 150$ m/s; (b) $\phi_0 = 0.83$ and $U_P = 150$ m/s.

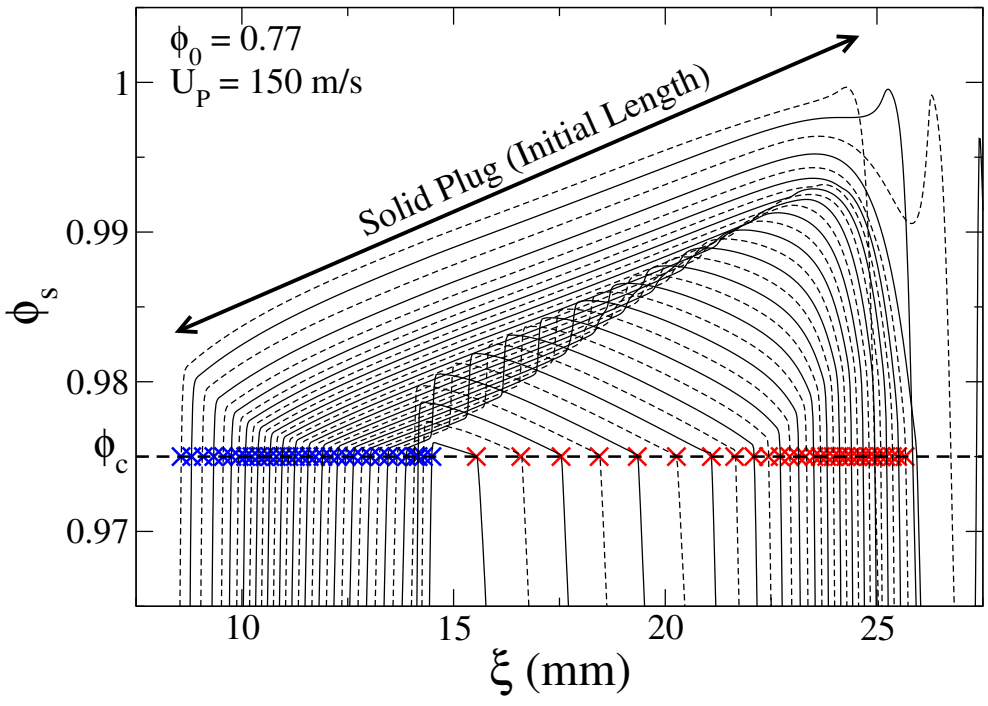

(a)

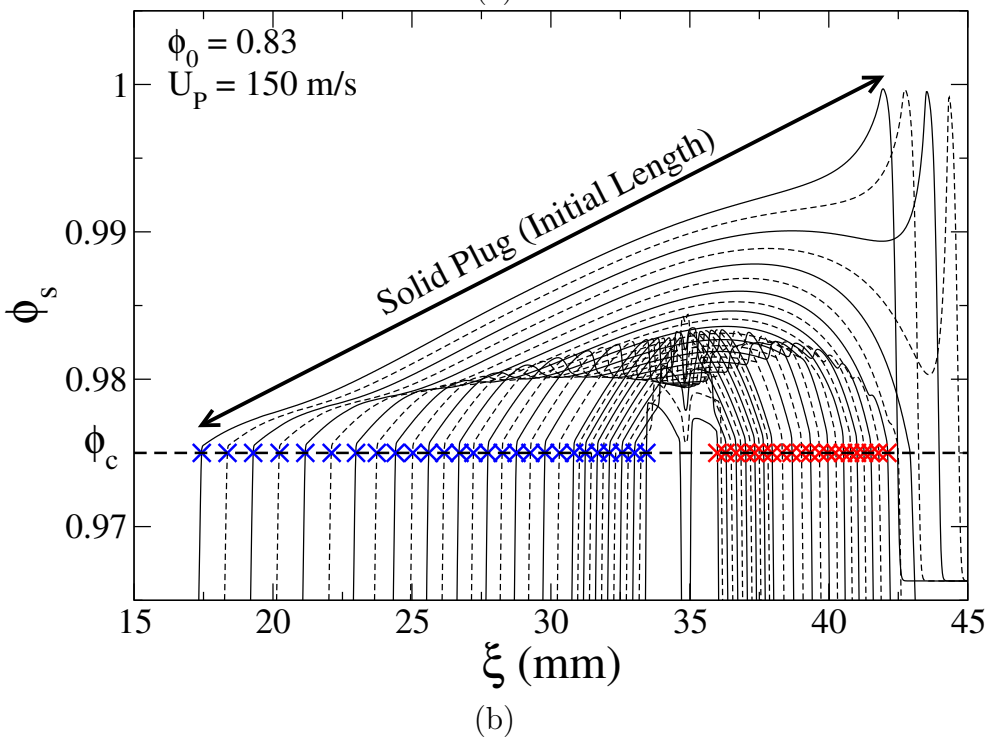

(b)

Figure 5.22: Magnified view of predicted spatial variation in explosive/solid volume fraction within the plug region for (a) $\phi_0 = 0.77$ and $U_P = 150$ m/s; (b) $\phi_0 = 0.83$ and $U_P = 150$ m/s. Blue and Red X point markers indicate the burn trajectory at the back and front end of the plug, respectively.

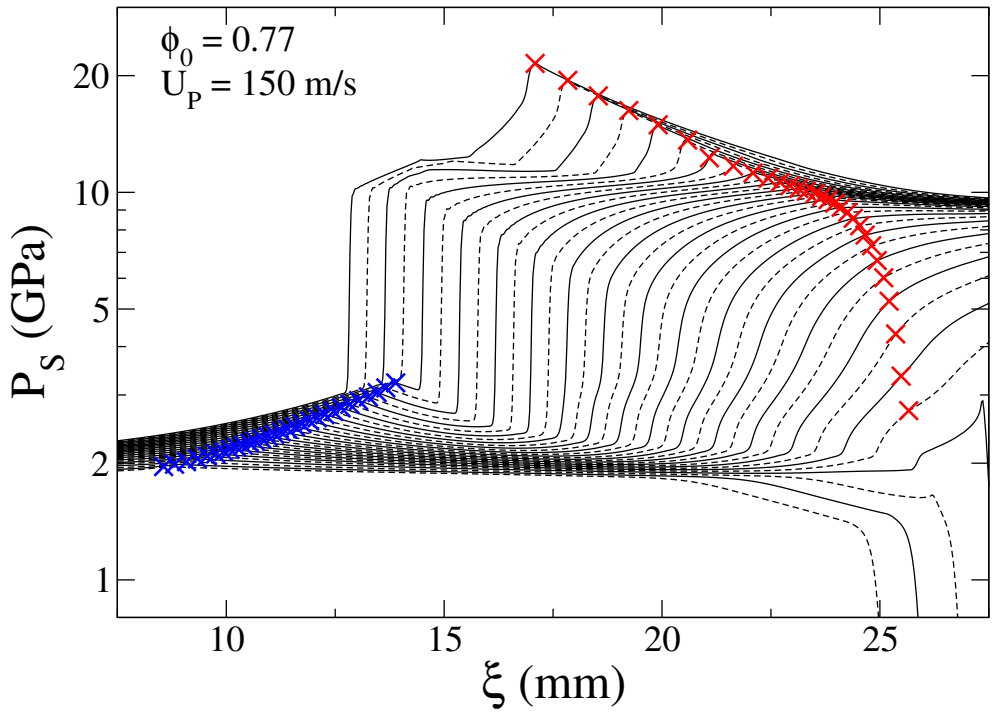

(a)

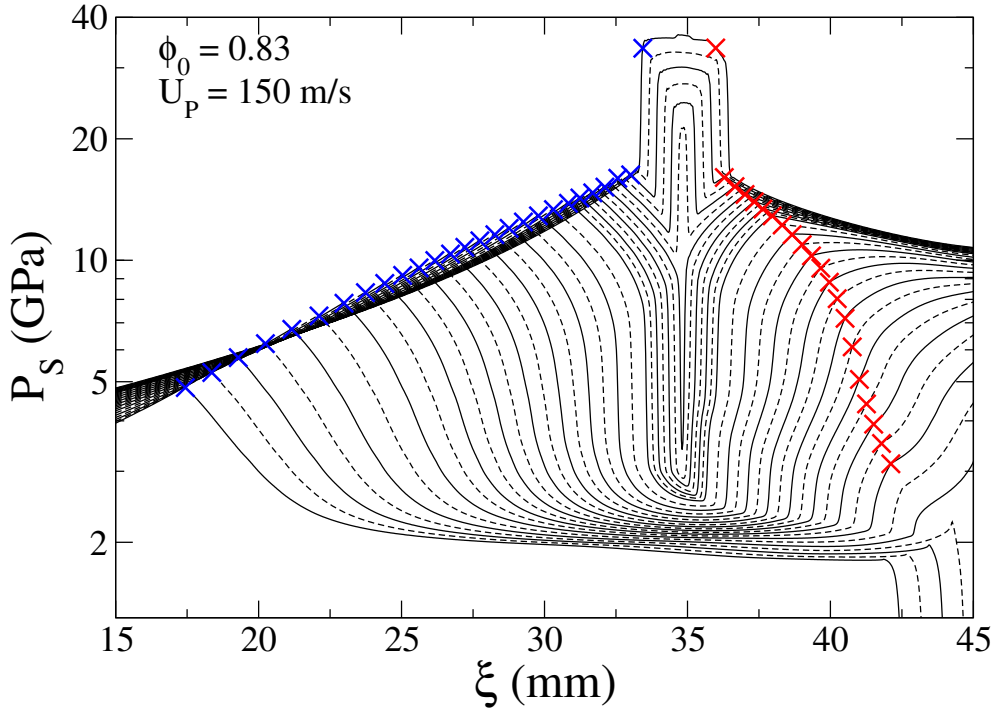

(b)

Figure 5.23: Magnified view of predicted spatial variation in bulk pressure within the plug region for (a) $\phi_0 = 0.77$ and $U_P = 150$ m/s; (b) $\phi_0 = 0.83$ and $U_P = 150$ m/s. Blue and Red X point markers indicate the burn trajectory at the back and front end of the plug, respectively.

respectively. Figures 5.18−5.20 give the comparative piston-attached spatial profiles for ϕ_s, P_s, and w_d, respectively, as the solution evolves into a steady detonation. To better understand the plug dynamics, Figs 5.21−5.23 give the comparative piston-attached magnified view of ϕ_s contours, spatial variation of ϕ_s and P_s, respectively within the plug region. For both simulations, a resolution of $\Delta\xi = 25$ μm was used to track the solution as it evolved into a steady detonation.

Transition Mechanism

- $\phi_0 = 0.77$ and $U_P = 150$ m/s

As seen in Figs. 5.16(a) and 5.17(a), the fully developed primary compaction wave propagates into the ambient bed at about 598 m/s corresponding to a input shock pressure of 0.173 GPa. The predicted solid volume fraction in the compacted region is $\phi_s = 0.95$ and the dissipative compaction work is approximately $w_d = 5.03$ kJ/kg. The onset of ignition is predicted to occur next to the piston surface at approximately $t_{ign} = 125$ μs. The predicted dissipative compaction work w_d behind the primary compaction wave in this case is lower than the threshold w_c, this results in initially low-speed regressive burn that results in plug formation.

Subsequently, regressive burn near the piston surface drives the formation of a secondary compaction wave, which eliminates the residual porosity resulting in the formation of a solid-plug, highlighted in Figs. 5.16(a) and 5.18(a). Here, the secondary compaction wave causes lower dissipation than that for $\phi_0 = 0.68$ due to the slightly lower residual porosity behind the primary compaction wave. The strength of the burn supported wave increases in time to form a strong shock, as indicated by increase in pressure in Figs. 5.19(a) and dissipative compaction work in Figs. 5.20(a). As $w_d \to w_c$, α quickly increases resulting in hot-spot facilitated burn which significantly intensifies secondary shock dissipation to $w_d > 200$ kJ/kg. This rapid onset of vigorous burn results in a thermal-explosion-like (or SDT-like) event which produces a forward propagating reactive shock and a backward propagating weak shock. The forward propagating reactive shock quickly transitions to

detonation becoming overdriven relative to the ambient material. The overdriven detonation subsequently overtakes the primary compaction wave and propagates into the ambient material as it relaxes to a CJ detonation. As seen in Figs. 5.21−5.23(a), the phenomenology associated with the backward propagating weak shock is very similar to that discussed for the base line case. The spontaneous reaction wave propagates at about $D = 10.09$ km/s and subsequently overtakes the low-speed burn front at the back of the plug further enhancing the burn leading to complete consumption of the plug.

- $\phi_0 = 0.83$ and $U_P = 150$ m/s

As seen in Figs. 5.16(b) and 5.17(b), the fully developed primary compaction wave propagates into the ambient bed at about 820 m/s corresponding to a input shock pressure of 0.24 GPa. The predicted solid volume fraction in the compacted region is $\phi_s = 0.967$ and the dissipative compaction work is approximately $w_d = 3.98$ kJ/kg. The onset of ignition is predicted to occur next to the piston surface at approximately $t_{ign} = 280$ μs. The predicted dissipative compaction work w_d behind the primary compaction wave in this case is lower than the threshold w_c, this results in initially low-speed regressive burn that results in plug formation.

Subsequently, regressive burn near the piston surface drives the formation of a secondary compaction wave, which eliminates the residual porosity resulting in the formation of a solid-plug, highlighted in Figs. 5.16(b) and 5.18(b). Here, the secondary compaction wave causes lower dissipation than that for $\phi_0 = 0.77$ due to the slightly lower residual porosity behind the primary compaction wave. The strength of the burn supported wave increases in time and simultaneously at about $t = 25$ μs, the burn-front at the back-end of the plug is predicted to start growing in strength and propagate at about 4.35 km/s. As seen in Fig. 5.22(b), this acceleration is due to the formation of a reactive compression waves at the back-end of the plug; analogous to spontaneous reaction waves discussed previously. As the secondary compaction wave grows in strength $w_d \rightarrow w_c$, α quickly increases resulting in hot-spot facilitated burn which significantly intensifies secondary shock dissipation

to $w_d > 200$ kJ/kg. This rapid onset of vigorous burn results in a thermal-explosion-like (or SDT-like) event which produces a forward propagating reactive shock and a backward propagating weak shock. The forward propagating reactive shock quickly transitions to detonation becoming overdriven relative to the ambient material. The overdriven detonation subsequently overtakes the primary compaction wave and propagates into the ambient material as it relaxes to a CJ detonation. As seen in Figs. 5.21−5.23(b), the backward propagating weak shock propagates into the plug at about $D = 3.51$ km/s and the low-speed burn-front propagating forward into the plug (at $D = 4.53$ km/s) interact at the location R causing a rapid increase pressure and shock dissipation. This increase in pressure leads to enhanced burn rate and significant gas production leading to complete consumption of the plug. Both cases are ignition controlled and the CJ detonation predicted a compaction-led spatial structure.

5.2.3 Strong−Shock Initiation

Strong−shock initiation refers to piston initiated DDT simulations where the dissipative compaction work behind the fully developed primary compaction wave is $w_d > w_c$, that is sufficient to cause widespread growth and agglomeration of hot-spots resulting in initially prompt hot-spot facilitated burn.

The first case considered here is a simulation for a initially stress-free and motionless bed corresponding to an initial solid volume fraction $\phi_0 = 0.68$ and a piston impact speed of $U_P = 300$ m/s. Figure 5.24(a) and 5.24(b) gives solid volume fraction (ϕ_s) and bulk pressure ($\overline{P} = P_s\phi_s + P_g\phi_g$) contours in the $\tau - \xi$ characteristic plane, respectively. Figures 5.25(a-b) and 5.26(a-b) give the piston-attached spatial profiles for ϕ_s, P_s, w_d and u_s as the solution evolves into a steady detonation, using $N = 2000$ cells and a grid resolution $\Delta\xi = 12.5$ μm.

Transition Mechanism

As seen in Figs. 5.24(a) and 5.25(a), the fully developed primary compaction wave, reduces the porosity within the material and propagates at about 624.72 m/s, corresponding to input shock pressure of 0.36 GPa. The predicted solid volume fraction in the compacted

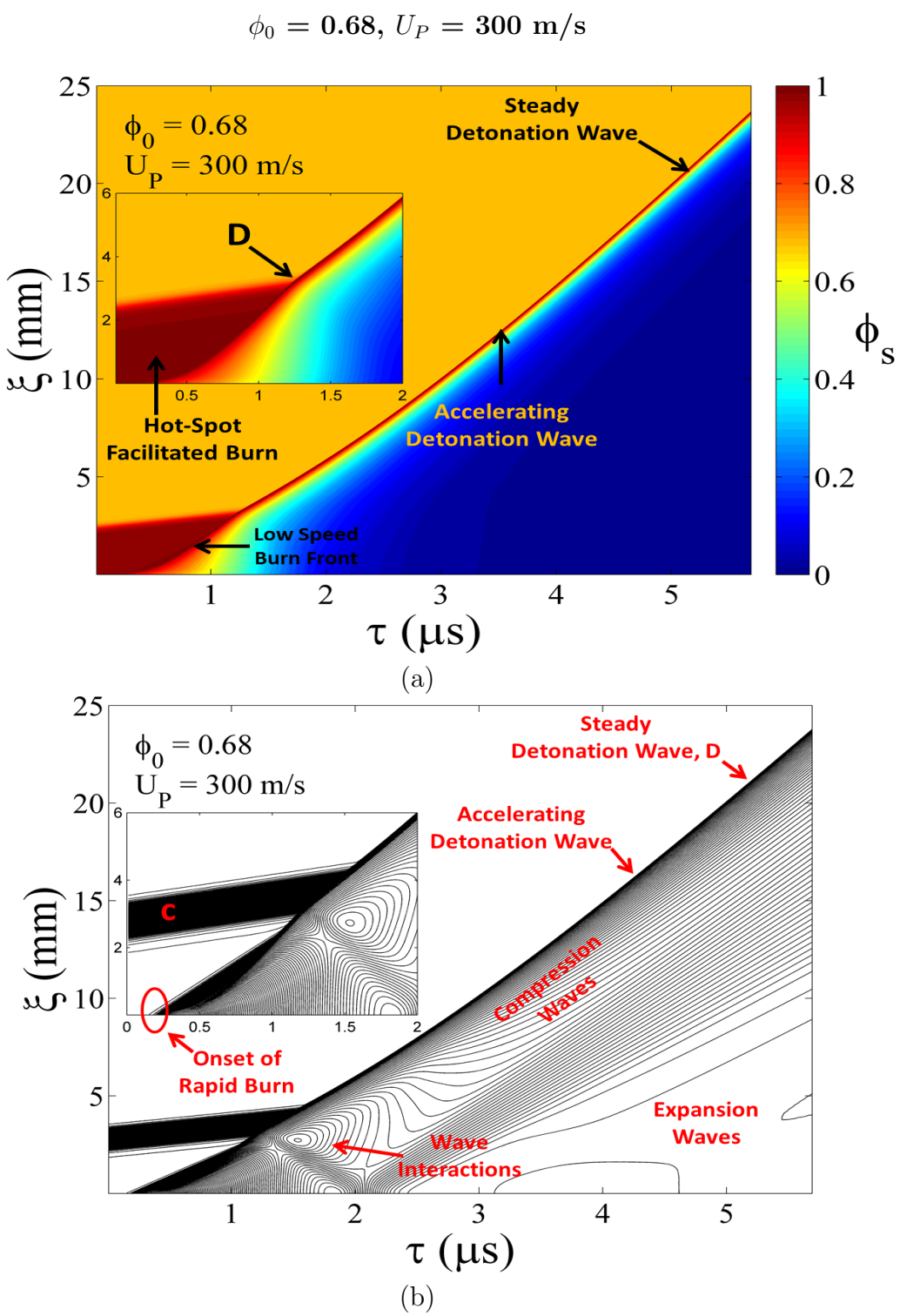

Figure 5.24: Predicted: (a) solid/explosive volume fraction contours; and (b) bulk pressure contours; in the generic $t - \xi$ diagram showing the predicted trajectories of compaction wave **c**, the accelerating detonation wave, and the steady detonation wave D for $\phi_0 = 0.68$ and $U_P = 300$ m/s. The location of onset of hot-spot facilitated burn us also highlighted.

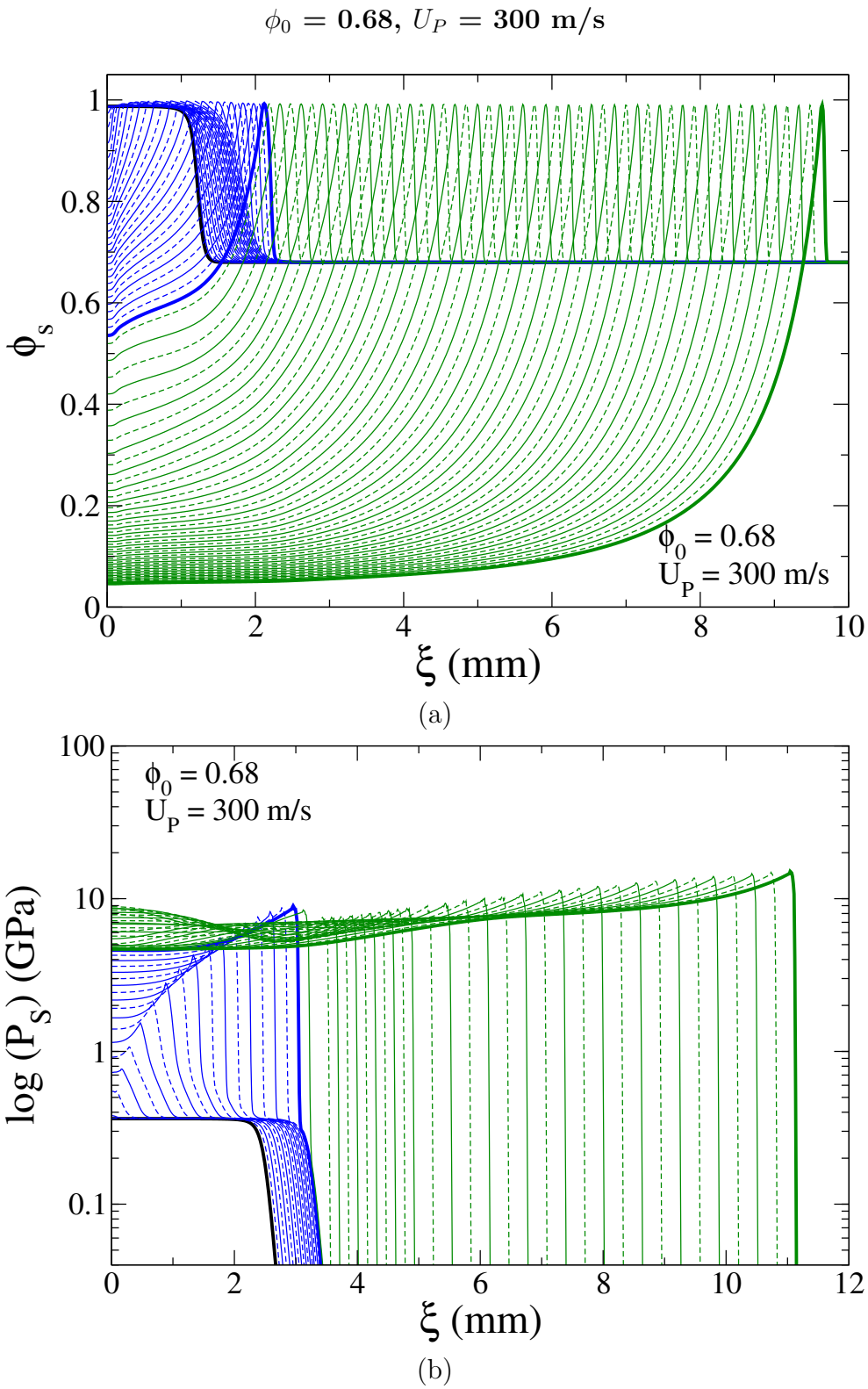

Figure 5.25: Predicted spatial variation in (a) solid/explosive volume fraction ϕ_s; and (b) solid phase pressure P_s; for $\phi_0 = 0.68$ and $U_P = 300$ m/s.

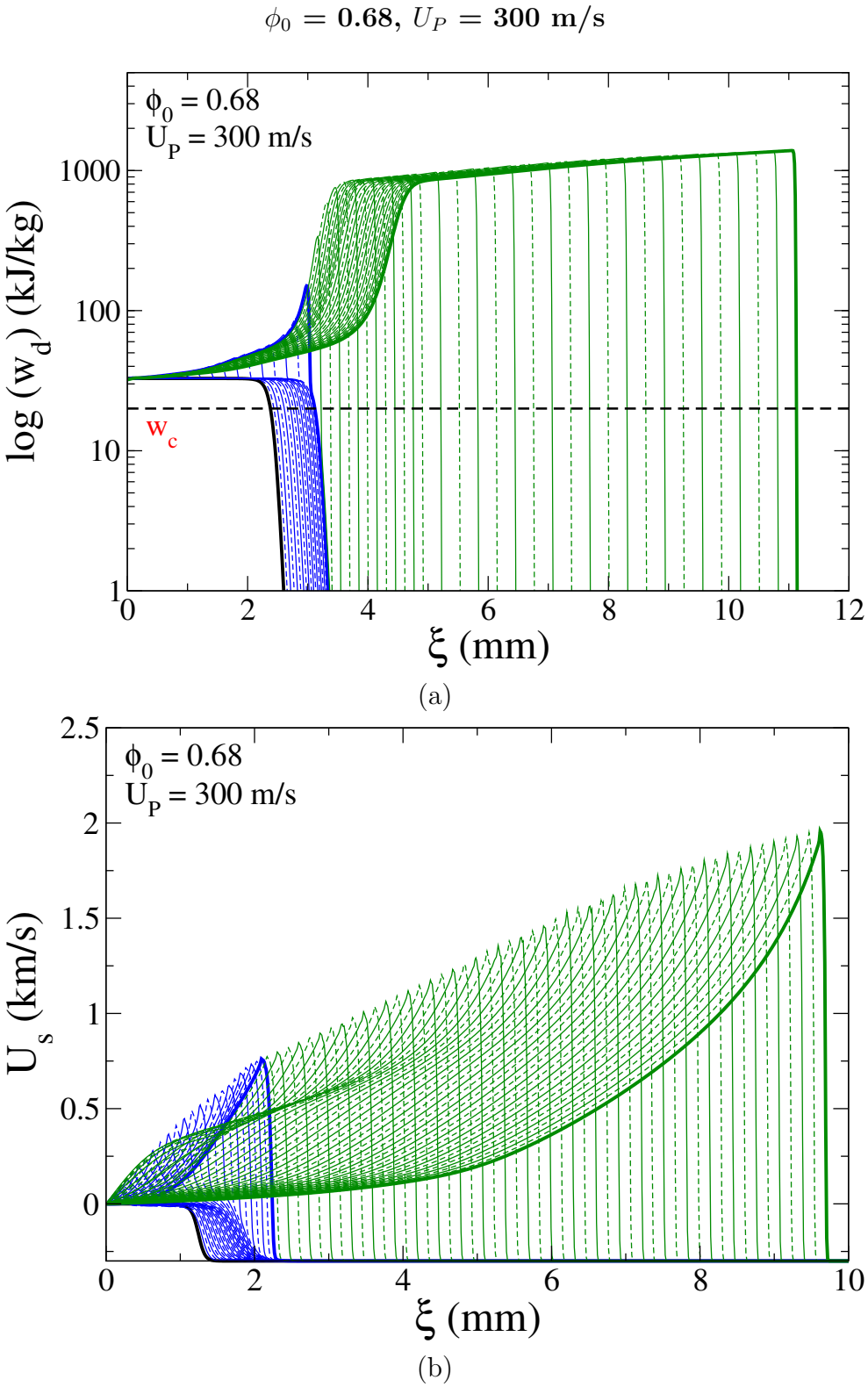

Figure 5.26: Predicted spatial variation in (a) dissipative compaction work w_d; and (b) solid phase particle velocity U_s with position; for $\phi_0 = 0.68$ and $U_P = 300$ m/s.

region is $\phi_s = 0.9875$ and the dissipative compaction work is approximately $w_d = 32.3$ kJ/kg. The predicted dissipative compaction work w_d behind the primary wave for this case is higher than the threshold w_c, this results in a initially "hot-spot" facilitated burn.

Following ignition near the piston surface at about $t = 6$ μs, a continuously accelerating combustion/detonation wave is predicted to form within the compacted region whose pressure exceeds the CJ value of the ambient material. The strength of the burn supported shock, quickly increases in strength as indicated by rapid increase in pressure and dissipate compaction work in Figs. 5.25(b) and 5.25(c). Since $w_d > w_c$, α quickly increases resulting in "hot-spot facilitated" burn which significantly intensifies shock dissipation that is sufficient to cause wide spread agglomeration of hot-spots indicating the likelihood of very fast reactive hot-spot interaction times. The strong combustion/detonation wave subsequently overtakes the lead wave, causing it to slightly decelerate with a reduction in pressure before re-accelerating to a CJ detonation as it propagates into the ambient material. In this simulation, the transition mechanism is largely continuous, with ignition induction time comparable to that required for transition following ignition, which is typically referred to as burn controlled and the CJ detonation predicted a compaction-led spatial structure.

- **Parametric Analysis**

For direct comparison, simulation predictions for material having $\phi_0 = 0.77$ and $\phi_0 = 0.83$ for a piston speed $U_P = 300$ m/s is given here. As discussed earlier, for a fixed U_P, increase in packing density (ϕ_0) results in higher wave speeds (D) and stronger shocks (P_s), but lower dissipative compaction work (w_d). Figure 5.27(a-b) and 5.28(a-b) gives comparative predictions of solid volume fraction (ϕ_s) contours and bulk pressure contours in the $\tau - \xi$ characteristic plane, respectively. Figure 5.29, 5.30 and 5.31 gives the comparative piston-attached spatial profiles for ϕ_s, P_s, and w_d, respectively, as the solution evolves into a steady detonation. For both simulations, a resolution of $\Delta\xi = 12.5$ μm was used to track the solution as it evolved into a steady detonation.

Transition Mechanism

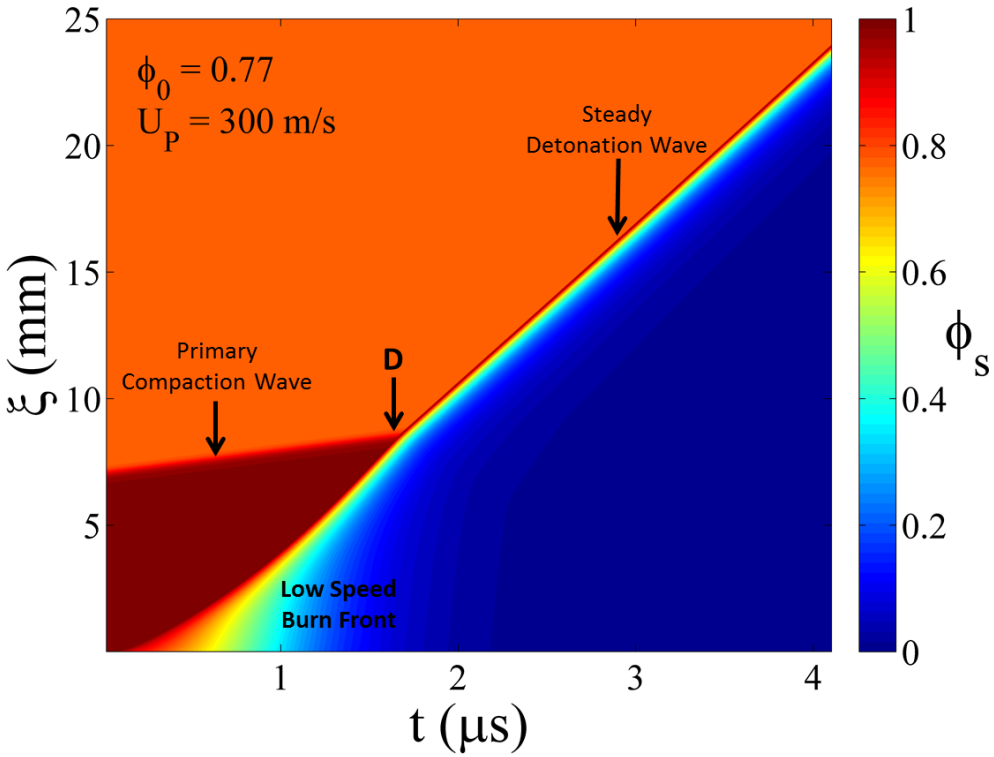

(a)

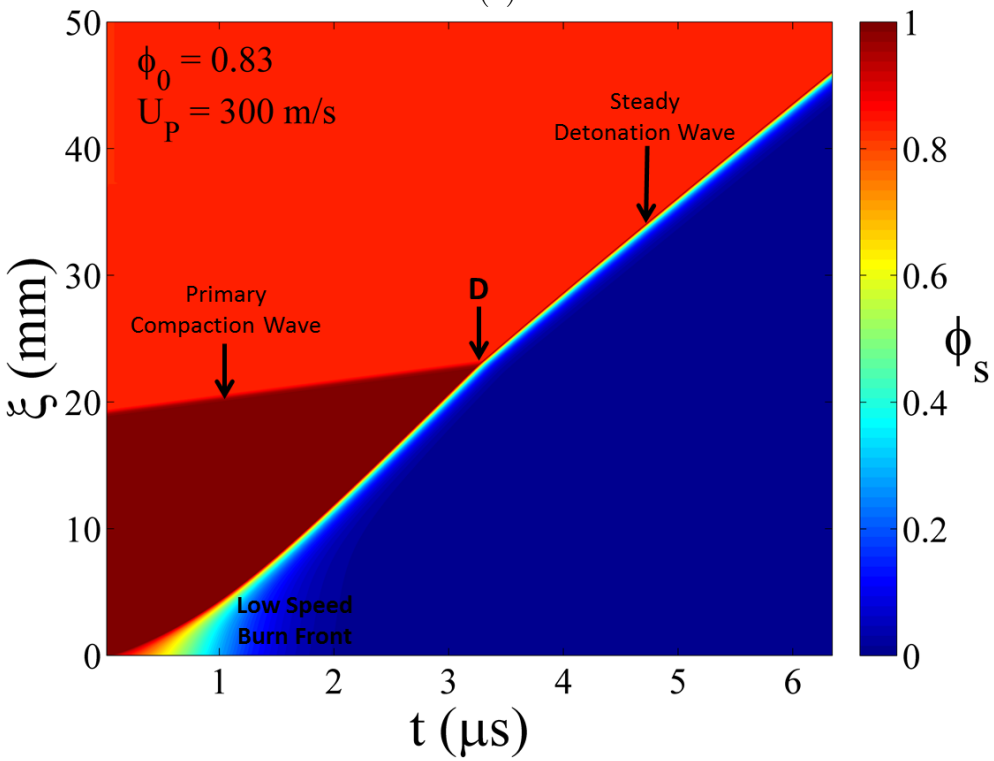

(b)

Figure 5.27: Predicted solid/explosive volume fraction contours in the generic $t-\xi$ diagram showing the predicted trajectories of compaction wave **c**, the accelerating detonation wave, and the steady detonation wave D; for (a) $\phi_0 = 0.77$ and $U_P = 300$ m/s; and (b) $\phi_0 = 0.83$ and $U_P = 300$ m/s. The location of onset of hot-spot facilitated burn is also highlighted.

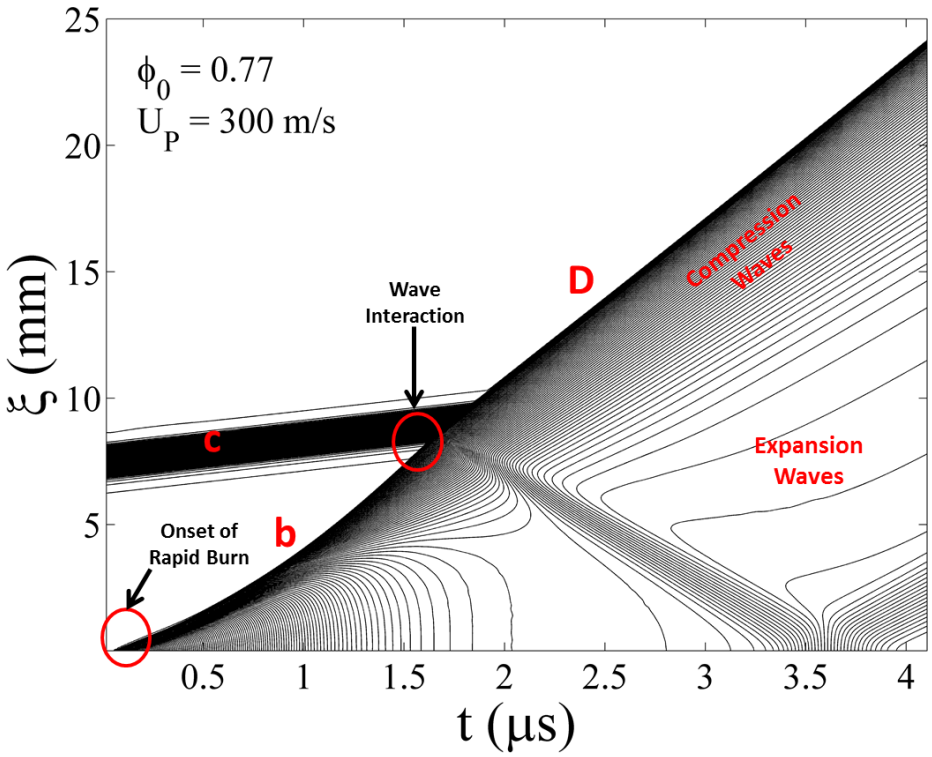

(a)

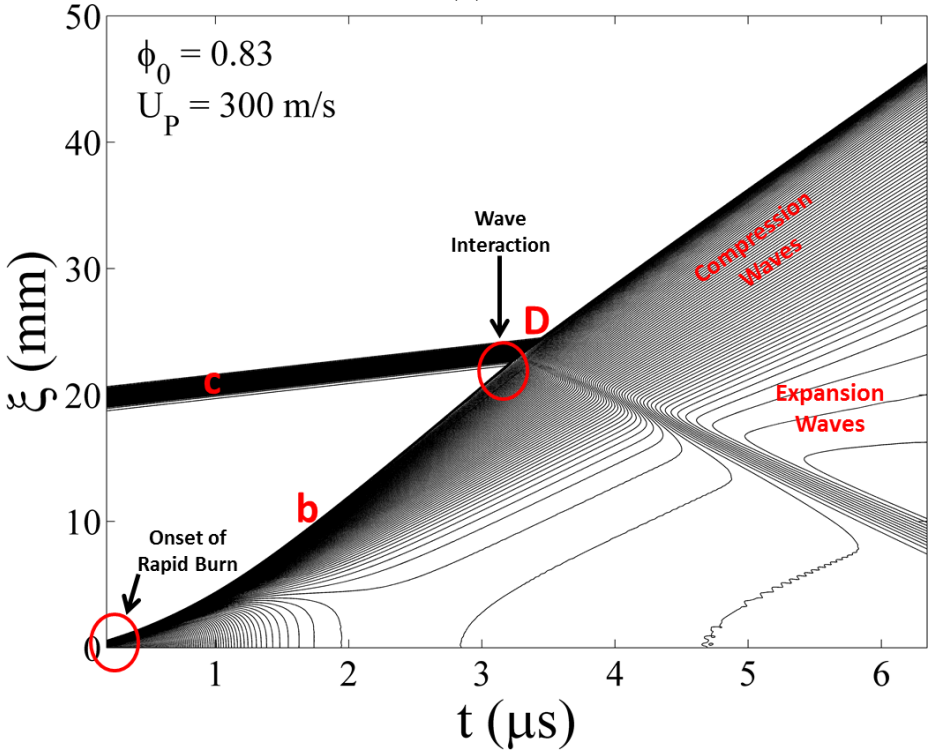

(b)

Figure 5.28: Predicted bulk pressure contours in the generic $t - \xi$ diagram showing the predicted trajectories of compaction wave **c**, the accelerating detonation wave, and the steady detonation wave D; for (a) $\phi_0 = 0.77$ and $U_P = 300$ m/s; and (b) $\phi_0 = 0.83$ and $U_P = 300$ m/s. The location of onset of hot-spot facilitated burn is also highlighted.

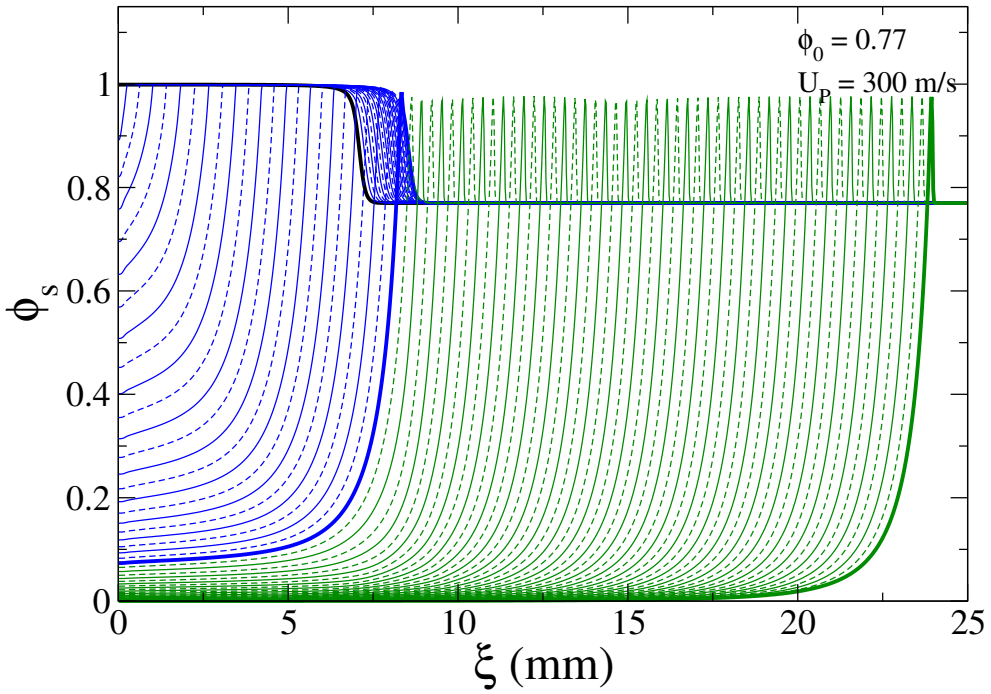

(a)

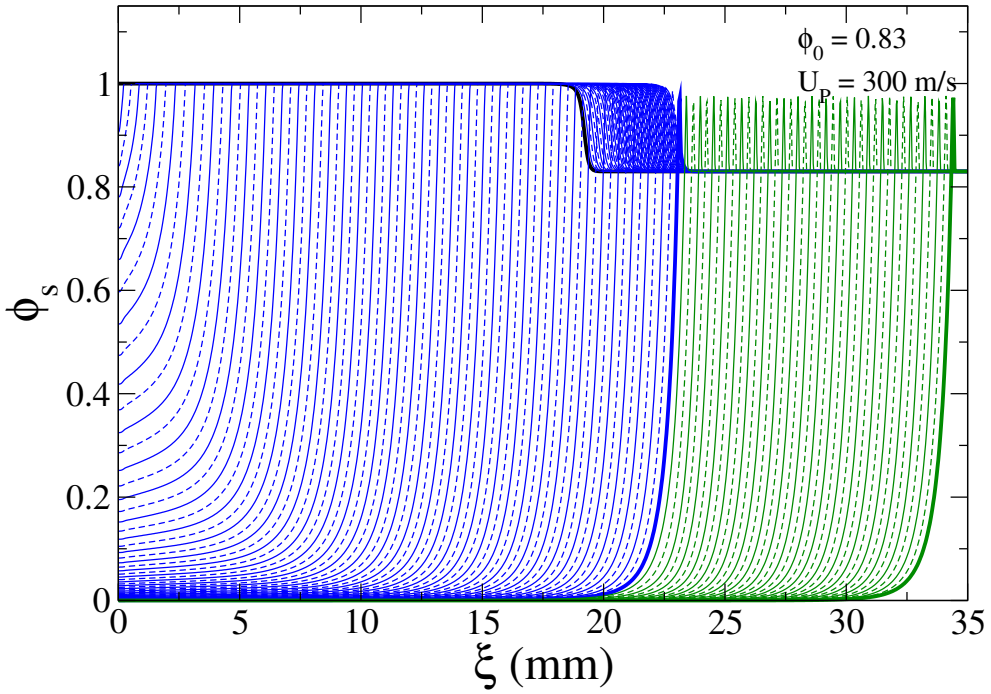

(b)

Figure 5.29: Predicted spatial variation in solid/explosive volume fraction ϕ_s for (a) $\phi_0 = 0.77$ and $U_P = 300$ m/s; and (b) $\phi_0 = 0.83$ and $U_P = 300$ m/s.

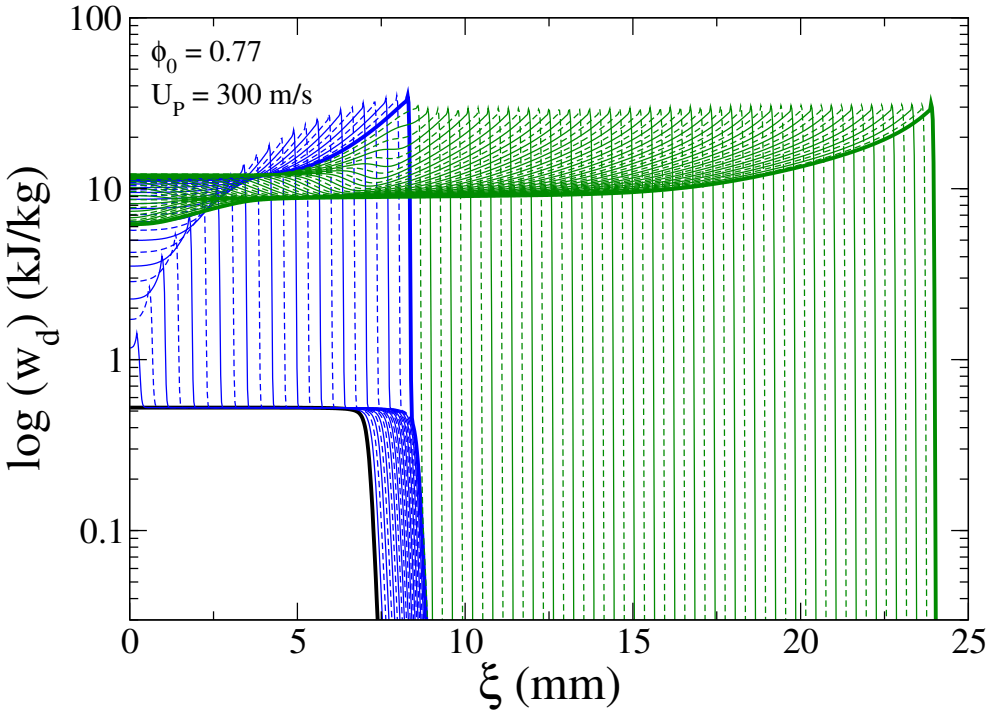

(a)

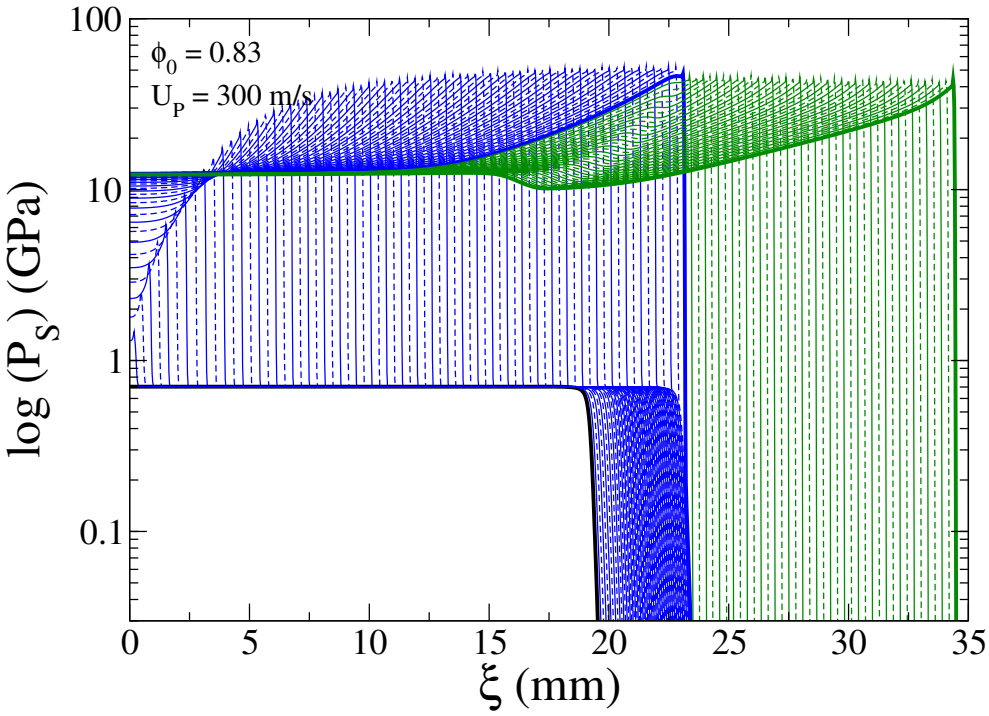

(b)

Figure 5.30: Predicted spatial variation in solid phase pressure P_s for (a) $\phi_0 = 0.77$ and $U_P = 300$ m/s; and (b) $\phi_0 = 0.83$ and $U_P = 300$ m/s.

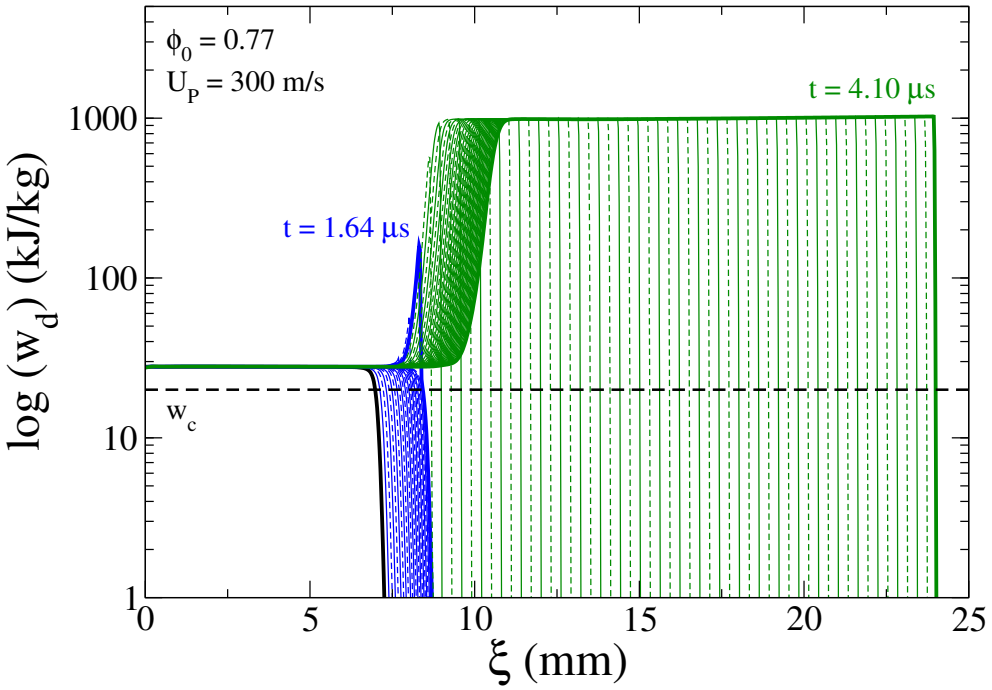

(a)

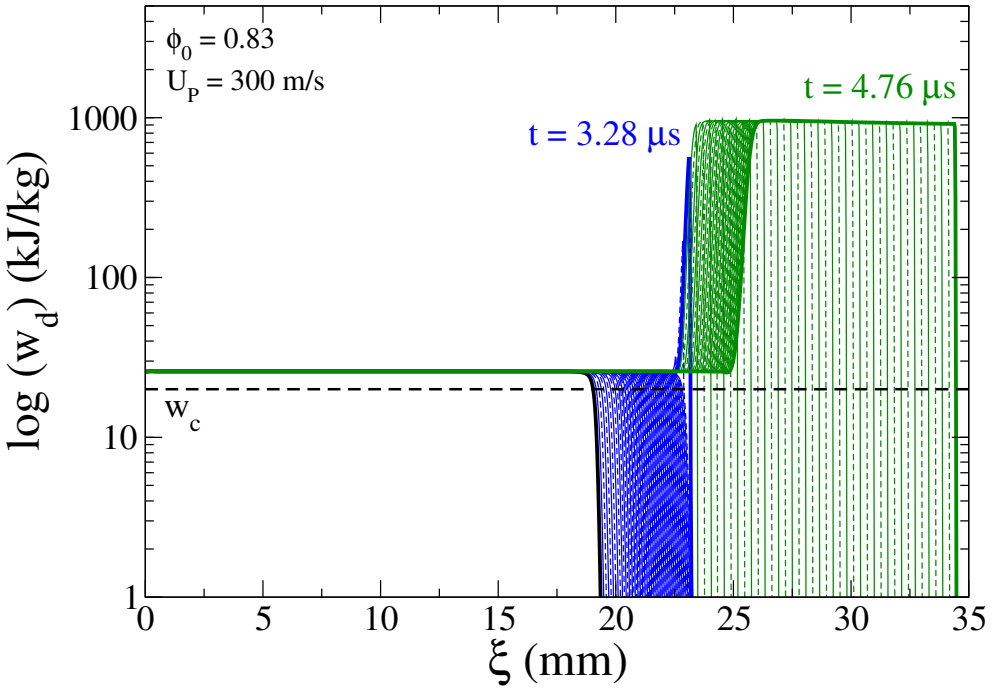

(b)

Figure 5.31: Predicted spatial variation in dissipative compaction work w_d for (a) $\phi_0 = 0.77$ and $U_P = 300$ m/s; and (b) $\phi_0 = 0.83$ and $U_P = 300$ m/s.

For $\phi_0 = 0.77$, as seen in Figs 5.27(a) and 5.29(a) the fully developed primary compaction wave eliminates the porosity completely ($\phi_s \approx 1$) within the material and propagates at about 892 m/s, corresponding to a input shock pressure of 0.52 GPa. The predicted dissipative compaction work behind the lead wave is about $w_d = 27.8$ kJ/kg. Following impact, ignition next to piston is predicted to occur approximately at $t_{ign} = 7.8$ μs. For $\phi_0 = 0.83$, as seen in Figs 5.27(b) and 5.29(b), the fully developed primary compaction wave eliminates the porosity completely ($\phi_s \approx 1$ within material and propagates at about 1185 m/s, corresponding to a input shock pressure of $P_{Input} = 0.7$ GPa. The predicted dissipative compaction work behind the lead wave is about $w_d = 25.8$ kJ/kg and ignition next to piston is predicted to occur at approximately $t_{ign} = 16$ μs. The predicted dissipative compaction work w_d behind the primary compaction wave for both cases is higher than the threshold w_c, this results in initially prompt hot-spot facilitated burn

In both cases, following ignition near the piston a continuously accelerating combustion/detonation wave is predicted to form within the compacted region whose pressure exceeds the CJ value of the ambient material. The strength of the burn supported shock, quickly increases in strength as indicated by rapid increase in pressure and dissipate work in Figs. 5.30(a-b) and 5.31(a,b). Since $w_d > w_c$, $\alpha = \alpha_2$ results in "hot-spot facilitated" burn which significantly intensifies shock dissipation that is sufficient to cause wide spread agglomeration of hot-spots indicating the likelihood of very fast reactive hot-spot interaction times. The strong combustion/detonation wave subsequently overtakes the lead wave, causing it to slightly decelerate with a reduction in pressure as it propagates into the ambient material. In both the cases, the transition mechanism is largely continuous, with ignition induction time comparable to that required for transition following ignition, which is referred to as burn controlled and the CJ detonation predicted a compaction-led spatial structure.

5.2.4 Moderate−Shock Initiation

In this section, intermediate cases between weak-shock and strong-shock initiation are considered. The first case considered here is a simulation for a initially stress-free and motionless bed corresponding to an initial solid volume fraction $\phi_0 = 0.68$ for a piston impact speed of $U_P = 200$ m/s.

Figure 5.32(a) and 5.32(b) gives solid volume fraction (ϕ_s) contours and bulk pressure ($\overline{P} = P_s\phi_s + P_g\phi_g$) contours in the $\tau - \xi$ characteristic plane, respectively. Figure 5.33 and 5.34 gives the piston-attached spatial profiles for ϕ_s, P_s, w_d and u_s as the solution evolves into a steady detonation. To better understand the plug dynamics, Figure 5.35 gives the magnified view of predicted variation in ϕ_s and P_s within the plug region for a simulation using $N = 2000$ computational cells and a grid resolution of $\Delta\xi = 25$ μm.

Transition Mechanism

As seen in Figs. 5.32(a) and 5.33(a), the fully developed primary compaction wave reduces the porosity within the material and propagates at about 474 m/s corresponding to a input shock pressure of 0.181 GPa. The predicted solid volume fraction in the compacted region is $\phi_s = 0.96$ and the dissipative compaction work is about $w_d = 13$ kJ/kg. Following impact, the compaction wave propagates a relatively long distance into the ambient material prior to onset of ignition near the piston surface at approximately $t_{ign} = 16$ μs. The predicted dissipative compaction work behind the lead wave is approximately $w_d = 13.05$ kJ/kg. The predicted dissipative compaction work w_d behind the primary wave for this case is lower than the threshold w_c, this results in an initially "low-speed" regressive burn.

The regressive burn next to the piston surface drives the formation of a burn-supported secondary compaction wave (**b**), which eliminates the residual porosity. However, the secondary compaction wave causes less dissipation than that for $U_P = 150$ m/s because of the slightly lower residual porosity left behind by the primary wave. The secondary wave overtakes the lead wave causing a significant increase in pressure and dissipation as indicated by Figs. 5.33(b) and 5.34(a) respectively. Consequently, the rapid onset of

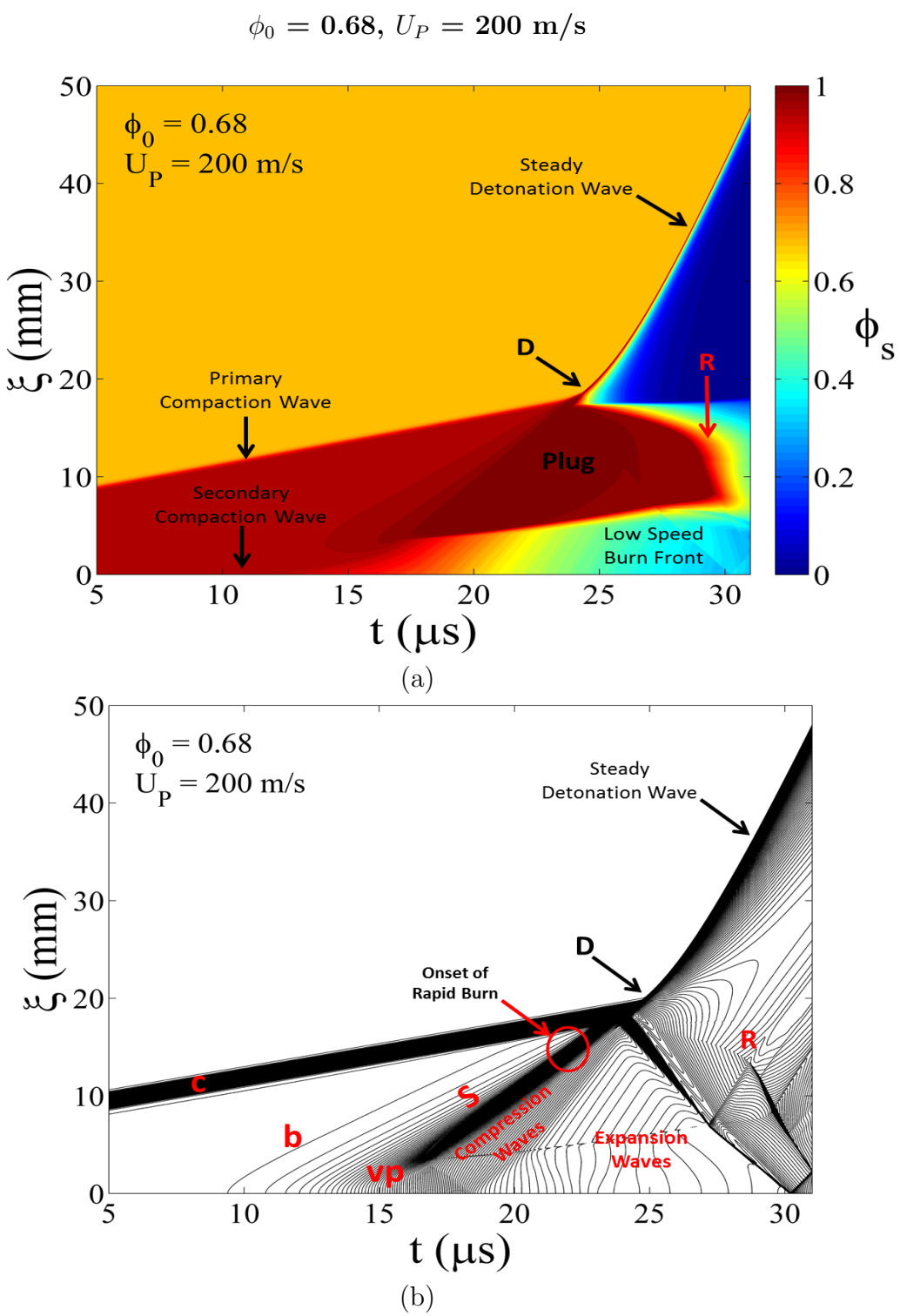

Figure 5.32: (a) The generic $t-\xi$ diagram showing the predicted trajectories of compaction wave **c**, ignition wave **b**, the rearward plug boundary **vp**, strong shock **S**, forward propagating detonation wave **D**, and rearward propagating spontaneous reaction wave **R**; (b) Predicted solid/explosive volume fraction contours; for $\phi_0 = 0.68$ and $U_P = 200$ m/s.

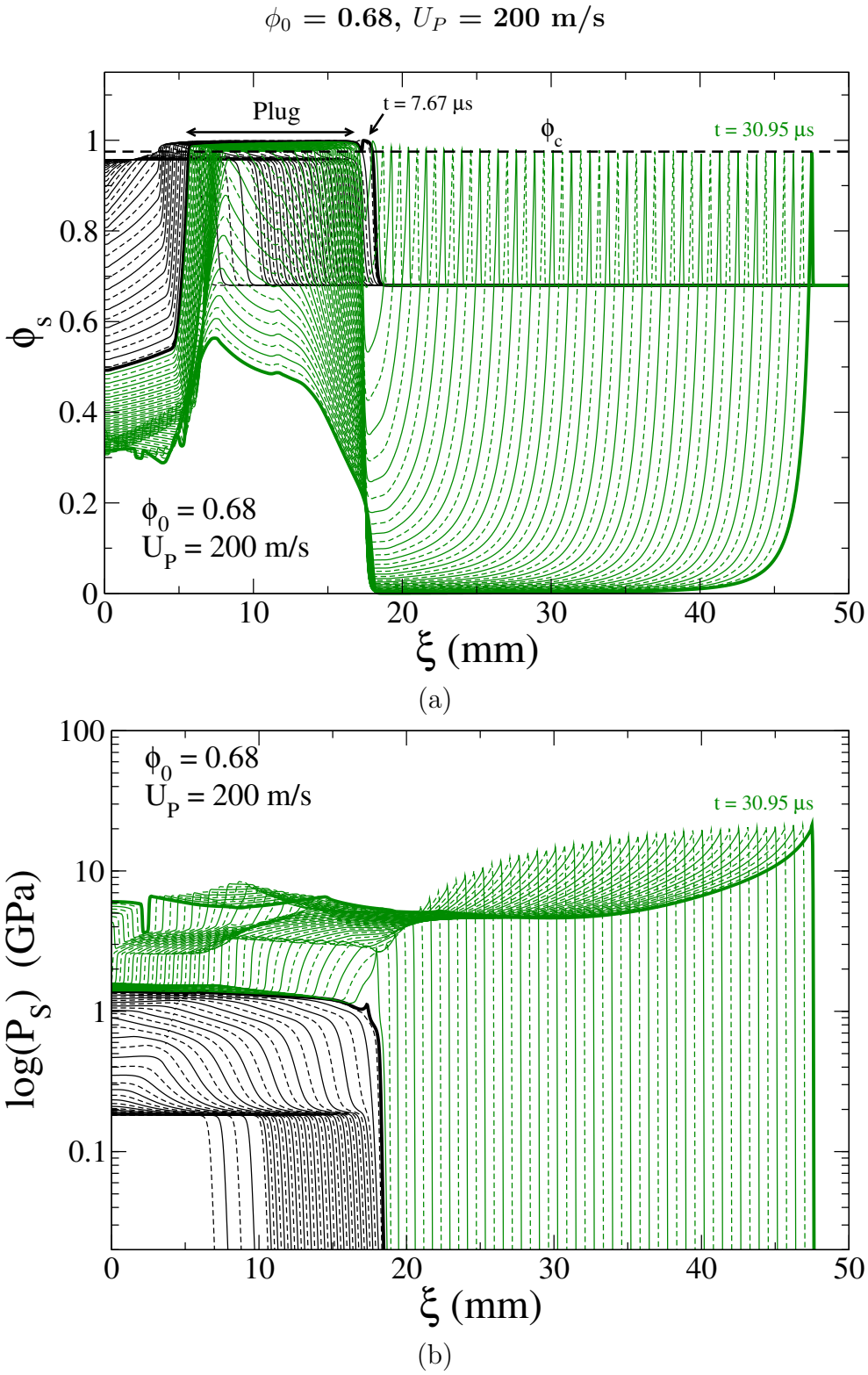

Figure 5.33: Predicted spatial variation in (a) solid/explosive volume fraction ϕ_s; (b) solid phase pressure P_s; for $\phi_0 = 0.68$ and $U_P = 200$ m/s.

$\phi_0 = 0.68$, $U_P = 200$ m/s

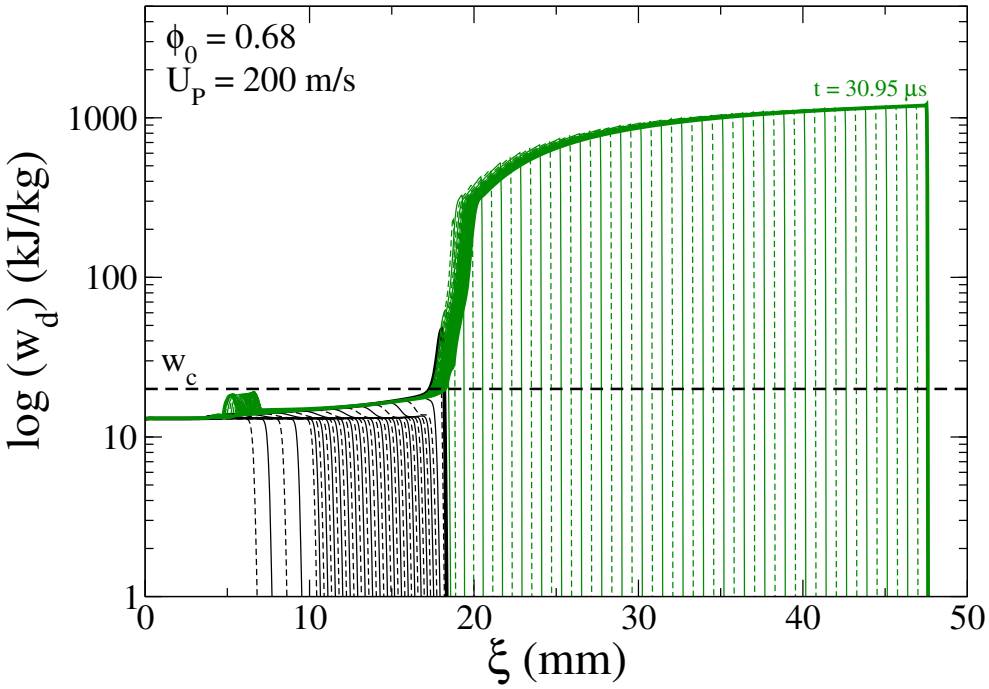

(a)

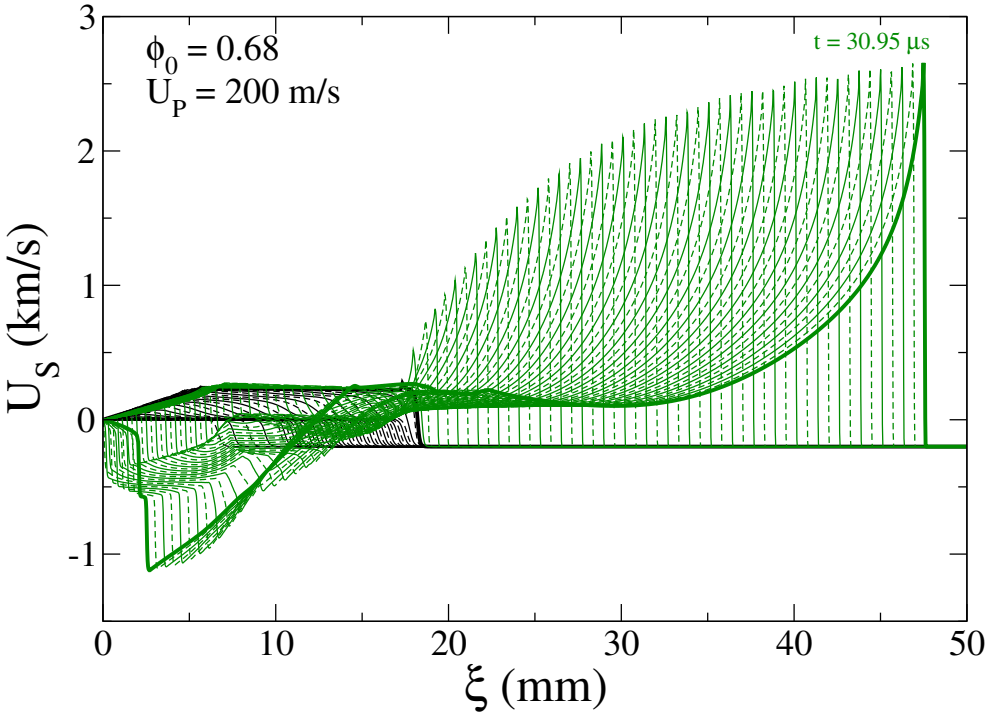

(b)

Figure 5.34: Predicted spatial variation in (a) dissipative compaction work w_d and (b) solid phase particle velocity U_s; for $\phi_0 = 0.68$ and $U_P = 200$ m/s.

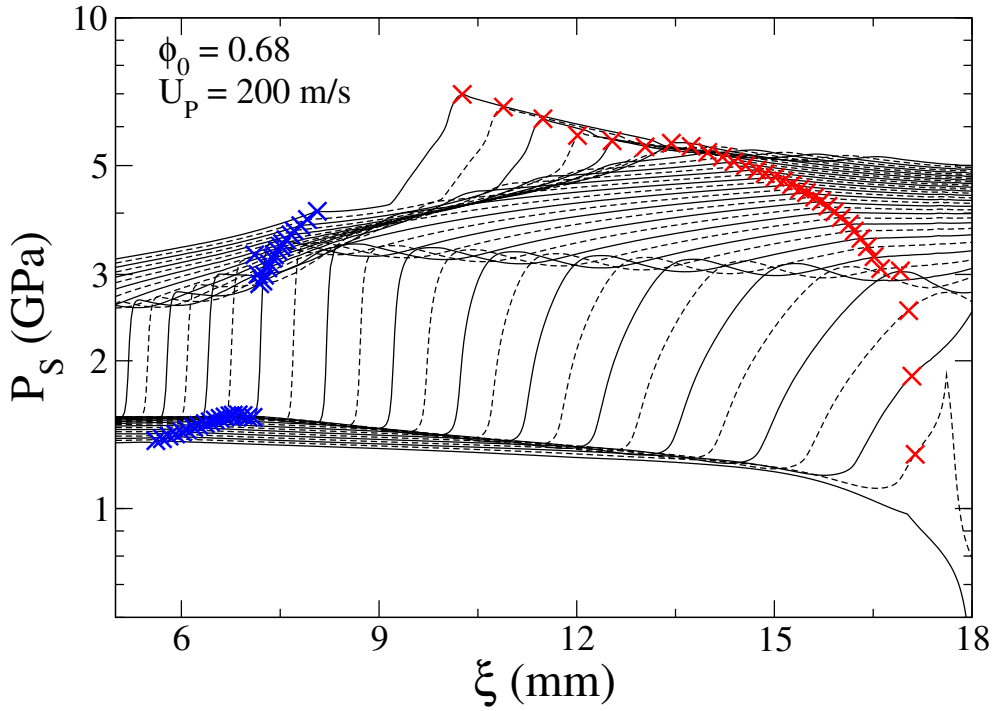

(a)

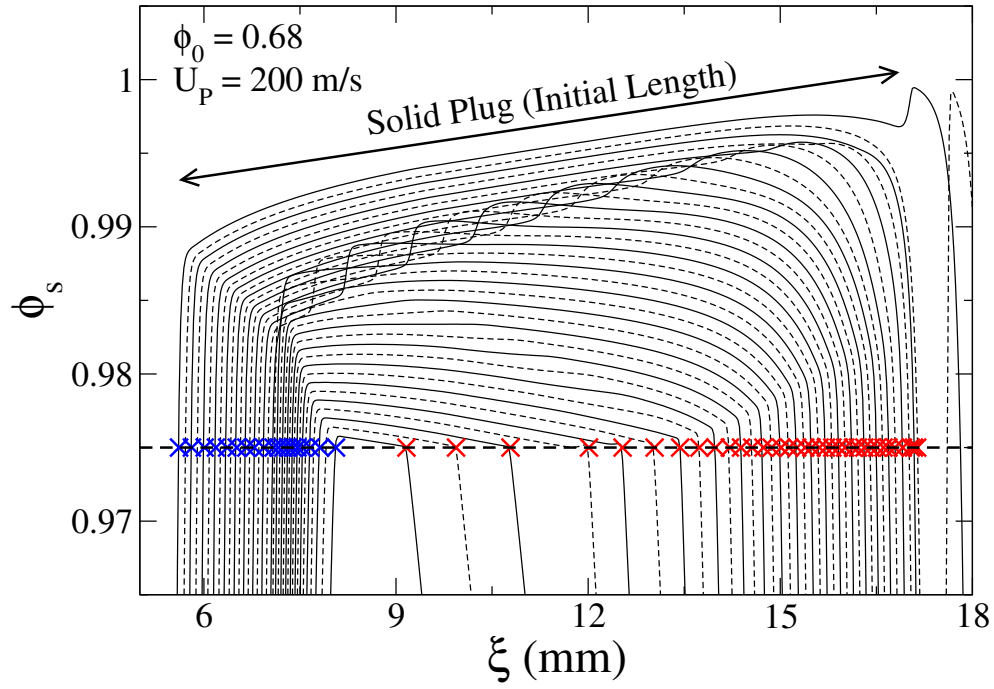

(b)

Figure 5.35: Magnified view of (a) solid/explosive volume fraction ϕ_s; (b) solid pressure P_s with position; and (c) solid/explosive volume fraction contours; within the "solid-plug" region for $\phi_0 = 0.68$ and $U_P = 200$ m/s. Blue and Red X point markers in (a) and (b) indicate the burn trajectories at the back and front end of the plug, respectively.

vigorous burn is predicted to occur within the compacted region after a short ignition delay following shock passage. Again, as $w_d \to w_c$, then α quickly increases resulting in hot-spot facilitated burn which significantly intensifies shock dissipation. A forward propagating reactive shock and backward propagating weak shock quickly develops in the material due to the SDT-like event. The reactive shock quickly transitions to detonation, whereas the weak shock slowly increases in strength until it abruptly transitions into a strong reactive compression wave (R). The overdriven detonation subsequently propagates into the ambient material as it relaxes to a CJ detonation. This case also involves the formation of the plug but the rapid onset of vigorous burn is predicted to occur only when the secondary wave overtakes the lead wave. This simulation demonstrates a transition mechanism that is typically referred to as ignition controlled and the CJ detonation predicted a compaction-led spatial structure.

- **Parametric Analysis**

For direct comparison, simulation predictions for material having $\phi_0 = 0.77$ and $\phi_0 = 0.83$ for a piston speed $U_P = 200$ m/s is given here. Figure 5.36(a-b) and 5.37(a-b) gives comparative predictions of solid volume fraction (ϕ_s) contours and bulk pressure contours in the $\tau - \xi$ characteristic plane, respectively. Figure 5.38, 5.39 and 5.40 gives the comparative piston-attached spatial profiles for ϕ_s, P_s, and w_d, respectively, as the solution evolves into a steady detonation. Figuress 5.41 and 5.42 give the comparative piston-attached magnified view of spatial variation of ϕ_s and P_s, respectively within the plug region. For both simulations, a resolution of $\Delta\xi = 12.5$ μm was used to track the solution as it evolved into a steady detonation.

For $\phi_0 = 0.77$, as seen in Figs. 5.36(a) and 5.37(a), the fully developed primary compaction wave, labelled **c**, reduces the porosity within the material and propagates at about 705 m/s, corresponding to a input shock pressure of 0.27 GPa. The predicted solid volume fraction in the compacted region is $\phi_s = 0.97$ and the dissipative compaction work is about $w_d = 10.7$ kJ/kg. Following impact, the compaction wave propagates a relatively

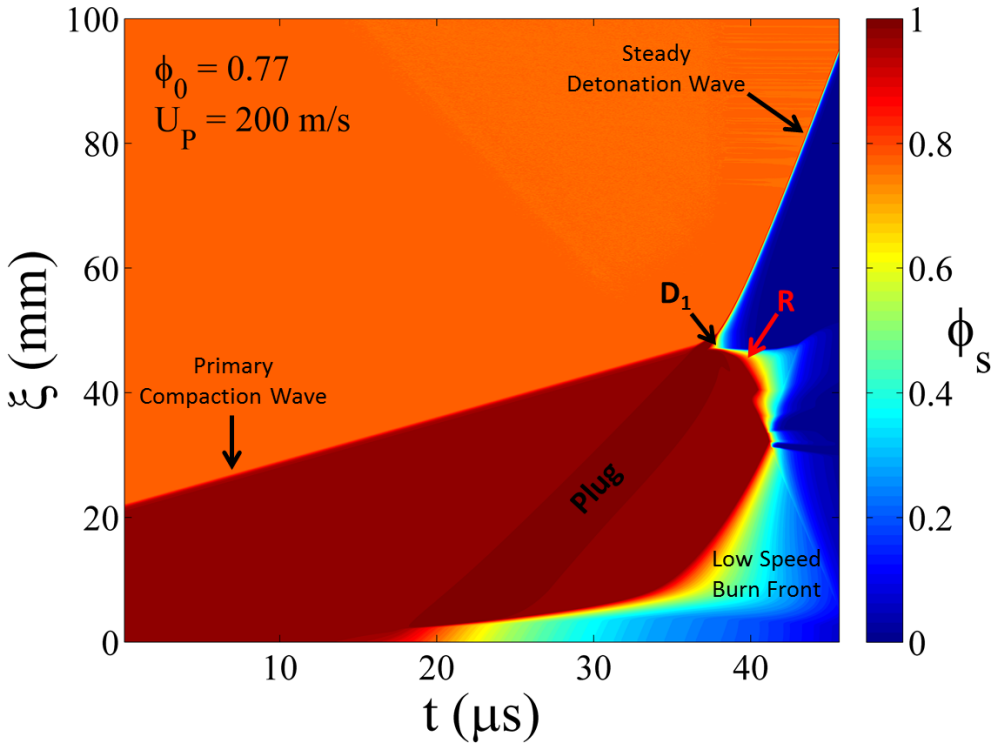

(a)

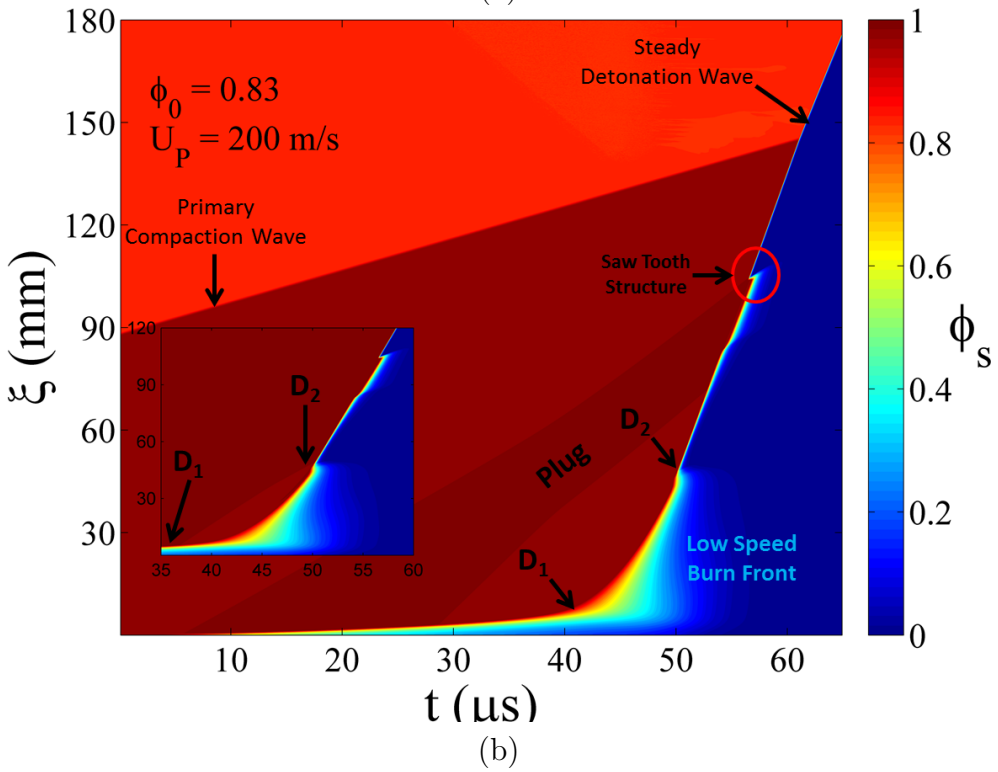

(b)

Figure 5.36: Predicted solid/explosive volume fraction contours in the generic $t-\xi$ diagram showing the predicted trajectories of compaction wave **c**, ignition wave **b**, the rearward plug boundary **vp**, strong shock **S**, forward propagating detonation wave **D**, and rearward propagating spontaneous reaction wave **R**; for (a) $\phi_0 = 0.77$ and $U_P = 200$ m/s; (b) $\phi_0 = 0.83$ and $U_P = 200$ m/s.

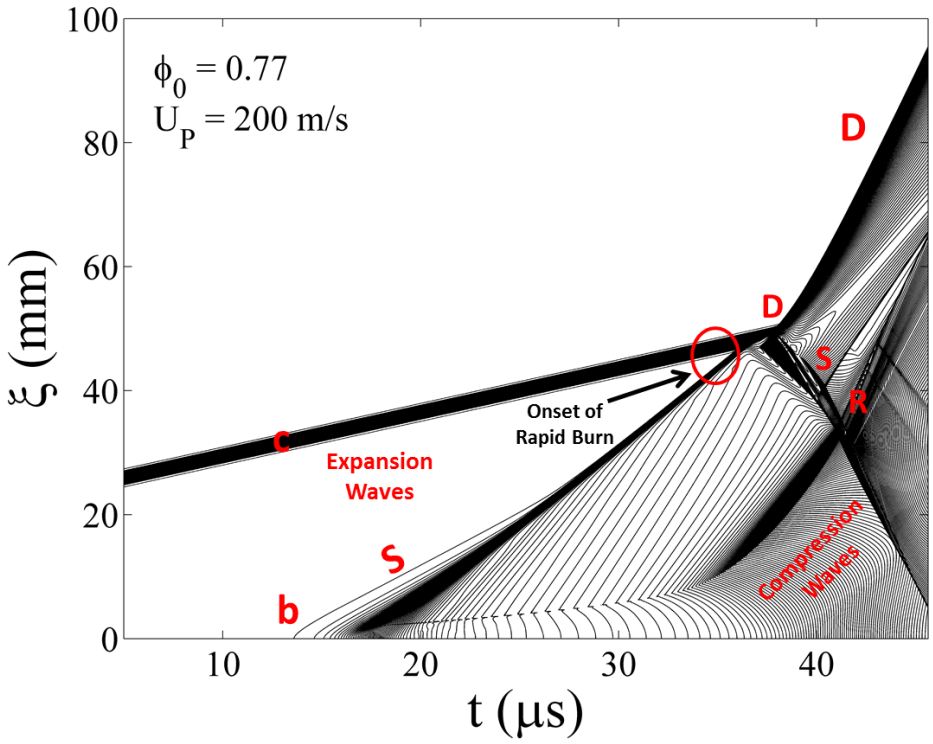

(a)

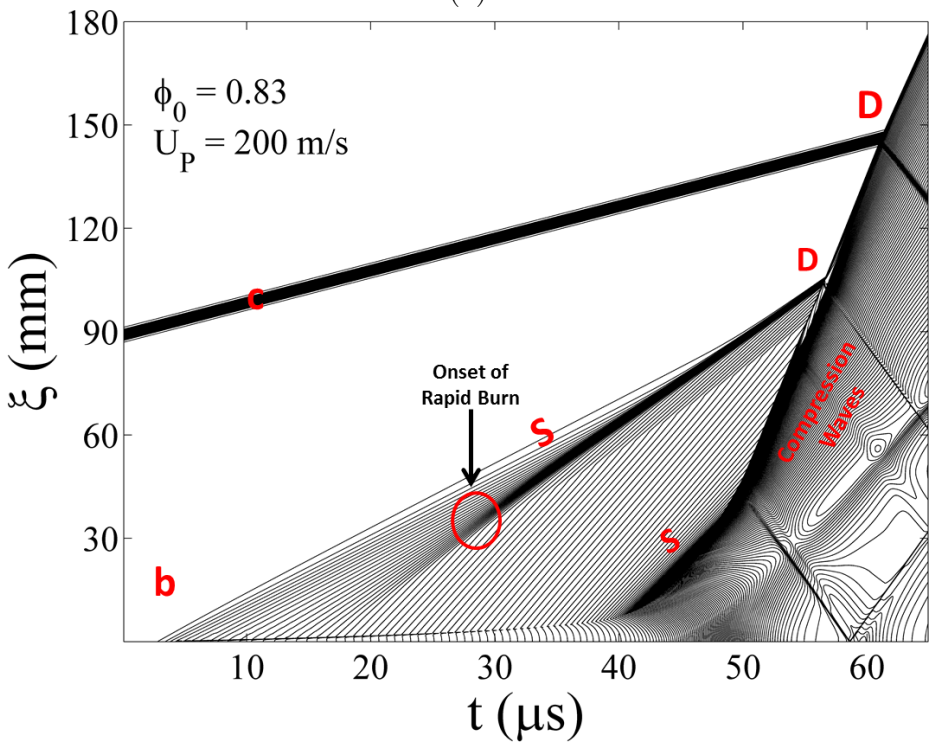

(b)

Figure 5.37: Predicted bulk pressure contours in the generic $t - \xi$ diagram showing the predicted trajectories of compaction wave **c**, ignition wave **b**, the rearward plug boundary **vp**, strong shock **S**, forward propagating detonation wave **D**, and rearward propagating spontaneous reaction wave **R**; for (a) $\phi_0 = 0.77$ and $U_P = 200$ m/s; (b) $\phi_0 = 0.83$ and $U_P = 200$ m/s.

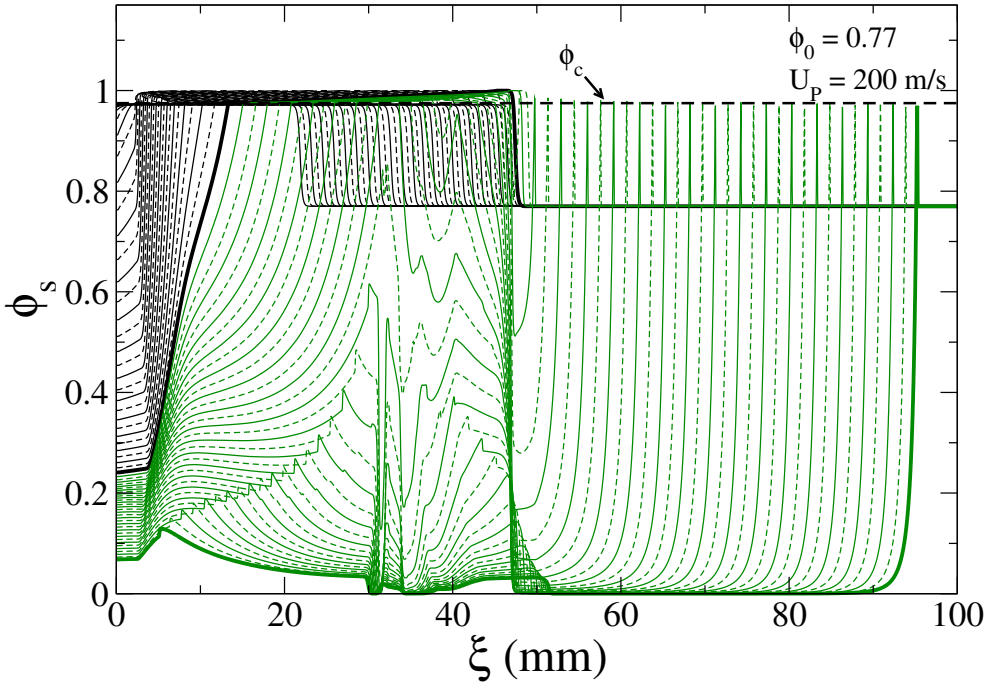

(a)

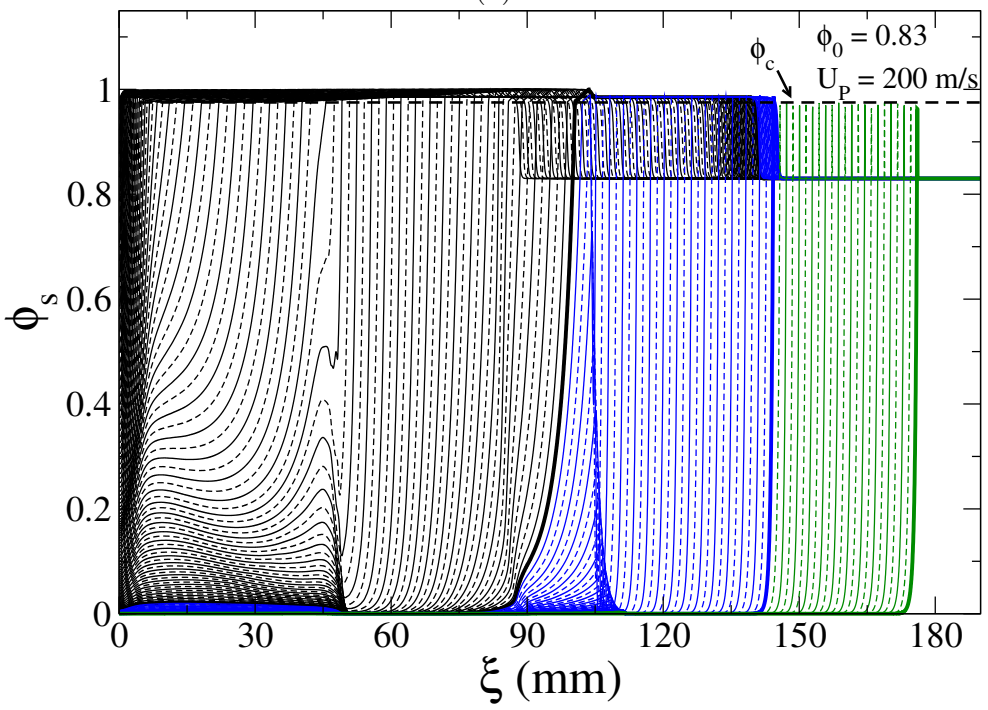

(b)

Figure 5.38: Predicted spatial variation in solid/explosive volume fraction ϕ_s for (a)$\phi_0 = 0.77$ and; (b) $\phi_0 = 0.83$, respectively for $U_P = 200$ m/s.

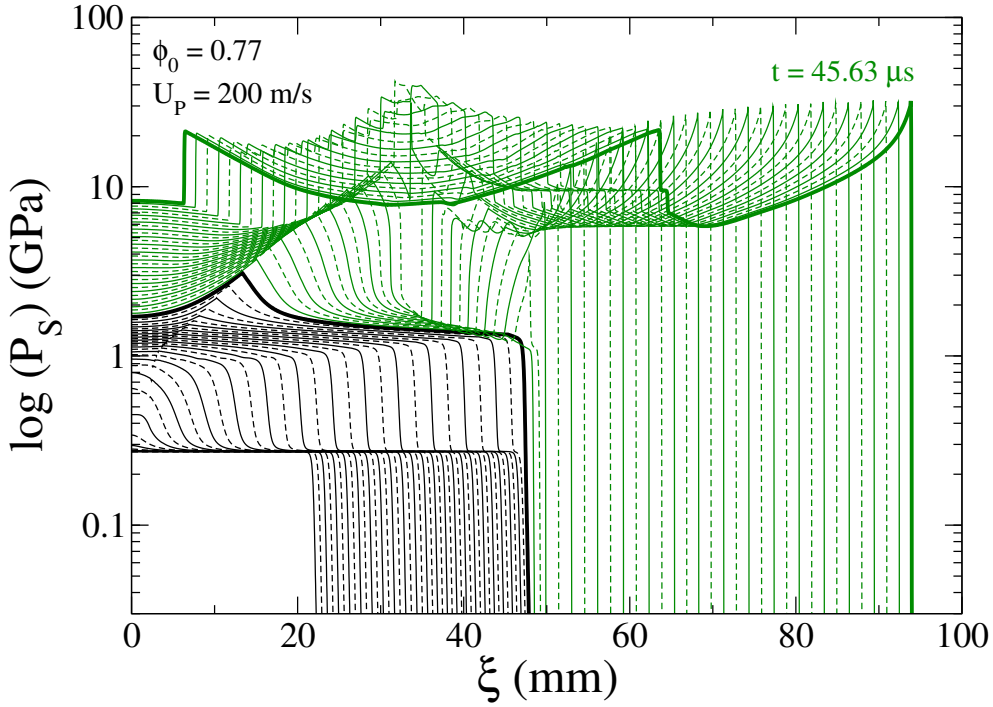

(a)

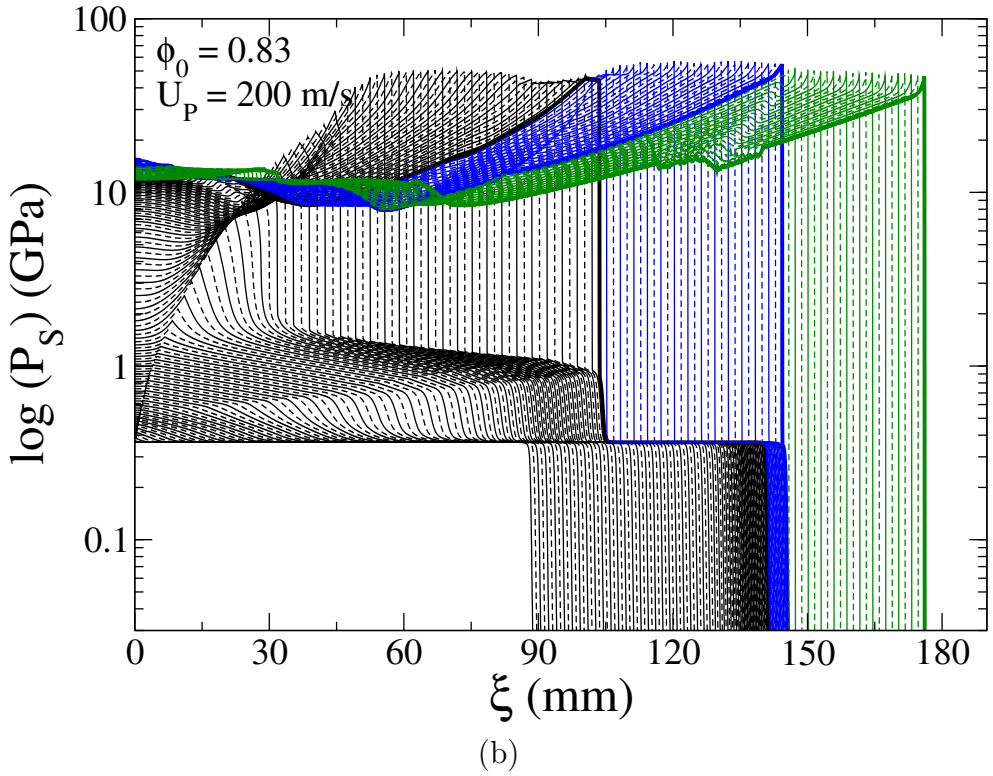

(b)

Figure 5.39: Predicted spatial variation in solid/explosive phase pressure P_s for (a)$\phi_0 = 0.77$ and; (b) $\phi_0 = 0.83$, respectively for $U_P = 200$ m/s.

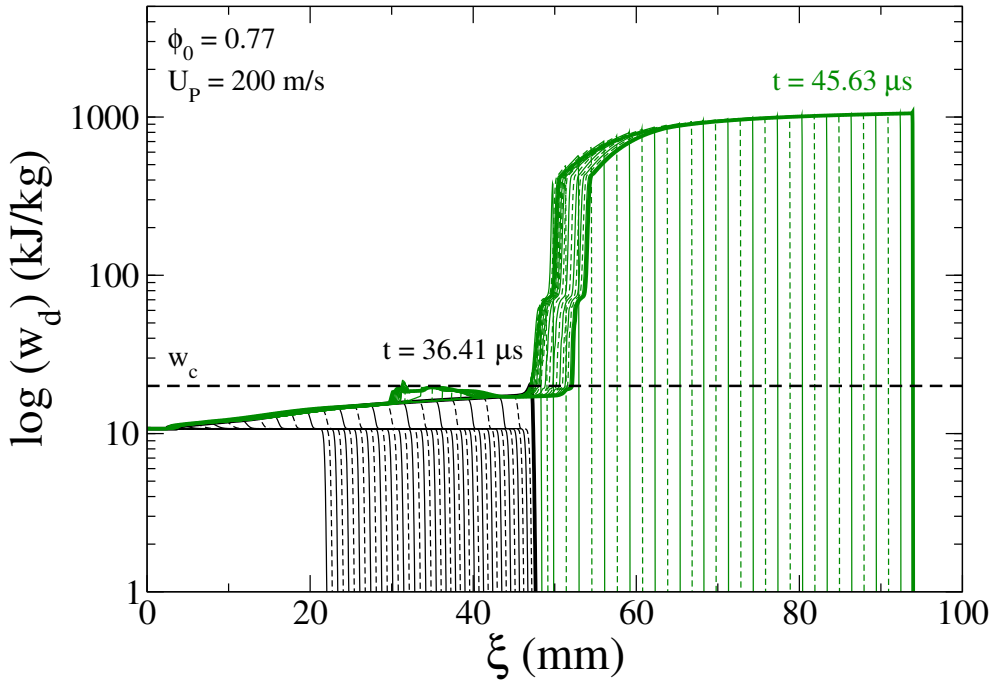

(a)

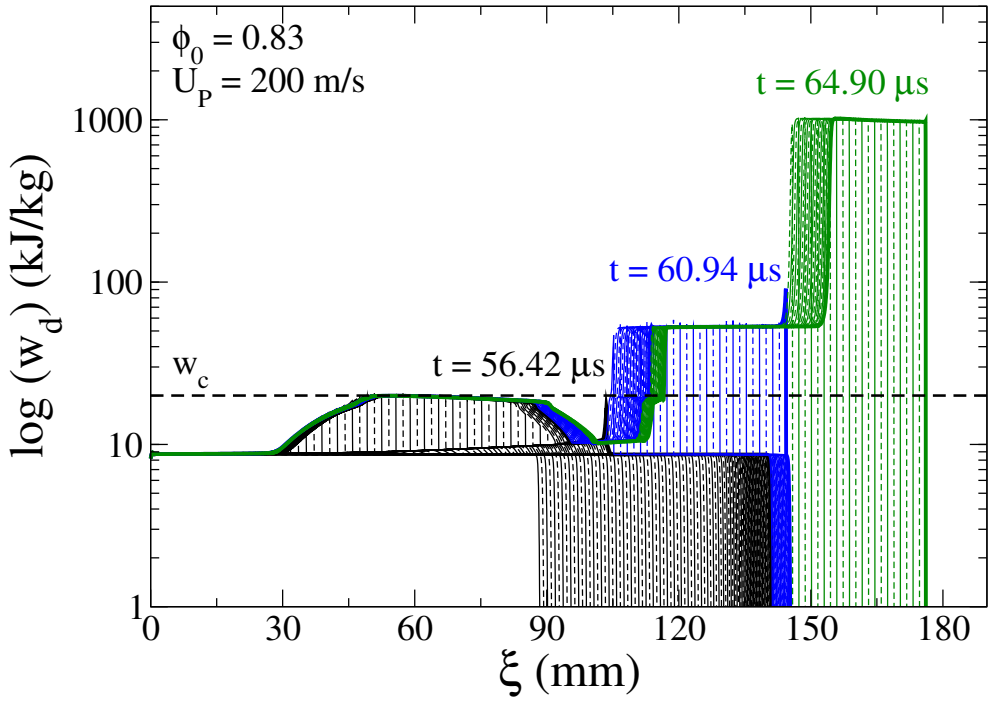

(b)

Figure 5.40: Predicted spatial variation in solid/explosive dissipative compaction work w_d for (a)$\phi_0 = 0.77$ and; (b) $\phi_0 = 0.83$, respectively for $U_P = 200$ m/s.

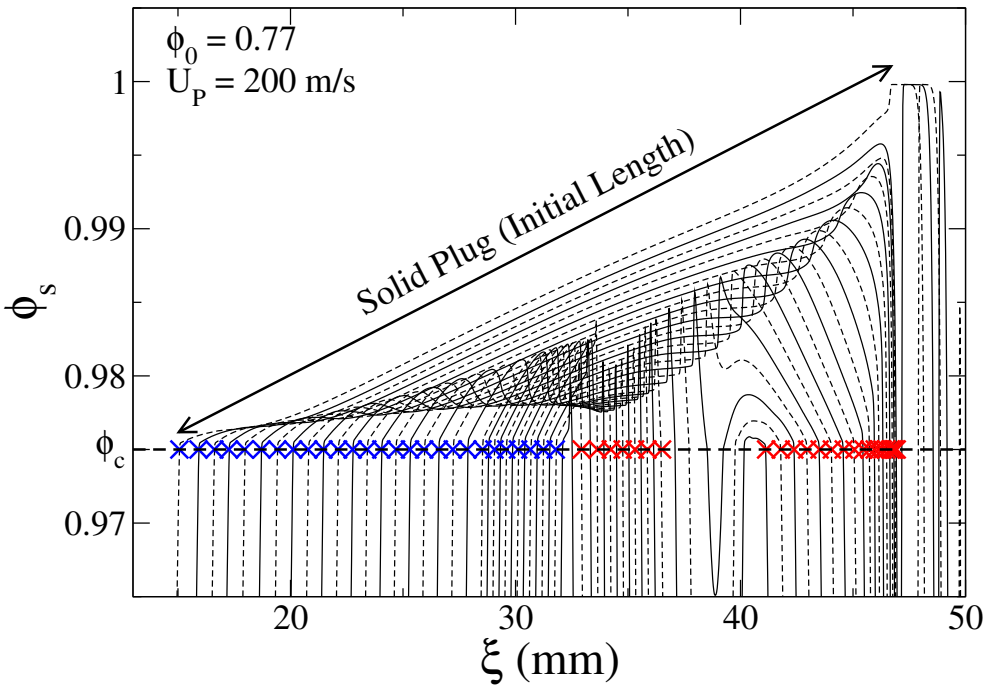

(a)

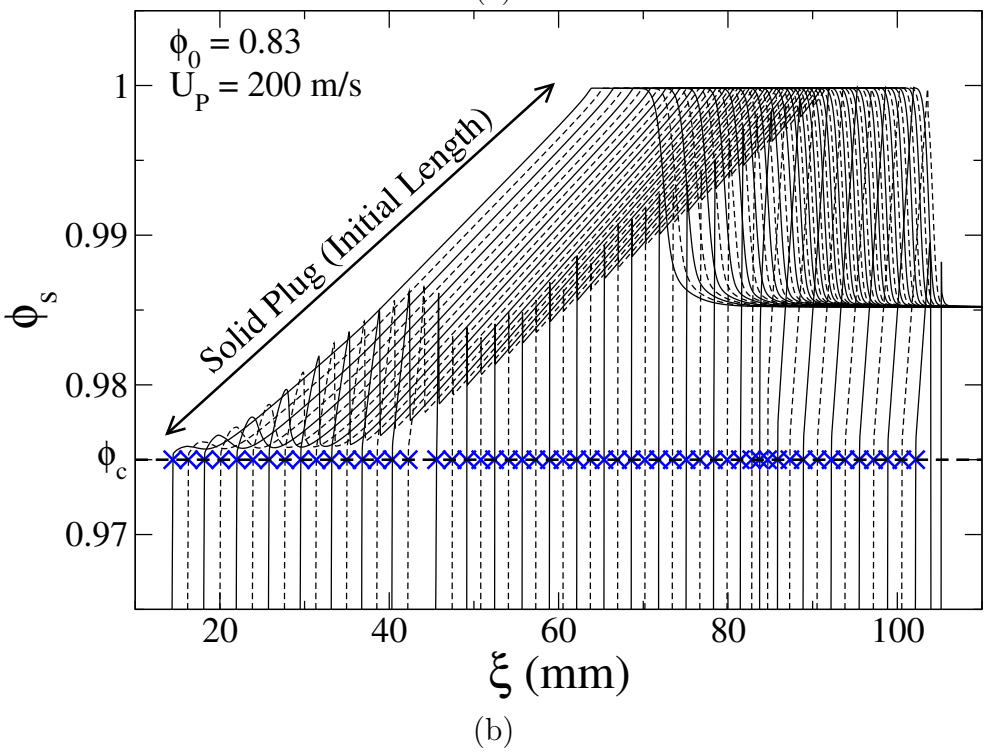

(b)

Figure 5.41: Magnified view of predicted spatial variation in explosive/solid volume fraction within the plug region for (a) $\phi_0 = 0.77$ and $U_P = 200$ m/s; (b) $\phi_0 = 0.83$ and $U_P = 200$ m/s. Blue and Red X point markers indicate the burn trajectory at the back and front end of the plug, respectively.

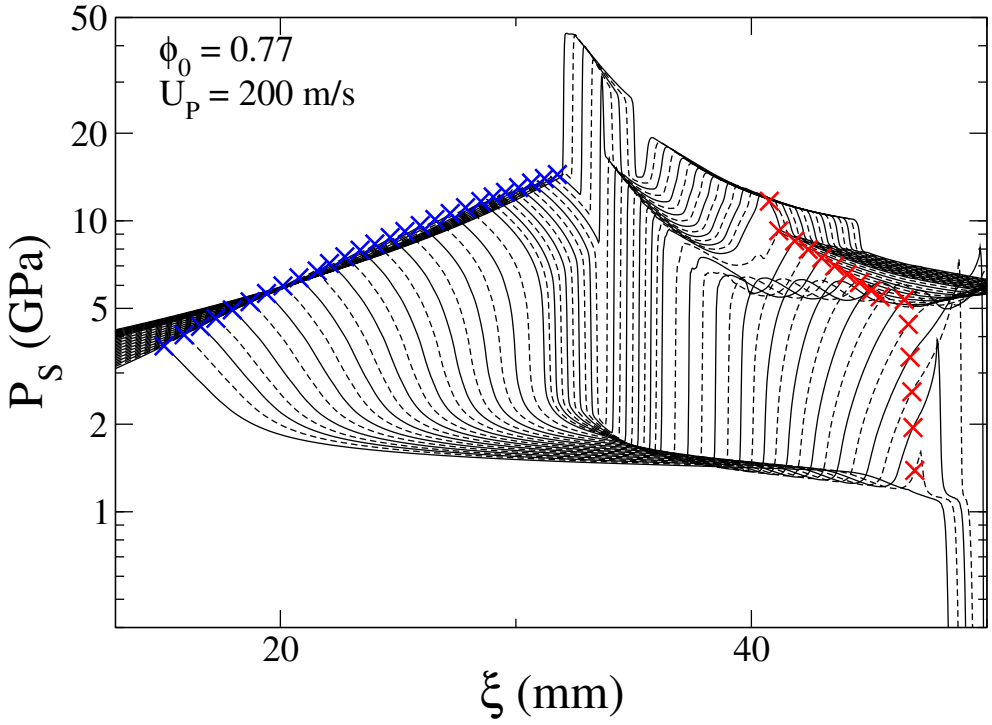

(a)

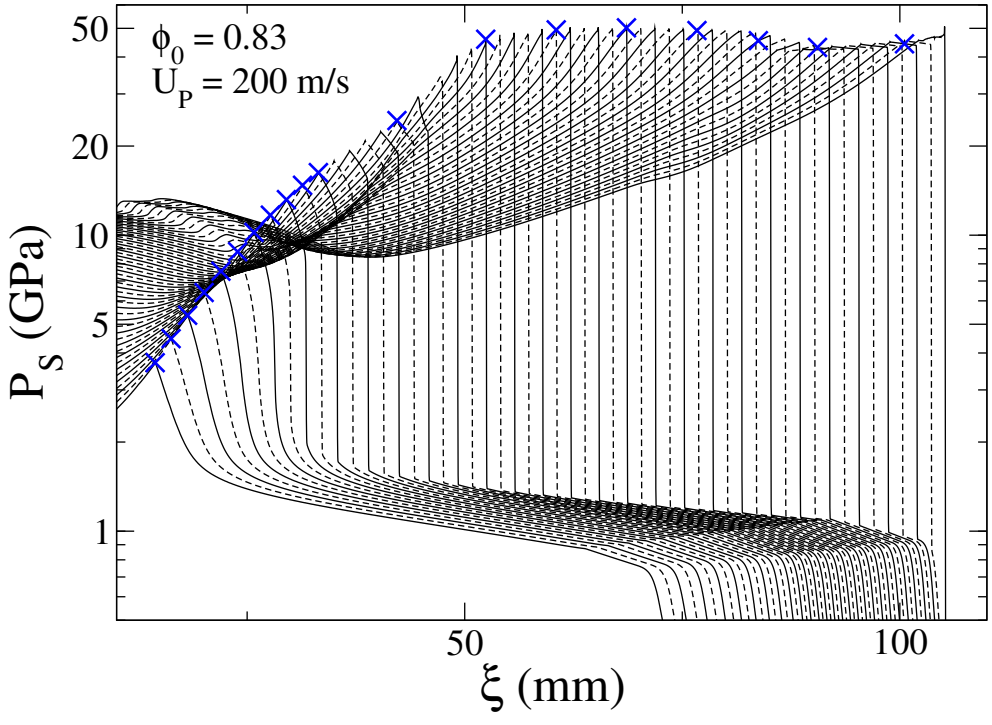

(b)

Figure 5.42: Magnified view of predicted spatial variation in bulk pressure within the plug region for (a) $\phi_0 = 0.77$ and $U_P = 200$ m/s; (b) $\phi_0 = 0.83$ and $U_P = 200$ m/s. Blue and Red X point markers indicate the burn trajectory at the back and front end of the plug, respectively.

long distance into the ambient material prior to onset of ignition near the piston surface at approximately $t_{ign} = 39$ μs. The predicted dissipative compaction work w_d behind the primary compaction wave for this case is lower than the threshold w_c, this results in initially "low-speed" regressive burn.

Subsequently, regressive burn near the piston surface drives the formation of a secondary compaction wave, which eliminates the residual porosity resulting in the formation of a solid-plug, highlighted in Figs. 5.36(a). The compaction dissipation associated with the secondary compaction wave is very minimal due very little porosity (about 3%) left behind by the lead wave as indicated in Fig. 5.38(a) and 5.40(a). As the secondary wave overtakes the lead wave the strength of the burn supported increases, as indicated by increase in pressure and dissipative compaction work in Figs 5.39(a) and 5.40(a). As $w_d \rightarrow w_c$, α quickly increases resulting in hot-spot facilitated burn which significantly increases secondary shock dissipation to $w_d > 200$ kJ/kg. The rapid onset of vigorous burn results in a thermal-explosion-like (or SDT-like) event which produces a forward propagating reactive shock and a backward propagating weak shock. The forward propagating reactive shock then quickly develops becoming overdriven relative to the ambient material. The overdriven detonation subsequently overtakes the primary compaction wave propagates into the ambient material as it relaxes to a CJ detonation. Thus the $U_P = 200$ m/s case also involves the formation of the plug but the rapid onset of vigorous burn is predicted to occur only when the secondary wave overtakes the lead wave. This case demonstrate a transition mechanism that is typically referred to as ignition controlled.

As seen in Figs. 5.41$-$5.41(a), the backward propagating weak shock propagates into the plug and the low-speed burn-front simultaneously propagates forwards into the plug due to additional compaction dissipation in the plug region. Subsequently the two shock interact at the location R causing a rapid increase in pressure and shock dissipation. This increase in pressure leads to enhanced burn rate and significant gas production leading to complete consumption of the plug. Additional pockets of burn are predicted to occur before

the shocks interact at the region R due to the dissipative compaction work w_d crossing the threshold w_c barrier at certain explosive material points. Though not shown here, during transition to detonation, the solid shock is accelerated ahead of the gas shock before waves approach steady speed for both cases. Since the solid shock accelerates ahead of the gas shock, the CJ detonation predicted a compaction-led spatial structure.

For $\phi_0 = 0.83$, as seen in Figs. 5.36(b) and 5.37(b), the fully developed primary compaction wave, labelled **c**, reduces the porosity within the material and propagates at about 935 m/s, corresponding to a input shock pressure of 0.36 GPa. The predicted solid volume fraction in the compacted region is $\phi_s = 0.985$ and the dissipative compaction work is about $w_d = 8.65$ kJ/kg. Following impact, the compaction wave propagates a relatively long distance into the ambient material prior to onset of ignition near the piston surface at approximately $t_{ign} = 94$ μs.

This case potentially exposes a limitation of the burn model developed in this study. The predicted solid volume fraction behind the primary compaction wave in this case is $\phi_s = 0.985$ and the chosen solid volume fraction threshold that accounts for effects of bed permeability on the burn is $\phi_c = 0.975$. Within the context of this model, since $\phi_s > \phi_c$, it results in initially minimal burn ($\alpha \to \alpha_1$). This results in very high induction period associated with the onset of visible burn. However, DDT experiments indicate that for initial conditions prescribed for this case, the induction times follow both quality and quantity as seen for other simulations presented in this study. To overcome this deficiency associated with model development, the volumetric burn surface area prefactor is artificially set to $\alpha = \alpha_0 > \alpha_1$ (prefactor for "low-speed" regressive burn) for about two particle diameters in the vicinity of the piston surface. One plausible physical justification for doing this is to account for frictional heating at the piston-particles interface, and particle-particle interface between neighboring explosive particles that can give rise to additional heating thereby increasing the burn rate. Though speculative, this technique helps maintain quality and quantity as other simulations and warrants additional study. This increase in burn

rate reduces the induction period and the distance-to-detonation and time-to-detonation plots agree with experiments (shown later).

Following the above discussion, induced regressive burn near the piston surface drives the formation of a secondary compaction wave that eliminates the residual porosity resulting in the formation of a solid-plug. Again, the secondary compaction wave causes lower dissipation than that for $\phi_0 = 0.77$ due to slightly lower residual porosity behind the primary compaction wave. The rearward burn-front highlighted with blue X point-markers in Figs. 5.41(b) and 5.42(b) is continuously pushed by the gas produced due to material burning next to the piston-surface and the back-end of the plug. This gas pressurization causes a shock to develop in the material ahead of it due to low permeability of the compacted material ahead of it. The strength of this burn supported wave increase in time to form a strong shock, as indicated by increase in pressure and dissipative compaction work in Figs. 5.39(b) and 5.40(b), respectively. As $w_d \rightarrow w_c$, α quickly increases resulting in hot-spot facilitated burn which significantly increases secondary shock dissipation to $w_d > 200$ kJ/kg. For brevity, the remainder of the transition process is similar to that for $\phi_0 = 0.77$. Though not shown here, during transition to detonation, the solid shock is accelerated ahead of the gas shock before waves approach steady speed for both cases. Since the solid shock accelerates ahead of the gas shock, the CJ detonation predicted a compaction-led spatial structure. This case also demonstrate a transition mechanism that is referred to as ignition controlled.

The simulations discussed Sections 5.2.2−5.2.4 illustrate different modes of detonation transition and can be summarized in Fig. 5.43 where the predicted variation of equilibrium end-state quantities of dissipative compaction work (w_d) and solid volume fraction (ϕ_s) for different piston impact speeds (U_P) are plotted. For weak-shock initiation, the primary compaction shock has insufficient strength to directly trigger hot-spot facilitated burn; consequently, a combustion-supported secondary compaction shock forms that accelerates and strengthens to the point of triggering such a burn. This complex transition mecha-

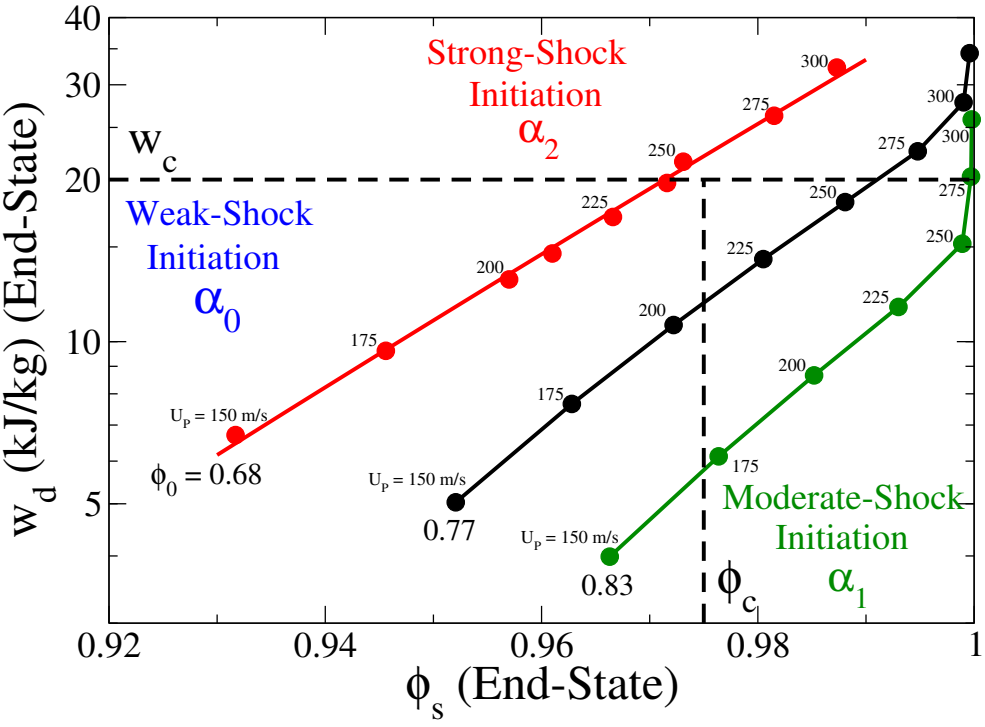

Figure 5.43: Predicted variation of equilibrium end-state quantities of dissipative compaction work w_d with solid volume fraction ϕ_s.

nism is referred to as ignition controlled. For strong-shock initiation, the primary shock is sufficiently strong to eliminate porosity and directly trigger hot-spot facilitated burn. In this case, the transition mechanism is largely continuous, with the ignition induction time comparable to that required for transition following ignition, which is referred to as burn controlled. For moderate-shock initiation, represents a intermediate transition mechanism, the primary compaction shock has insufficient strength to directly trigger hot-spot facilitated burn, but it is strong enough to eliminate substantial porosity. Therefore, a secondary shock forms but the dissipation is only sufficient to achieve hot-spot facilitated burn when the secondary shock overtakes the primary shock. The three modes are highlighted in Fig. 5.43.

5.3 Pop-Plot

The distance-to-detonation versus initial shock pressure is a key characterization of shock initiation in granular explosives. Ramsay and Popolato [65] first observed that on a

log-log scale the data is well represented by a straight line. This representation of shock initiation date is known as a Pop-Plot. To the very minimum, reactive ignition and burn models developed for granular explosives must reproduce the experimental Pop-Plot data to accurately predict DDT and SDT phenomena.

Figure 5.44 illustrates two techniques used to establish the time and run distance to detonation in the ξ-t plane for the cases discussed above. In Technique $-$ 1, shown in Fig. 5.44(a), the transition point located at ξ^* and t^*, is uniquely determined for a given simulation as the intersection of extrapolated steady input shock and detonation trajectories. Once identified, the run distance in the piston frame is expressed in the laboratory frame by $x^* = \xi^* + U_P t^*$. This technique is analogous to that used by Dick [141] to identify these quantities based on transit time measurements taken at a number of porous HMX sample thicknesses for a given input pressure. In this technique, the transition point defined here is based on the break-out of detonation into the ambient material and does not explicitly account for the initial onset of detonation that occurs within material compacted by the lead shock at lower input pressures. For the case shown in Fig. 5.10, the initial onset of detonation within the compacted material would result in a marginally smaller run to detonation distance than estimated based on wave break-out into the ambient material. In Technique $-$ 2, shown in Fig. 5.44(b), allows for determining the detonation transition point more accurately in that the transition point within the compacted region and transition point based on break-out can be identified using a single contour plot for solid volume fraction. A more appreciable difference in run distances would result as input shock pressure is further reduced and well-defined transitions to steady detonation are predicted to occur within shock compacted material.

Figure 5.45 summarizes the predicted variation in t^* and x^* with input shock pressure for granular HMX having $\overline{\phi}_0 = 0.68$, 0.77 and 0.83. Also shown in the figure are initiation time and run distance data reported in the literature for porous HMX having $\overline{\phi}_0 = 0.65$ [5, 67, 140, 141] and $\overline{\phi}_0 = 0.86$ [140]. Though these materials have similar packing densities,

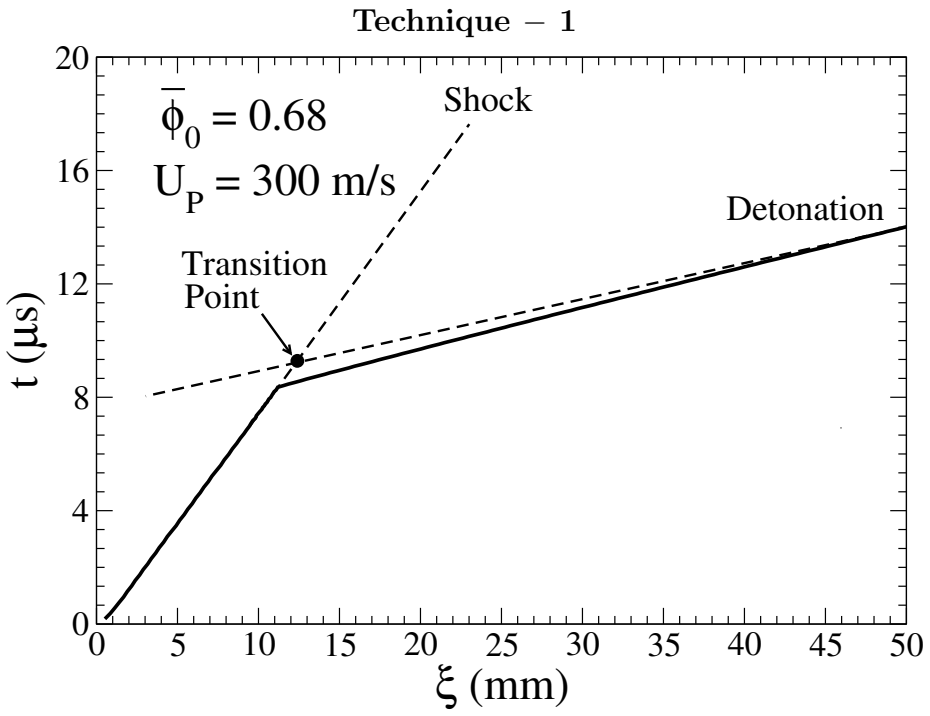

(a)

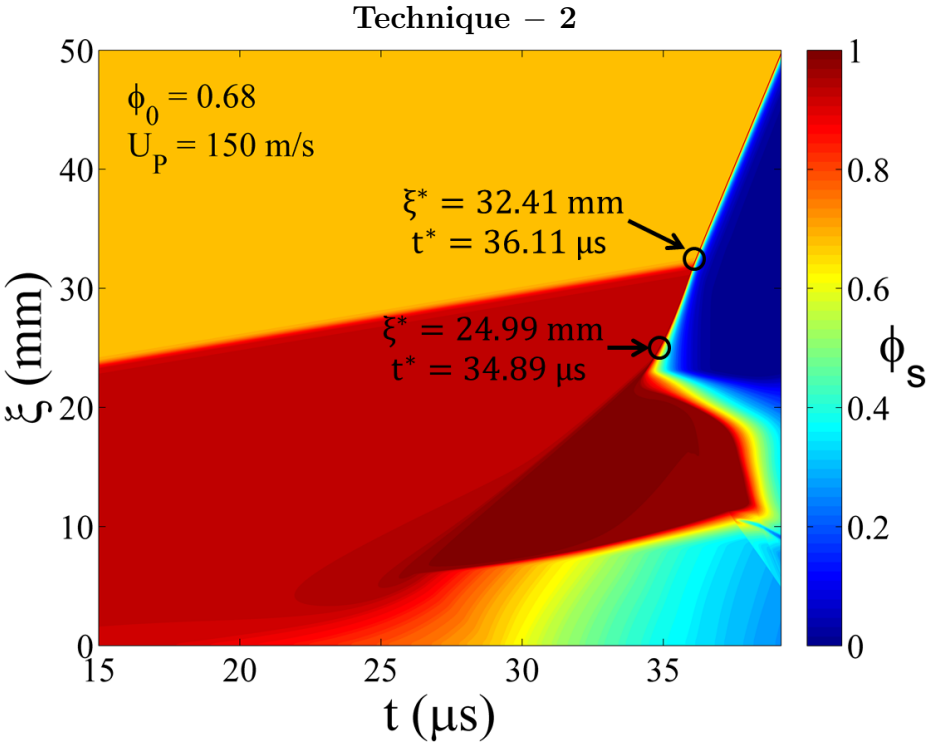

(b)

Figure 5.44: (a) Predicted wave trajectory used to establish the detonation initiation point based on wave-breakout and; (b) Predicted solid volume fraction contours used to establish the detonation initiation point in the compacted region. Position is measured relative to the piston surface. Position in the laboratory frame is obtained using the transformation $x^* = \xi^* + U_p t^*$.

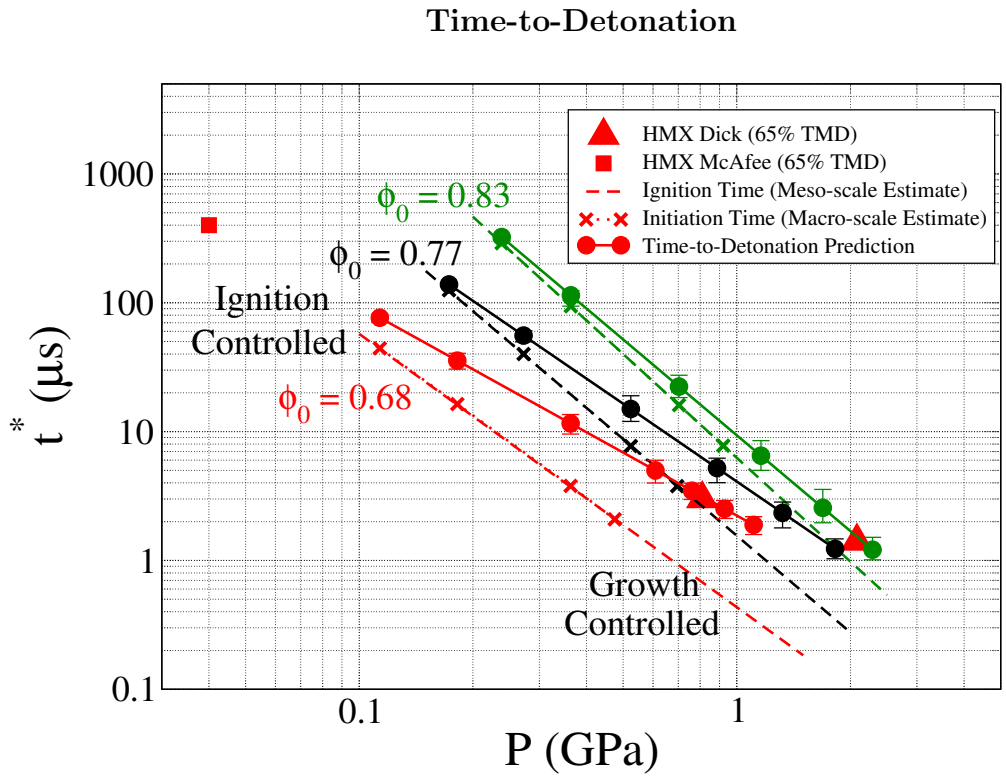

(a)

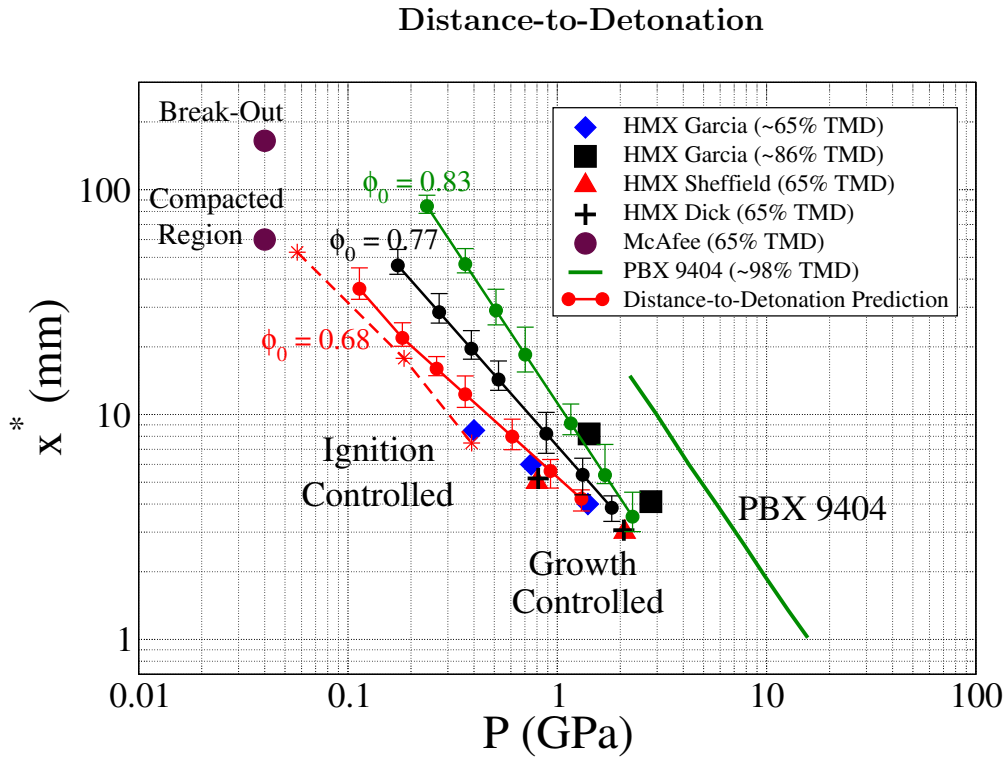

(b)

Figure 5.45: Plots showing the (a) initiation distances, and (b) ignition and initiation times for $\overline{\phi}_0$= 0.68, 0.77 and 0.83. Also shown are data provided in Refs. [5, 67, 140, 141].

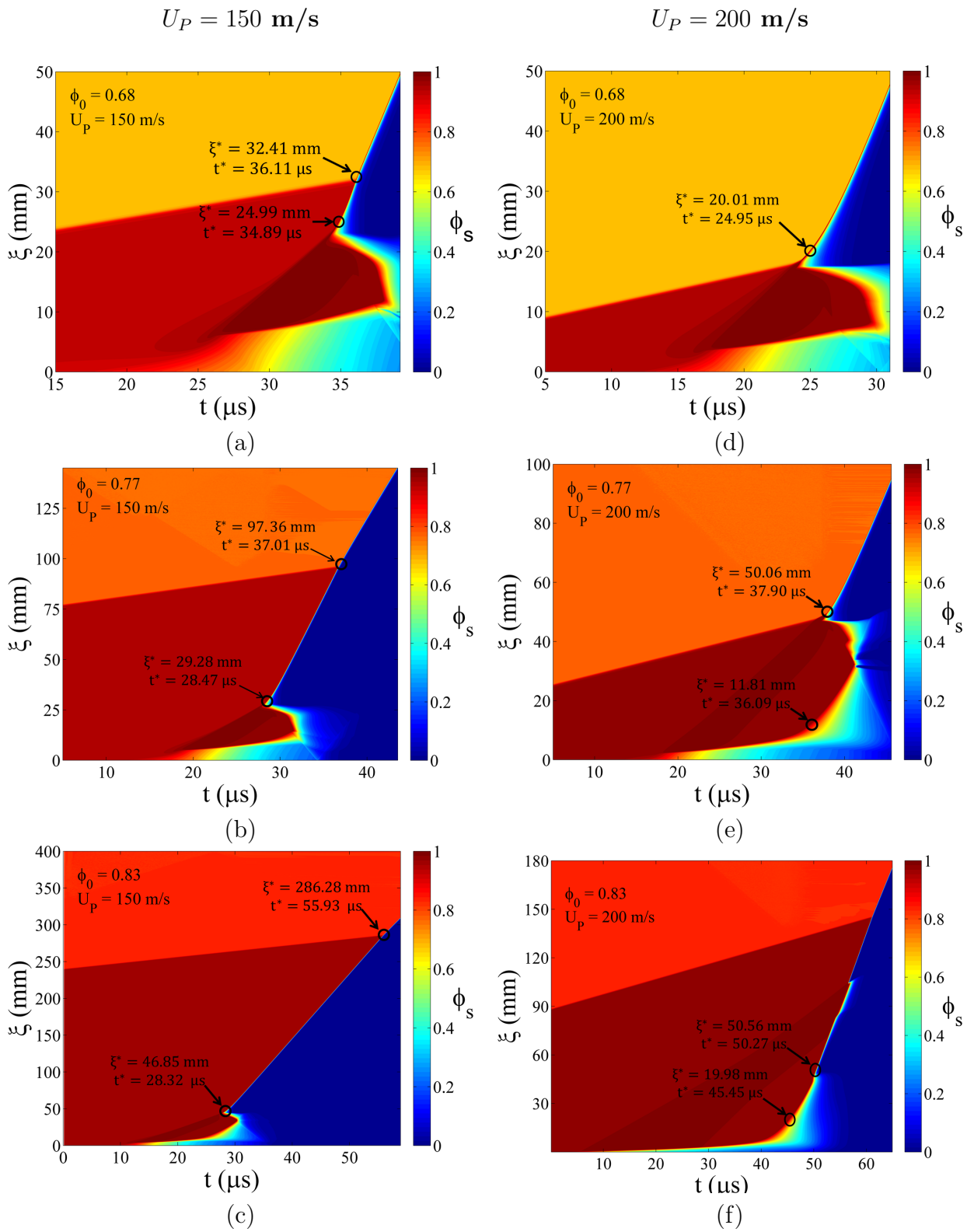

Figure 5.46: Predicted solid volume fraction contours used to establish the detonation initiation point based on wave-breakout and in the compacted region using Technique − 2 for $\phi_0 = 0.68$, 0.77 and 0.83 at U_P =150 and 200 m/s. Position is measured relative to the piston surface. Position in the laboratory frame is obtained using the transformation $x^* = \xi^* + U_p t^*$.

$U_P = 300$ **m/s**

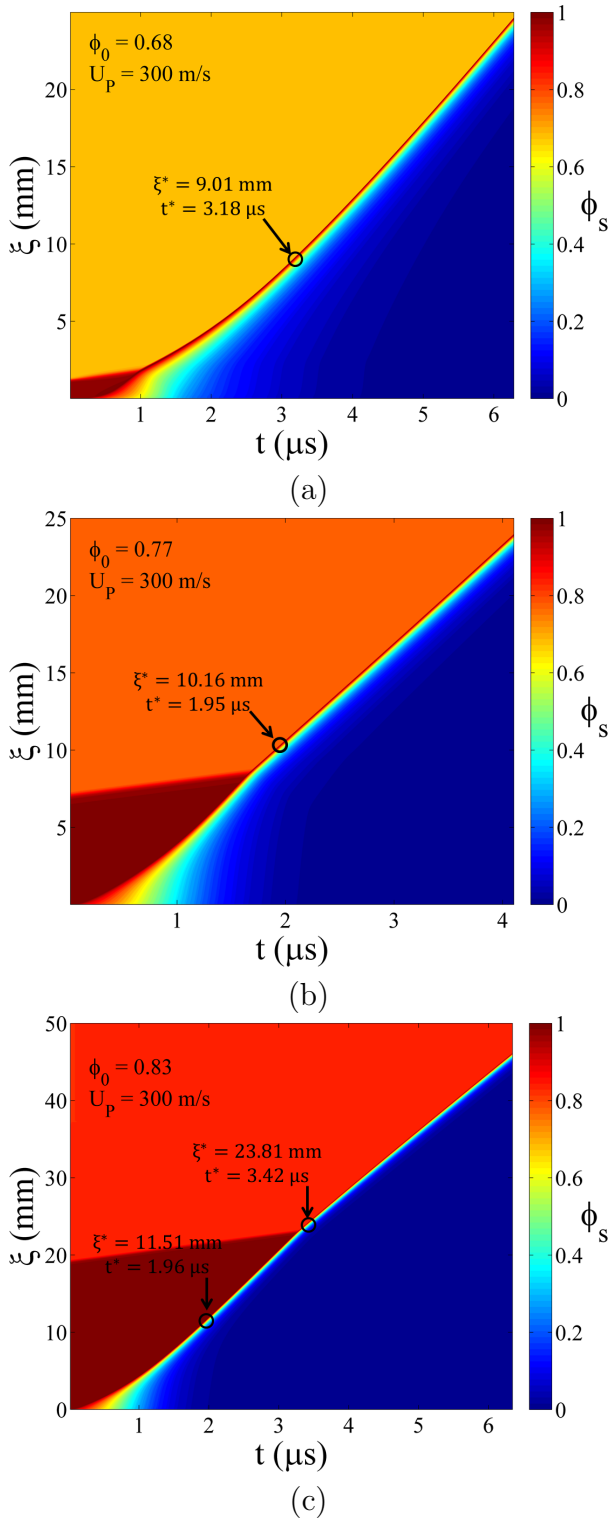

Figure 5.47: Predicted solid volume fraction contours used to establish the detonation initiation point based on wave-breakout and in the compacted region using Technique $-$ 2 for $\phi_0 = 0.68$, 0.77 and 0.83 at $U_P = 300$ m/s. Position is measured relative to the piston surface. Position in the laboratory frame is obtained using the transformation $x^* = \xi^* + U_p t^*$.

the particle size distributions differ; therefore, these results are only intended to illustrate the leading-order effects of packing density on ignition and initiation. As seen in Fig. 5.45(a), the initiation time for each material (X··X curve) is largely controlled by ignition for low shock pressures, where ignition time curves given by Eq. (5.9) are plotted as dashed ($- -$) lines. Although not easily seen in this figure, the ignition curves are slightly offset from those predicted by the continuum theory due to the influence of shock rise time on the implementation of Eq. (5.9). Using the terminology of Sheffield [67], such initiation processes are referred to as ignition controlled. As input pressure increases, predicted initiation times are long compared to ignition times and are controlled by the growth of reaction to detonation; such processes are therefore referred to as growth controlled. Predicted initiation times for $\phi_0 = 0.68$ compare favorably to those measured by Dick [141] for high pressure shocks. The shock pressure required for transition from ignition to growth controlled initiation increases with packing density, and is estimated to be approximately 0.2 GPa for $\phi_0 = 0.68$, 0.3 GPa for $\phi_0 = 0.77$ and 0.4 GPa for $\phi_0 = 0.83$.

Figure 5.45(b) summarizes the corresponding predicted variation in run distance to detonation. A couple observations are noteworthy. First, due to a complex transition mode, ignition controlled initiation is characterized by run distances associated with the evolution of detonation in compacted material behind the lead shock and the break-out of detonation into ambient material. These distances merge with increasing shock pressure as the initiation process becomes growth controlled. Second, slopes of the initiation curves (given by $\partial \log x^* / \partial \log \overline{P}$) slightly decrease with increasing shock pressure for ignition controlled processes, but approach an approximately constant value for growth controlled processes that depends on initial packing denstity ($\overline{\phi}_0$). Higher $\overline{\phi}_0$ results in a marginally higher slope, possibly due to the larger change in effective hot-spot formation rate with pressure as indicated in Fig. 5.3(b). Also shown in Fig. 5.45(b) for perspective is the measured run distance to detonation for the plastic-bonded explosive PBX 9404 (98% TMD HMX) [67]. Relative to $\overline{\phi}_0 = 0.84$, the run distance curve for this material has

higher slope, suggesting a larger variation in hot-spot formation rate with pressure, and requires higher shock pressure for a given run distance; as such, it is considered less sensitive that low density HMX. Predicted distance-to-detonation for $\phi_0 = 0.68$ compare favorably to those measured by Dick [141] for both low pressure and high pressure shocks. The error bars shown in Figs. 5.46 and 5.47 correspond to the error bounds in determining the time and distance to detonation from simulation predictions. To determine the lower bound a metric of 95% CJ detonation pressure was used when the detonation evolves in the compacted region. To determine the upper bound, the wave position and time corresponding to when the secondary wave overtakes the lead wave and relaxes back to CJ detonation pressure was chosen. For ignition controlled initiation, since the two positions are reasonably close an average value for the position and time with error bounds have been plotted. For burn controlled initiation, that corresponds to a continuously accelerating combustion/detonation wave the same metric of 95% CJ detonation pressure is used for the lower bound and for the upper bound the wave position and time corresponding to steady detonation is considered. Figures 5.46 and 5.47 summarize the predicted variation of distance-to-detonation and time-to-detonation for for $\phi_0 = 0.68$, 0.77 and 0.83 at $U_P =$ 150, 200 and 300 m/s using Technique$-$2.

Though the burn model formulated in this study gives transition processes that are commensurate with those observed in experiments, there are minor discrepancy in time to detonation and run distance predicted by these simulations. This deficiency is apparent for both ignition controlled and growth controlled initiation that involves complex temporal and spatial interactions between compaction and combustion waves within the material behind lead shock.

5.4 Parametric Analysis

The predictions presented in Sections 5.2.2 $-$ 5.2.4 highlight the variation in detonation transition mechanism with initial solid volume fraction (ϕ_0) and strength of the incident wave (P_s) that is controlled by varying the piston impact speed (U_P). The burn model

formulated in Section 5.1.2 has been used to predict these mechanisms and is given by

$$\mathcal{C} = -\alpha \left(\frac{\phi_s}{d_0} \right) u_{ref} \rho_s \left(\frac{P_g}{P_{ref}} \right)$$

where the terms $\mathcal{C}$, ϕ_s etc., have their usual meaning. In particular, the volumetric burn surface area prefactor α is given by

$$\alpha = \alpha_0 \left[1 + \frac{1}{\left(1 + \exp\left(\frac{-(w_d - w_c)}{\Delta w}\right)\right)\left(1 + \exp\left(\frac{-(\phi_s - \phi_c)}{\Delta \phi}\right)\right)} \right] - \frac{\alpha_1}{\left(1 + \exp\left(\frac{-(\phi_s - \phi_c)}{\Delta \phi}\right)\right)} + \frac{\alpha_2}{\left(1 + \exp\left(\frac{-(w_d - w_c)}{\Delta w}\right)\right)}$$

where α_0, α_1, α_2, ϕ_c, w_c, Δw and $\Delta \phi$ are numerical constants. Several numerical experiments were performed to calibrate the parameter values to replicate features of the LANL DDT experiment. However, the transition mechanism may be sensitive to the choice of these parameters that control the burn model.

In this Section, predictions are first given that highlight the effect of varying parameters ϕ_c and w_c on the transition mechanism. Δw and $\Delta \phi$ is then varied and the effect on the transition mechanism is highlighted. The parametric analysis is performed on the base line case discussed in Section 5.2.2. Third, issues regarding required resolution for the simulations are addressed. Lastly, simulation predictions for material having $\phi_0 = 0.58$ and $\phi_0 = 0.90$ is discussed as a check for viability of the developed ignition and burn model.

5.4.1 Effect of Varying: ϕ_c and w_c

The parameter ϕ_c in the burn rate expression was chosen based on DDT tube test data that indicated a drop in burn rate beyond a certain range of explosive solid volume fraction. This parameter allows for accounting the effects of bed permeability on the burn rate. To this end, if the solid volume fraction of the bed is above this value (i.e., $\phi_s > \phi_c$), the bed

restricts the flow of hot-gas through it, thereby reducing the burning rate considerably. The parameter w_c in the burn rate expression was chosen based on inert meso-scale simulations that indicated that beyond a certain range of compaction dissipative work causes a rapid increase in burn rate due widespread agglomeration of hot-spots indicating the likelihood of fast reactive hot-spot interaction times. In this study, a value of $\phi_c = 0.975$ and $w_c = 20$ kJ/kg was chosen that replicated the features of the LANL DDT experiment. For $w_c = 20$ kJ/kg, corresponds to a bulk temperature rise of $\Delta T = w_d/c_v$ of 13K. For the parametric analysis, simulations are performed for $0.95 \leq \phi_c \leq 0.99$ and $17.5 \leq w_c \leq 22.5$ kJ/kg corresponding to a bulk temperature rise of $8.75 \leq \Delta T \leq 15$ K.

Figure 5.48 shows the transition mechanism through the spatial variation of solid volume fraction (ϕ_s) and dissipative compaction work (w_d) for $\phi_c = 0.95$, 0.975 and 0.99. Figure 5.49 shows the transition mechanism through the spatial variation of solid volume fraction (ϕ_s) and dissipative compaction work (w_d) for $\phi_c = 17.5$ kJ/kg, 20 kJ.kg and 22.5 kJ/kg. For comparison, simulation predictions for the base line case is also given here.

As seen in Fig. 5.48 for $\phi_c = 0.95$, regressive burn near the piston surface drives the formation of a "inert-solid-plug" that increases in width as the shock propagates forward. The plug is largely inert and because of very little burn occurring within the plug the secondary compaction wave takes time to grow in strength to facilitate hot-spot facilitated burn that can result in prompt transition to detonation. Compared to the baseline case, for the same simulation time a large residual plug is left behind which is due to the inert behavior imposed by the burn model which also results in higher values for distance- and time-to-detonation for the simulation. For $\phi_c = 0.99$, regressive burn near the piston surface drives the formation of a "inert-solid-plug", that is quickly consumed because of the highly reactive behavior imposed by the burn model. Compared to the baseline case, for the same simulation time the plug is completely consumed and because of rapid burn lower values of distance- and time-to-detonation is predicted. The features predicted in the transition mechanism for these values of ϕ_c are found to be very different and the choice of ϕ_c plays

Effect of varying ϕ_c

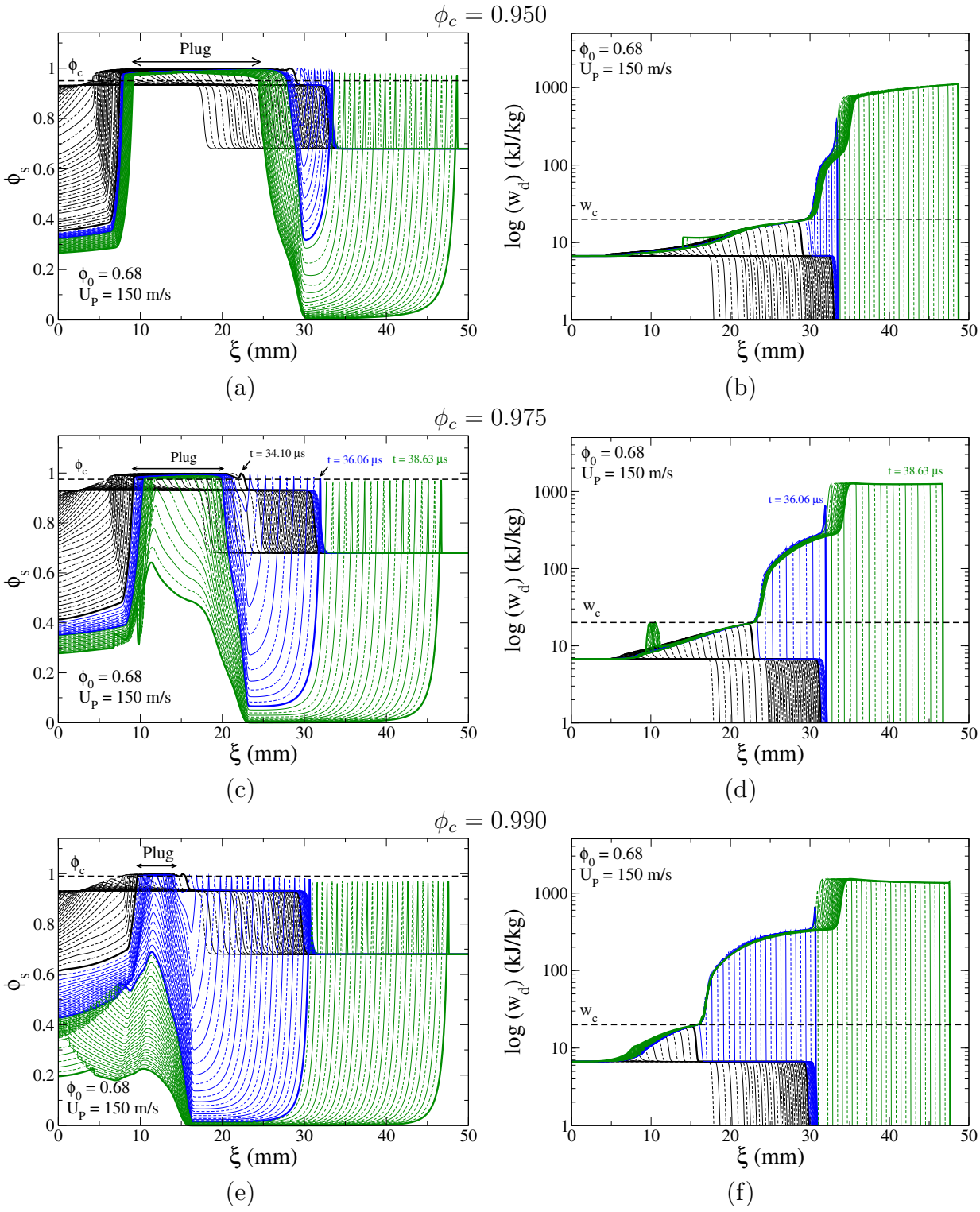

Figure 5.48: Predicted: (a,c,e) variation in solid/explosive volume fraction ϕ_s; and (b,d,f) variation in dissipative work w_d for $\phi_0 = 0.68$ and $U_P = 150$ m/s for ϕ_c=0.950, 0.975 and 0.990 respectively.

Effect of varying w_c

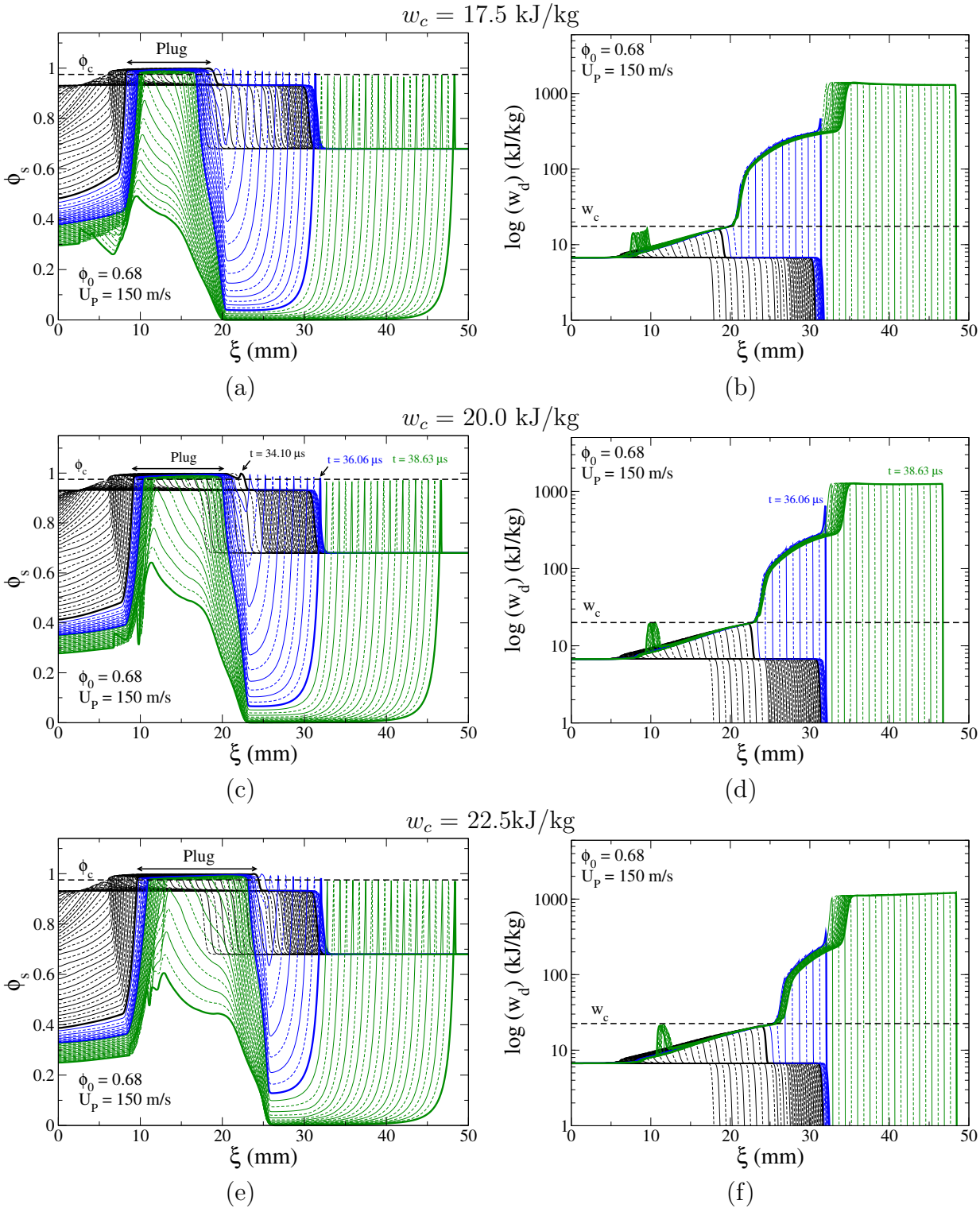

Figure 5.49: Predicted: (a,c,e) variation in solid/explosive volume fraction ϕ_s; and (b,d,f) variation in dissipative work w_d for $\phi_0 = 0.68$ and $U_P = 150$ m/s for w_c=17.5 kJ/kg, 20 kJ/kg and 22.5 kJ/kg respectively.

a key role in replicating the features to the LANL DDT tube test.

As seen in Fig. 5.49 for all three cases, regressive burn near the piston surface drives the formation of a secondary compaction wave that increases in strength resulting in the formation of a "inert-solid-plug". The strength of the burn supported wave increase in time to form a strong shock. As $w_d \rightarrow w_c$, α quickly increases resulting in hot-spot facilitated burn. Therefore, hot-spot facilitated burn results for $w_c = 17.5$ kJ/kg the earliest and latest for $w_c = 22.5$ kJ/kg. Again compared to the baseline case, for the same simulation time, these values of w_c predict lower and higher values of distance- and time-to-detonation transition, respectively. However, the features predicted in the transition mechanism are similar to the baseline case but occur at different location and simulation time. Though not shown here, varying $\Delta\phi$ and Δw also changes the detonation transition mechanism, and care was takes such that the accuracy of the solution was maintained.

5.4.2 Effect of Varying: N

In this section, issues regarding the resolution for the simulation are addressed. Figure 5.50 shows the transition mechanism through the spatial variation solid volume fraction (ϕ_s) and dissipative compaction work (w_d) for the baseline case for $N = 1000$, 2000 and 4000 corresponding to resolution of $\Delta\xi = 50$ μm, 25 μm, and 12.5 μm, respectively. Complete details of the resolution of detoantion structure is given in Ref. [90] and details particular to effect of resolution on detonation transition mechanism is given here.

Here, it is evident that the detonation wave and the relaxation zone following it is under-resolved. Numerical experiments indicate that these regions continue to be under-resolved even for $N > 4000$, suggesting an inherent limitation of using uniformly-spaced grids to predict detonation phenomena. Schwendeman et al. employ an adaptive mesh refinement (AMR) method, where the authors claim that a resolution of 0.005mm is needed to properly resolve the reaction zone. Therefore in the current study, such resolutions are computationally prohibitive. However, as shown in Fig. 5.15, the predictions approach the analytical end state at the end of the reaction zone and the under-resolved physical length

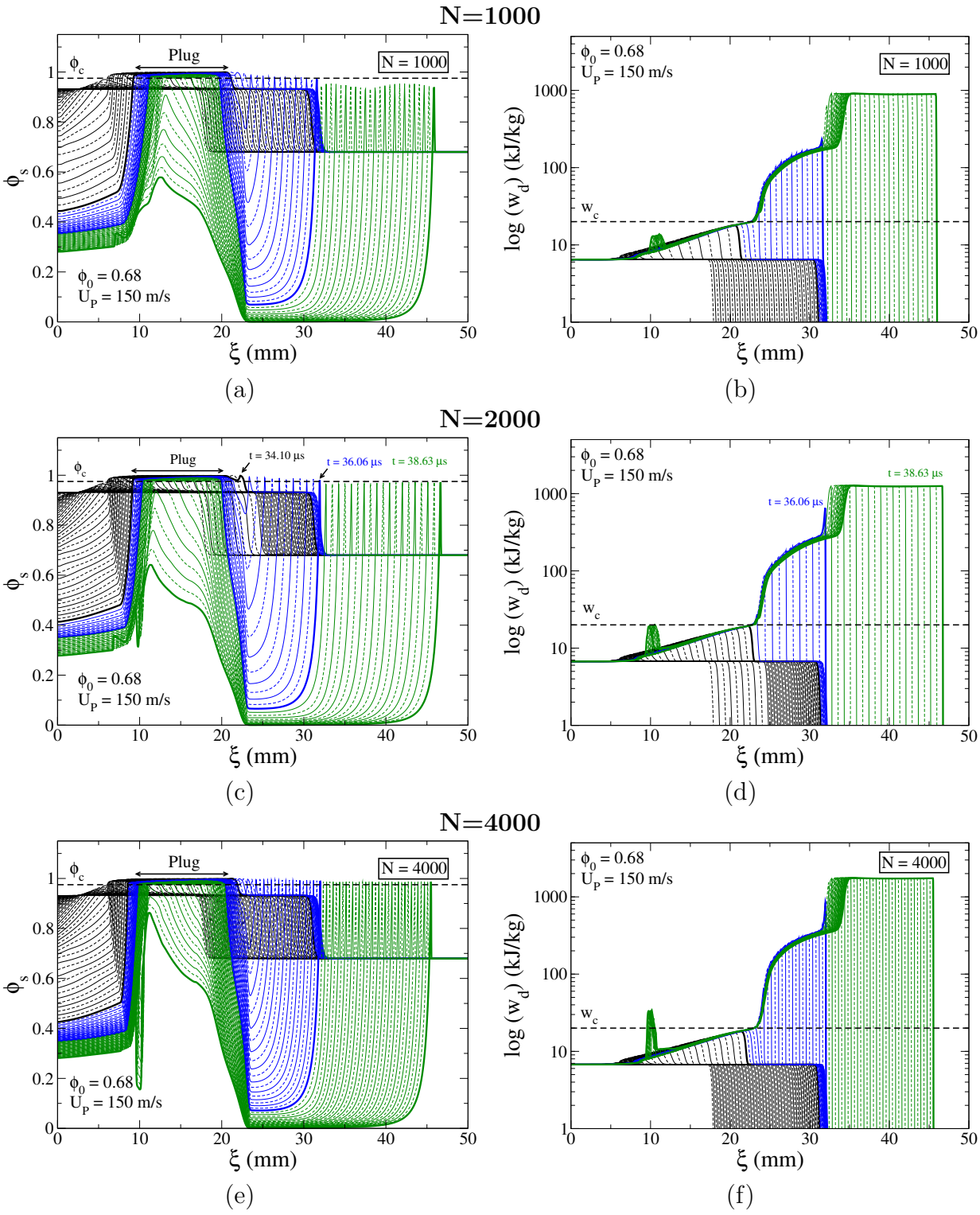

Figure 5.50: Predicted: (a,c,e) variation in solid/explosive volume fraction ϕ_s; and (b,d,f) variation in dissipative work w_d for $\phi_0 = 0.68$ and $U_P = 150$ m/s for N=1000, 2000 and 4000 respectively.

and time scales associated with post-detonation state is very small due to large drag and heat transfer. Consequently, the predictions within the remainder of the reaction zone do not vary substantially with increasing resolution.

For all three cases, the transition mechanism are nearly identical, with increased resolution providing better accuracy within the wave. As seen in Fig. 5.50, the variation in solid volume fraction is identical and slightly enhanced compaction is predicted where retonation originates. The dissipative compaction work is measured as area under a curve, due to additional points under the curve, slightly higher dissipation is predicted to occur as the backward propagating inert shock further compacts the material within the plug. However, the features predicted in the transition mechanism, the distance- and time-to-detonation predicted for all three cases are identical. These results suggest the accuracy of the numerical simulation is sufficient within the reaction zone and expansion wave behind the detonation front. However, AMR schemes is necessary to resolve fine scale structures in the vicinity of the lead shock.

5.4.3 Effect of Varying: ϕ_0

In this section, simulations for solid volume fraction $\phi_0 = 0.58$ and $\phi_0 = 0.90$ are discussed as a check for viability of the developed ignition and burn model. The rate equation for the ignition variable λ_I is given by Eq. 5.1.1. Within the context of this study, to completely describe ignition for a material having initial solid volume fraction ϕ_0, the values of a/I^* and n have to prescribed using meso-scale simulations. Due to unavailability of meso-scale data for $\phi_0 = 0.58$ and $\phi_0 = 0.90$, linearly extrapolated values are used to describe the evolution of the ignition variable. To this end, the same burn model developed in Section 5.1.2 was used for both simulations.

Figure 5.51(a) and 5.51(b) gives the predicted solid volume fraction contours in the $t - \xi$ characteristic plane for $\phi_0 = 0.58$ and $U_P = 150$m/s and $\phi_0 = 0.90$ and $U_P = 300$m/s, respectively. For $\phi_0 = 0.58$, as seen in Fig. 5.51(a), the predicted transition mechanism is similar to the baseline case. As expected, features identical to those discussed in Sec-

tion 5.2.2 are seen here as well. However, within the time simulation time, the plug is not fully consumed and detonation is predicted to occur at the head of the plug. The case demonstrates a transition that is ignition controlled and the predicted CJ detonation has a compaction-led spatial structure. For $\phi_0 = 0.90$, as seen in Fig. 5.51(b), the predicted transition mechanism is similar to the case discussed in Section 5.2.3. As expected, a continuously accelerating combustion/detonation wave is predicted to form within the compacted region whose pressure exceeds the CJ value of ambient material which intensifies dissipation resulting in hot-spot facilitated burn. The burn controlled transition mechanism is predicted here, and the predicted CJ detonation has a compaction-led spatial structure.

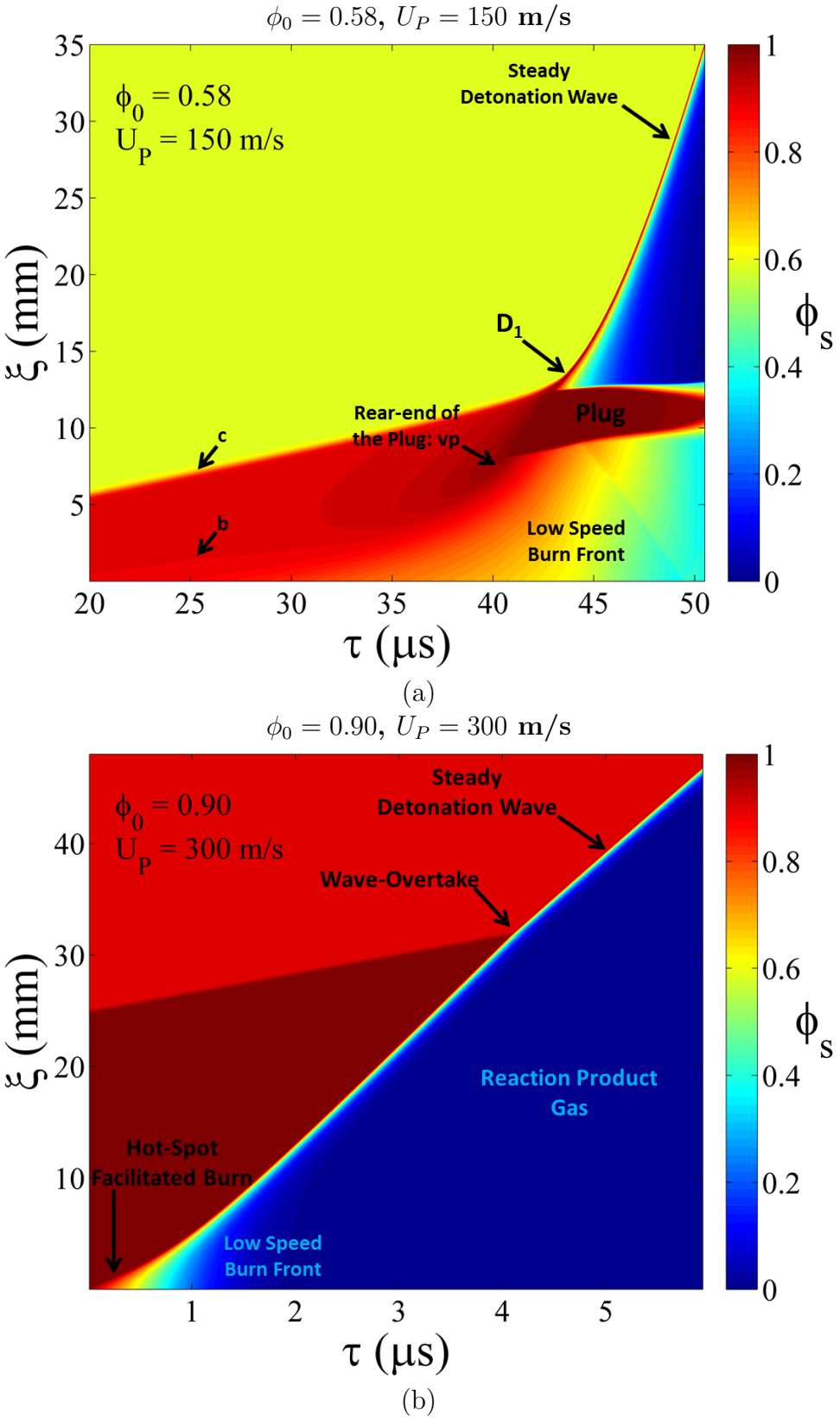

Figure 5.51: Predicted solid/explosive volume fraction contours in the generic $t-\xi$ diagram for (a) $\phi_0 = 0.58$ and $U_P = 150$ m/s; and (b) $\phi_0 = 0.90$ and $U_P = 300$ m/s.

Chapter 6
Conclusions and Recommendations

Continuum theories are routinely used to examine shock initiation of solid explosives that occurs over length scales that are appreciably larger than the particle scale. These theories describe the effective/bulk response of the material and do not resolve the formation, growth, and interaction of reactive hot-spots within the micro-structure. The relative importance of dissipation mechanisms, their dependence on micro-structure and loading conditions, and their influence on macro-scale behavior remain fertile areas of research. Both meso-scale and macro-scale M&S have been performed independently to address these and other issues, but these studies have largely focused on sustained single shocks to establish a foundation for analyzing more complex loading scenarios that may result in detonation.

Successful application of commonly used hot-spot motivated burn models, such as Ignition and Growth [94], hinges on proper tuning of large parameter sets to initiation data. Though many parameters have a physical interpretation based on hot-spots, it can be difficult to establish their values in the absence of hot-spot and initiation data for specific micro-structures under consideration. This effort represents a preliminary step toward the development of a simple technique to incorporate micro-structure-dependent hot-spot features into an ignition and burn model for low density explosives without the complexity of having to resolve particle scale ignition and burn.

In this study, the key objective of the modeling and computational effort was to utilize results from meso-scale M&S to formulate a micro-structure dependent ignition and burn model for low density HMX. The model was used with a macro-scale multi-phase flow theory and a high-resolution computational technique to examine shock initiation. The model is conceptually similar to Ignition and Growth but accounts for ignition in terms of parameters that are explicitly determined from hot-spot fields. Meso-scale models form a

broad class of computational models that simulate particle-scale details, whereas macro-scale models simulate the bulk response of the materials. Both models can be used together to understand different aspects of the same problem. However, the complexity of problems addressed by meos-scale models leads to inherent complexity in the models themselves, and the scalability of meso-scale model can be tens or hundreds of times larger than its corresponding macro-scale model.

6.1 Ignition and Burn Model

In this study, a history-variable dependent ignition model based on variation in hot-spot formation frequency is constructed. Similar history variable approaches, such as the History Variable Reactive Burn (HVRB) model, have been used to account for detonation initiation and propagation in PBXs based on the material's pressure loading history [127]. The rate equations for the ignition variable are posed in terms of history variables: solid pressure (P_s) and dissipative compaction work (w_d) so that differences in the models can be examined for successive shock loading of granular HMX. Pressure is chosen because it represents a conventional measure of shock strength, whereas dissipative compaction work is chosen because of its relevance to hot-spot formation. The ignition model establishes the induction period during which the hot-spots cook-off before the onset of vigorous burn. Though multiple history variable ignition models were formulated, the shock pressure dependent ignition model was used in this study because of simplicity in implementation and reasonable accuracy provided by it.

The volumetric burn rate that describes the explosive combustion rate is constructed as a phenomenological burn model that can describe transition to detonation due to shock initiation of low density HMX. The burn-rate expression associated with gas production and energy release is proportional to the dimensional shape factor (ϵ) and the pressure of the gas phase (P_g). The shape factor accounts for the available burn surface-to-volume ratio of the particles (α), the depletion of the particle size due to combustion ($\frac{\phi_s}{d_0}$), and a characteristic recession velocity for the individual particles (u_{ref}). In particular, the in-

terpretations of the LANL DDT experiment is used to model α that potentially describes various processes leading to detonation transition. Though the transition process is continuous, four prominent phases were identified and a phenomenologically consistent expression for α was developed. The expression for α was found to depend on the mass specific shock dissipative work w_d that accounts for dissipation, and the solid volume fraction ϕ_s that accounts for effects of bed permeability on the burn.

6.2 Transition Mechanism

The final objective of this work was to apply the developed ignition and burn model to a explosive−gas granular bed subjected to piston-impact to predict and analyze transition to detonation mechanism for several impact (U_P) and initial bed configurations (ϕ_0). This analysis provides the ability to predict various features observed in the transition mechanism that are difficult to identify and investigate experimentally due to the short time and length scales associated with transition.

Simulations were performed to illustrate how ignition and burn affect the shock loading HMX having $0.68 \leq \phi_0 \leq 0.83$ for piston speeds within the range of $150 \leq U_P \leq 600$ m/s because of their relevance to DDT and SDT. Within the context of this study, the cases span the range of weak to strong shock initiation. Weak-shock initiation refers to simulations where the dissipative compaction work behind the fully developed primary wave is $w_d \leq w_c$, resulting in initially low speed regressive burn. Strong- shock initiation refers to simulations where the dissipative compaction work behind the lead compaction wave is $w_d > w_c$, resulting in prompt hot-spot facilitated burn. Several numerical experiments were preformed to calibrate the burn model for replicating the features of the LANL DDT experiment.

The ignition and burn model predicts features that are indicative of both ignition and burn controlled transition mechanisms. Weak-shock initiation results in ignition controlled initiation that is characterized by a long ignition time, followed by relatively fast burn and detonation transition. The transition mechanism involves formation of a combustion-

supported secondary shock that accelerates, strengthens, and eliminates residual porosity resulting in initiation once its strength is sufficient to trigger the onset of "hot-spot" facilitated burn. A characteristic feature of this mechanism is the formation of an inert solid plug by the secondary shock that mostly remains intact after initiation. Strong-shock initiation results in burn controlled initiation that is characterized by fast ignition followed by rapid burn and transition to detonation. Because the primary shock strength is sufficient to eliminate porosity, the transition mechanism does not involve formation of a solid plug; rather, it involves continuous acceleration of the burn front to detonation within consolidated material behind the primary shock. As indicated in Pop-Plots, the model reasonably estimates the time- and distance-to-detonation over a wide range of input shock pressure. A parametric analysis was performed to study the effect of varying the model parameters for the burn model and substantial reasoning was provided for choice of parameter values. Simulations were also preformed for $\phi_0 = 0.58$ and $\phi_0 = 0.90$ as a check for viability of the developed model. The model reasonably predicts the features, distance, and time for transition to detonation for the extreme case as-well.

6.3 Recommendations

Several avenues for future work are available to massage the current two-phase model. Multi-phase continuum models have demonstrated an ability to reasonably predict features of DDT, however their validation requires accurate data. In particular, specification of interphase source terms is difficult due to ambiguities concerning their physical interpretation at the continuum scale. Within the energetics community, a long-term modeling objective is the use of meso-scale model predictions to provide better estimates for the source terms. Although a preliminary step in this direction is taken in this study, properly accounting for micro-structure dependent hot-spot features within the context of continuum models remains unclear.

Though the burn model formulated in this study describes many experimental features of DDT, discrepancies exist between predcitions and data for the time and run distance

to detonation. As a near-term objective, a detailed study of other plausible flow variables that could be used to describe the ignition and burn can be performed. As discussed in Section 5.1 and Ref. [111], the dissipative work-dependent ignition model may serve as a better measure to describe ignition because it represents a Lagrangian shock history-dependent variable. Unlike pressure, which depends on the local flow and can decrease as a result of shock interaction processes, dissipative work monotonically increases in accordance with the dissipation inequality. Therefore, dissipative work is constitutionally capable of systematically describing shock desensitization effects. The burn model (discussed in Section 5.1.2) contains parameters that were calibrated by performing several numerical experiments to replicate features of the LANL DDT experiment. Though the choice of parameters predict features commensurate with those observed in experiments, a detailed study to better calibrate these parameters with length and time scale data can be performed. McAfee and co-workers [5] also observed formation of multiple plugs in DDT experiments on granular HMX where the original bed density was 75% TMD. Within the context of the model and burn parameters formulated in this study, such features are not predicted. Though speculative, splitting the second term in Eq. (5.14) by choosing two values of ϕ_c can possibly replicate multiple plug formation because it gives additional flexibility to control the bed permeability which controls the dynamics of plug formation.

Piston initiated tube-tests are often used to study DDT in solid explosives. The initiation of solid explosives by gasless pyrotechnic igniters is also commonly used as an initiation source because of their relative simplicity. A gasless igniter is a device containing a pyrotechnic composition used primarily to ignite other, more difficult-to-ignite materials. They often use electric bridge-wires to heat and ignite the material without producing an input shock unlike piston driven initiation. Once the explosive begins burning, pressurized product gases subsequently trigger transition mechanisms that are qualitatively similar to those described in this study. It would be instructive to simulate initiation by gasless igniters and to validate predictions using available data.

Mandal and Gonthier [151] performed two-dimensional computational analysis of inert compaction wave-boundary interaction with nonplanar rigid boundaries. Extension of their work to reactive systems using the ignition and burn model formulated in this study would enable researchers to characterize how complex multi-dimensional shock-boundary interactions can affect initiation which is important in applications.

A longstanding issue with these models is their inability to resolve fine-scale physical flow features in the vicinity of the detonation wave with the use of uniformly−spaced grids. The required resolution is computationally expensive, which suggests the use of adaptive mesh refinement (AMR) technique as a plausible solution. Further, to reduce the computation time, the FORTRAN 90 code implemented in this study can be parallelized using message passing interface (MPI) and domain decomposition techniques.

References

[1] Krien G, Licht HH, Zierath J (1973) Thermochemical investigation of nitramines. Thermochimica Acta. 6: 465-472.

[2] Munjiza, Antonio A. The combined finite-discrete element method. John Wiley and Sons, 2004.

[3] Davies, P. A. "Accidental initiation of condensed phase explosives during road and rail transport." Journal of hazardous materials 38, no. 1 (1994): 75-88.

[4] Bowden, F. P., and Yoffe, A. D. (1952). Initiation and growth of explosion in liquids and solids. CUP Archive.

[5] McAfee, J. M., Asay, B., Campbell, A. W., and Ramsay, J. B. (1991). The deflagration-to-detonation transition in granular HMX (No. LA-UR-91-2103; CONF-9104269–1-Vugraphs). Los Alamos National Lab., NM (USA).

[6] McAfee, J. M., B. W. Asay, and J. B. Bdzil. Deflagration-to-detonation in granular HMX: Ignition, kinetics, and shock formation. No. LA-UR–93-1754; CONF-930713–14. Los Alamos National Lab., NM (United States), 1993.

[7] Baer, M. R., and Nunziato, J. W. (1986). A two-phase mixture theory for the deflagration-to-detonation transition (DDT) in reactive granular materials. International journal of multiphase flow, 12(6), 861-889.

[8] Butler, P. B., and Krier, H. (1986). Analysis of deflagration to detonation transition in high-energy solid propellants. Combustion and flame, 63(1), 31-48.

[9] Gonthier K. A., Computational Characterization of Impact Induced Multiscale Dissipation in Reactive Solid Composites, DTRA Report.

[10] Gonthier, K. A., and Powers, J. M. (2000). A high-resolution numerical method for a two-phase model of deflagration-to-detonation transition. Journal of Computational Physics, 163(2), 376-433.

[11] Massoni, J., Saurel, R., Baudin, G., and Demol, G. (1999). A mechanistic model for shock initiation of solid explosives. Physics of Fluids (1994-present), 11(3), 710-736.

[12] Bdzil, J. B., and A. K. Kapila. "Shocktodetonation transition: A model problem." Physics of Fluids A: Fluid Dynamics (1989-1993) 4, no. 2 (1992): 409-418.

[13] Kapila, A. K., S. F. Son, J. B. Bdzil, R. Menikoff, and D. S. Stewart. "Two-phase modeling of DDT: Structure of the velocity-relaxation zone." Physics of Fluids (1994-present) 9, no. 12 (1997): 3885-3897.

[14] Bdzil, J. B., Menikoff, R., Son, S. F., Kapila, A. K., and Stewart, D. S. (1999). Two-phase modeling of deflagration-to-detonation transition in granular materials: A critical examination of modeling issues. Physics of Fluids (1994-present), 11(2), 378-402.

[15] Kapila, A. K., Menikoff, R., Bdzil, J. B., Son, S. F., and Stewart, D. S. (2001). Two-phase modeling of deflagration-to-detonation transition in granular materials: Reduced equations. Physics of Fluids (1994-present), 13(10), 3002-3024.

[16] Chinnayya, Ashwin, Eric Daniel, and Richard Saurel. "Modelling detonation waves in heterogeneous energetic materials." Journal of Computational Physics 196, no. 2 (2004): 490-538.

[17] Gonthier, K. A. (2003). Modeling and analysis of reactive compaction for granular energetic solids. Combustion Science and Technology, 175(9), 1679-1709.

[18] Gonthier, K. A. (2004). Predictions for weak mechanical ignition of strain hardened granular explosive. Journal of applied physics, 95(7), 3482-3494.

[19] Menikoff, Ralph. "Granular explosives and initiation sensitivity." http://lib-www. lanl. gov/la-pubs/00796456. pdf (1999): 2.

[20] Menikoff, R., and Kober, E. (2000, April). Compaction waves in granular HMX. In SHOCK COMPRESSION OF CONDENSED MATTER-1999 (Vol. 505, No. 1, pp. 397-400). AIP Publishing.

[21] Benson, D. J., Nesterenko, V. F., Jonsdottir, F., and Meyers, M. A. (1997). Quasistatic and dynamic regimes of granular material deformation under impulse loading. Journal of the Mechanics and Physics of Solids, 45(11), 1955-1999.

[22] Benson, D. J., and Conley, P. (1999). Eulerian finite-element simulations of experimentally acquired HMX microstructures. Modelling and Simulation in Materials Science and Engineering, 7(3), 333.

[23] Menikoff, Ralph. "Compaction wave profiles: simulations of gas gun experiments." Journal of Applied Physics 90, no. 4 (2001): 1754-1760.

[24] Baer, M. R. (2002). Modeling heterogeneous energetic materials at the mesoscale. Thermochimica acta, 384(1), 351-367.

[25] Mas, E. M., B. E. Clements, and D. C. George. "Direct numerical simulations of PBX 9501." In SHOCK COMPRESSION OF CONDENSED MATTER-2003: Proceedings of the Conference of the American Physical Society Topical Group on Shock Compression of Condensed Matter, vol. 706, no. 1, pp. 389-392. AIP Publishing, 2004.

[26] Clements, B. E., and E. M. Mas. "Modeling high explosives with the method of cells and Mori-Tanaka effective medium theories." In AIP CONFERENCE PROCEEDINGS, no. 1, pp. 427-430. IOP INSTITUTE OF PHYSICS PUBLISHING LTD, 2002.

[27] Baer, M. R., M. E. Kipp, and F. van Swol. Micromechanical modeling of heterogeneous energetic materials. No. SAND–98-1945C; CONF-980803–. Sandia National Labs., Albuquerque, NM (United States), 1998.

[28] Menikoff, Ralph, J. J. Dick, and D. E. Hooks. "Analysis of wave profiles for single-crystal cyclotetramethylene tetranitramine." Journal of applied physics 97, no. 2 (2005): 023529.

[29] Borg, J. P., and T. J. Vogler. "Mesoscale simulations of a dart penetrating sand." International Journal of Impact Engineering 35, no. 12 (2008): 1435-1440.

[30] Panchadhar, R., and Gonthier, K. A. (2009). Energy partitioning within a micro-particle cluster due to impact with a rigid planar wall. Computational Mechanics, 44(5), 717-744.

[31] Panchadhara, R., and Gonthier, K. A. (2011). Mesoscale analysis of volumetric and surface dissipation in granular explosive induced by uniaxial deformation waves. Shock Waves, 21(1), 43-61.

[32] Lubarda, Vlado A. Elastoplasticity theory. CRC press, 2001.

[33] Palmer, S. J. P., and J. E. Field. "The Deformation and Fracture of β-HMX." In Proceedings of the Royal Society of London A: Mathematical, Physical and Engineering Sciences, vol. 383, no. 1785, pp. 399-407. The Royal Society, 1982.

[34] Barua, A., and Zhou, M. (2011). A Lagrangian framework for analyzing microstructural level response of polymer-bonded explosives. Modelling and Simulation in Materials Science and Engineering, 19(5), 055001.

[35] Borg, J. P., and T. J. Vogler. "Rapid compaction of granular material: characterizing two-and three-dimensional mesoscale simulations." Shock Waves 23.2 (2013): 153-176.

[36] Hardin, D. B., J. J. Rimoli, and M. Zhou. "Analysis of thermomechanical response of polycrystalline HMX under impact loading through mesoscale simulations." AIP Advances 4, no. 9 (2014): 097136.

[37] Rai, Nirmal K., and H. S. Udaykumar. "Mesoscale simulation of reactive pressed energetic materials under shock loading." Journal of Applied Physics 118, no. 24 (2015): 245905.

[38] Sheffield, S. A., and R. P. Engelke. "Condensed-phase explosives: Shock initiation and detonation phenomena." Shock Wave Science and Technology Reference Library 3: 1.

[39] Griffiths, N., and Groocock, J. M. (1960). 814. The burning to detonation of solid explosives. Journal of the Chemical Society (Resumed), 4154-4162.

[40] Campbell, A. W., W. C. Davis, J. B. Ramsay, and J. R. Travis. "Shock initiation of solid explosives." Physics of Fluids (1958-1988) 4, no. 4 (1961): 511-521.

[41] Campbell, A. W., Davis, W. C., and Travis, J. R. (1961). Shock initiation of detonation in liquid explosives. Physics of Fluids (1958-1988), 4(4), 498-510.

[42] Campbell, A. W. (1980). Deflagration-to-detonation transition in granular HMX (No. LA-UR-80-2016). Los Alamos Scientific Lab., NM (USA).

[43] Chaiken, R. F. "Comments on hypervelocity wave phenomena in condensed explosives." The Journal of Chemical Physics 33, no. 3 (1960): 760-761.

[44] Korotkov, A. I., Sulimov, A. A., Obmenin, A. V., Dubovitskii, V. F., and Kurkin, A. I. (1969). Transition from combustion to detonation in porous explosives. Combustion, Explosion, and Shock Waves, 5(3), 216-222.

[45] Bernecker, R. R., and Price, D. (1974). Studies in the transition from deflagration to detonation in granular explosivesII. Transitional characteristics and mechanisms observed in 91/9 RDX/Wax. Combustion and Flame, 22(1), 119-129.

[46] Bernecker, R. R., and Price, D. (1974). Studies in the transition from deflagration to detonation in granular explosivesIII. Proposed mechanisms for transition and comparison with other proposals in the literature. Combustion and Flame, 22(2), 161-170.

[47] Price, D., and Bernecker, R. R. (1975). Sensitivity of porous explosives to transition from deflagration to detonation. Combustion and Flame, 25, 91-100.

[48] Price, D., and Bernecker, R. R. (1981). DDT behavior of porous columns of simple propellant models and commercial propellants. Combustion and Flame, 42, 307-319.

[49] Bernecker, R. R., H. W. Sandusky, and A. R. Clairmont. "Deflagration-to-detonation transition studies of porous explosive charges in plastic tubes." In 7th Symposium (International) on Detonation, Annapolis, MD, pp. 119-137. 1981.

[50] Bernecker, R. R., H. W. Sandusky, and A. R. Clairmont Jr. "Deflagration-to-detonation transition (DDT) studies of a double-base propellant." In Proceedings of Eighth Symposium (International) on Detonation, pp. 86-194. 1985.

[51] Fifer, R. A., and J. E. Cole. "Transitions from laminar burning for porous crystalline explosives." In Proceedings of the Seventh Symposium (International) of Detonation, Annapolis, MD, Office of Naval Research, NSWC MP-82-334, p. 164. 1981.

[52] Samirant, M. "Deflagration detonation transition in waxed RDX." In 7th Symposium (International) on Detonation, Annapolis, MD. 1981.

[53] Samirant, M. "DDT in RDX and ball powder: Behavior of the porous bed." In 8th Symposium (International) on Detonation, Albuquerque, NM. 1985.

[54] Samirant, M. "DDT-determination of the successive phases of phenomena." In 9th Symposium (Int.) on Detonation, Portland, OR, August, p. 259. 1989.

[55] Luebcke, P. E., Dickson, P. M., and Field, J. E. (1995, March). An experimental study of the deflagration-to-detonation transition in granular secondary explosives. In Proceedings of the Royal Society of London A: Mathematical, Physical and Engineering Sciences (Vol. 448, No. 1934, pp. 439-448). The Royal Society.

[56] Luebcke, P. E., Dickson, P. M., and Field, J. E. (1996). Deflagrationtodetonation transition in granular pentaerythritol tetranitrate. Journal of applied physics, 79(7), 3499-3503.

[57] Baer, Melvin R., Robert J. Gross, Jace W. Nunziato, and Eugene A. Igel. "An experimental and theoretical study of deflagration-to-detonation transition (DDT) in the granular explosive, CP." Combustion and flame 65, no. 1 (1986): 15-30.

[58] Burnside, Nathan J., Steven F. Son, and Blaine W. Asay. "THICK WALLED DDT TUBE EXPERIMENTS1." (1996).

[59] Gifford, M. J., P. E. Luebcke, and J. E. Field. "A new mechanism for deflagration-to-detonation in porous granular explosives." Journal of applied physics 86, no. 3 (1999): 1749-1753.

[60] Gifford, M. J., W. G. Proud, and J. E. Field. "Development of a method for quantification of hot-spots." Thermochimica Acta 384, no. 1 (2002): 285-290.

[61] Gifford, Michael John, W. G. Proud, and J. E. Field. "Observations on type II deflagration-to-detonation transitions." In AIP CONFERENCE PROCEEDINGS, no. 2, pp. 878-881. IOP INSTITUTE OF PHYSICS PUBLISHING LTD, 2002.

[62] Parker, Gary R., Peter Dickson, Blaine W. Asay, and John M. McAfee. "DDT of hot, thermally damaged PBX 9501 in heavy confinement." In 14th International Detonation Symposium. 2010.

[63] Proud, William G., David M. Williamson, John E. Field, and Stephen M. Walley. "Diagnostic techniques in deflagration and detonation studies." Chemistry Central Journal 9, no. 1 (2015): 1-14.

[64] Asay, B. W. (2010). Shock Wave Science and Technology Reference Library, Volume 5, Non-shock initiation of explosives.

[65] Ramsay, J. B., and A. Popolato. Analysis of shock wave and initiation data for solid explosives. No. LA-DC-6992; CONF-651003-3. Los Alamos Scientific Lab., Univ. of California, N. Mex., 1965.

[66] Dallman, J. C., and Jerry Wackerle. Temperature-dependent shock initiation of TATB-based high explosives. No. LA-UR–93-2904; CONF-930713–28. Los Alamos National Lab., NM (United States), 1993.

[67] Sheffield, S. A., Gustavsen, R. L., and Anderson, M. U. (1997). Shock loading of porous high explosives. In High-Pressure Shock Compression of Solids IV (pp. 23-61). Springer New York.

[68] Seay, G. E., and Seely Jr, L. B. (1961). Initiation of a lowdensity PETN pressing by a plane shock wave. Journal of Applied Physics, 32(6), 1092-1097.

[69] Dienes, J. K. (1983, January). Frictional hot-spots and propellant sensitivity. In MRS Proceedings (Vol. 24, p. 373). Cambridge University Press.

[70] Benson, D. J., and Conley, P. (1999). Eulerian finite-element simulations of experimentally acquired HMX microstructures. Modelling and Simulation in Materials Science and Engineering, 7(3), 333.

[71] Frey, R. B. (1980). The initiation of explosive charges by rapid shear. ARMY BALLISTIC RESEARCH LAB ABERDEEN PROVING GROUND MD.

[72] Kipp, M. E. (1985). Modeling granular explosive detonations with shear band concepts (No. SAND-84-1860C; CONF-850706-20). Sandia National Labs., Albuquerque, NM (USA).

[73] Copp, J. L., Napier, S. E., Nash, T., Powell, W. J., Skelly, H., Ubbelohde, A. R., and Woodward, P. (1948). The sensitiveness of explosives. PHILOSOPHICAL TRANSACTIONS OF THE ROYAL SOCIETY OF LONDON SERIES A-MATHEMATICAL AND PHYSICAL SCIENCES, 241(831), 25.

[74] Chaudhri, M. M., and Field, J. E. (1974, September). The role of rapidly compressed gas pockets in the initiation of condensed explosives. In Proceedings of the Royal Society of London A: Mathematical, Physical and Engineering Sciences (Vol. 340, No. 1620, pp. 113-128). The Royal Society.

[75] Baer, M. R., and Trott, W. M. (2002, July). Mesoscale descriptions of shock-loaded heterogeneous porous materials. In AIP Conference Proceedings (No. 1, pp. 713-716). IOP INSTITUTE OF PHYSICS PUBLISHING LTD.

[76] Kumar, D. R., Kumar, R. K., and Philip, P. K. (1999). Simulation of dynamic compaction of metal powders. Journal of applied physics, 85(2), 767-775.

[77] Williamson, R. L. (1990). Parametric studies of dynamic powder consolidation using a particlelevel numerical model. Journal of Applied Physics, 68(3), 1287-1296.

[78] Do, I. P., and Benson, D. J. (2001). Micromechanical modeling of shock-induced chemical reactions in heterogeneous multi-material powder mixtures. International Journal of Plasticity, 17(4), 641-668.

[79] Lowe, C. A., and Greenaway, M. W. (2005). Compaction processes in granular beds composed of different particle sizes. Journal of applied physics, 98(12), 123519.

[80] Chakravarthy, S., Gonthier, K. A., and Panchadhara, R. (2013). Analysis of mesoscale heating by piston supported waves in granular metalized explosive. Modelling and Simulation in Materials Science and Engineering, 21(5), 055016.

[81] Gilbert, J., Chakravarthy, S., and Gonthier, K. A. (2013). Computational analysis of hot-spot formation by quasi-steady deformation waves in porous explosive. Journal of Applied Physics, 113(19), 194901.

[82] Bardenhagen, S. G., and Brackbill, J. U. (1998). Dynamic stress bridging in granular material. Journal of Applied Physics, 83(11), 5732-5740.

[83] Moulard, H. (1989, August). Particular aspect of the explosive particle size effect on shock sensitivity of cast PBX formulations. In Proc. 9th (Int.) Symp. on Detonation (pp. 18-24).

[84] Kuo, K. K., Vichnevetsky, R., and Summerfield, M. (1973). Theory of flame front propagation in porous propellant charges under confinement. AIAA Journal, 11(4), 444-451.

[85] Butler, P. B., and Krier, H. (1986). Analysis of deflagration to detonation transition in high-energy solid propellants. Combustion and flame, 63(1), 31-48.

[86] Powers, J. M., Stewart, D. S., and Krier, H. (1987). Two-phase steady detonation analysis (No. CONF-870868-1). Illinois Univ., Urbana (USA).

[87] Powers, J. M., Stewart, D. S., and Krier, H. (1989). Analysis of steady compaction waves in porous materials. Journal of Applied Mechanics, 56(1), 15-24.

[88] Powers, J. M., Stewart, D. S., and Krier, H. (1990). Theory of two-phase detonation-Part II: Structure. Combustion and Flame, 80(3), 280-303.

[89] Crochet, M. W., and Gonthier, K. A. (2013). Numerical investigation of a modified family of centered schemes applied to multiphase equations with nonconservative sources. Journal of Computational Physics, 255, 266-292.

[90] Crochet, M. W. (2013). MODELING, NUMERICAL ANALYSIS, AND PREDICTIONS FOR THE DETONATION OF MULTICOMPONENT ENERGETIC SOLIDS (Doctoral dissertation, Louisiana State University).

[91] Crochet, M. W., and Gonthier, K. A. (2014). A Riemann problem solution methodology for a class of evolutionary mixture equations with an arbitrary number of components. Applied Numerical Mathematics, 76, 145-165.

[92] Carroll, M. M., and Holt, A. C. (1972). Static and Dynamic PoreCollapse Relations for Ductile Porous Materials. Journal of Applied Physics, 43(4), 1626-1636.

[93] Gonthier, K. A., and Rumchik, C. G. (2007). A multiphase continuum theory for shock loading of metalized explosive. Technical Report ME-TS1-09. Louisiana State University.

[94] Lee, E. L., and Tarver, C. M. (1980). Phenomenological model of shock initiation in heterogeneous explosives. Physics of Fluids (1958-1988), 23(12), 2362-2372.

[95] J. Wackerle, R. L. Rabie, M. J. Ginsberg, and A. B. Anderson. A shock initiation study of PBX-9404. In Actes du Symposium International sur le Comportement des Milieux Denses sour Hautes Pression Dynamiques, pages 127138, 1978.

[96] Anderson, Allan B., M. J. Ginsberg, W. L. Seitz, and Jerry Wackerle. Shock initiation of porous TATB. No. LA-UR-81-871; CONF-810602-20. Los Alamos National Lab., NM (USA), 1981.

[97] Johnson, J. N., Tang, P. K., and Forest, C. A. (1985). Shockwave initiation of heterogeneous reactive solids. Journal of Applied Physics, 57(9), 4323-4334.

[98] Vorthman, John, G. Andrews, and J. Wackerle. Reaction rates from electromagnetic gauge data. No. LA-UR-85-2459; CONF-850706-29. Los Alamos National Lab., NM (USA), 1985.

[99] Nichols , A. L., and Tarver, C. M. (2002, August). A statistical hot spot reactive flow model for shock initiation and detonation of solid high explosives. In Twelfth International Symposium on Detonation, Office of Naval Research, San Diego, CA.

[100] Wescott, B. L., Stewart, D. S., and Davis, W. C. (2005). Equation of state and reaction rate for condensed-phase explosives. Journal of applied physics, 98(5), 053514.

[101] Handley, C. A. (2007, December). The CREST reactive burn model. In SHOCK COMPRESSION OF CONDENSED MATTER2007: Proceedings of the Conference of the American Physical Society Topical Group on Shock Compression of Condensed Matter (Vol. 955, No. 1, pp. 373-376). AIP Publishing.

[102] James, H. R., and B. D. Lambourn. "On the systematics of particle velocity histories in the shock-to-detonation transition regime." Journal of applied physics 100, no. 8 (2006): 084906.

[103] Menikoff, R., and Shaw, M. S. (2010). Reactive burn models and ignition & growth concept. In EPJ Web of Conferences (Vol. 10, p. 00003). EDP Sciences.

[104] Petitpas, F., Richard Saurel, E. Franquet, and A. Chinnayya. "Modelling detonation waves in condensed energetic materials: Multiphase CJ conditions and multidimensional computations." Shock waves 19, no. 5 (2009): 377-401.

[105] Lee, J. H., Knystautas, R., and Yoshikawa, N. (1978). Photochemical initiation of gaseous detonations. Acta Astronautica, 5(11-12), 971-982.

[106] Montgomery, C. J., Khokhlov, A. M., and Oran, E. S. (1998). The effect of mixing irregularities on mixed-region critical length for deflagration-to-detonation transition. Combustion and flame, 115(1), 38-50.

[107] Khokhlov, A. M., Oran, E. S., and Thomas, G. O. (1999). Numerical simulation of deflagration-to-detonation transition: the role of shockflame interactions in turbulent flames. Combustion and Flame, 117(1), 323-339.

[108] Kapila, A. K., D. W. Schwendeman, J. J. Quirk, and T. Hawa. "Mechanisms of detonation formation due to a temperature gradient." Combustion Theory and Modelling 6, no. 4 (2002): 553-594.

[109] Rao, P., Chakravarthy, S., and Gonthier, K. A. (2013, January). Computational Analysis of Compaction Wave Dissipation in Porous Solid Explosives. In 51st AIAA Aerospace Sciences Meeting including the New Horizons Forum and Aerospace Exposition (p. 819).

[110] Rao, P. T., and Gonthier, K. A. (2015). Analysis of Dissipation Induced by Successive Planar Shock Loading of Granular Explosive.

[111] Rao, P. T., and Gonthier, K. A. (2014, July). Mesostructure Dependent Reactive Burn Modeling of Porous Solid Explosives. In 50th AIAA Joint Propulsion Conference.

[112] Rao, P., and Gonthier, K. (2015). Analysis of Compaction Shock Interactions During DDT of Low Density HMX. Bulletin of the American Physical Society, 60.

[113] Rao, P., Chakravarthy, S., and Gonthier, K. A. (2016). Compaction shock dissipation in low density granular explosive. Journal of Applied Physics. 119, 224904.

[114] Kurganov, Alexander, and Eitan Tadmor. "New high-resolution central schemes for nonlinear conservation laws and convectiondiffusion equations." Journal of Computational Physics 160, no. 1 (2000): 241-282.

[115] Kurganov, Alexander, and Eitan Tadmor. "New high-resolution semi-discrete central schemes for HamiltonJacobi equations." Journal of Computational Physics 160, no. 2 (2000): 720-742.

[116] Kurganov, Alexander, and Eitan Tadmor. "Solution of twodimensional Riemann problems for gas dynamics without Riemann problem solvers." Numerical Methods for Partial Differential Equations 18, no. 5 (2002): 584-608.

[117] Strang, Gilbert. "On the construction and comparison of difference schemes." SIAM Journal on Numerical Analysis 5, no. 3 (1968): 506-517.

[118] Hindmarsh, Alan C. Ordinary differential equation system solver. No. LSODE; 000216IBMPC00. Lawrence Livermore National Laboratory, 1992.

[119] Hindmarsh, Alan C. "LSODE and LSODI, two new initial value ordinary differential equation solvers." ACM Signum Newsletter 15, no. 4 (1980): 10-11.

[120] Radhakrishnan, Krishnan, and Alan C. Hindmarsh. "Description and use of LSODE, the Livermore solver for ordinary differential equations." (1993).

[121] Kurganov, Alexander, Sebastian Noelle, and Guergana Petrova. "Semidiscrete central-upwind schemes for hyperbolic conservation laws and Hamilton–Jacobi equations." SIAM Journal on Scientific Computing 23, no. 3 (2001): 707-740.

[122] Tarver, C. M., Chidester, S. K., and Nichols, A. L. (1996). Critical conditions for impact-and shock-induced hot spots in solid explosives. The Journal of Physical Chemistry, 100(14), 5794-5799.

[123] Kooker, D. E. (1990). Modeling of compaction wave behavior in confined granular energetic material (No. BRL-TR-3138). ARMY BALLISTIC RESEARCH LAB ABERDEEN PROVING GROUND MD.

[124] Sandusky, H. W., and Bernecker, R. R. (1985, July). Compressive reaction in porous beds of energetic materials. In Eighth International Symposium on Detonation (pp. 881-891).

[125] Elban, W. L., and Chiarito, M. A. (1986). Quasi-static compaction study of coarse HMX explosive. Powder technology, 46(2), 181-193.

[126] Passman, S. L., Nunziato, J. W., and Walsh, E. K. (1984). A theory of multiphase mixtures (pp. 286-325). Springer New York.

[127] Butler, G. C., Horie, Y., and Richards, W. A., "Hydrocode Simulations of Small-Scale Sympathetic Detonation Tests Involving Reactive Liners," AFRL-RW-EG-TR-2010-052, April 2010.

[128] Engquist, Bjorn, Mitchell Luskin, and Andrew Majda, eds. Computational fluid dynamics and reacting gas flows. Vol. 12. Springer Science & Business Media, 2012.

[129] Li, S. C., F. A. Williams, and S. B. Margolis. Effects of two-phase flow in a model for nitramine deflagration. Combustion and Flame 80, no. 3 (1990): 329-349.

[130] Gambino, James Rosario, Ashwani Kumar Kapila, and Donald William Schwendeman. Sensitivity of run-to-detonation distance in practical explosives. Combustion Theory and Modelling 20, no. 6 (2016): 1088-1117.

[131] Sandusky, H. W., and Bernecker, R. R. (1985, July). Compressive reaction in porous beds of energetic materials. In Eighth International Symposium on Detonation (pp. 881-891).

[132] Kooker, D. E. (1990). Modeling of compaction wave behavior in confined granular energetic material (No. BRL-TR-3138). ARMY BALLISTIC RESEARCH LAB ABERDEEN PROVING GROUND MD.

[133] Gibbs, T. R. (1980). LASL explosive property data (Vol. 4). Univ of California Press.

[134] Hornig, H. C., E. L. Lee, M. Finger, and J. E. Kurrle. EQUATION OF STATE OF DETONATION PRODUCTS. No. UCRL–72173; CONF-700803–5. California Univ., Livermore. Lawrence Radiation Lab., 1970.

[135] Schwendeman, D. W., Wahle, C. W., and Kapila, A. K. (2008). A study of detonation evolution and structure for a model of compressible two-phase reactive flow. Combustion Theory and Modelling, 12(1), 159-204.

[136] S. P. Marsh, *LASL Shock Hugoniot Data* (University of California Press, Berkeley, 1980).

[137] Fickett, W., and W. C. Davis. "Detonation University of California Press." Berkeley, CA (1979): 17.

[138] Krier, Herman, and James R. Stewart. Prediction of Detonation Transition in Porous Explosives from Rapid Compression Loadings. No. UILU-ENG-85-4007. ILLINOIS UNIV AT URBANA DEPT OF MECHANICAL AND INDUSTRIAL ENGINEERING, 1985.

[139] S. Chakravarthy, K. A. Gonthier, and R. Panchadhar, Modelling Simul. Mater. Sci. Eng., 2013, 21 055016.

[140] Garcia, F., Vandersall, K. S., and Tarver, C. M. (2014, May). Shock initiation experiments with ignition and growth modeling on low density HMX. In Journal of Physics: Conference Series (Vol. 500, No. 5, p. 052048). IOP Publishing.

[141] Dick, J. J. (1983). Measurement of the shock initiation sensitivity of low density HMX. Combustion and Flame, 54(1), 121-129.

[142] Son, S. F., Asay, B. W., and Bdzil, J. B. (1996, May). Inert plug formation in the DDT of granular energetic materials. In Proceedings of the conference of the American Physical Society topical group on shock compression of condensed matter (Vol. 370, No. 1, pp. 441-444). AIP Publishing.

[143] Xu, S., and Stewart, D. S. (1997). Deflagration-to-detonation transition in porous energetic materials: a comparative model study. Journal of engineering mathematics, 31(2-3), 143-172.

[144] Menikoff, Ralph. "Errors when shock waves interact due to numerical shock width." SIAM Journal on Scientific Computing 15, no. 5 (1994): 1227-1242.

[145] Menikoff, R. Numerical anomalies mimicking physical effects. No. LA-UR–95-2628; CONF-950846–9. Los Alamos National Lab., NM (United States), 1995.

[146] Menikoff, R., and K. S. Lackner. Anomalous physical effects from artificial numerical length scales. No. LA-UR–95-2135; CONF-9507152–3. Los Alamos National Lab., NM (United States), 1995.

[147] Afanasenkov, A. N. "Retonation Wave upon Shock-Wave Initiation of Detonation of Solid Explosives." Combustion, Explosion and Shock Waves 38, no. 4 (2002): 470-472.

[148] Luebeke, P. E., P. M. Dickson, and J. E. Field. "Investigation of the Process of Deflagration-to-Detonation Transition (DDT) in Granular Secondary Explosives with High-Speed Photography." Defence Science Journal 46, no. 5 (2013): 393-398.

[149] Parker, G. R., and McAfee, J. M. July 2016. Private Communication.

[150] Fedkiw, Ronald P., Tariq Aslam, Barry Merriman, and Stanley Osher. "A non-oscillatory Eulerian approach to interfaces in multimaterial flows (the ghost fluid method)." Journal of computational physics 152, no. 2 (1999): 457-492.

[151] Mandal, Anirban, Computational examination of compaction wave-boundary interaction in granular explosive (2010). LSU Master's Theses. 2944. http://digitalcommons.lsu.edu/gradschool˙theses/2944

Appendix A
End-State Analysis

The end state behind a steady detonation wave corresponding to complete explosive reaction is performed in a manner similar to that of Schwendeman and co-workers [135]. The mixture equations discussed in Chapter 3.2.1 are used here. For the two phase (solid and gas) system, the resulting system of ODE's is given by:

$$\frac{d}{d\xi}\left(\phi_e\rho_e w_e + \phi_g\rho_g w_g\right) = 0, \tag{A.1}$$

$$\frac{d}{d\xi}\left(\phi_e\rho_e w_e^2 + \phi_e P_e + \phi_g\rho_g w_g^2 + \phi_g P_g\right) = 0, \tag{A.2}$$

$$\frac{d}{d\xi}\left[\phi_e\rho_e w_e\left(E_e + \frac{P_e}{\rho_e}\right) + \phi_g\rho_g w_g\left(E_g + \frac{P_g}{\rho_g}\right)\right] = 0, \tag{A.3}$$

where the subscripts e and g denote the solid explosive and gas phases, respectively. The velocities $w_e = u_e - D$ and $w_g = u_g - D$ are the flow velocities calculated relative to the detonation wave. The end state is obtained by integrating Eqs.(A.1)-(A.3) between the limits $\xi = 0$ and $\xi \to -\infty$:

$$\rho_f w_f = \phi_{e_0}\rho_{e_0} w_{e_0} + \phi_{g_0}\rho_{g_0} w_{g_0}, \tag{A.4}$$

$$\rho_f w_f^2 + P_f = \phi_{e_0}\rho_{e_0} w_{e_0}^2 + \phi_{e_0} P_{e_0} + \phi_{g_0}\rho_{g_0} w_{g_0}^2 + \phi_{g_0} P_{g_0}, \tag{A.5}$$

$$\begin{aligned}\rho_f w_f\left(e_f + \frac{w_f^2}{2} + \frac{P_f}{\rho_f}\right) &= \phi_{e_0}\rho_{e_0} w_{e_0}\left(e_{e_0} + \frac{w_{e_0}^2}{2} + \frac{P_{e_0}}{\rho_{e_0}}\right) \\ &\quad + \phi_{g_0}\rho_{g_0} w_{g_0} + \left(e_{g_0} + \frac{w_{g_0}^2}{2} + \frac{P_{g_0}}{\rho_{g_0}}\right),\end{aligned} \tag{A.6}$$

where the quantities on the left correspond to the final state and quantities on the right correspond to the initial state. Assuming the mixture is at rest (i.e. $u_e = u_g = 0$), then Eqs.(A.4)-(A.6) become,

$$\rho_f w_f = -\rho_{m0} D, \tag{A.7}$$

$$\rho_f w_f^2 + P_f = \rho_{m0} D^2 + P_{m0}, \tag{A.8}$$

$$\rho_f w_f \left(e_f + \frac{w_f^2}{2} \right) + w_f P_f = -D \left(e_{m0} \rho_{m0} + P_{m0} + \frac{\rho_{m0} D^2}{2} \right), \tag{A.9}$$

where

$$\rho_{m0} = \phi_{e0} \rho_{e0} + \phi_{g0} \rho_{g0}, \qquad P_{m0} = \phi_{e0} P_{e0} + \phi_{g0} P_{g0}, \qquad e_{m0} = \frac{\phi_{e0} \rho_{e0} e_{e_0} + \phi_{eg0} \rho_{g0} e_{g_0}}{\phi_{e0} \rho_{e0} + \phi_{g0} \rho_{g0}} \tag{A.10}$$

The end-state velocity from Eqs. (A.7) is given by:

$$w_f = -\frac{D v_f}{v_{m0}} \tag{A.11}$$

Using Eqs. (A.11) in Eqs. (A.8) when expressed in terms of mixture quantities yields:

$$P_m = P_{m0} - \left(\frac{D}{v_{m0}} \right)^2 (v_f - v_{m0}) \tag{A.12}$$

This equation involving the pressure and specific volume of the mixture is analogous to the Rayleigh line relation with D specifying the slope of the line the $p_m - v_m$ plane. Eliminating velocity from Eqs. (A.9) gives the locus of the fully reacted Hugoniot:

$$e_f = e_{m0} - \frac{1}{2} (P_f + P_{m0}) (v_f - v_{m0}) \tag{A.13}$$

For a JWL equation of state given by Eqs. (3.22) used in this study, it can easily be showed that the fully reacted Hugoniot is of the form:

$$P_f = \frac{2\omega}{2 v_f + \omega (v_f - v_{m0})} \left[e_{m0} - \frac{P_{m0}}{2} (v_f - v_{m0}) + \frac{v_f}{\omega} \left(A e^{Z_1} + B e^{Z_2} \right) - v_{st} \left(\frac{A e^{Z_1}}{R_1} + \frac{B e^{Z_2}}{R_2} \right) \right] \tag{A.14}$$

where

$$Z_1 = \frac{-R_1 v_f}{v_{st}}, \qquad Z_2 = \frac{-R_2 v_f}{v_s t} \tag{A.15}$$

Table A.1: Initial Conditions and Equation of State Parameters for HMX Detonation.

ρ_{g0} (kg/m^3)	1.0	A (Pa)	778.3 x 10^9
ρ_{e0} (kg/m^3)	1900	B (Pa)	7.071 x 10^9
P_{g0} (Pa)	1.0 x 10^5	C (Pa)	0.643 x 10^9
P_{e0} (Pa)	1.0 x 10^5	R_1	4.2
ϕ_{e0}	0.68, 0.84	R_2	1.0
v_{st} (m^3/kg)	5.26316 x 10^{-4}	ω	0.30

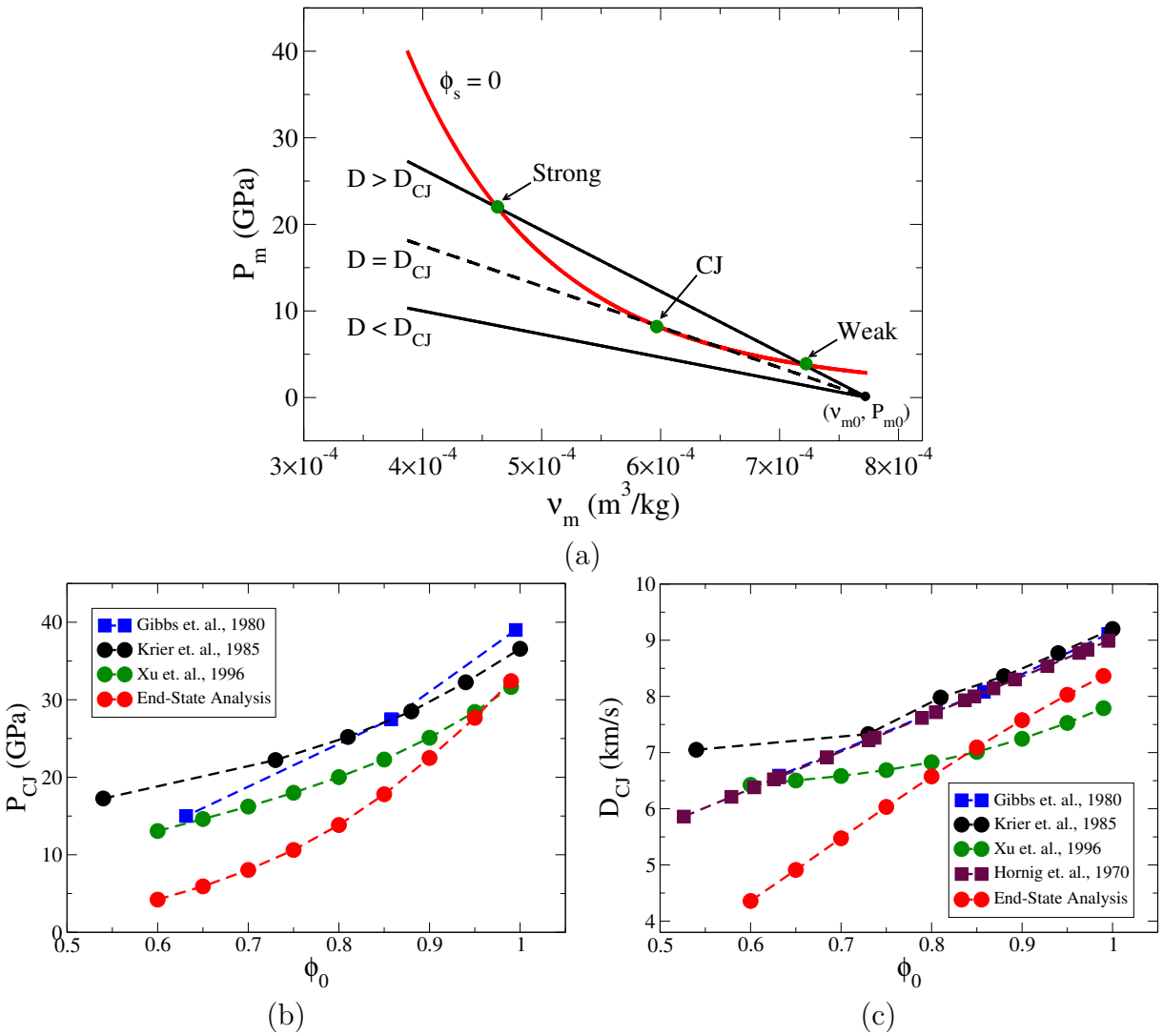

Figure A.1: (a): Fully reacted Hugoniot curve in red ($\phi_s = 0$) with Rayleigh Lines in black for three values of D. Experimental and predicted variation of: (b) steady detonation pressure; and (c) steady detonation wave speed, with initial solid volume fraction.

The values of the constants A, B, ω, R_1, R_2 and other quantities needed to determine the end-state pressure is given in Table A.1. Figure A.1(a) shows the steady solution in the $p_m - v_m$ space. The fully-reacted Hugoniot curve given by Eqs. (A.14) has two vertical asymptotes, one for $v_f < 0$ and one for $v_f > 0$. Only the physically admissible part of the curve is shown here. The Rayleigh line given by Eqs. (A.12), is shown for three values of D. For a given value of D, the Rayleigh line may intersect the fully reacted Hugoniot curve at two points, one point or may not intersect at all. When the Rayleigh line is tangent to the fully reacted Hugoniot, the slope of the line determines the minimum wave speed required for a steady detonation to exist. This minimum wave speed is referred to as the *Chapman-Jouguet* wave speed, D_{CJ}, and the resulting detonation is referred to as CJ detonation. For $D < D_{CJ}$, no steady solution exists, and for $D > D_{CJ}$ there are two steady solutions corresponding to two detonation wave speeds, one on the strong branch with $P_f > P_{CJ}$ and the other on the weak branch with $P_f < P_{CJ}$ [137]. Figures A.1(b) and A.1(c) give the predicted variation in the steady detonation pressure and wave speed with initial solid volume fraction computed using the steady analysis discussed above. This analytical solution for the reaction end-state allows for a verification of the predictions obtained for the macro-scale model discussed in the next section.

Appendix B

Successive Shock Loading

Shock compaction of granular explosives can trigger combustion that results in detonation, even for relatively mild shocks. It is well established that a primary (or lead) shock can desensitize the material to subsequent shocks by reducing porosity. This phenomenon, referred to as shock desensitization, has been observed to occur during DDT of low density granular explosives in which complex interactions between impact and combustion-supported shocks influence the initiation process. In this study, a computational analysis is performed to characterize how rapid successive shock loading of low density HMX affects dissipation and ignition associated with the onset of vigorous burn. Meso-scale simulations are used to predict effective shock profiles and to examine hot-spot fields induced by pore collapse. Resolved shock profiles are compared to those given by macro-scale compaction theory, and both are analyzed in a thermodynamic space that highlights shock desensitization effects.

The problem simulated in this study is generically illustrated in Fig. B.1. Here, a rigid, planar piston impacts a granular explosive having ambient solid volume fraction ϕ_0 with constant speed U_{P1}. The piston supports the transient development of a steady compaction shock that propagates at speed D_1, where $D_1 > U_{P1}$. The shock possesses a thin spatial structure (i.e., compaction zone) within which the initial porosity is reduced resulting in localized dissipative heating in the form of hot-spots at the pore scale. The intensity, size, and spatial proximity of hot-spots depends on both ϕ_0 and shock strength. The hot-spots undergo an induction (or incubation) period following shock passage during which they intensify and begin to interact at the pore scale leading to the onset of a detectable and vigorous burn at the macro-scale referred to in this study as *ignition*. The induction time following shock passage is referred to as the *ignition time*. At a prescribed

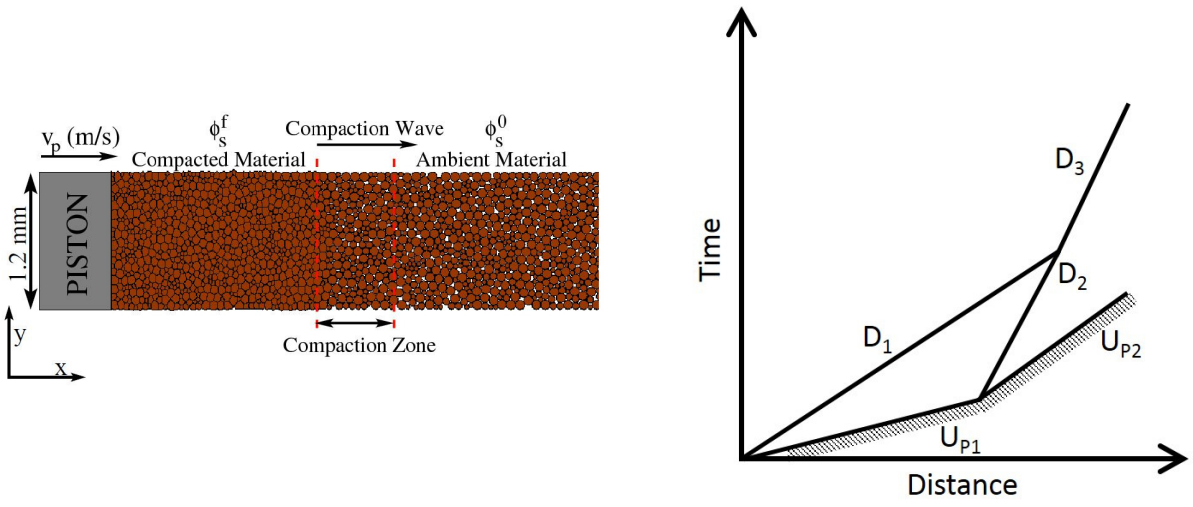

(a) (b)

Figure B.1: (a) Schematic of a typical dynamic compaction process; (b) Position-Time plot illustrating successive shock loading

time following initial impact, the piston's speed is rapidly increased to a higher value U_{P2} which supports the development and propagation of a secondary shock within material precompacted by the lead shock. The secondary shock propagates at speed D_2, where $D_2 > D_1$, and it induces additional dissipative heating as residual porosity is further reduced or eliminated, depending on its strength, which can alter ignition of the material. Because the secondary shock is overdriven with respect to the ambient material, it can result in significant dissipation as it overtakes the lead shock. Subsequently, the resulting transmitted shock strength decays and its speed decreases until a steady shock results in the long time limit propagating at speed D_3 which depends on ϕ_0 and U_{P2}.

- **Results**

Predictions are given in this section that illustrate how successive shock loading of granular HMX affects dissipation and ignition for $\phi_0 = 0.68$ and $\phi_0 = 0.83$, with $U_{P1} = 300$ m/s and $U_{P2} = 500$ m/s. Meso-scale simulations are performed for an ensemble that consists of 6000 deformable particles on a domain length of 10 mm, where each particle is discretized into approximately 400 finite elements. Macro-scale simulations are performed on a piston attached domain of length 50 mm having 5000 computational cells which nu-

merical experiments indicate is sufficient to resolve compaction shocks (≈ 60 cells/shock width). Though different domain lengths are used for the meso- and macro-scale simulations, quasi-steady lead and secondary compaction shocks evolve in all cases enabling shock profiles and interaction structures to be meaningfully compared. The meso-scale domain length is constrained by computational considerations; thus, the longer macro-scale domain enables longer-time wave behavior to be assessed in a computational feasible manner. Position in piston-attached and laboratory frames are related by $\xi = x - U_P t$, where U_P is given by either U_{P1} or U_{P2} depending on the prescribed piston speed transition time. Ignition, prescribed by Eqs. (5.2) and (5.10), is analyzed for macro-scale simulations only.

Figures B.2 and B.4 shows the spatial variation in P_s, u_s, and w_d at different times following initial impact predicted by the meso- and macro-scale simulations for $\phi_0 = 0.68$ and $\phi_0 = 0.84$, respectively. Corresponding times differ between the simulations due to differences in domain lengths and piston transition times. For both simulations, the lead compaction shock, which eliminates much of the initial porosity, propagates a relatively long distance into the domain before the piston speed increases to U_{P2}. Subsequently, a quasi-steady secondary shock quickly develops that eliminates residual porosity in material precompacted by the lead shock. The secondary shock is overdriven relative to the ambient material which has lower impedance than the denser material through which it propagates. Consequently, it experiences a gradual decay in pressure P_s as it overtakes the lead shock and transits to the ambient material. The pressure decay predicted by the meso-scale simulation is faster than that of the macro-scale simulation due to its shorter domain length that facilitates rapid reverberation of release waves between the shock and piston. The shock transmission process is accompanied by a relatively modest increase in solid particle velocity and a substantial increase ($\approx 350\%$) in dissipative compaction work which meso-scale simulations indicate may result in ubiquitous formation of hot-spots [139]. The meso- and macro-scale simulations predict qualitatively similar features that exhibit reasonable quantitative agreement. Quantitative discrepancies may also be due to the stiff equation

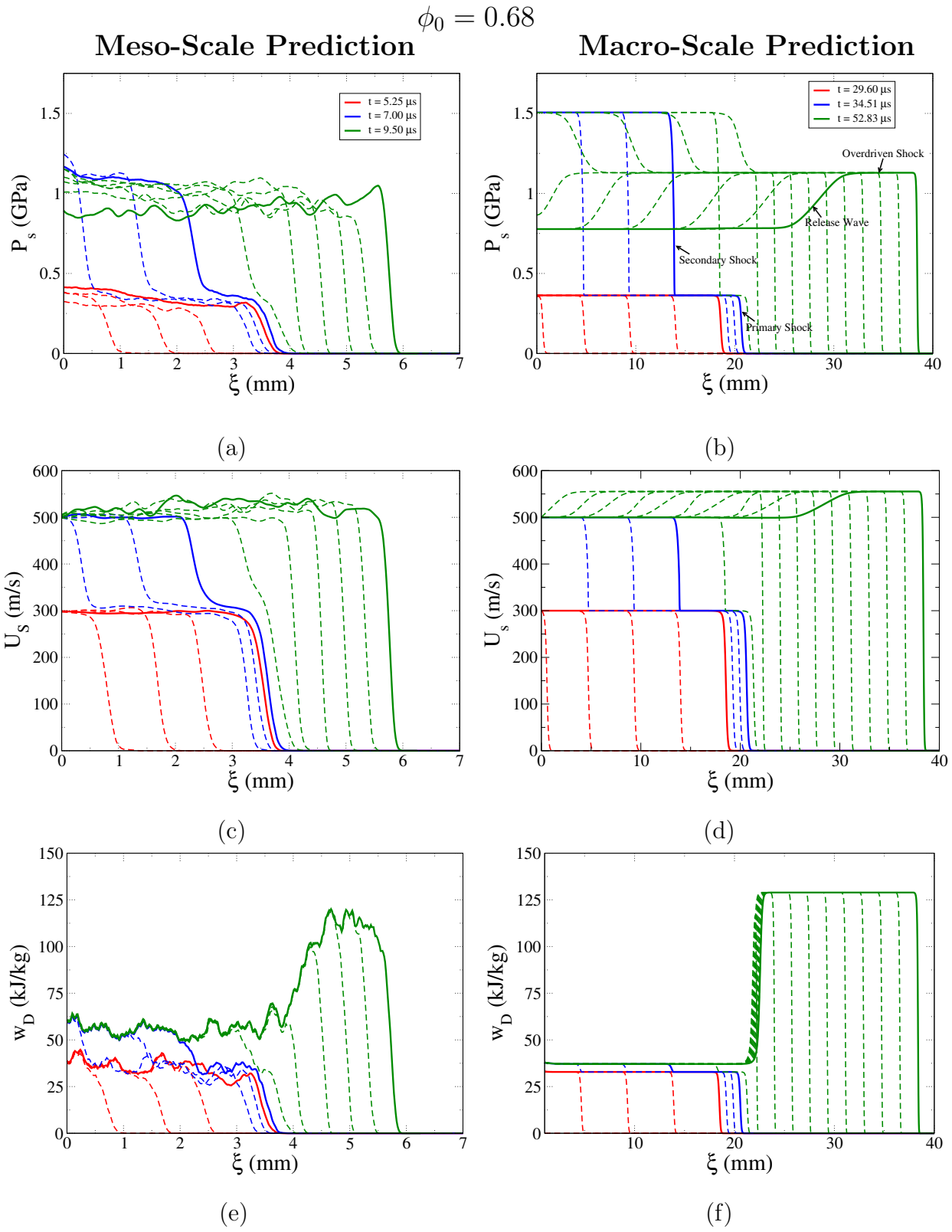

Figure B.2: Comparison of meso- and macro-scale predictions for $\phi_0 = 0.68$ with $U_{P1} = 300$ m/s and $U_{P2} = 500$ m/s: (a)-(b) solid pressure P_s; (c)-(d) solid velocity u_s expressed in a stationary laboratory frame; (e)-(f) dissipative compaction work w_d.

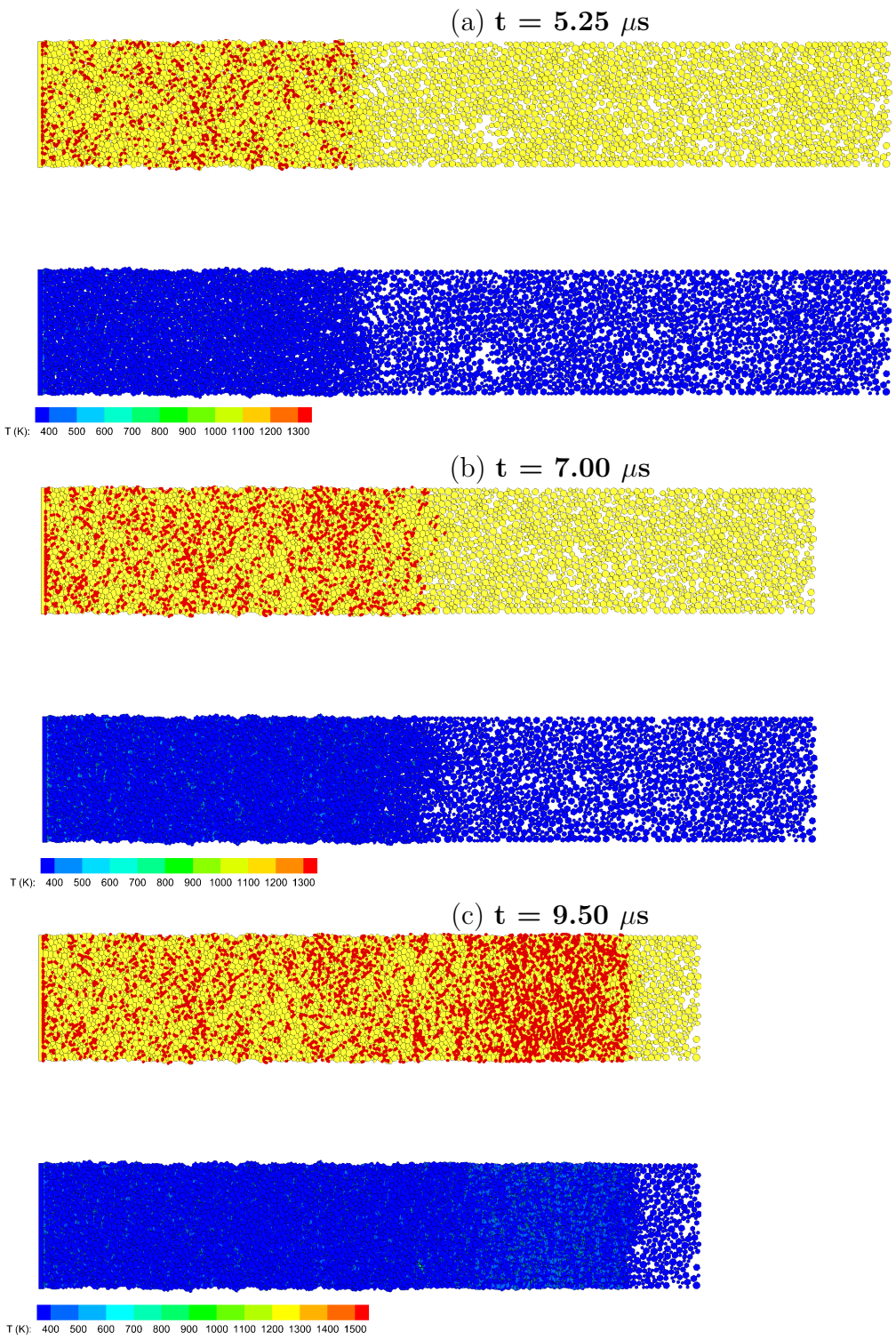

Figure B.3: Contours for the resulting hot-spot fields and temperature for $\phi_0 = 0.68$ with $U_{P1} = 300$ m/s and $U_{P2} = 500$ m/s at: (a) $t = 5.25$ μs; (b) $t = 7.00$ μs; and (c) $t = 9.50$ μs. Regions in red indicate hot-spots and yellow particles represent explosive.

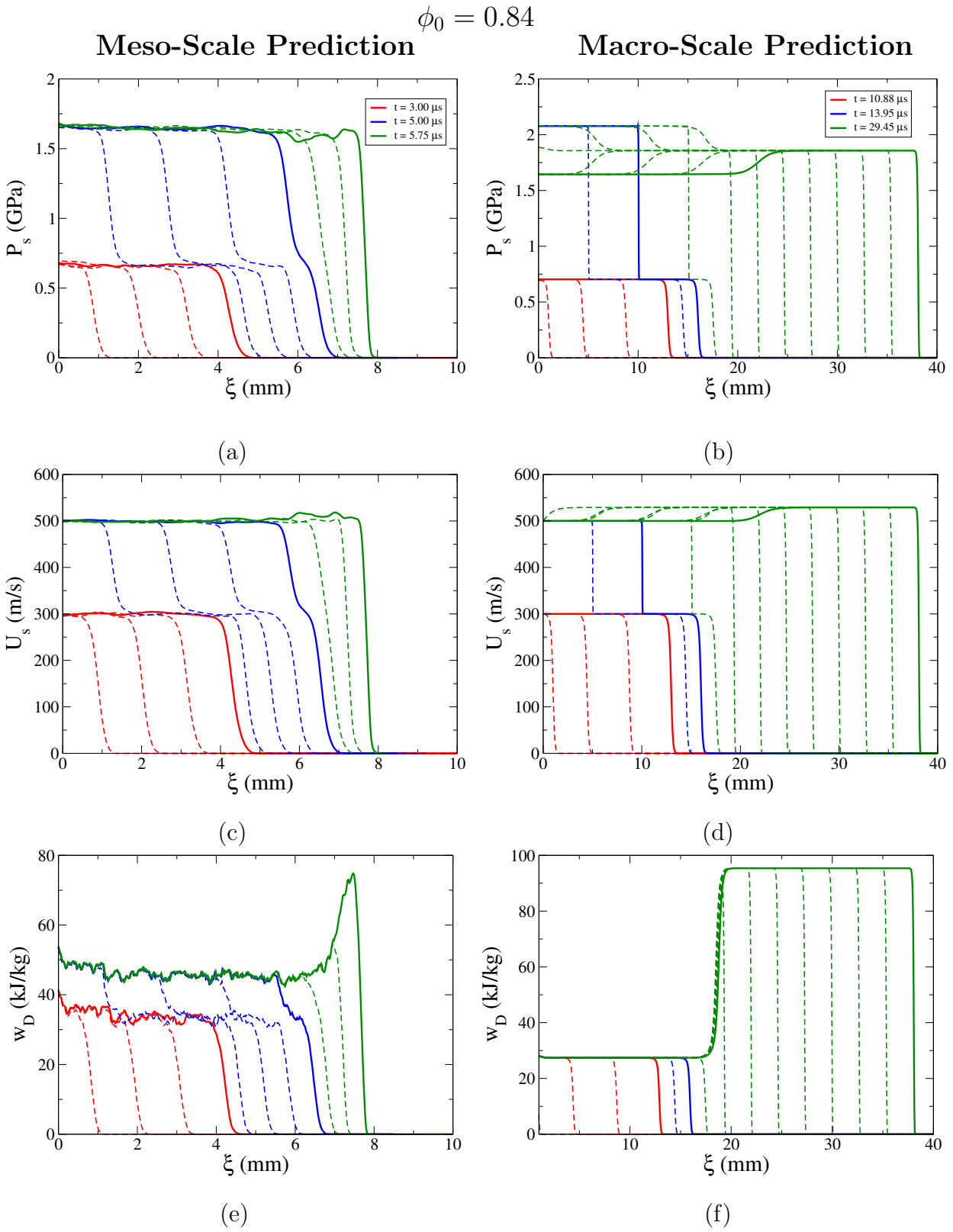

Figure B.4: Comparison of meso- and macro-scale predictions for $\phi_0 = 0.84$ with $U_{P1} = 300$ m/s and $U_{P2} = 500$ m/s: (a)-(b) solid pressure P_s; (c)-(d) solid velocity u_s expressed in a stationary laboratory frame; (e)-(f) dissipative compaction work w_d.

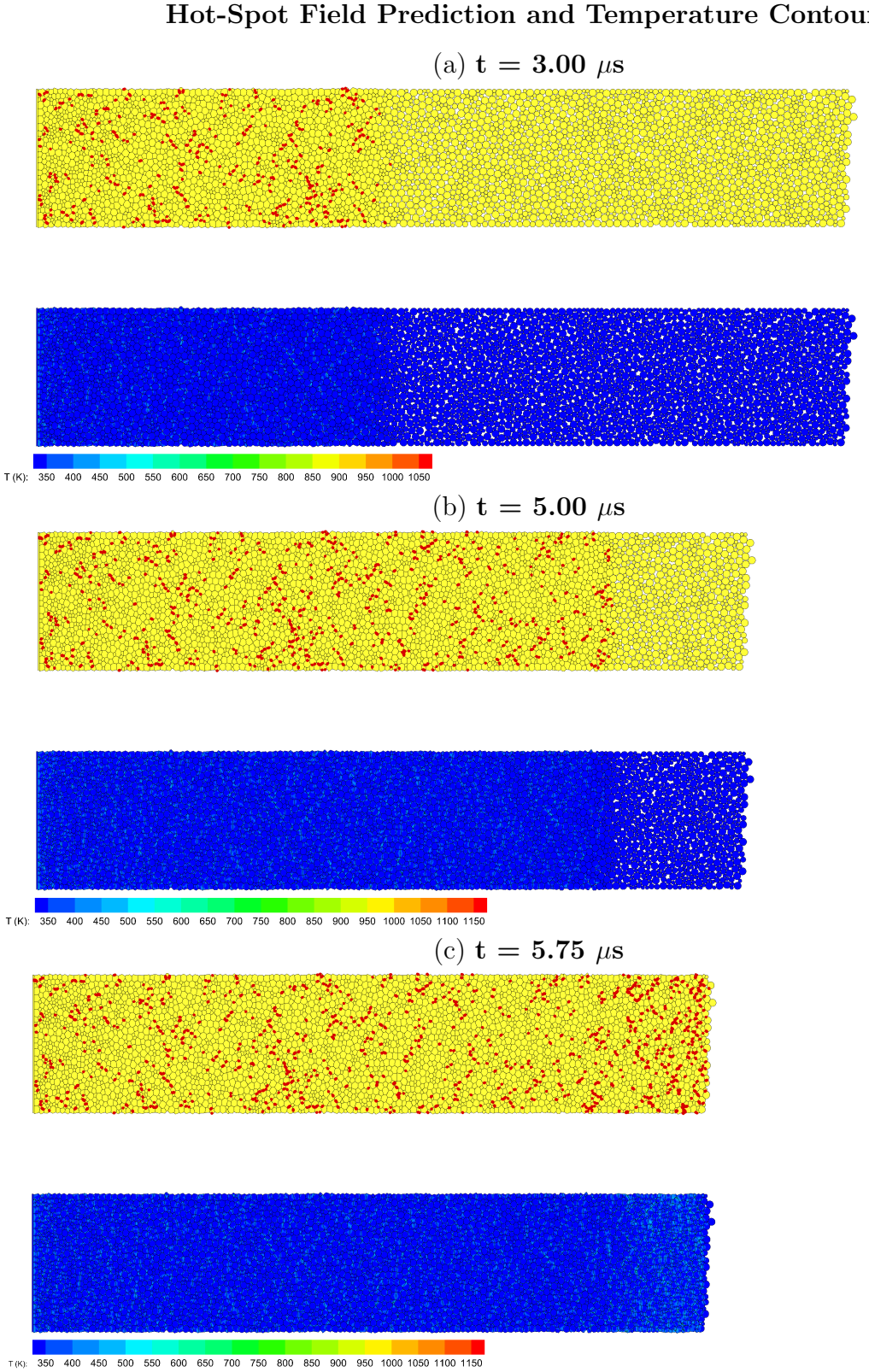

Figure B.5: Contours of the resulting hot-spot fields and temperature for $\phi_0 = 0.84$ with $U_{P1} = 300$ m/s and $U_{P2} = 500$ m/s at: (a) $t = 5.25$ μs; (b) $t = 7.00$ μs; and (c) $t = 9.50$ μs. Regions in red indicate hot-spots and yellow particles represent explosive.

of state used for HMX with the macro-scale model.

Figures B.3 and B.5 shows the complex hot-spot and temperature fields behind the primary shock, secondary shock and overdriven shock for $\phi_0 = 0.68$ and $\phi_0 = 0.84$ corresponding to $U_{P1} = 300$ m/s and $U_{P2} = 500$ m/s. It is evident from the contours that the resulting hot-spot fields consists of hot-spots with varying size, shapes, intensity and proximity. More intense and larger hot-spots are observed in the low density material ($\phi_0 = 0.68$) than the high density material ($\phi_0 = 0.84$) because of higher dissipative heating associated with inelastic pore collapse. This observation is consistent with the wave end-states plots which show larger dissipative work in low density material compared to high density material.

Figure B.6 expresses the predictions of Figs. (B.2) and (B.4) in a phase space characterized by P_s and w_d. This space is chosen because P_s represents a measure of shock strength and w_d represents a measure of hot-spot formation within the material. For comparative purposes, single shock end state predictions given by both the meso- and macro-scale simulations are also shown in the figure. Meso-scale simulations of single shocks indicate that appreciable hot-spot agglomeration results for approximately $w_d > 100$ kJ/kg and $P_s > 1.6$ GPa for $\phi_0 = 0.68$, and for approximately $w_d > 128$ kJ/kg and $P_s > 2.4$ GPa for $\phi_0 = 0.84$; these regions are also highlighted in the figure for reference. Though speculative in the absence of reactive meso-scale data, it is reasonable to expect that shocked material having tightly packed agglomerated hot-spots may significantly reduce reactive hot-spot interaction times, possibly resulting in prompt ignition and initiation. This assertion is consistent with the almost "discontinuous" initiation events observed by McAfee, et al., [5] during DDT in low density HMX resulting from the interaction of piston and combustion driven compaction shocks. Such observations reinforce the need to better characterize dissipation and ignition by rapid and successive shock loading of low density explosives.

Identified on the autonomous solution trajectories of Fig. (B.6) are the equilibrium end states behind the lead and secondary quasi-steady shocks, where the lead shock end states

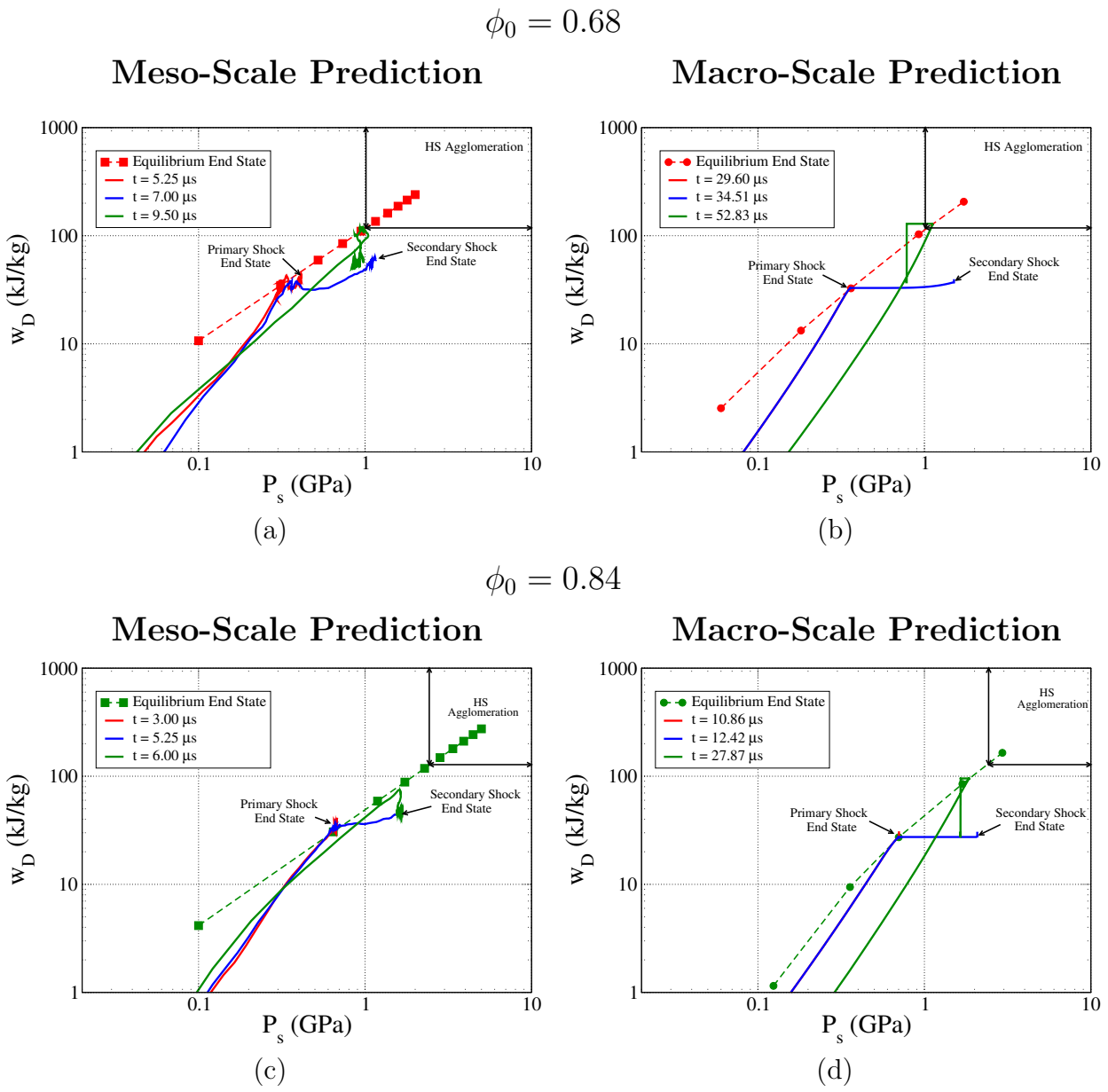

Figure B.6: Comparison of meso- and macro-scale predictions expressed in P_s-w_d phase space for (a)-(b) $\phi_0 = 0.68$ and (c)-(d) $\phi_0 = 0.84$ with $U_{P1} = 300$ m/s and $U_{P2} = 500$ m/s.

lie on the single shock equilibrium curves. Unlike these autonomous solution trajectories, those associated with the interaction process between the lead and secondary shocks are time-dependent; only a single representative trajectory is shown for each of these processes in the plots.

- **Conclusions**

Again, the meso- and macro-scale simulations give comparable results. A few features are noteworthy. First, the lead shock strength is sufficient to eliminate most porosity resulting in relatively small additional increases in w_d by the secondary shock. Consequently, in all cases the value of w_d induced by the secondary shock is substantially lower than that induced by a single shock of equivalent pressure which is indicative of significant shock desensitization. Second, based on an analysis of hot-spots, appreciable agglomeration only results as the secondary shock overtakes the lead shock for the values of U_{P1} and U_{P2} imposed here. This prediction demonstrates how the strength of the secondary shock needed to induce agglomeration is dependent on the strength of the lead shock and the value of ϕ_0. Third, increasing ϕ_0 tends to suppress dissipation and enhance desensitization.

Vita

Pratap Thamanna Rao is from the city of Bangalore, in India. He obtained his Bachelors in Mechanical Engineering degree in 2009 from People's Education Society's Institute of Technology, Bangalore, affiliated to the Visveswaraya Technological University, Karnataka, India. He then worked for about two years as a Trainee Engineer with Mercedes Benz Research and Development India Pvt. Ltd. in the Powertrain: Engine and Transmission group. In Spring 2011, he began his doctoral program in the Department of Mechanical and Industrial Engineering at Louisiana State University under the guidance of Dr. Keith A. Gonthier. He is a candidate for the Ph.D. degree in Mechanical Engineering to be awarded at the Fall 2017 commencement. After his graduation, he plans to work in industry.